QUENCHED RANDOM DISORDER STUDIES IN LIQUID CRYSTAL + AEROSIL DISPERSIONS

by

Aleksander Roshi

A Dissertation
Submitted to the Faculty
of the

WORCESTER POLYTECHNIC INSTITUTE

In partial fulfillment of the requirements for the
Degree of Doctor of Philosophy
in
Physics
by

April 26, 2005

APPROVED:

Germano S. Iannacchione, Professor, Advisor, Chair of Committee

---

Carl W. Garland, Prof. Emeritus, Dept. of Chemistry, MIT

Rafael Garcia, Professor, Dept. of Physics, WPI

Abstract

This thesis presents a series of studies of quenched random disorder (QRD) on liquid crystals. We have used high-resolution AC-Calorimetry, high-resolution X-Ray Diffraction (XRD), X-Ray Intensity Fluctuation Spectroscopy (XIFS), Turbidity, Integrated Low-Angle Light Scattering (ILALS), as well as Polarizing Microscopy to characterize the effects of a nano-colloidal dispersions of aerosils in the phase transitions of several liquid crystals. The aerosil (SIL) is made of 70 Å diameter SiO_2 particles coated with hydroxyl (-OH) groups. The coating allows the SIL particles to hydrogen-bond together, to form a very low density gel in an organic solvent. This provides the quenched random disorder. The liquid crystals of interest are: octyloxycyanobiphenyl ($8OCB$), 4-n-pentylphenylthiol-4'-n-octyloxybenzoate ($\bar{8}$S5), 4'-transbutyl-4-cyano-4-heptyl-bicyclohexane ($CCN47$), and octylcyanobiphenyl ($8CB$). Studies have been carried out as a function of aerosil concentration and temperature spanning the following phase transitions, Isotropic to Nematic (I-N), nematic to smectic-A (N-SmA), smectic-A to smectic-C (SmA-SmC), and crystallization.

A double heat capacity feature is observed at the I-N phase transition with a SIL independent overlap of the heat capacity wings far from the transition and having a non-monotonic variation of the transition temperature. A crossover between low and high SIL density behavior is observed. These features are generally consistent with those on the $8CB + SIL$ system. Differences between the $8CB + SIL$ and our systems lie in the magnitude of the transition temperature shifts, heat capacity suppression, and crossover density between the two regimes of behavior; these indicate a liquid crystal specific effect. Calorimetry, light scattering, and microscopy data coherently combine to allow for an accurate determination of the temperature dependence of the onset of the nematic state. The nematic order develops through two distinct processes while the nematic correlation length mildly decreases. We understand the doubling of the phase transition as due to a cross-over between a random dilution regime - where the silica gel couples to the scalar part of the nematic order parameter - to a random field regime - where the

coupling induces distortions in the director field.

High-resolution XRD has been carried out on SIL dispersions in the liquid crystal $8OCB$. The measurements were made over a temperature range around the bulk *N-SmA* transition temperature. The random gel leads to observable broadening of the x-ray reflection from the smectic layers. The structure factor is well described by modeling the effect of the SILs as a quenched random-field. Dispersed silica surfaces are thought to pin both the direction of the translational ordering and the position of the smectic layers. The latter appears to have the greatest effect on the x-ray lineshape. We show that the SIL gel surface area, as verified by small angle scattering, equates to the variance of the random field. Calorimetric results reveal substantial changes to the specific heat peak associated with the *N-SmA* transition. As the concentration of the SIL increases, the specific heat peak remains sharp yet deceases in magnitude and shifts in temperature in a non-monotonic fashion. Above a certain SIL concentration, the specific heat peak becomes highly smeared and begins to shift smoothly to lower temperatures. The effective critical character of the *N-SmA* transition evolves consistently with the Harris criteria for the relevance of QRD, over the entire range of introduced QRD, and is dominated by finite-size effects.

The *SmA-SmC* remains mean-field for all samples studied consistent with a random-field XY transition being effectively at its upper critical dimension. Its heat capacity maximum at the transition scales as $\rho_S^{-0.5}$ with an apparent evolution from tricritical to a simple mean-field step behavior. Although finite-size scaling is playing a role, these results may be understood as a general stiffening of the liquid crystal (both the nematic elasticity as well as the smectic layer compression modulus B) with silica density.

Finally, we have used multispeckle XIFS to study the structure and the dynamics of a nano-colloidal silica gel dispersed in $8CB$ as a function of the silica density. The silica density of the dispersed SIL gel samples ranged from 0.030 to 0.200 g cm^{-3} and the silica scattering were probed over the q range from 0.03 to 0.15 nm^{-1} (corresponding to length scales from 42 to 209 nm) at a constant temperature of 301.7 K. The gel structure has a fractal dimension in this density range of $d_{\mathrm{f}} \simeq 2.15$ and all samples showed no sign of restructuring (aging) during the experiment. The time autocorrelation functions of the gels show clear density dependent, nonergodic, complex dynamics. The gel relaxation times are very long and (become) bimodal with nonergodic character for densities from 0.100 to 0.160 g cm^{-3}. In this same density range, the fluctuation contrast (strength) is a minimum while a diffusion analysis finds a pseudo-diffusion coefficient near zero. Interestingly the 0.200 density sample shows fast dynamics. This behavior might be related to the nonmonotonic temperature shifts observed in the calorimetric studies.

Table of Contents

List of Figures viii

List of Tables xiii

List of Symbols xv

Acknowledgments xix

Chapter 1
Introduction 1
1.1 Introduction to Liquid Crystals . . . 7
1.2 Nematic Order and the Order Parameter . . . 8
1.3 Smectic Order . . . 11
1.4 Thermodynamics . . . 14
1.5 Phase Transitions . . . 16
1.5.1 Properties of Phase Transitions . . . 17
1.5.1.1 Critical Points . . . 17
1.5.1.2 Symmetry . . . 19
1.5.1.3 Critical Exponents and Universality Classes . . . 20
1.5.1.4 Finite Size and Crossover Effects . . . 23

Chapter 2
Theory 25
2.1 Landau-DeGennes Theory of Phase Transitions . . . 25
2.1.1 *I-N* Transition . . . 27
2.1.2 *N-SmA* Transition . . . 28
2.1.3 *SmA-SmC* Transition . . . 30
2.2 Quenched Random Disorder Models . . . 30
2.2.1 Random Field Ising Model . . . 31
2.2.2 Random Field XY Model . . . 32
2.3 Predictions of Random Field Theories . . . 33

2.3.1 Imry - Ma Domain - Wall Argument 33

Chapter 3
Experimental Techniques **35**
3.1 *AC* Calorimetry 35
3.1.1 Introduction to *AC* Calorimetry 35
3.1.2 Theory of Operation 37
3.1.3 Test of Theory 41
3.1.4 Design and Operation of the *AC* Calorimeter 46
3.1.4.1 Cell Design 46
3.1.4.2 Temperature Control 48
3.1.4.3 Electronic Circuitry 50
3.1.4.4 Thermometry 52
3.1.4.5 Data Acquisition 54
3.2 Non Adiabatic Scanning Calorimetry 57
3.2.1 Introduction to *NAS* Calorimetry 57
3.2.2 Theory of Operation 58
3.2.3 Data Acquisition 60
3.3 Light Scattering 62
3.3.1 Introduction to Light Scattering 62
3.3.2 Turbidity 63
3.3.3 Integrated Low Angle Light Scattering (ILALS) 66
3.4 X-Ray Diffraction 67
3.4.1 X-Ray Diffraction Setup at NSLS-BNL 67
3.4.2 Characterization of background scattering 69
3.5 X-Ray Intensity Fluctuation Spectroscopy 71
3.5.1 Introduction to XIFS 71
3.5.2 X-Ray Beam at APS-ANL 72
3.5.3 Data Reduction and Analysis 76
3.6 Sample Preparation 79
3.6.1 Calorimetry Sample Preparation 79
3.6.2 Light Scattering Sample Preparation 80
3.6.3 X-Ray Diffraction Sample Preparation 81
3.6.4 XIFS Sample Preparation 81
3.7 General Characteristics of Aerosil Gels and Bulk LC's 82
3.7.1 Characteristics of the Aerosil Gel 82
3.7.2 Characteristics of 8CB 84
3.7.3 Characteristics of 8OCB 85
3.7.4 Characteristics of $\bar{8}$S5 86
3.7.5 Characteristics of $CCN47$ 88

Chapter 4
Isotropic to Nematic Phase Transition in Aerosil Disordered Liquid Crystal **90**
4.1 Introduction . . . 90
4.2 *I-N* Transition in $8OCB$ . . . 93
4.2.1 General Description . . . 93
4.2.2 The *I-N* Transition Enthalpies . . . 97
4.2.3 Transition Temperatures . . . 100
4.2.4 Effect of Crystallization . . . 100
4.3 *I-N* Transition in $CCN47$ . . . 104
4.3.1 General Description . . . 104
4.3.2 Calorimetry Results . . . 107
4.3.3 Light Scattering Results . . . 112
4.3.4 Connection of Light Scattering with Calorimetry . . . 117
4.4 Discussion . . . 121

Chapter 5
Nematic to Smectic-*A* Phase Transition in Aerosil Disordered Liquid Crystal **126**
5.1 Introduction . . . 126
5.2 *N-SmA* Transition in $8OCB$ . . . 130
5.2.1 Calorimetric Results . . . 130
5.2.2 X-Ray Scattering Results . . . 140
5.3 *N-SmA* Transition in $\bar{8}S5$ . . . 151
5.3.1 The XY-like *N-SmA* scaling analysis . . . 154
5.4 *N-SmA* Transition in $CCN47$ . . . 158
5.4.1 Calorimetric Results . . . 159
5.5 Discussion . . . 171

Chapter 6
Smectic-*A* to Smectic-*C* Phase Transition in Aerosil Disordered Liquid Crystal **178**
6.1 Introduction . . . 178
6.2 *SmA-SmC* Transition in $\bar{8}S5$ . . . 179
6.2.1 The Landau mean-field *SmA-SmC* scaling analysis . . . 181
6.3 Discussion . . . 183

Chapter 7
XIFS Study of the Structure and the Slow Dynamics of the Aerosil Nano-Gel Dispersed in Liquid Crystal **185**
7.1 Introduction . . . 185
7.2 Structure and Aging . . . 187
7.3 Dynamics . . . 191

7.4 Discussion 199

Chapter 8
Concluding Remarks **201**
8.1 Future Directions 202

Appendix A
AC Calorimetry Control Program **204**
A.1 Fitting the wave-form 204
A.2 Calculation of C_p and φ when using double frequency heating. . . . 205
A.3 Typical Configuration File (*Acp_All.ini*) 206
A.3.1 Notes On How To Use The *Acp_All.ini* File. 207
A.4 C++ Program for AC Calorimetry 208
A.5 C++ Program for Frequency Scan 208

Appendix B
IDL Program for the XIFS Data Analysis **209**

Bibliography **218**

List of Figures

1.1 Cartoon of (a) Isotropic and (b) Nematic phase. 2
1.2 Cartoon of (a) Smectic-A and (b) Smectic-C phase. 3
1.3 Molecular structure of typical rod-like mesogens. 7
1.4 Schematic diagram of the nematic phase. 9
1.5 Schematic diagram of the monolayer Smectic-A phase. 12
1.6 Schematic diagram of the monolayer Smectic-C phase. 13
1.7 18

3.1 Schematic diagram of the One Lump Thermal Model used for AC Calorimetry. 37
3.2 Log - log plot of T_{AC} (upper panel) and φ (lower panel) vs. the frequency ω. 42
3.3 Log - log plot of ωT_{AC} vs ω 44
3.4 Cell designs. a) Envelope type cell. b) Cup and lid type cell 47
3.5 Design of the AC Calorimeter. 49
3.6 Block diagram of Calor A and B, showing all the connections to the instruments. 51
3.7 Schematic draw of the typical behavior of C_{eff} for a first order transition. 60
3.8 Typical configuration of the light scattering geometry. 64
3.9 Typical configuration of x-ray diffraction geometry. 68
3.10 Characteristic background X-ray scattering intensity as a function of wave-vector transfer for three $8OCB + SIL$ dispersions at 353 K. 69
3.11 Schematic diagram of the optical path at the 2-ID-B beamline outside the hutch. 72
3.12 Schematic diagram of the optical path at the 2-ID-B beamline inside the hutch. 73
3.13 Temperature of the XIFS stage as a function of the image number. 74
3.14 Schematics of CCD setup and the ROI definition. 75
3.15 Dependence of the Ring Current Intensity and the Total Image Intensity, on the image number. 77

3.16 Average spatial intensity autocorrelation function. 78
3.17 Cartoon of an aerosil gel formed by diffusion limited aggregation. . 83
3.18 Electron microscope picture of the fractal gel formed by the aggregation of aerosil particles. 84
3.19 Molecular structure of the $8CB$ molecule. 85
3.20 Molecular structure of the $8OCB$ molecule. 85
3.21 Molecular structure of the $\bar{8}$S5 molecule. 86
3.22 Molecular structure of the $CCN47$ molecule. 88

4.1 Excess specific heat, ΔC_p, as a function of temperature about T_{IN} for bulk $8OCB$ and $8OCB + SIL$ samples. 94
4.2 Expanded view of the excess specific heat about the *I-N* transition as a function of temperature. 96
4.3 The real and imaginary *I-N* transition enthalpy as a function of ρ_S. 99
4.4 Dependence on ρ_S of the *I-N* transition temperature, T_{IN}, for $8OCB+SIL$ and $8CB + SIL$ samples. 101
4.5 Behavior of the *I-N* and *N-SmA* excess specific heat of the $\rho_S = 0.051$ sample as a function of temperature relative to T_{IN} before and after sample crystallization. 102
4.6 Behavior of the *I-N* and *N-SmA* excess specific heat of the $\rho_S = 0.220$ sample as a function of temperature about T_{IN} before and after sample crystallization. 103
4.7 Temperature dependence of the specific heat capacity C_p and the birefringence Δn for bulk CCN47. 105
4.8 Close view of the excess specific heat ΔC_p,and the imaginary specific heat C_p'', for cooling scans, about the *I-N* transition, as a function of the *I-N* transition temperature. 108
4.9 Density dependence of the *I-N* transition temperature T_{IN}, of $CCN47$ for heating and cooling scans. 109
4.10 Density dependence of the *I-N* two-phase coexistence region, scaled to the bulk values for three liquid crystals, $8CB$, $8OCB$ and $CCN47$.110
4.11 Density dependence of the *I-N* excess transition enthalpy δH_{IN}^* and the imaginary transitional enthalpy $\delta H_{IN}''$, as measured by *AC* calorimetry. 111
4.12 Temperature dependence of the turbidity τ of $CCN47$, for different silica densities. 113
4.13 $Log - log$ plot of the ρ_S dependence of nematic correlation length ξ_N for $CCN47$. 114
4.14 Plot of the temperature dependence of the nematic correlation length $\xi_N(\Delta T)$ in the two-phase coexistence region as extracted from the $ILALS$ experiment. 115

4.15 Excess specific heat ΔC_B (a) and turbidity τ (b-left axis) measured as a function of the temperature shift ΔT within the two-phase coexistence region for the $CCN47 + SIL$ $\rho_S = 0.075$ sample. 116
4.16 Upper Left Panel: Nematic correlation length ξ_N and ΔC_B for the $\rho_S = 0.075$ sample measured as a function of ΔT. Panels (a), (b), (c): Optical cross-polarized microscope pictures. 118
4.17 Nematic volume fraction ϕ_N obtained from the integral of $\Delta C_B(0.075)$ (solid dots) and deduced from optical measurements $\phi_N \propto \tau/(\Delta n^2 \xi_N)$ (open dots) as a function of ΔT through the two-phase coexistence region. Inset: N volume fraction ϕ_{N2} converted through the low temperature C_p peak, as a function of ρ_S. 119
4.18 Proposed interpretation of the $I - N$ transition mechanism. 120

5.1 Specific heat due to the *N-SmA* phase transition, ΔC_p(NA), as a function of temperature about T* for bulk $8OCB$ and $8OCB$+aerosil samples. 131
5.2 The ρ_S dependence of the *N-SmA* pseudo-transition enthalpy $\delta H_{NA} = \int \Delta C_p(\mathrm{NA}) dT$, scaled by the transition enthalpy of pure $8OCB$ . . 133
5.3 Dependence on ρ_S of the pseudo-transition *N-SmA* temperature, T^* scaled by the bulk value for $8OCB + SIL$ samples 135
5.4 The nematic phase temperature range $\Delta T_N = T_{IN} - T^*$ scaled by the bulk value for $8OCB + SIL$ samples 136
5.5 Dependence on ρ_S of the pseudo-transition *N-SmA* temperature, T* scaled by the pure $8OCB$ *N-SmA* transition temperature for $8OCB$+aerosil samples. 138
5.6 Behavior of the *N-SmA* heat capacity maximum $h_M = \Delta C_p^{max}(NA)$ at T* as a function of ρ_S for the $8OCB$+aerosil samples and for the $8CB$+aerosil samples. 140
5.7 Normalized x-ray scattering intensity of $8OCB$+aerosil dispersions due to short-ranged smectic-A order at low temperatures, (approx. $T^o_{NA} - 25$ K) as a function of wave-vector transfer. 142
5.8 Normalized x-ray scattering intensity due to short-ranged smectic-A order for a typical $8OCB$+aerosil dispersion with $\rho_S = 0.105$ as a function of wave-vector transfer. 143
5.9 Plots showing intensities as a function of temperature. (a) Integrated intensity of the random field term $S^{LT}(\mathbf{q})$ for $\rho_S = 0.051$, 0.220, and 0.489; (b) The amplitude of the thermal contribution to the scattering. 147
5.10 Variation of a_2/σ_1^{LT} for $8OCB$+aerosil as a function of ρ_S. 148
5.11 Parallel correlation lengths for smectic order as a function of temperature for three $8OCB$+aerosil samples. 149
5.12 Plot of the low-temperature mean correlation length for smectic order as a function of ρ_S. 150

5.13 The specific heat of bulk $\bar{8}$S5 on cooling spanning the nematic, smectic-A, and smectic-C phases. 151
5.14 Excess specific heat ΔC_p of the N-SmA transition ± 3.5 K about T_{NA} for bulk $\bar{8}$S5 and $\bar{8}$S5+aerosil samples. 152
5.15 Finite-size scaling analysis of the N-SmA phase transition in $\bar{8}$S5+aerosil on log-log scales. 156
5.16 Excess specific heat capacity and imaginary heat capacity of the N-SmA transition in $CCN47$, about T_{NA}, for heating scans. 160
5.17 Density dependence of the N-SmA, real and imaginary heat capacity peak maximum for $CCN47 + SIL$ samples, as measured by AC calorimetry. 162
5.18 Density dependence of the N-SmA excess transition enthalpy δH^*_{NA}, and imaginary transitional enthalpy $\delta H''_{NA}$, for $CCN47 + SIL$ samples, as measured by AC calorimetry. 164
5.19 a- Upper panel: Density dependence of the T_{NA}, T_{IN}, transition temperatures and the nematic range ΔT_N for $CCN47 + SIL$ samples. Bottom panel: Density dependence of the nematic range, for $CCN47 + SIL$ samples 165
5.20 Density dependence of the effective heat capacity exponent α and the amplitude ratio A^-/A^+ for heating and cooling scans, for $CCN47+$ SIL samples 168
5.21 Density dependence of the temperature gap $T^- - T^+$ and the baseline jump $B^- - B^+$ from the fit, for $CCN47 + SIL$ samples. 170
5.22 Comparison of effective specific heat critical exponent α_{eff} obtained from fitting Eq. (5.6) to the N-SmA phase transition between $8CB$, $8OCB$, $\bar{8}$S5 and $CCN47$, + aerosil samples. See the figure inset for symbol definitions. The solid lines are guide to the eye. 175

6.1 Excess specific heat δC_p of the SmA-SmC phase transition for bulk $\bar{8}$S5 and $\bar{8}$S5+SIL samples. 179
6.2 ρ_S dependence of the mean-field specific heat step δC_{AC}^{Step} of the SmA-SmC phase transition for $\bar{8}$S5+SIL samples. 180
6.3 Scaling plot of A (δC_p at $T = T_{AC}$), obtain from fitting the excess specific heat of the SmA-SmC phase transition to Eq. (6.2), against ρ_S. 182

7.1 Static intensity dependence on the scattering wave vector q. 188
7.2 Static intensity time evolution for the density 0.080 gcm^{-3} (upper panel) and for the density 0.160 gcm^{-3}, (lower panel). 189
7.3 Time evolution of the average dimensionality as given by Eq. 7.1. . 190
7.4 Typical intensity autocorrelation functions $g^{(2)}(q,t)$. 191
7.5 Typical semilog plot of the shifted to 1 autocorrelation functions $g^{(2)}(q,t)$ for $\rho_s = 0.050$, 0.160 and 0.200 samples. 192

7.6 Initial decay time dependence on the experiment duration time. . . 193
7.7 q dependence of the stretching exponent β. 195
7.8 q dependence of the contrast Γ_c and and the decay time tau, from the fit with Eq. (7.3), where β is fixed to 1. 196
7.9 Dependence of the relaxation rate, τ^{-1}, on q^2. 197
7.10 ρ_S dependence of the: a- Upper panel: pseudo-diffusion coefficient, b- Middle panel: average decay time (scaled to the 0.030 sample value), c- Bottom panel: fluctuation contrast. 198

List of Tables

1.1 Summary of the definitions of the standard critical exponents in the language of magnetic systems. 22
1.2 Scaling relations between the critical exponents. 22

3.1 Summary of the frequency scan fit results. 45
3.2 Summary of X-ray background characterization for $8OCB + SIL$ samples 70

4.1 Summary of the calorimetric results for the $I - N$ transition in $8OCB + SIL$ samples. 93
4.2 Summary of the ac-calorimetric results for $CCN47 + SIL$ samples. 107

5.1 Summary of the calorimetric results for the $8OCB$ and $8OCB$+aerosil samples. 132
5.2 Results from fitting the excess specific heat $\Delta C_p(NA)$ associated with the *N-SmA* pseudo-transition of the $8OCB$+aerosil samples with Eq. (5.6). 134
5.3 Sample parameters for seven $8OCB$+aerosil dispersions studied with x-rays. 141
5.4 Summary of the calorimetric results for $\bar{8}$S5+aerosil samples. 153
5.5 Heating scan summary of the results of fitting Eq. (5.6) to the excess specific heat peak ΔC_p of the *N-SmA* phase transition on $\bar{8}$S5+aerosil samples. 155
5.6 Cooling scan summary of the results of fitting Eq. (5.6) to the excess specific heat peak ΔC_p of the *N-SmA* phase transition on $\bar{8}$S5+aerosil samples 157
5.7 Summary of the calorimetric results for $CCN47$+aerosil samples for the *N-SmA* transition. 163
5.8 Results from fitting the excess specific heat $\Delta C_p(NA)$ associated with the heating scans of the *N-SmA* transition of $CCN47$+aerosil samples with Eq. (5.21). 166

5.9 Results from fitting the excess specific heat $\Delta C_p(NA)$ associated with the cooling scans of the *N-SmA* transition of $CCN47$+aerosil samples with Eq. (5.21). 167

6.1 Summary of the results of fitting Eq. (6.2) to the excess specific heat peak δC_p of the *SmA-SmC* phase transition for $\bar{8}$S5+SIL samples. 183

List of Symbols

A	area, Landau free energy phenomenological parameter
$A^{\pm}$	heat capacity critical amplitudes
α	heat capacity critical exponent
$B^{\pm}$	heat capacity critical backgrounds
B	Landau free energy phenomenological parameter
β	order parameter critical exponent
C	heat capacity, Landau free energy phenomenological parameter
C_p	specific heat capacity
ΔC_p	excess specific heat capacity
ΔC_B	excess effective specific heat capacity, $\Delta C_B = C_p^{(NAS)} - C_p^{(AC)}(coex)$
$C\,'$	real heat capacity
$C\,''$	imaginary heat capacity
C^*	preliminary measured heat capacity
γ	susceptibility critical exponent
D	Landau free energy phenomenological parameter
$D^{\pm}$	correction to scaling amplitudes
d	dimensionality of a system, sample thickness
Δ	correction to scaling exponent
δ	equation of state critical exponent

E	energy
F	Landau free energy
f	Landau free energy density
$G^{(2)}$	intensity-intensity autocorrelation function
H	enthalpy, magnetic field intensity
δH	transition enthalpy
δH^*	effective transition enthalpy as measured from AC calorimetry
$\delta H''$	imaginary transition enthalpy
ΔH	latent heat
h	random field interaction strength
I	light intensity, current intensity
i	imaginary constant $= \sqrt{-1}$
η	pair correlation length critical exponent
J	spin-spin exchange interaction
$\vec{k}$	wavevector,
k, k_0	wavevector amplitude, $k_0 = 2\pi/\lambda$
L	coupling constant of the Landau free energy
ℓ_θ	thermal diffusion length
λ	wavelength
M	magnetization
m	magnetization density
n	refractive index
Δn	birefringence
$\hat{n}$	nematic director
ν	correlation length critical exponent
ω	frequency of AC power, tilt angle of SmC phase

Ω	solid angle
P	pressure
P_0	amplitude of AC power
Ψ	N-A complex order parameter
Q	heat
Q_{ij}	I-N tensor order parameter
$\vec{q}$	scattering wave vector
q	scattering wave vector amplitude
R	thermal resistance, radius, ohmic resistance
$\vec{r}$	position vector
r	position vector amplitude
ρ	density
ρ_S	conjugate density, (grams of silica per volume of liquid crystal)
ϱ	Sma-SmC order parameter
S	entropy, I-N scalar order parameter
σ	diffusion crosssection
T	temperature
T_{AC}	amplitude of temperature oscillations
t	reduced temperature, time
τ	characteristic time constant, turbidity
T_c	critical temperature
T^{**}	nematic superheating temperature
U	internal Energy
V	volume
ξ_N	nematic correlation length
W	work

Φ absolute phase shift between temperature and power oscillations

ϕ, θ, ω angles

ϕ_N nematic fraction

φ relative phase shift between temperature and power oscillations, phase of *Sma-SmC* order parameter

Acknowledgments

I am deeply indebted to my advisor Professor Germano S. Iannacchione, for his excellent guidance, assistance and encouragement throughout this work. Germano taught me a lot about experimental physics, technical writing and presentation techniques. He also gave me the opportunity to take part in several other projects that are part of this thesis, as well as supported me financially with the NSF-Career grant No. DMR-0092786. Germano, Thank you very much.

I really appreciate a lot the help from all the members of the Physics department at WPI, but especially that of the two secretaries, Earline S. Rich and Jacqueline H. Malone. Special thanks go to the department heads, Thomas Keil and John Norbury for providing financial and moral support. I would like to thank also Roger Steele for his technical assistance, and Professor Rafael Garcia for serving on my thesis committee.

I would like to thank all the people outside the department with which I had the pleasure and honor to collaborate. Firstly, Paul Clegg and his advisor Robert Birgeneau from the University of Toronto, Marco Caggioni and his advisor Tomaso Bellini, from Italy, David Paterson and Ian McNulty, from the Argonne National Laboratory. Special thanks go to Professor Carl W. Garland for his excellent comments and insights on my thesis, and for serving on my thesis committee.

Here is my chance to thank my cousins Spiro and Arian for their help in my application for the PhD program at WPI. I am also very grateful to my mother and my sister for their moral support. Lastly and most importantly, I thank my lovely fiancee, Edlira Zeneli, for her love, support and understanding. Edi, thank you.

Dedicated to my late father, Kosta Roshi.

Dedicated to my mother Vasilika

and my sister Eftimia Roshi.

For their immense love and support.

Chapter 1

Introduction

In 1888, the Austrian born botanist Friedrich Reinitzer, working in the Institute of Plant Physiology at the University of Prague, discovered a new phenomenon. Reinitzer was conducting experiments on a cholesterol based substance trying to figure out the correct formula and molecular weight of cholesterol. When he tried to determine the melting point, which is an important indicator of the purity of a substance, he was struck by the fact that this substance seemed to have two melting points. At 145.5°C the solid crystal melted into a cloudy liquid until 178.5°C where the cloudiness suddenly disappeared, giving way to a clear transparent liquid. Initially Reinitzer thought this might be a sign of impurities in the material, but further purification did not alter this behavior.

At this time Otto Lehmann, a German physicist from Karlsruhe and an expert in crystal optics, had invented a microscope that allowed control of the sample temperature. Reinitzer sent some of his purified cholesterol samples to Lehmann for study. Gradually, Lehmann became convinced that this sample was not a simple mixture of solid and liquid components but was, instead, a newly discovered state of matter that showed liquid and solid properties simultaneously. In time Lehmann came up with the name "***Liquid Crystals***" for these substances. Today, thanks to Reinitzer, Lehmann and their followers, we know that thousands of other substances have a diversity of states between the well known solid and liquid states.

Liquid crystals (LC) are partly ordered materials that exhibit many intermediate thermodynamically stable phases between their solid and liquid states, two of the most important being the "**Nematic**" and the "**Smectic**" phases. Their

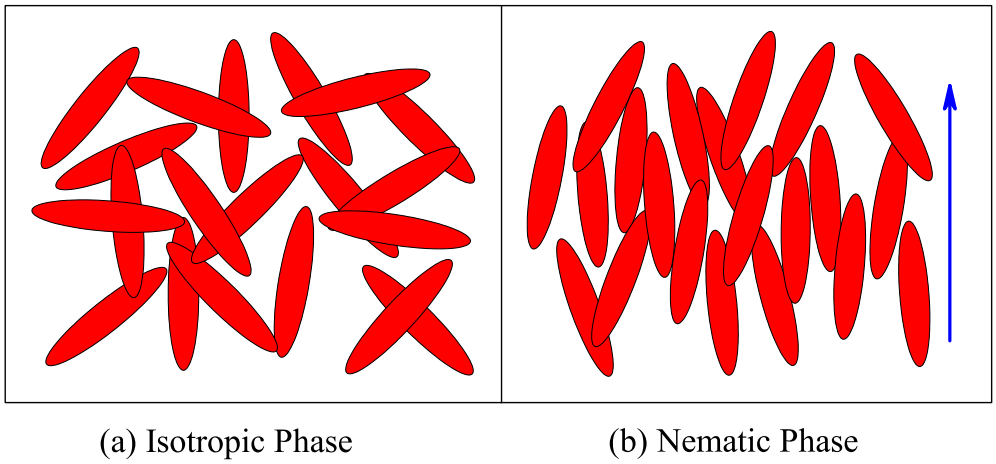

Figure 1.1. Cartoon of (a) Isotropic and (b) Nematic phase.

molecules are often shaped like rods or plates or some other anisotropic form that encourage them to align collectively along a certain direction. We shall be interested in rod-shaped LCs and will discuss and illustrate only this case. In their Isotropic (I) phase [Fig. 1.1 (a)], these molecules display neither positional nor orientational order. This is the normal liquid phase. In the Nematic (N) phase [Fig. 1.1 (b)] the LC molecules have a high degree of long-range orientational order but no long-range translational order. The direction of the preferred alignment can be described by a unit vector, $\hat{n}$, the so-called "**Nematic Director**".

In reality, the orientation of individual molecules varies significantly from that of the director. Furthermore the director is not the same throughout the sample. Thus the sample can be considered a collection of large domains, where, inside a domain a single director can be defined. The transition from one domain to another is smooth and continuous, so there are no real boundaries or surfaces that define these domains (except for defects). Thus the director smoothly changes from one domain to another. A special type of nematic phase, called a chiral nematic or cholesteric (N^*), is formed when the molecules are chiral. They organize themselves in a strongly twisted manner with a helix-like orientation of the director. The distance over which the director rotates one full turn in the helix is called the "**Pitch**".

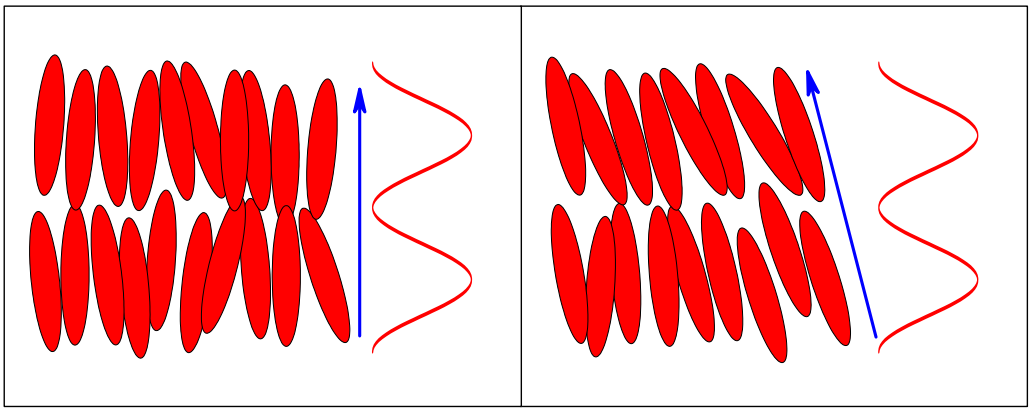

Figure 1.2. Cartoon of (a) Smectic-A and (b) Smectic-C phase.

The smectic phases are characterized by additional degrees of transitional order where the molecules are arranged in layers, which can be considered as one-dimensional (*1-d*) density waves or (*2-d*) liquids. In the **Smectic-*A*** (*SmA*) phase [Fig. 1.2 (a)] the orientation of the molecules is perpendicular to the layer plane (parallel to the layer normal), whereas in the **Smectic-*C*** (*SmC*) phase [Fig. 1.2 (b)] the molecules and the director are tilted with respect to the layer plane. For both *SmA* and *SmC* phases, in-layer positioning of molecules is completely random and liquid like. There exist many sub-phases of the smectic phase, which exhibit variations of the layer spacing, the twist, and the tilt. Some other variations exhibit in-layer bond-orientational ordering, like the Hexatic-*B* or Smectic-*I*, for example. These phases have a closer resemblance to a solid, which is fully ordered translationally.

In general, from a mechanical point of view, *LC*s are more similar to liquids. They can flow easily and show little or no resistance to stresses (shear modulus $\simeq 0$). As a result of their orientational order their mechanical properties are anisotropic; hence they differ from simple liquids by showing effects like elastic or frictional torques which act on director deformations. Related to the partial ordering of molecules are their remarkable electro-optical properties which make *LC*s more similar to solids. *LC*s show optical birefringence, nonlinear optical

behavior as well as anisotropic dielectric and magnetic susceptibilities. The fact that these properties are carried from a soft material makes them very sensitive to external mechanical, electrical or optical manipulations. This is the origin of most of their useful applications in everyday life.

There are several aspects related with LCs that make them very suitable for research purposes.

- First is their richness of phases and phase transitions. Some of the very well known phases were mentioned above, but there exist many more phases with different degrees of translational ordering; sub-varieties of SmA, SmC, hexatic as well as their twisted (chiral) analog, twisted-grain boundary and blue phases to name a few.

- Second, these phases occur mostly near or above room temperature, thus being easy to reach without the need of complicated temperature control systems.

- Third, the transition from one phase to the other can be easily controlled by changing the temperature (thermotropic phase transitions) or concentration (lyotropic phase transitions).

- Fourth, the materials themselves are generally easily available, or not very expensive to produce.

- Fifth and above all, the developments in renormalization group theory and the idea of universality make the results of studies on phase transitions and critical phenomena in liquid crystals applicable to many other different physical systems. They also provide insights to the behavior of the critical exponents or parameters near the critical points for systems that share the same universality class.

Liquid crystals also provide the opportunity to study many types of phase transitions in the presence of surfaces or quenched disorder. These are of great interest in the theoretical understanding of the statistical mechanics of disordered systems. To date, statistical mechanics has been very successful in describing pure systems or those with annealed disorder. Theoretical predictions have been proved by experiment and there is a solid understanding of the basic phenomena. Quenched

disorder on the other hand is more difficult to implement and quantify, than annealed disorder. A considerable amount of theoretical and experimental work has been expended on the study of the effect of quenched random disorder on phase transitions and critical phenomena. Many experimental methods, like calorimetry, x-ray, neutron, light scattering, NMR, optical microscopy, etc. have been used to study the disordered *LC*s at different phase transitions, disorder densities and types of disordering components. Each of these techniques are sensitive to a specific property of the liquid crystal and, when results are taken together, there is a better understanding of their behavior. For example, x-ray scattering provides information about the structure and the correlation lengths of translational order; NMR can probe the molecular/director orientation and intermolecular relaxation rates. And light scattering can provide information about the energy, structure and dynamics up to the length scale of the light used. In contrast, high-resolution *AC* calorimetry is a direct measure of the thermal response of the system; is sensitive to all the thermal excitations present, and their effect on the energy of the system. As such it provides direct and unambiguous evidence of a phase transition, since there is always an associated heat capacity feature related to a phase transition. This, although it might seem to complicate any possible interpretations, provides a means of viewing all of the various influences like surface interactions, finite size effects, coupled order parameters, external fields etc., acting together on a phase transition.

Unlike idealized or pure systems that physicists study most of the time, the real world is full of "imperfections." Ideal systems are usually an exception rather than the normal state of affairs in nature. As an example consider biological systems which are never pure single component systems. The self organization of molecules and proteins to form very complex structures almost never happens in the clean room environment of the lab. Phase transitions also are modified by the presence of the random disorder which can be modelled as a random field present in the system. Studying the effect of disorder on various phase transitions has been a very challenging task both theoretically and experimentally. Since the work of Fishman and Aharony in a dilute anti-ferromagnet [1], there has been a lot of research interest in the field of quenched random disorder and of the random-field theories. Furthermore, the study of random disorder in *LC*s has been given a lot

of attention recently, because of the abundance of phase transitions in them, some of which don't have a magnetic analog. For example, putting LC in a random aerogel network was easily achieved and such systems have been studied with several methods including calorimetry, x-ray or light scattering.

Unlike the LC + Aerogel systems, where the aerogel network is rigid and elastically quite stiff, LC + Aerosil (SIL) systems created by dispersing silica aerosil particles in a liquid crystal, result in a much weaker fractal gel structure. This structure can easily distort, bend, and even cut and reform. These systems have an advantage with respect to the LC + Aerogel ones and are very interesting to study for two reasons:

1. Elastically these systems are much more compliant than the aerogel ones, thus the character of the phase transition is not affected as much.

2. The ability to achieve very low levels of disorder opens a very interesting, weaker regime of disorder strength, for study.

As a result of this, the heat capacity peak gets smeared less than with similar aerogel densities. This led to the discovery of a double peak feature in the first order transitions, as well as a different phase transitional behavior from the aerogel systems.

The gel by itself shows very interesting slow dynamics which can couple to that of the liquid crystal. This by itself is a very interesting phenomenon. The study of the dynamics of the random fractal gel was done by the newly developed technique of X-Ray Intensity Fluctuation Spectroscopy, which is the equivalent of Dynamic Light Scattering for x-ray wavelengths. Studying the gel by itself and its interaction with the LC molecules will give a better understanding of the very complex problems of the soft regime of quenched random disorder. Therefore, this thesis will present a study of the effect of quenched random disorder on several phase transitions for different liquid crystals, as well as a study of the dynamics of the aerosil fractal nano-gel in the host LC.

This thesis is divided into 8 chapters. This chapter introduces the most basic ideas needed to discuss the $LC + SIL$ system as well as some of the building blocks of the theory behind phase transitions and quenched random disorder. Chapter 2 presents the basic theoretical approaches to phase transitions and the quenched

random disorder systems. Chapter 3 deals with the experimental techniques used in this thesis, i.e., *AC* calorimetry, x-ray scattering, turbidity and x-ray intensity fluctuation spectroscopy. Chapters 4, 5, and 6 deal respectively with the *I-N*, *N-SmA* and *SmA-SmC* transition with quenched random disorder, which is introduced by the dispersion of *SIL* particles. Chapter 7 discusses the results of the XIFS study of the silica gel dynamics, embedded in a *LC* environment, while Chapter 8 gives a brief summary and future directions.

1.1 Introduction to Liquid Crystals

The term liquid crystal phase is synonymous with a state of matter that is intermediate between the crystalline solid and the liquid phase. In the literature, these phases are also called "**mesophases**," a term which is considered more appropriate and the molecules that show **mesomorphic** phases are called "**mesogens**." Most of the *LC* molecules have several features in common. One of the most important of these features is the fact that the molecules have a highly anisotropic molecular geometry. The most common of them are rod-like, but there also exist disk-like (discotics) or banana-like shaped molecules. Figure 1.3 shows the basic structure of the most commonly occurring rod-like mesogens. Their core is comprised of

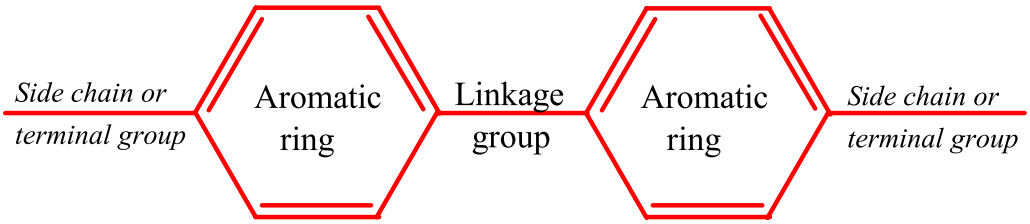

Figure 1.3. Molecular structure of typical rod-like mesogens.

two or more aromatic rings, connected by central linkage groups. This part is in general rigid and planar and has a dipole moment, or is easily polarizable. On each side of the rigid core are usually connected flexible aliphatic (hydrocarbon) tails or terminal groups. All the physical and optical properties of *LC*s as well as

the chemical stability of the molecules, their susceptibility to temperature change, UV or x-ray radiation, moisture etc., are governed by the properties of the central core. In general, compounds without a central linkage group are considered to be among the most stable *LC* molecules.

Liquid crystals are usually classified as either **lyotropic** or **thermotropic**. Lyotropic *LC*s are obtained usually as a mixture of different substances, e.g., liquid crystal molecules and solvent, with the most common systems being mixtures of water and amphiphilic molecules (molecules that posses a hydrophilic and a hydrophobic part). The variable that controls the existence of the liquid crystalline phase in these systems is the amount of solvent, i.e. the concentration of the sample. Lyotropic *LC*s are of great interest in biological studies. The term "thermotropic" arises from the fact that this class of liquid crystals shows different phases as temperature changes. They are the most widely studied, and used in applications. Another classification is based on the phases and symmetries that mesogens display. Several tens of thousands of mesogens are known to show one or more mesomorphic phases. Although there are many mesomorphic phases corresponding to different degrees of order and symmetries, most materials exhibit only a few of them.

Three different phase transitions were studied in this thesis: the Isotropic to Nematic (*I-N*), the Nematic to Smectic-*A* (*N-SmA*), and the Smectic-*A* to Smectic-*C* (*SmA-SmC*). The *LC*s used in this work and exhibiting these phases, were: *octylcyanobiphenyl* (8*CB*), *octyloxycyanobiphenyl* (8*OCB*), *4'-transbutyl-4-cyano-4-heptyl-bicyclohexane* (*CCN*47) and *4-n-pentylphenylthiol-4'-n-octyloxybenzoate* ($\bar{8}$S5), which will be described in detail in section 3.7. In the following two sections we will limit ourselves to giving a more detailed description of the characteristics of the phases that the above liquid crystals exhibit.

1.2 Nematic Order and the Order Parameter

The name nematic has its root from the Greek word $\nu\eta\mu\alpha$, meaning *thread*, because of the thread-like defects often observed in these structures under an optical microscope. A snapshot of the molecular order characteristic of a nematic *LC* is shown in Fig. 1.4. The molecules are free to bounce around, as in a liquid state,

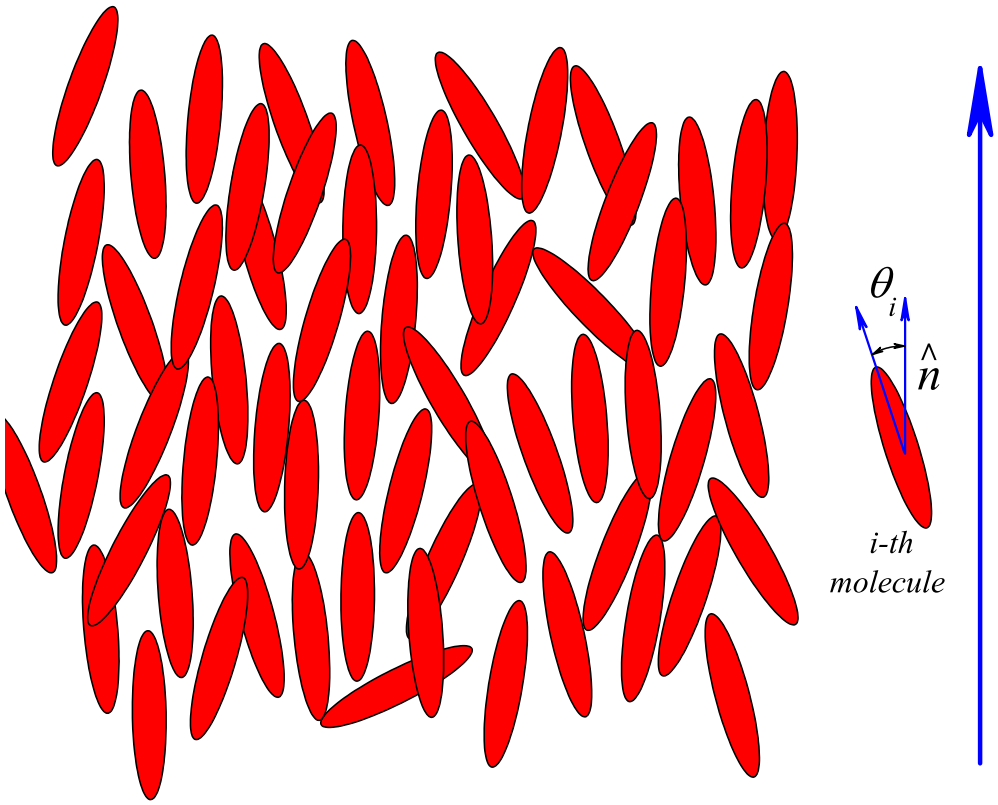

Figure 1.4. Schematic diagram of the nematic phase.

but two more features are also easily noticeable:

1. The molecules tend to align parallel to each other, i.e., *there is long-range orientational order*.

2. The positions of the centers of mass of the molecules are completely random, i.e., there is *no long-range positional order*.

The direction the molecules tend to align is represented by the unit vector $\hat{n}$ and is known simply as, the *"director"*. Note that for uniaxial *LC* molecules, this is a "headless" vector, i.e., the $+\hat{n}$ is indistinguishable from $-\hat{n}$ state. The director determines only the preferred orientation of the molecules. Depending on thermal fluctuations, the orientation of individual molecules can deviate a lot from that of the director. The scalar ***"order parameter"***(S), introduced by Tsvetkov [2], provides a measure of the magnitude of orientational order, (alignment) along $\hat{n}$. In the most general case the order parameter is a second-rank tensor [3]. However, by

ignoring any biaxial character of the molecules, and aligning the orientation of the axis with the local director, this tensor can be split into a scalar order parameter, S, and a pseudo vector, $\hat{n}$, which is the director. The scalar order parameter can be written in many ways, but the most useful formulation is to find the average of the second Legendre polynomial, as:

$$S = \langle P_2(cos(\theta)\rangle \; = \frac{1}{2} \; \left\langle 3cos^2\theta - 1 \right\rangle \; = \; \frac{3}{2} \; \left\langle cos^2\theta \right\rangle \; - \; \frac{1}{2} \tag{1.1}$$

where, θ is the angle between the axis of an individual molecule and the director, and the brackets indicate an ensemble average over all molecules. It is interesting to note that S varies from $-1/2$ to 1, where $-1/2$ corresponds to the unstable case, when all the molecules are perfectly aligned perpendicular to the director. The most important property of any order parameter, is that it should be zero in the higher symmetry (disordered) phase and different from zero in the lower symmetry (ordered) phase. When molecules are completely randomly oriented then $S = 0$, but, if the molecules are perfectly oriented with the director then $S = 1$. The first case corresponds to the isotropic liquid phase, while the latter to the crystalline phase. Typical values of the order parameter, deep in the nematic phase, lie between $0.6 - 0.8$.

This definition of the order parameter is especially suitable for the nematic phase, which displays cylindrical symmetry and when the director is fixed in space, which is the case when strong external fields or ordering surfaces are present. In bulk, the orientation of molecules, and thus the director, is not dictated by any external influences. Therefore it can point in any direction in space. Furthermore, it can change smoothly in different parts of the nematic sample, even in the presence of weak electric fields or far away from surfaces. If we consider also the motion of molecules about the long axis (denoted as z) of the cylindrical symmetry, then an average non-zero degree of order appears in the two perpendicular x and y axes. To account for spatial variations and ordering in directions other than the preferred one, the more general 2^{nd} rank tensor order parameter quantity Q_{ij} should be used. For uniaxial molecules, Q_{ij} is given as:

$$Q_{ij} = \frac{1}{2} \; \langle 3 \, cos \, \theta_i \, cos \, \theta_j \; - \; \delta_{ij} \rangle \tag{1.2}$$

where, *i,j,* = *x,y,z,* denote the axes of the coordinative system, while θ_i, θ_j, are the angles that the orientation of a molecule forms with the axes. It can be proven that in this case, this tensor is symmetric and traceless, i.e., $Q_{ij} = Q_{ji}$ and $Q_{xx} + Q_{yy} + Q_{zz} = 0$, hence possessing only 5 independent parameters. Note also, that the order parameter should depend on temperature, since the thermal fluctuations depend on it. The order parameter is a very important quantity in the characterization of mesophases and can be measured directly by different experimental methods, like NMR, electron spin resonance, or by methods that measure the electrical or diamagnetic susceptibilities.

1.3 Smectic Order

The name smectic comes from the Greek word $\sigma\mu\eta\gamma\mu\alpha$ meaning *soap*, because of the similarity in properties between them. As already introduced, there are plenty of smectic phases with different degrees of translational order. In this thesis we will only discuss the fundamental properties of the smectic-A and smectic-C phases. Snapshot pictures of *SmA* and *SmC* phases are illustrated in Fig. 1.5 and Fig. 1.6, respectively. Again, the molecules are free to bounce around quite randomly as in the N phase, but in this phase they not only tend to point along the director but also arrange themselves in layers, i.e., it is more likely for a molecule to spend more time in the layer plane than in between the layers. This forms stratified structures with the director in the *SmA* phase being parallel to the layer normal, while in the *SmC* phase the director forming an angle ω with the layer normal. Within each layer the molecules are randomly placed forming a *2-d* liquid. The inter-layer interactions are generally much weaker than the in-layer ones, hence the layers can slide over each other relatively easily. This gives the smectics the fluid-like properties very similar to soaps, although they are much more viscous than nematics.

The stratified structure of them gives rise to a one dimensional density wave. In fact, the density modulation is almost perfectly sinusoidal; so that the density of the system can be written in terms of the positional order parameter, Ψ, as:

$$\rho(z) = \rho_0 \left[1 + \Psi \cdot \exp\left(-i\frac{2\pi}{d}z\right)\right] \tag{1.3}$$

where, ρ_0 is the average density and d is the layer spacing. The modulus of Ψ, $\mid \Psi \mid$, is the amplitude of the density modulation, and is the most important part of the order parameter. The phase of Ψ merely describes where the layers are located relative to a fixed coordinative system. Typical values for $\mid \Psi \mid$ are much less than one, and they decrease with increasing temperature.

Depending on the relation between the layer spacing d and the length l of the molecule, the *SmA* or *SmC* can form different subclasses. For example, for polar *LC*s like $8CB$, when d has a value between l and $2l$ the partial bilayer phase

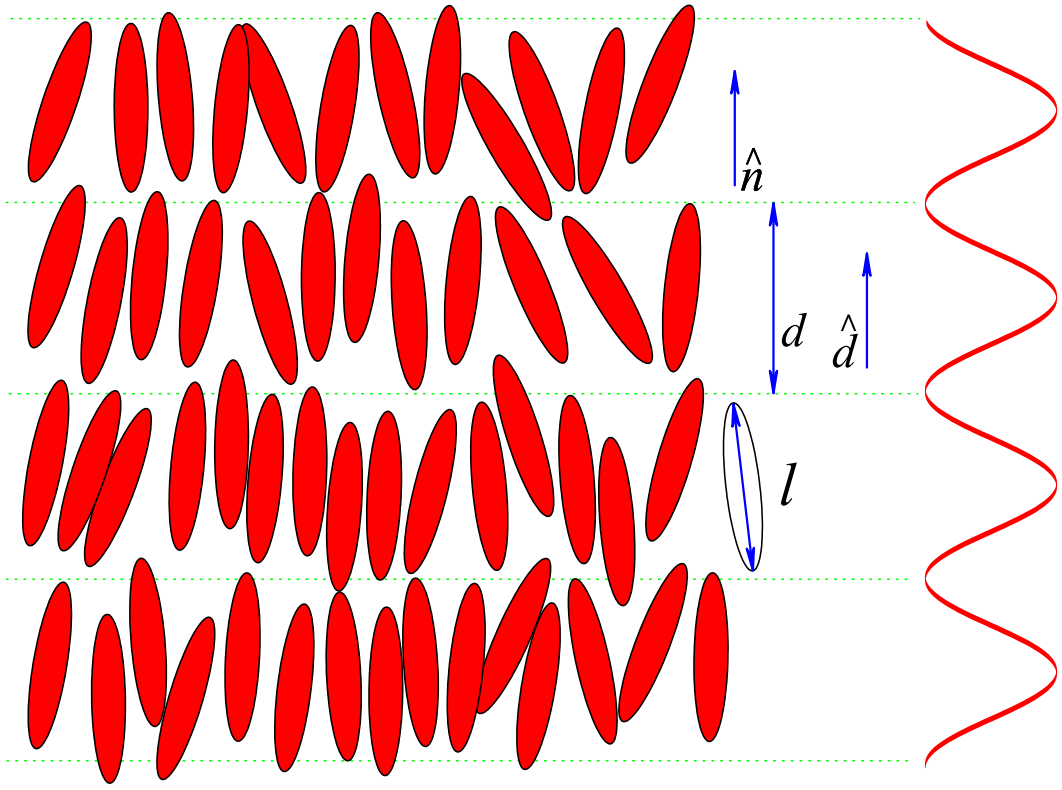

Figure 1.5. Schematic diagram of the monolayer Smectic-A phase (SmA_1 or SmA_m). The quantity l is the molecular length, d is the layer spacing, $\hat{d}$ is the layer normal, and $\hat{n}$ is the director.

is called a smectic-A_d phase (SmA_d). When $d = l$, or $d = 2l$, then the phases are called respectively smectic-A_1 (SmA_1) and smectic-A_2 (SmA_2). For nonpolar LCs like $\bar{8}$S5, there is only one single possibility $d \simeq l$, and this phase is just called smectic-A (SmA or sometimes SmA_m).

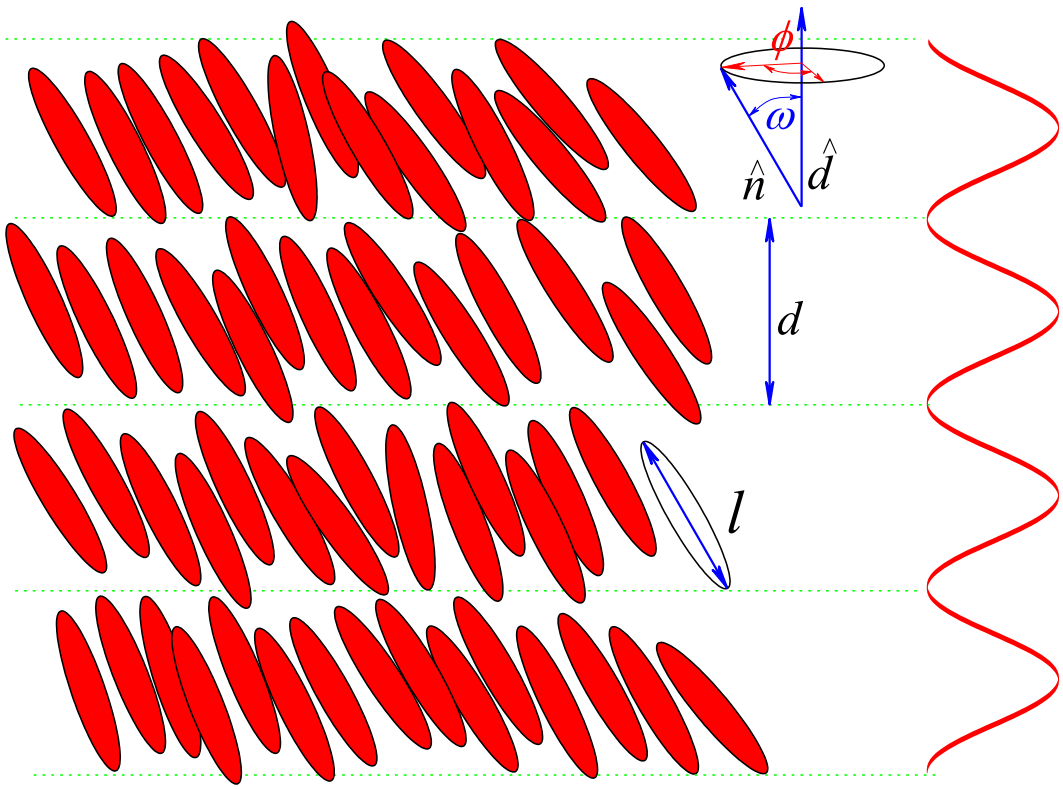

Figure 1.6. Schematic diagram of the monolayer Smectic-C phase. The quantity l is the molecular length, d is the layer spacing, $\hat{n}$ is the director. The tilt direction is described by the angle ω between the director $\hat{n}$ and the layer normal $\hat{d}$, and by the azimuthal angle ϕ for the director about the layer normal.

1.4 Thermodynamics

The bulk of the material presented in this thesis will involve parameters like heat capacity, enthalpy, latent heat, entropy, etc. In this section will be given a brief review of the basic definitions of these parameters, as well as some of the basic thermodynamic relations among them. A good review can be found in reference [4].

One key concept in thermodynamics is the ***state of a system***. A system is in a definite state when it is at equilibrium under a specific set of conditions. In a state, the system is described by different parameters which are a function of the state only, not of the path by which the system got there. These parameters, like temperature, pressure, volume, internal energy, enthalpy, entropy, Gibbs free energy etc., are called ***thermodynamic potentials*** or ***state functions***. The relationships between them form the so called ***equations of state***. A very simple equation of state for example, is the ideal gas law. Below are given the definitions of the ***Internal Energy*** of the system U, the ***Enthalpy*** H, and the ***Gibbs Free Energy*** G, in their differential form.

$$dU = TdS - PdV \tag{1.4a}$$

$$dH = TdS - VdP \tag{1.4b}$$

$$dG = -SdT + VdP \tag{1.4c}$$

Equation 1.4a is another expression of the ***First Law of Thermodynamics***:

$$dU = đQ + đW \tag{1.5}$$

which means: **A change in system's internal energy U = Heat flow into the system Q + Work done on the system W.** Note that $đQ$ is a small amount of heat, and is *not* the differential of a heat function Q. Similarly for $đW$, it is *not* the differential of a work function W. But dU is the differential of the internal energy function U.

A very important quantity, which will be mentioned the most here, is ***Heat Capacity***. It is a measure of the amount of heat necessary to raise the temperature of the material by one degree. The heat capacity per unit mass, or the ***Specific***

Heat Capacity is a unique property of the material. From its definition this property is a measure of the energetics of the system and as such, responds to all thermal excitations present in the system. Mathematically it can be expressed as:

$$C_x = \left(\frac{đQ}{dT}\right)_x = T\left(\frac{\partial S}{\partial T}\right)_x \tag{1.6}$$

where, $đQ$ is the heat going in or out, dT is the temperature response, ∂S is the change in entropy and x is a conjugate variable that is held constant during the process. If x is the volume, then C_v is the isochoric heat capacity, and if x is the pressure C_p is the isobaric heat capacity. The latter one can be written in terms of other thermodynamic potentials:

$$\begin{aligned} C_p \quad &= \left(\frac{đQ}{dT}\right)_p = \left(\frac{\partial U}{\partial T}\right)_p + p\left(\frac{\partial V}{\partial T}\right)_p = \\ &= T\left(\frac{\partial S}{\partial T}\right)_p = \left(\frac{\partial H}{\partial T}\right)_p = -T\left(\frac{\partial^2 G}{\partial T^2}\right)_p \end{aligned} \tag{1.7}$$

So, by knowing the heat capacity one can find the change in the enthalpy δH or the entropy ΔS of the system, when going from state 1 to state 2, by simply integrating the heat capacity:

$$\delta H = H_2 - H_1 = \int_1^2 C_p dT \tag{1.8a}$$

$$\Delta S = S_2 - S_1 = \int_1^2 \frac{C_p}{T} dT \tag{1.8b}$$

Another quantity is the ***Latent Heat***, (ΔH), which is the amount of energy released in a first order transition. It is defined from the relation:

$$\Delta H = T\Delta S = T\left(S_a - S_b\right) \tag{1.9}$$

where, S_a and S_b are the entropies of the coexisting phases at the transition. Thus calorimetric studies provide a direct measure of the system's free energy.

1.5 Phase Transitions

Although **phases** are conceptually very simple, they are hard to define precisely. A good definition of the **phase of a system** is a region in the parameter space of the system's thermodynamic variables in which the free energy is analytic, i.e., the free energy and all its derivatives like entropy, heat capacity, magnetization, etc., are continuous. When a system goes from one phase to another, there will generally be a stage where the free energy is non-analytic. This is known as a **phase transition**. Familiar examples of phase transitions are melting (solid to liquid), freezing (liquid to solid), boiling (liquid to gas), and condensation (gas to liquid). Due to this non-analyticity, the free energies on either side of the transition are two different functions, so one or more thermodynamic properties will behave very differently after the transition. The property most commonly examined in this context is the heat capacity. During a transition, the heat capacity may become infinite, jump abruptly to a different value, or exhibit a "kink" or discontinuity in its derivative.

Ehrenfest classification

The first attempt at classifying phase transitions was the Ehrenfest classification scheme, which grouped phase transitions based on the degree of non-analyticity involved. Ehrenfest proposed that phase transitions could be classified as 'n^{th} *order*' if any n^{th} derivative of the free energy with respect to any of its arguments is discontinuous at the transition. Under the Ehrenfest classication scheme, there could in principle be third, fourth, and higher-order phase transitions.

Modern classification of phase transitions

But the Ehrenfest scheme is an inaccurate method of classifying phase transitions, for it is based on a mean-field theory of phases (to be described in a Chap. 2). Mean-field theory is inaccurate in the vicinity of phase transitions, as it neglects the role of thermodynamic fluctuations. For instance, it predicts a finite discontinuity in the heat capacity at the ferromagnetic transition, which is implied by Ehrenfest's definition of "second-order" transitions. In real ferromagnets, the heat capacity diverges to infinity at the transition.

In the modern classification scheme, phase transitions are divided into two

broad categories, named similarly to the Ehrenfest classes:

1. The ***first-order phase transitions*** are those that involve a latent heat. During such a transition, a system either absorbs or releases a fixed (and typically large) amount of energy. Because energy cannot be instantaneously transferred between the system and its environment, first-order transitions are associated with the "***two-phase coexistence region***," in which some parts of the system have completed the transition and others have not. Systems in the two-phase coexistence region are difficult to study, because their dynamics are hard to control. However, many important phase transitions fall in this category, including the solid/liquid/gas transitions.

2. The ***continuous phase transitions***, which are also called ***second-order phase transitions***, have no associated latent heat. Examples of second-order phase transitions are the ferromagnetic transition, the superfluid transition, and Bose-Einstein condensation.

3. A subclass of the continuous phase transitions are the so called ***infinite-order phase transitions***. They are continuous but break no symmetries. The most famous example is the Kosterlitz-Thouless [5] transition in the two-dimensional XY model.

1.5.1 Properties of Phase Transitions

1.5.1.1 Critical Points

Critical points are usually associated with continuous phase transitions. One of the best known examples is that of a ferromagnet. At high temperatures and zero external field the system is in the paramagnetic phase. Any spin at any time points in all possible directions with equal frequency, thus the system as a whole has a zero net magnetization. Below the ***critical temperature***, T_c, the spins tend to align along a particular direction in space even in the absence of an external field. The onset of this behavior is, as mentioned above, an example of a continuous phase transition, and the net magnetization M(T) can be used as an order parameter for the transition.

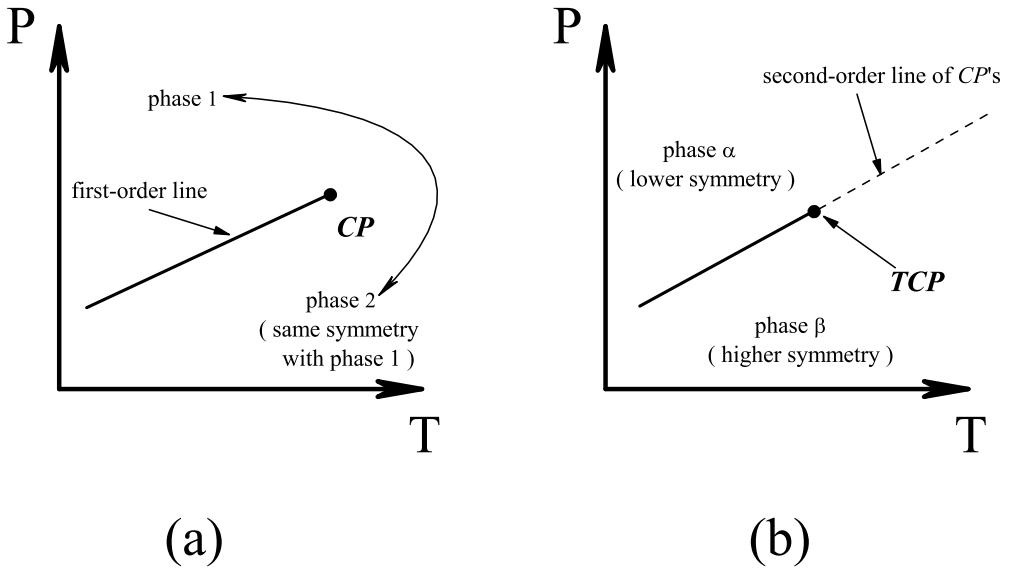

Figure 1.7. (a) Phase transition ending in a critical point (CP). (b) Phase transition with a tricritical point (TCP).

Other examples of critical points may include special points in the phase diagram of certain systems. The best known example of such a special critical point is that of a system containing liquid and gaseous phases. Below the so called critical temperature and/or critical pressure the transition from one phase to the other is first order; there is a discontinuous jump in the density [1]. Near the critical point, the fluid is sufficiently hot and compressed that the distinction between the liquid and gaseous phases is almost non-existent. At the critical point the transition between liquid and gas becomes second-order. The density discontinuity becomes zero, but there is an infinite singularity in the temperature and pressure derivatives of the density. Above the critical point the transition ceases to exist, since there is no way to tell one phase from the other. So, it is possible to go from one phase to the other without undergoing a phase transition. See Fig 1.7(a). However, if the transition involves a change in symmetry, then there is a way to tell one phase from the other, although the order parameter is not discontinuous. In this case, the order parameter discontinuity decreases with increasing temperature and pressure to a point where it becomes zero, the so called "***tricritical point***." The transition

[1]Note that in this example the density difference, ρ_{liquid} - ρ_{gas}, is the order parameter for the transition.

continues to exist above the tricritical point, where it simply changes from first to second-order. This is illustrated in Fig 1.7(b).

In many cases the number of variables that drive the transition is higher than one, for instance, the electric or magnetic fields, concentration, chemical potential, stresses etc. In this case the phase diagram becomes multi-dimensional and the critical points become lines or surfaces or hyper-surfaces. Moving on this line (surface), one may reach special points (lines or surfaces), at which some properties of the transition change abruptly. These points are referred to, as a ***multicritical points***, and their dimensionality can be higher than one. Thus there exist *bicritical*, *tricritical*, *tetracritical* or higher-order critical points.

1.5.1.2 Symmetry

In the ferromagnetic transition mentioned above, the system goes from the paramagnetic phase, where it displays a fully rotational and translational symmetry, to the ferromagnetic phase, where the rotational symmetry is broken (since the random direction that was picked by the magnetization is the preferred direction). Phase transitions often (but not always, for instance the liquid-gas transition breaks no symmetry) take place between phases with different symmetry.

Typically, the more symmetrical phase is on the high-temperature side of a phase transition, and the less symmetrical phase on the low-temperature side. This is certainly the case for the solid-fluid and ferromagnetic transitions. The transition from the more symmetrical phase to the less symmetrical one is a symmetry-breaking process. In the fluid-solid transition, for example, we say that a continuous translational symmetry is broken.

The presence of symmetry-breaking (or nonbreaking) is important to the behavior of phase transitions. It was pointed out by Landau that, given any state of a system, one may unequivocally say whether or not it possesses a given symmetry. Therefore, is not possible to analytically (continuously) 'deform' a state in one phase into another phase possessing a different symmetry. This means, for example, that it is impossible for the solid-liquid phase boundary to end in a critical point like the liquid-gas boundary. However, symmetry-breaking transitions can still be either first or second order.

This happens because the full Hamiltonian of a system usually exhibits all the

possible symmetries of the system, whereas the low-energy states lack some of these symmetries (this phenomenon is known as spontaneous symmetry breaking.) At low temperatures, the system tends to be confined to the low-energy states. At higher temperatures, thermal fluctuations allow the system to access states in a broader range of energy, and thus more of the symmetries of the Hamiltonian.

When symmetry is broken, one needs to introduce one or more extra variables to describe the state of the system. For example, in the ferromagnetic phase one must provide the net magnetization, whose direction is spontaneously chosen when the system cooled below the Curie point. Such variables are instances of order parameters. However, note that order parameters can also be defined for all types of transitions, whether or not they are related to some measurable quantity, or are pure abstract constructions.

1.5.1.3 Critical Exponents and Universality Classes

Continuous phase transitions are easier to study than first-order transitions due to the absence of latent heat, and the two-phase coexistence. They have been discovered to have many interesting properties. The phenomena associated with continuous phase transitions are called ***critical phenomena***, due to their association with critical points.

It turns out that continuous phase transitions can be characterized by parameters known as ***critical exponents***. For instance, let us examine the behavior of the heat capacity near such a transition. We vary the temperature T of the system while keeping all other thermodynamic variables fixed, and find that the transition occurs at some critical temperature T_c. When T is near T_c, the heat capacity C typically has a power law behavior:

$$C \propto \left| \frac{T - T_c}{T_c} \right|^{-\alpha} = |t|^{-\alpha} \tag{1.10}$$

where $t = \frac{T - T_c}{T_c}$ is known as the ***reduced temperature***. The constant α is the critical exponent associated with the heat capacity. Of course we must always expect that over any finite range there will be some correction terms. Thus, even

for an asymptotically pure power law, one will generally have

$$C = A\,|t|^{-\alpha}\left(1 + D_1\,|t|^{\Delta 1} + D_2\,|t|^{\Delta 2} + ...\right) \tag{1.11}$$

where A is known as the amplitude and the terms inside the brackets are known as ***corrections to scaling*** terms with their amplitudes D_i's and correction to scaling exponents Δ_i's. On approaching the transition from t^+ or t^- one would expect two amplitudes, A^+ and A^-, two critical exponents α^+, α^-, two correction to scaling amplitudes $D_i^{\pm}$'s and exponents $\Delta_i^{\pm}$ for each term. It was not until the advent of the renormalization group theory that it was finally explained why $\alpha^+ = \alpha^- = \alpha$, and $\Delta_i^+ = \Delta_i^- = \Delta_i$. Depending on the universality class (to be explained right after), the renormalization group theory gives predictions for the leading exponent α, and for the ratios A^-/A^+, D^-/D^+. The correction to scaling exponent is also predicted to be $\Delta_1 \approx 0.5$, in many real situations.

The critical exponent α must be less than 1 in order for the transition to have no latent heat. Its actual value depends on the type of phase transition we are considering. For -1 $< \alpha <$ 0, the heat capacity has a large but finite value at the transition temperature. This is the behavior of liquid helium at the "lambda transition" from a normal state to the superfluid state, for which experiments have found α = -0.013±0.003 [6]. For 0 $< \alpha <$ 1, the heat capacity diverges at the transition temperature (though, since $\alpha < 1$, the divergence is not strong enough to produce a latent heat.) An example of such behavior is the 3-dimensional ferromagnetic phase transition. In the three-dimensional Ising model for uniaxial magnets, detailed theoretical studies have yielded the exponent $\alpha \sim 0.110$.

Some model systems do not obey a power-law behavior. For example, mean field theory predicts a finite discontinuity of the heat capacity at the transition temperature, and the two-dimensional Ising model has a logarithmic divergence. However, these systems are an exception to the rule. Most phase transitions exhibit power law behavior. Several other critical exponents - β, γ, δ, ν, and η - are defined. Each of them determines the power law behavior of a measurable physical quantity near the phase transition. Their defining relations are shown in Table 1.1.

The importance of critical exponents is that they are universal, i.e., they depend only on the spatial dimensionality of the system and the number of components of

Heat Capacity	$C \sim \|t\|^{-\alpha}$
Order Parameter [2]	$m \sim \|t\|^{-\beta}$
Susceptibility	$\chi \sim \|t\|^{-\gamma}$
Correlation Length	$\xi \sim \|t\|^{-\nu}$
Pair Correlation Function (t=0) [3]	$G(r) \sim r^{-(d-2+\eta)}$
Equation of State (t=0) [4]	$m \sim H^{-1/\delta}$

Table 1.1. Summary of the definitions of the standard critical exponents in the language of magnetic systems.

the order parameter. They are insensitive to the underlying microscopic properties of the system, or the details of the interactions. It is a remarkable fact that phase transitions arising in different systems often possess the same set of critical exponents. This phenomenon is known as ***universality***. For example, the critical exponents at the liquid-gas critical point have been found to be independent of the chemical composition of the fluid. More amazingly, they are an exact match for the critical exponents of the ferromagnetic phase transition in uniaxial magnets. Systems that share the same set of critical exponents are said to be in the same ***universality class***. The critical exponents are not completely independent. They are related by ***scaling relations***. Some of the critical exponents relations are given in Table 1.2.

Fisher	$\gamma = \nu(2 - \eta)$
Josephson [5]	$\nu d = 2 - \alpha$
Rushbrooke	$(\alpha + 2\beta + \gamma = 2$
Widom	$\gamma = \beta(d - 1)$

Table 1.2. Scaling relations between the critical exponents.

Universality is a prediction of the renormalization group theory of phase transitions [7]. The ideas of universality appear to be also applicable to phase transitions in complex fluids: liquid crystals, polymers and polymer solutions, microemulsions, fluids in porous media, gels, and foams. Large fluctuations, strong susceptibility to external perturbations, and mesoscopic structure are characteristic for all such

[2] $m = M/V$ is the magnetization density. See section 2.2 for typical magnetic systems.
[3] d is the dimensionality of the system.
[4] H is the magnitude of the external magnetic field.
[5] This is also known as the hyperscaling relation because it is the only one that has the dimensionality d explicitly in it.

systems.

The world around us is full of phenomena for which the language of phase transitions, either the usual thermodynamics, dissipative or geometrical (percolation), appears to be the most appropriate. Spontaneous symmetry breaking in the early stages of the evolution of the Universe, and the beginning of life on Earth are but the most exciting examples. The ideas of universality unify under the same theoretical approach fields as diverse as earthquake science to neural networks and the human brain, from superconductivity to galaxy clustering, from the biological self-organization of molecules to forest fires [8, 9]. Our research in liquid crystals is a part of this fascinating science.

1.5.1.4 Finite Size and Crossover Effects

The finite size of a system is expected to clearly affect its phase transitional behavior [10, 11]. On pure thermodynamic grounds there is no true second order phase transition except for infinite size systems i.e., in the thermodynamic limit. In practice the thermodynamic limit is not relevant since our instrumental resolution is not perfect, and thus we are insensitive to changes that come from the system's finite size (provided that the system is big). As a rule of thumb, ***finite size effects*** become important when the bulk correlation length of the system becomes comparable to its size, or to the distance between the confining surfaces. As a result, in simple ***finite size scaling***, (FSS) the bulk critical correlations are cut off by this distance, which will correspond to a minimum reduced temperature, below which the transition gets truncated. When these surfaces are arranged randomly, with high void connectivity, the distance between the surfaces may not be the maximum length in the system, as is our case with the aerosil gel. The finite size of the system will lead in general to the following calorimetric effects:

1. Premature truncation of the transition.

2. Suppression of the heat capacity maximum.

3. Suppression of the transition enthalpy.

4. Saturation in the growth of the ordered phase, for the case of a transition that breaks a continuous symmetry. This prevents the system from attaining

long range order (LRO), and thus may complicate or even prevent the system to attain its critical asymptotic scaling regime.

Crossover phenomena rise as a consequence of the failure of a system to attain its critical asymptotic scaling regime. This can occur for several reasons:

1. Small external fields may be present. This is the case for very pure transitions where, for instance, the effect of the Earth's gravity or magnetic field can be sensed.

2. Weak interactions neglected in the Hamiltonian may break the symmetry and generate flows toward other *fixed points* [6]. Small neglected anisotropies in the interactions, may be an example of this case.

3. Disorder under certain conditions influences the critical behavior. This case certainly applies to almost all systems, since very rarely one will find pure systems in a real situation. This is the case we are mostly interested in this study, where the disorder is introduced on purpose. It was shown by Harris [12] that if $\alpha < 0$ the behavior of the system is not affected. For $\alpha > 0$ the system will move towards its underlying critical behavior. The case $\alpha = 0$ is a marginal case. This simple heuristic criterion is known as the ***Harris Criterion***.

[6] In renormalization group (RG) theory, the recursive application of a "well designed" renormalization group transformation, generates flows (trajectories) in the space of Hamiltonians. These flows usually will come to an asymptotic halt at a ***fixed point*** of the RG. The nontrivial fixed points represent critical states. Furthermore, each point defines (in general) a completely new universality class. From each critical fixed point there will be at least two "unstable" or outgoing trajectories. These correspond to one or more ***relevant variables*** (like temperature and external magnetic field in the case of magnetic systems). If there are further relevant trajectories, than one can expect crossover to a different critical behavior, since these trajectories may lead to other fixed points. See Ref. [7] for more details.

Chapter 2

Theory

2.1 Landau-DeGennes Theory of Phase Transitions

Landau theory of phase transitions is a phenomenological theory based on general considerations of symmetry and analyticity. As such it applies, at least in spirit, to all types of phase transitions. Landau theory postulates that

1. The free energy of the system F (known as the ***Landau Free Energy*** (LFE) or the ***Landau functional***) can be written as a function of the order parameter Q and the coupling constants K_i.

2. The state of the system is specified by the absolute minimum of F with respect to Q.

3. All the thermodynamic functions can be calculated by differentiating F as if it was the real Gibbs free energy. It turns out that the Landau free energy is related to the Gibbs free energy, but they are not identical.

4. Close to a phase transition the LFE can be expanded in a power series in terms of Q where only the terms compatible with the symmetry of the system are included. So the free energy density for *homogenous* systems will be given as:

$$f \equiv \frac{F}{\Omega} = \sum_{n=0}^{\infty} a_n([K], t)\ Q^n \tag{2.1}$$

where Ω is the volume of the d-dimensional system and a_n's are phenomenological constants that may be temperature dependent.

For *inhomogeneous* systems, where the order parameter varies in space, i.e., $Q = Q(\mathbf{r})$ the free energy is given by,

$$F = \int_{\Omega} d^d\mathbf{r} \left[f([K], t, Q(\mathbf{r})) + \frac{1}{2}\gamma \left(\nabla Q(\mathbf{r})\right)^2 \right] \tag{2.2}$$

where the first term is the homogenous *LFE* density of Eq. 2.1, while the second term is proportional to the square of the gradient of $Q(\mathbf{r})$. This term is added in order to allow for a smooth variation of $Q(\mathbf{r})$ across the sample. A simple minimization without this term would minimize F without taking into account the fact that, ***wildly spatially varying*** $Q(\mathbf{r})$ ***is energetically not favorable***. The proportionality constant γ is another phenomenological constant, whose value should be positive. Its temperature dependence is generally very weak as to be negligible near T_c.

For continuous transitions where the order parameter is vanishingly small close to T_c, i.e., $Q \to 0$ as $t \to 0$, the *LFE* expansion is assumed to be correct. In this case, the state of the system is specified by the absolute minimum of the Q, i.e.,

$$\frac{\partial f}{\partial Q} = a_1 + 2a_2 Q + 3a_3 Q^2 + 4a_4 Q^3 + O(Q^4) = 0 \tag{2.3}$$

where we have expanded up to $O(Q^4)$. For $T > T_c$, $Q \equiv 0$. Hence $a_1 = 0$.

Now lets consider the symmetry constraints in the spatially homogenous case for simplicity. Consider a case where the Hamiltonian of the system is symmetric with Q, i.e., $H(Q) = H(-Q)$. As a consequence $F(Q) = F(-Q)$. The evenness of F in this case implies that,

$$a_3 = a_5 = a_7 = ... = 0 \tag{2.4}$$

thus the *LFE* up to $O(Q^6)$ becomes,

$$f = f_0 + a_2([K], t)Q^2 + a_4([K], t)Q^4 + O(Q^6) \tag{2.5}$$

In this case only by symmetry arguments the odd power terms are all zero. However, for many systems these terms are not zero. A detailed discussion of all different cases is outside the scope of our thesis. The reader might find valuable insights in the literature for other systems [13].

If the system is under the influence of external fields, is in contact with surfaces, or the material's elasticity is considered, then additional terms corresponding to the respective free energies should be added to the homogenous Landau free energy density.

For first order transitions this expansion is still possible and meaningful, although at T_c the order parameter jumps from 0 in the disordered phase, to a finite but not vanishingly small value in the ordered phase. In this case the cubic term in the expansion must exist, to account for the discontinuity in Q on both sides of T_c. Thus, if there is no symmetry argument to force the cubic term coefficient to be zero, then this term will cause a first order transition to occur most of the time. The existence of the cubic term in the *LFE* expansion does not mean automatically that the transition will be first order. There are systems whose symmetry allows for the cubic term although they show a continuous transition [14, 15]. Furthermore, Landau's theory is a mean field theory. As such it neglects the effect of fluctuations, which can effect strongly the character of a transition, by driving it to first or second order, depending on the case.

2.1.1 *I-N* Transition

DeGennes built a detailed mean field theory, based on the Landau theory, that describes at least qualitatively the main characteristics of the *LC*s and their phase transitions [3]. For the *I-N* transition the full Landau-DeGennes free energy density is:

$$\begin{aligned} f = \;& f_0 \;+\frac{1}{2}A\cdot Q_{\alpha\beta}Q_{\beta\alpha} - \frac{1}{3}B\cdot Q_{\alpha\beta}Q_{\beta\gamma}Q_{\gamma\alpha} + \frac{1}{4}C\cdot\left(Q_{\alpha\beta}Q_{\beta\alpha}\right)^2 \\ &+ \;\; D\left(\nabla Q_{\alpha\beta}\right)^2 + L\left(\widehat{n}\cdot\nabla Q_{\alpha\beta}\right)^2 + f_{BE} + f_{SE} + f_{EM} + O(Q^5) \end{aligned} \tag{2.6}$$

where $Q_{\alpha\beta}$ is the symmetric and real second rank tensor order parameter, A,B,C,D and L are phenomenological parameters that may be in general temperature dependent. To correctly account for the behavior of most *LC*s, only the parameter

A needs to depend on temperature, as:

$$A = a(T - T^*) \tag{2.7}$$

where, a is some phenomenological constant and T^* is the lowest temperature for the isotropic stability, or namely the *supercooling temperature*. The last three terms f_{BE}, f_{SE} and f_{EM} contain respectively the bulk elastic free energy (otherwise known as Frank elastic free energy), surface elastic free energy (if the system is confined by surfaces), and electromagnetic interaction free energies (if the system is under some external electromagnetic field). The terms that contain the gradient of the order parameter account for the spatial variations of the latter. The existence of the cubic term in the free energy makes the *I-N* transition first order for the mean field theory description. The heat capacity in the nematic phase diverges close to T_{IN} as

$$C \sim |t|^{-0.5} \tag{2.8}$$

where $t = (T^{**} - T)/T_c$, and T^{**} is the *superheating temperature of the nematic phase*. In the Isotropic phase $C = C_{p_0}$ is constant. At T^{**} the heat capacity shows a step-like discontinuity equal to

$$\Delta C_p = \frac{2a^2}{C} \tag{2.9}$$

2.1.2 *N-SmA* Transition

A natural choice for the order parameter of the *N-SmA* transition is a scalar equal to the amplitude of the density modulation of the smectic phase, as given by Eq. 1.3. In the nematic phase $|\Psi| = 0$, whereas in the smectic phase this becomes increasingly bigger. With this order parameter, and since the $\pm$ Ψ values differ only in the choice of the origin of the coordinative system, the free energy density of the system can be written as:

$$f_s = f_{s0} + \frac{1}{2}a_s|\Psi|^2 + \frac{1}{4}b_s|\Psi|^4 + \frac{1}{6}c_s|\Psi|^6 + ... \tag{2.10}$$

where, $a_s \simeq \alpha(T - T_{NA})$. Below T_{NA}, a_s vanishes and above T_{NA}, a_s is positive. With this approximation alone one could have a second order transition.

However, there are a lot of other complications that can not be neglected. A more thorough model must include in the free energy all the effects that are considered separately in different models. Some of the most important are:

1. The coupling between the magnitude of the nematic order parameter, S, and the smectic-A order parameter Ψ, adds a term to the free energy which to lowest order can be given as: $f_1 = -C|\Psi|^2\delta S$, where $\delta S = S - S_A$, is the increase in the nematic order that comes from the smectic ordering of molecules. This coupling will effect the coefficient b in Eq. (2.10), and can drive the *N-SmA* transition from XY-like[1] ($b \gtrsim 0$), to tricritical ($b = 0$), to weakly first order ($b < 0$), with increasing nematic susceptibility (χ_N) [2].

2. The director fluctuations in the nematic phase as in Ref. [17, 18]. This coupling adds a term of the form $f_{\hat{n}} = -C_{\hat{n}}|\Psi|^2\delta\hat{n}$ to the LFE, and leads to anisotropic smectic correlation lengths in the parallel ($\chi_\parallel$) and perpendicular ($\chi_\perp$) directions to the nematic director $\hat{n}$.

3. The nematic elastic free energy $f_N = f_N(S_0) + \frac{1}{2\chi}(\delta S)^2$.

4. The layer fluctuations in the smectic phase.

5. The coupling between the full tensor nematic order parameter (not only the scalar amplitude) with the smectic order parameter as in the model of Keyes [19]

The De Gennes model modifies the Landau simple model by adding the effects of the Frank elasticity energy and from the coupling to the amplitude of the nematic order parameter. With these additions the model exhibits first or continuous phase transitions and belongs to the 3D-XY Heisenberg magnet, universality class (the same with the normal to superconductor transition). So far no theory exists that can explain the richness of experimental findings. The critical exponents for the *N-SmA* transition are not quite the same as those of the 3D-XY universality class. So the exponent α for most of the liquid crystals that were studied in this work

[1] See section 2.2.2 for the details of the XY model.

[2] The nematic susceptibility (χ_N) is directly related to the McMillan ratio ($R_M = T_{NA}/T_{IN}$). See the following paragraph and Ref. [16] for the details.

were far from $\alpha_{3D-XY} = -0.013$. The correlation length critical exponent ν in the model is a single value $\nu_{3D-XY} = 0.699$, while experimentally the correlation length is anisotropic and $\nu_{\|} \neq \nu_{\perp}$.

A very thorough compilation of the available data shows that the effective critical exponents, found experimentally, mostly lie between the 3D-XY and tricritical values [20]. Furthermore their behavior is dependent on the McMillan ratio ($R_M = T_{NA}/T_{IN}$). In general, the bigger the McMillan ratio (the closer the T_{NA} is to T_{IN}) the more tricritical-like the exponents become, in qualitative agreement with what McMillan suggested in his theory [16].

2.1.3 *SmA-SmC* Transition

The onset of the Smectic-C order can be characterized by the two real parameters, the tilt angle ω and the azimuthal angle ϕ, or equivalently, by the complex number

$$\varrho = \omega \exp^{i\phi} \tag{2.11}$$

This order parameter is analogous with that for the superfluid helium transition. Of course, a change in the phase angle ϕ does not modify the free energy, so the free energy expression is the same with the *N-SmA* free energy. This analogy makes the *SmA-SmC* transition display the following characteristics, in the mean field approximation:

1. The transition may be continuous or first order in special circumstances. When it is continuous the critical exponents fall in the 3D-XY class.

2. The coupling between the tilt angle and layer thickness and other couplings, bring the system close to tricriticality. This was suggested even in the absence of these arguments [3, 21]

2.2 Quenched Random Disorder Models

In the theory of quenched random disorder models play a big role. Among the most popular models are the Ising model and the Heisenberg model. Both of them are very simple models of magnetic spins in a lattice with nearest neighbor or longer

order interactions. What seems very easy to state and formulate as a problem is, surprisingly, sometimes very difficult and nontrivial to solve. The problem becomes increasingly more complex with the introduction of external fields, disorder or confinement effects. So far, there are exact solutions for these systems only in a few simple cases, *1-d* or *2-d*, or in dimensions higher than *4*. The *3-d* cases are generally very difficult to solve exactly. Although the Hamiltonian for these models is often written in terms of spin variables and the language used is for magnetic systems, these models are applicable to many non-magnetic systems.

The dimensionality of a system is very important in determining whether there is a phase transition, and if so, its critical properties. Of particular interest are the so called ***lower critical dimension*** and ***upper critical dimension***. When the spatial dimensionality is low, the role of fluctuations becomes important, driving T_c to lower values. **The dimension below which the transition occurs at $\mathbf{T_c = 0}$, is called the lower critical dimension**. When the spatial dimension of a system is high, the opposite happens. The high connectivity of the system makes fluctuations less important and eventually mean field theory becomes exact at the upper critical dimension. So **the upper critical dimension is the dimension above which mean field theory is exact**.

2.2.1 Random Field Ising Model

The Ising Model is probably one of the simplest and best known order-disorder models. It has been a popular starting point of many theoretical considerations. Its Hamiltonian is given by:

$$\mathcal{H} = J \sum_{<ij>} s_i s_j - H \sum_i s_i \tag{2.12}$$

where s_i can have only ± 1 values, i,j, are the site numbers, J denotes the strength of the exchange interaction between spins, and H is a uniform external field applied to the system. The lattice on which the spins reside is d-dimensional. At low temperature the system becomes ferromagnetic when $J < 0$, or anti-ferromagnetic when $J > 0$. The order parameter of the system is the magnetization of the system,

M:

$$M = \frac{1}{N} \sum_{<i>} s_i \quad . \tag{2.13}$$

The above Hamiltonian can be easily expanded to that of the *Random Field Ising Model* (RFIM) to include disorder.

$$\mathcal{H} = J \sum_{<ij>} s_i s_j - \sum_i h_i s_i - H \sum_i s_i \tag{2.14}$$

where h_i is a random field at each spin site i, that satisfies the following conditions:

$$\langle h_i \rangle_{\vec{r}} = 0; \qquad \left\langle h_i^2 \right\rangle_{\vec{r}} = h_0^2; \tag{2.15}$$

where the $\langle\ \rangle_{\vec{r}}$ indicate spatial averages. The direction and value of the field may be chosen randomly, but once chosen it remains fixed in time and space; hence the name ***Quenched***. The external field is usually set to zero, ($H = 0$) in order not to further complicate the problem.

If the random field is very strong, i.e., when $h_0 \gg J$, then, at low temperature, each spin will just follow the random field direction which is fixed. The most interesting case is for weak and very weak disorder strength $h_0 \lesssim J$, or $h_0 \ll J$, for which there is a competition between the ordering effect of the exchange interaction J and the disordering effect of the random field. The random field dramatically changes the nature of the transition even in the very weak limit. For example, ordering of the *2-d* Ising model that was solved exactly by Onsager [22], is completely destroyed by the introduction of any finite random field.

2.2.2 Random Field XY Model

A model that is more relevant to the current study is the *Random Field XY Model* (RFXYM). This model shows a planar (XY) continuous symmetry, since the spins are confined to rotate in a plane. Furthermore, they are classical unit vectors, and not quantum spins as in the Ising model. As such they are allowed to get any value between ± 1. The order parameter of the system is once again the magnetization of the system M = (M_x,M_y). The order parameter has only 2 components, although the dimensionality of the system (the lattice) may be *d = 1,2,3,4 . . ...* Spontaneous

symmetry breaking can occur at non-zero temperature for $d > 2$. For $d = 2$, the Kosterlitz - Thouless phase transition occurs, although its order parameter is not the magnetization.

The Hamiltonian for the RFXYM can be written as:

$$\mathcal{H} = J \sum_{<ij>} \vec{s}_i \vec{s}_j - \sum_i \vec{h}_i \vec{s}_i - \vec{H} \sum_i \vec{s}_i \tag{2.16}$$

Again, we consider only the case without any applied uniform external field ($\vec{H} = 0$), and the random field $\vec{h}(\vec{r})$ satisfies the conditions:

$$\left\langle \vec{h}_i \right\rangle_{\vec{r}} = 0 \qquad \left\langle \vec{h} \cdot \vec{h} \right\rangle_{\vec{r}} = h_0^2 \neq 0 \tag{2.17}$$

2.3 Predictions of Random Field Theories

2.3.1 Imry - Ma Domain - Wall Argument

It is now believed that there is no long range order in random field XY magnets, with quenched disorder, in less than 4 dimensions. This comes as a consequence of the classical domain wall argument of Imry and Ma [23]. According to this argument, the energy cost to create a domain of size R, in a pure system, comes from the energy of the broken bonds on the domain walls. If it is an Ising system the energy cost is simply proportional to the surface area, while for a continuous symmetry type system the energy cost is optimized by a continuous rotation of the order parameter over a distance comparable to R. Thus,

$$E_{cost}(Ising) \sim JR^{d-1} \tag{2.18}$$

$$E_{cost}(XY) \sim JR^{d-2} \tag{2.19}$$

So for pure systems, there is no long range order if the $d \leq 1$ and $d \leq 2$ for the Ising model or continuous symmetry systems, respectively.

In the presence of disorder, the energy gain is of the order $\sim R^{d/2}$. Thus, the net energy cost to form a domain can be written as:

$$E_{cost}(Ising) \sim JR^{d-1} - h_0 R^{d/2} \tag{2.20}$$

$$E_{cost}(XY) \sim JR^{d-2} - h_0 R^{d/2} \tag{2.21}$$

Therefore, whenever

$$d/2 \geq d-1 \Rightarrow d \leq 2, \quad for \ \ RFIM \tag{2.22}$$

$$d/2 \geq d-2 \Rightarrow d \leq 4, \quad for \ \ RFXYM \tag{2.23}$$

there will be some sufficiently large R, for which it will be energetically favorable to have domains of size R even with an arbitrarily small random field. As seen from the above argument the lower critical dimension for the RFIM and RFXYM are *2* and *4*, respectively. This means that no true phase transition is expected in the *3-d* case of the RFXYM, ($3DXY$).

The Imry-Ma, domain wall argument, is not quite exact because:

1. No consideration is given to thermal fluctuations and entropic effects.
2. Only smooth domain walls were considered.
3. No consideration is given to the existence of domains within domains.

Therefore, a more elaborate theoretical treatment is needed to prove or disprove the existence of true long range order in the case of $d < 4$ of the RFXYM.

Chapter 3

Experimental Techniques

3.1 AC Calorimetry

3.1.1 Introduction to AC Calorimetry

AC calorimetry was introduced by Sullivan and Seidel [24], and Handler et al. [25], simultaneously in 1968. Today it has become a classical method, well-established, widely used, and most of all, very reliable. Among the different techniques that are capable of measuring the heat capacity, AC calorimetry is very suitable for scientific purposes. This is because the AC technique has several advantages compared to other calorimetric methods, that measure the heat capacity:

1. Extremely high relative caloric sensitivity. Results better than 0.001% at low temperatures are typical.

2. Very wide temperature range, from 50 mK to above 3000 K

3. Very high temperature resolution (in the μK range)

4. Small and very small sample mass, ranging from μg to mg yield reasonably good signal. This is, potentially, a very crucial factor when large batches of material are not readily available, or very difficult to make, such as the case for thin film studies and superconductors.

5. The best method for studying samples under extreme environments, such as high pressure, high fields, and or very low temperatures. Because of the oscil-

lating signal, this method can be used even under mechanically or electrically noisy environment, by implementing filtering or lock-in techniques.

6. Appropriate for taking data in scanning temperature mode or stepwise temperature mode, in heating, cooling, or even under isothermal conditions.

7. Appropriate to study the dependence on the frequency, electric or magnetic field, pressure, concentration etc., under isothermal conditions.

8. It can be extended to give information about other sample characteristics like thermal conductivity or the dynamic heat capacity $C_p(\omega)$

Our calorimeters can be operated in three different temperature scanning modes; stepwise, scanning or time mode (isothermal). The latter can be used to study dependencies of the heat capacity on parameters other than temperature. All three modes are completely computer controlled through a single program, which can alternate between them, as specified from the user. In the scanning temperature mode the normal scanning speeds lie between 20 and 200 $mK/hour$, but we can use much faster scan rates in preliminary studies when the only purpose is to identify the transition temperatures.

The technique and even the design of the actual calorimeter at WPI is very versatile; it allows the user to extract latent heat information by means of the ***Non-Adiabatic Scanning*** (NAS) calorimetry, with exactly the same setup. This overcomes the one significant deficiency of AC calorimetry; as a direct measure of C_p it is not very sensitive to transition latent heats, if present. It should be mentioned that although the relative accuracy is very high, the absolute accuracy of the measured heat capacity is modest, about 1-10%, due to the sensitivity to the internal and external thermal relaxation times. The appropriate choice of the operation frequency is decisive for the dynamic behavior of the calorimeter and the measurement's reliability. Care should be taken to remain closely within the limits of the heat flow model, where the data' interpretation is easily understood. The most important factor in the behavior of the calorimeter is to have a very good and reproducible thermal link between the heater-sample-thermometer arrangement.

3.1.2 Theory of Operation

In the *AC* calorimetric technique the sample is heated with a periodically modulated power (usually sinusoidal), and the induced temperature oscillations above the average are detected. Knowing the frequency and the amplitude of the power, one can deduce the heat capacity of the sample. A very crude, basic operating equation can be derived very simply from the definition of the heat capacity, by taking the time derivatives of the numerator and the denominator as:

$$C_p = \frac{|\partial Q|}{|dT|} = \frac{|\partial Q/dt|}{|dT/dt|} = \frac{P_0}{\omega T_{AC}} \tag{3.1}$$

where, P_0 is the amplitude of the power oscillation, T_{AC} the amplitude of the temperature oscillation, and ω the power frequency.

The derivation of the fundamental operating equations of the *AC* calorimetry were worked out in the paper by Sullivan and Seidel [24], who did a thermal analysis of the simple model that is shown in Fig. 3.1.

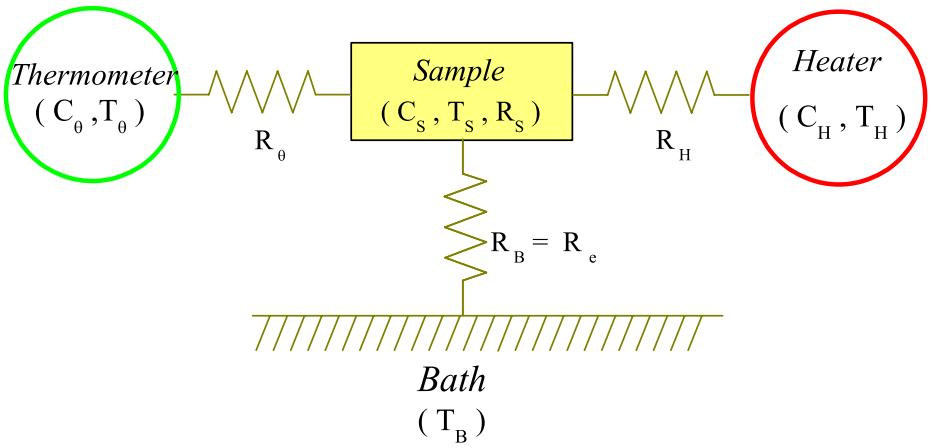

Figure 3.1. Schematic diagram of the One Lump Thermal Model used for *AC* Calorimetry. T_i, C_i and R_i denote respectively the **T**emperature, the heat **C**apacity, and the thermal **R**esistance, of the sample, heater, thermometer and bath, labeled respectively by the indices $i = S, H, \theta, B$.

This model becomes geometry independent i.e., the locations of heater, thermometer, as well as the cell geometry, are not important, as long as certain require-

ments are met. The model assumes a zero thermal resistance between the sample and the cell, and one single thermal path between the thermometer-sample-heater arrangement and the bath. The ***Thermal Resistance*** (R), is defined as the reciprocal of the ***Thermal Conductance*** (K). We also define the following ***Time Constants***:

$$\tau_S = R_S \cdot C_S, \tag{3.2a}$$

$$\tau_H = R_H \cdot C_H, \tag{3.2b}$$

$$\tau_\theta = R_\theta \cdot C_\theta, \tag{3.2c}$$

for the sample(S), heater(H), and thermometer(θ), indicating the characteristic thermal relaxation time for each element.

If the total heat capacity of the system is

$$C = C_H + C_S + C_\theta \tag{3.3}$$

then the ***External Time Constant*** (τ_e), (time for the heater-sample-cell-thermometer arrangement to reach thermal equilibrium with the bath), can be defined as:

$$\tau_e = R_e \cdot C \tag{3.4}$$

The ***Internal Time Constant***, (τ_i), (internal relaxation time for thermal diffusion of the heater-sample-cell-thermometer arrangement) related to the internal thermal resistance R_i, can be defined in two ways as:

$$\tau_i = \tau_H + \tau_S + \tau_\theta \tag{3.5a}$$

$$R_i = \tau_i / C \tag{3.5b}$$

The temperature of each element, thermometer, sample, heater, and bath is respectively denoted by, T_θ, T_S, T_H, and T_B.

The energy balance equation requires that the *Power Input = Rate of Heat absorbed + Rate of Heat lost to the bath.* The power input is sinusoidal of the form: $P_0 e^{i\omega t}$. The three heat balance equations, one for each path or element, are:

$$C_H \quad \frac{\partial T_H}{\partial t} = P_0 e^{i\omega t} - \frac{T_H - T_S}{R_H} \tag{3.6a}$$

$$C_S \quad \frac{\partial T_S}{\partial t} = \frac{T_H - T_S}{R_H} - \frac{T_S - T_\theta}{R_\theta} - \frac{T_B - T_S}{R_e} \tag{3.6b}$$

$$C_\theta \quad \frac{\partial T_\theta}{\partial t} = \frac{T_S - T_\theta}{R_\theta} - \frac{T_B - T_\theta}{R_e} \tag{3.6c}$$

The solution of the above equations is rather complicated, but if we assume that,

a. The heat capacities of the heater and of the thermometer are much less than that of the sample

b. The sample-heater-thermometer arrangement come to equilibrium with a time constant much less than the heating period ($2\pi/\omega$), i.e., $\omega \ll 1/\tau_i$

c. The frequency is much larger than the inverse of the sample to bath relaxation time (external time constant), i.e., $\omega \gg 1/\tau_e$

than, the steady state simplified solution for T_θ, is

$$T_\theta = T_B + T_{DC} + T_{AC} e^{i(\omega t + \Phi)} \tag{3.7}$$

where,

$$T_{DC} = P_0 \cdot R_e \tag{3.8a}$$

$$T_{AC} = \frac{P_0}{\omega C} \left(1 + \frac{1}{\omega^2 \tau_e^2} + \omega^2 \tau_{ii}^2 + \frac{2}{3} \frac{R_i}{R_e} \right)^{-\frac{1}{2}} \tag{3.8b}$$

$$\Phi = -\frac{\pi}{2} + \arctan\left(\frac{1}{\omega \tau_e} - \omega \tau_i \right) \tag{3.8c}$$

T_{DC} is the RMS temperature raise, Φ is the absolute phase difference between the temperature and the power oscillations, and the time constant τ_{ii} is defined as

$$\tau_{ii}^2 = \tau_H^2 + \tau_S^2 + \tau_\theta^2 \tag{3.9}$$

We usually use the relative phase shift φ, which doesn't carry the constant

$-\pi/2$ phase difference, between the temperature and the power. So we define:

$$\varphi = \Phi + \pi/2 \tag{3.10}$$

As can be seen from Eq. (3.8c), φ can be expressed as:

$$tan(\varphi) = \frac{1}{\omega\tau_e} - \omega\tau_i \tag{3.11}$$

Furthermore, the heat capacity can be complex and frequency dependent:

$$C(\omega) = C\,'(\omega) - iC\,''(\omega) \tag{3.12}$$

with $C\,'(\omega)$ and $C\,''(\omega)$ being the real and imaginary parts respectively. Solving Eqs. (3.8b) and (3.11) for $C\,'$ and $C\,''$, yields:

$$C\,'(\omega) = \frac{P_0}{\omega T_{AC}} \cos\varphi * f(\omega) \tag{3.13a}$$

$$C\,''(\omega) = \frac{P_0}{\omega T_{AC}} \sin\varphi * g(\omega) - \frac{1}{\omega R_e} \tag{3.13b}$$

The functions $f(\omega) \approx g(\omega) \approx 1$ are small correction factors to account for the non-negligible internal thermal resistance R_i of the sample and cell compared to R_e. These corrections were applied to all samples studied here.[1] The value of the external thermal resistance R_e is typically the same for all samples, $R_e \sim$ 200 K W^{-1}.

The ***Specific Heat Capacity***, C_p , can then be found as

$$C_p = \frac{C\,'(\omega) - C_{empty}}{m_{sample}} = \frac{C^* cos(\varphi) f(\omega) - C_{empty}}{m_{sample}} \,, \tag{3.14}$$

$$C\,''(\omega) = C^* sin(\varphi) g(w) - \frac{1}{\omega R_e} \,, \tag{3.15}$$

where, C_{empty} is the heat capacity of the empty cell, $C^* = P_0/(\omega T_{AC})$, m_{sample} is

[1]The correction factors are, explicitly, $f(\omega) = [1 + cos^2(\varphi)(\frac{2R_i}{3R_e} + \frac{2\tau_i}{\tau_e} - 2\tau_s\tau_c\omega^2)]^{-1/2}$ and $g(\omega) = f(\omega)[1 + \frac{\omega\tau_i}{tan(\varphi)}]$ where the internal thermal relaxation time is the sum of that for the sample and cell, τ_i and τ_e are given from Eqs. (3.5a) and (3.4). In the limit of zero internal thermal resistance, or $\tau_i \ll \tau_e$, both $f(\omega)$ and $g(\omega)$ approach one for all ω.

the mass in grams of the sample.

Eqs. (3.14) and (3.15) are the basic equations used in the calculation of the real and imaginary heat capacities for our calorimeters. Experimentally, the amplitude of the temperature oscillations T_{AC}, and the relative phase shift φ, are measured. At the beginning of each experiment, for a set frequency ω, the amplitude of the power dissipated in the resistive heater, P_0, as well as its phase shift, are measured.

The phase shift contains information about the heat capacity and the internal time constant, which is directly related to the sample's thermal conductivity. Empirically, it has been observed that for a weak first order transition there is always a peak in the phase, while, for strong first order transitions, the phase might show a 1 point anomaly or a simple discontinuity. This is because the transition happens very fast and pre-transitional fluctuations are very small compared with the latent heat of the transition. For the case of the weak first order transitions, the width of the phase peak has been associated with the two-phase coexistence region where the release or absorption of the latent heat occurs. In this case, another heat source or heat sink appears which has an energy spectrum. This spectrum is generally, completely different from the one applied at the heater (delta function), which is being detected. This shows up as a peak in the imaginary heat capacity, the width of which is equal to the two-phase coexistence. In most of the other cases, i.e., outside the two-phase coexistence region, and for most of the second order phase transitions, the heat capacity is purely real and independent of ω, so $C\,''(\omega) \equiv 0$. This fact may be used to extract the external resistance R_e directly from the AC technique.

3.1.3 Test of Theory

The most important approximation needed to solve Eqs. (3.6) required that the operating frequency ω, should be such that:

$$\frac{1}{\tau_e} \;<\; \omega \;<\; \frac{1}{\tau_i} \tag{3.16}$$

Experimentally there are several ways to achieve the above requirement:

a. The external time constant is dependent on the thermal link of the cell to the bath R_e. This is usually made through the electrical leads for the heater

and the thermometer and the atmosphere of the bath. All three parameters can be tailored to achieve a long relaxation time. This is about $40s$ for a typical cell in our lab.

b. The internal time constant is mostly dominated by the sample thickness (in thick samples), since the time constants for the heater and the thermometer

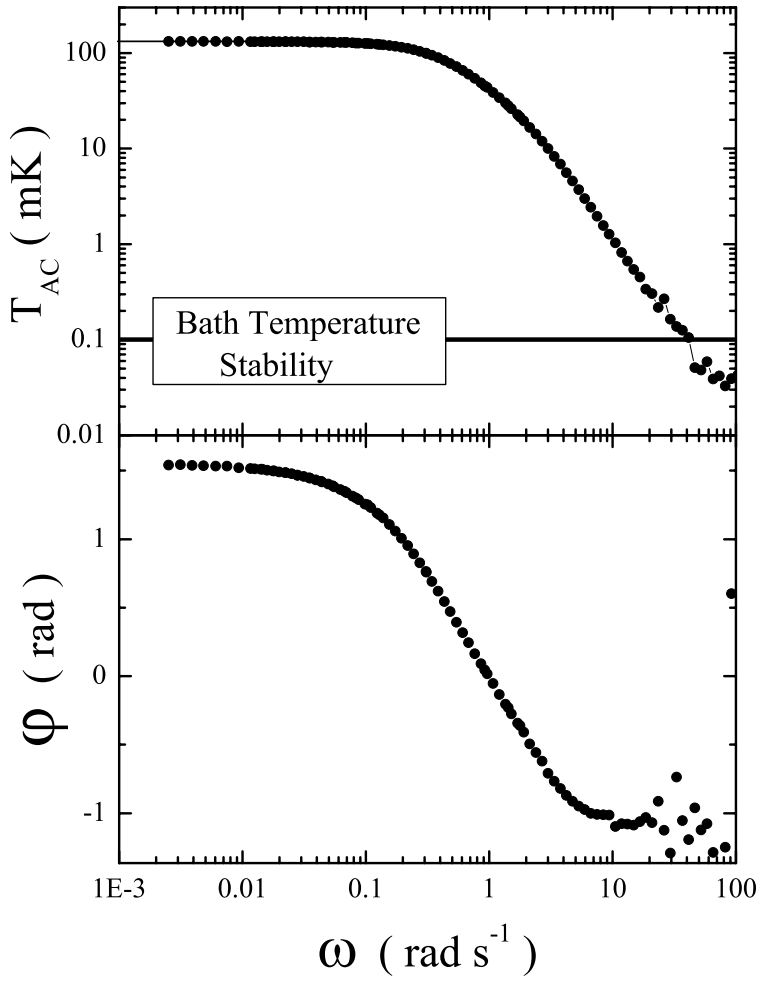

Figure 3.2. a- Upper panel: Log - log plot of the amplitude of temperature oscillations, T_{AC}, vs. the frequency ω. The solid line represents typical noise level of the bath temperature.
b- Lower panel: Semilog plot of the relative phase shift, φ, vs. the frequency ω.

are typically short and temperature independent. In order to satisfy the above frequency requirement, and to not create thermal gradients in the sample, the thickness of the sample should be less than the thermal diffusion length, ℓ_θ, given by:

$$\ell_\theta \;=\; \sqrt{\frac{2A}{\omega\tau_S}} \;=\; \sqrt{\frac{2A}{\omega R_S C_S}} \tag{3.17}$$

where τ_S, R_S, C_S, are respectively the internal time constant, the thermal resistance and the heat capacity of the sample, and A is the cross-sectional area. Another way of increasing the thermal conductivity of the sample-cell arrangement is to make the cell out of very good thermal conductor materials, like gold or silver. To this purpose, including a gold coil wire inside the cell also helps.

The realization of the frequency requirements, can be verified experimentally, by means of a frequency scan. Here, the only varying parameter is ω, the frequency of the power, while the amplitude of the power and the temperature of the bath are kept constant. The dependencies of T_{AC} and φ, on omega, for a heater-thermistor arrangement (no silver cell, no sample) are plotted in Fig. 3.2. As seen in the upper panel of Fig. 3.2, T_{AC} approaches asymptotically the value of T_{DC} at low frequencies. T_{DC} depends only on P_0 and the external thermal resistance according to Eq. (3.8a). In the lower panel of Fig. 3.2 is shown the frequency dependence of the relative phase shift φ. The behavior of both parameters, T_{AC} and φ is qualitatively the same for typical cells used in our experiment. Fitting the phase shift to

$$\varphi = A * atan[(\omega * \tau_e)^{-1} - \omega * \tau_i] \tag{3.18}$$

allows the determination of the external and internal time constants.

However, we usually extract the internal and external time constants by fitting the dependence of the product ωT_{AC} on ω. Plotting this dependence in a log-log scale has the benefit of clearly visualizing the plateau region, where the applicability of the AC technique, for a given cell arrangement, is possible. This type of

plot is shown in Fig. 3.3. A fit of this dependence to

$$\omega T_{AC} = \frac{A}{\sqrt{1 + (\omega\tau_e)^{-2} + (\omega\tau_i)^2 + R}} \tag{3.19}$$

allows the determination of the external and internal time constants as well as the ratio $2R_i/3R_e = R$. The fit parameter, R, is typically fixed to zero, because it is generally very small and the nonlinear least squares fit is insensitive to this parameter.

We performed frequency scans on three different cell arrangements. The first was a typical envelope LC filled cell (FC), the second was an empty cell (EC), while the third one was a very simple heater-thermistor arrangement $(H\text{-}Th)$, where the

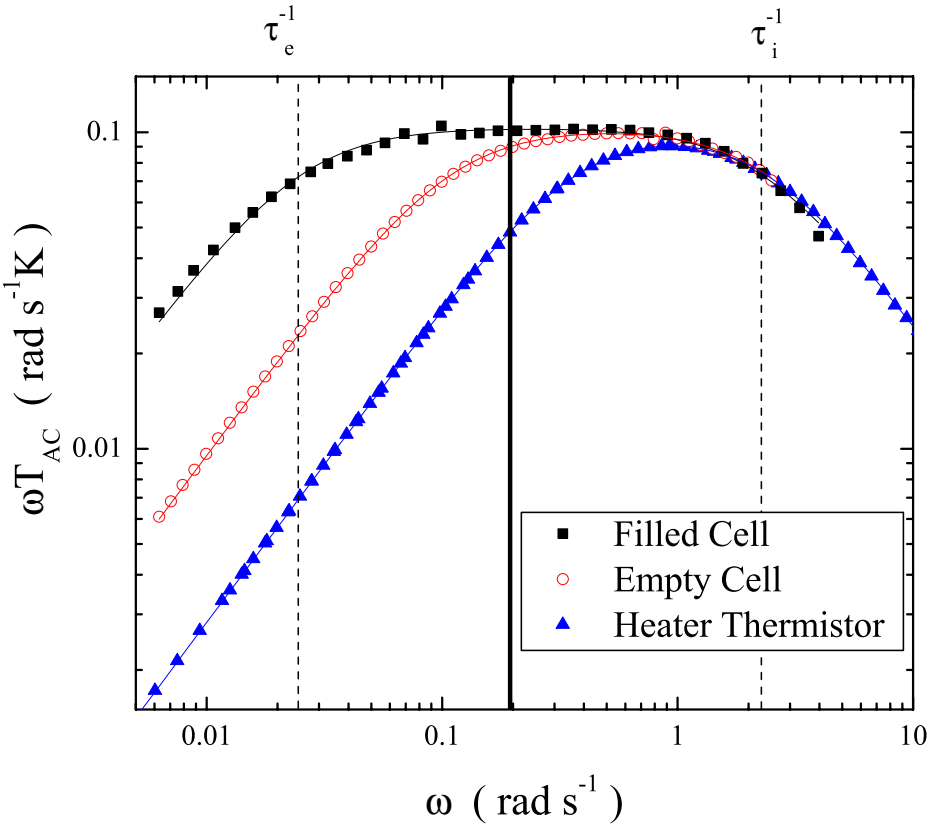

Figure 3.3. Log - log plot of ωT_{AC} *vs* ω. Data were multiplied by a constant factor, so that the amplitudes of the fit with Eq. (3.19) matched. Solid lines through the data points are fits. The dashed lines represent $1/\tau_e$ and $1/\tau_i$ for the Filled Cell, (FC), case, while our typical AC calorimetry working frequency is $\omega = 0.196\ rad/s$, and is represented by the vertical solid line. See legend for symbols definitions.

$Cell$	A	τ_i	τ_e	C	χ^2/DoF
FC	103.24 ± 0.62	0.436 ± 0.012	40.035 ± 0.94	$\simeq 0.090$	5.03×10^{-6}
EC	103.24 ± 0.25	0.412 ± 0.005	9.260 ± 0.061	$\simeq 0.026$	4.98×10^{-7}
$H-Th$	103.24 ± 0.11	0.412 ± 0.001	2.740 ± 0.006	$\simeq 0.006$	4.41×10^{-8}

Table 3.1. Summary of the frequency scan fit results from fitting with Eq. (3.19). Shown are the cell type, the normalized amplitude A in 10^{-3} ($radKs^{-1}$), τ_i and τ_e in s, the heat capacity of the samples at the scanning temperature C in JK^{-1}, and χ^2/DoF.

thermistor was attached directly to the heater with a very small amount of GE Varnish. (See Sec. 3.1.4.1 for more details on the cell designs.) Of course the total heat capacity decreases significantly from the *FC*, to the *EC*, to the *H-Th*.

For easier comparison the data were scaled, so that their fit amplitudes, A, matched. This was needed since the power was not the same for the three tests. The scaling involved multiplication by a constant factor, (18.7029) for the *EC* and (2.16119) for the *H-Th* data, to match with the *FC* data [2]. This will effectively shift the data upward in a log scale. The shift does not effect the time constants or the R parameters; it only effects the amplitude A, which is related to the power and the heat capacity of the cell as, $A = P_0/C$ (See Eq. (3.8b)). The scaled data are shown in Fig. 3.3. The solid lines through the data are the respective nonlinear least squares fits with Eq. (3.19). Interestingly, the "high" frequency wing of the data overlap very nicely. The high frequency rollover is mostly dominated by the internal time constant τ_i, suggesting that the internal time constants for the three cells are very similar. Indeed, as can be seen in Table 3.1, τ_i values for all three cases are very similar, with τ_i of the *FC* being slightly bigger then the other two. This confirms that the sample thickness, in a typical *LC* filled envelope cell, does not cause any appreciable change on τ_i. Furthermore, the major contribution on τ_i remains the intrinsic internal time constant of the thermistor in all three cases.

Quite contrary, the low frequency rollover, which is dominated from the external time constant, shows remarkable differences between the three arrangements. These differences are to be expected, since τ_e depends linearly on the total heat capacity of the cell arrangement and R_e, as given in Eq. (3.4). R_e should not change much, since the heater and thermometer leads' lengths are very similar for

[2]The actual scaling factor can be calculated as $C \cdot P_0(FC)/C(FC) \cdot P_0$ where $C(FC)$ and $P_0(FC)$ are respectively the values of the heat capacity and the power for the *FC* experiment while C and P are the values for the other arrangements.

the three arrangements. The heat capacity on the other hand decreases significantly, thus, making the external time constant of the smaller cells smaller. This is the reason the data with smaller C show narrower plateaus. The external time constants are proportional to the cells' heat capacity, which are given in Table 3.1.

The nonlinear least squares fit for the *FC*' data yielded the following values: $\tau_i = 0.436 \pm 0.012$ s, and $\tau_e = 40.0 \pm 0.9$ s. The range of the "green zone" for the *AC* calorimetry spans about two decades in frequency, as is shown from the dashed vertical lines in Fig. 3.3. This gives us quite a wide range of frequencies to choose from, for the *AC* experiment, and is a definite proof of the applicability of the one-lump thermal model to our calorimeters.

3.1.4 Design and Operation of the *AC* Calorimeter

Three calorimeters were constructed, two of which are identical (named Calor A and Calor B), and the third one (named Calor LT, for cryogenic temperatures), uses a different detection technique from the first ones. All of the work for this thesis was done on the first type of calorimeters, so we'll focus only on their description. In the design and construction of the calorimeters major concern was given to the ease of sample placement, versatility, wide range of temperature operation, and very high resolution.

3.1.4.1 Cell Design

Before this work, the most used cell in the WPI Lab was the ***Cup and Lid*** design, which has been described in detail by Stine[26], Chan[27] and Garland. For this work we tried and used mostly a new design, namely the ***Envelope*** design. In the cup and lid design the lid is cold welded to the cup, providing a better handling of reactive or very sensitive samples, since it completely seals the sample from the outside environment. On the other hand, the envelope design is advantageous in almost every other aspect.

1. It improves the sensitivity of the technique and lowers the noise, by reducing the addendum heat capacity. The envelope design uses generally less silver, and does not need any of the In-Sn alloy, used in the cold weld of the cup and lid, thus reducing the addendum heat capacity.

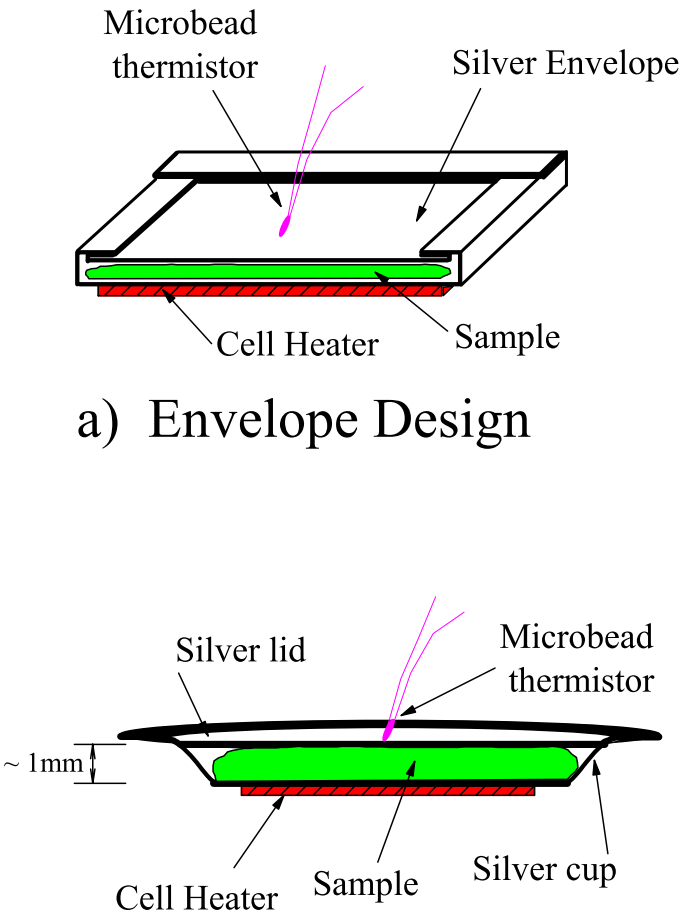

Figure 3.4. Cell designs. a) Envelope type cell. b) Cup and lid type cell

2. It improves the frequency scan profile. This is an important factor because the smaller the deviation from the one-lump thermal model, the smaller the error in calculating C_p. The reduction of the background heat capacity, a better match between the geometric shape of the cell and the heater, a generally thinner cell, are all factors that contribute towards the improvement of the frequency scan profile.

3. It is much easier to construct, thus, saves a lot time, materials, and frustration.

4. It can be used in concentration dependence studies, where the concentra-

tion varies continuously. For example, measurements of heat capacity can be carried out while the solvent is evaporating from a mixture; this will continuously change the sample's concentration. Of course, the bath temperature remains constant during this experiment.

The envelope cell, shown schematically in Fig. 3.4a, is made of 99.95% pure silver foil, $0.025mm$ thick, from Alfa Aesar [28]. Before loading the sample, we usually degas it at a high temperature, well into the isotropic phase of the LC sample, for at least 1 hour, in order to remove possible adsorbed water. This procedure is the same for all samples, since we want to make sure that all samples have the same thermal history. After the sample is loaded, typically 15 - 30 mg, the 'envelope' is closed by folding and tightly ironing together the edges of the cell. The dimensions of a closed cell are $\sim 9 \times 13mm$.

As heater was used a strain gauge of type FAE-25-12-S13EL, that was purchased from BLH Electronics, Inc. [29], with a nominal resistance of 120Ω. We trim the Kapton edges of the heater to $\sim 4 \times 12mm$ size, in order to reduce the background heat capacity of the heater. Then the heater is attached to the bottom of the cell, using acetone diluted GE 7031 varnish.

The temperature sensor is then attached by a small drop of GE varnish at the center of the cell, on the opposite side from where the heater is attached. The sensor is an ultra-small bead, type 61A8, from YSI Temperature [30]. The bead diameter is about 0.254 mm, and the leads are about 8 mm long. These beads have a time constant of about 0.5 s in still air, as specified by their manufacturer. The mass of the bead itself is less than $0.0001mg$. The whole cell arrangement is allowed to dry under a lamp, for several hours, before mounting it on the calorimeter.

3.1.4.2 Temperature Control

The cell which holds the sample needs to be inside a bath, which can provide very good temperature control as well as a controlled environment, like vacuum, or inert gas atmosphere. Therefore, the bath is made of a massive copper cylinder with a central cylindrical cavity where the cell is situated. This bath, as can be seen in the diagram depicted in Fig. 3.5, is placed inside a modified Lauda bath model KS 20D, which provides a first temperature control stage with a stability of

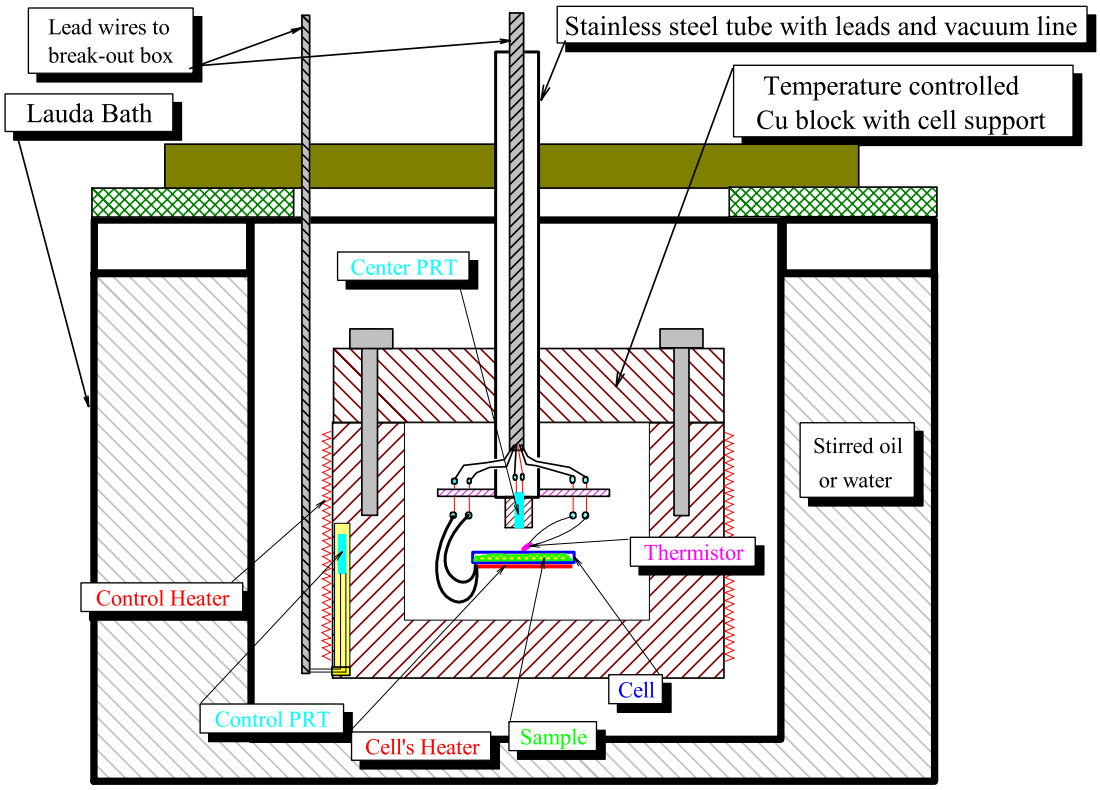

Figure 3.5. Design of the *AC* Calorimeter. The sample lies inside a massive copper block, which is temperature controlled to better than $\pm 1mK$ in the stepwise mode. The circuit for the Lauda bath is not shown.

$\pm 0.1\ K$. The temperature of the copper block is controlled from a Lakeshore, model 340 temperature controller, via a proportional-integral-derivative (PID) feedback loop [31].

The observed temperature stability, which is crucial for the stepping operational mode, at the rim of the cylinder is $\pm 1mK$ for over 1 hour; while it is $\sim 100\mu K$ inside the cavity where the cell is situated, because of the damping that comes from the massive copper block. The temperature scanning is achieved by 'rapidly' changing the setpoint of the temperature controller. Adjusting the PID settings for a slow response the bath does effectively follow the changing setpoint in a very linear way, by smoothing out the very small steps. In this way we can achieve very linear temperature scanning with rates varying from $10mK/hour$ to $5K/hour$, and

with noise better than $100\mu K$.

A Kapton insulated flexible heater from Omega Engineering, with dimensions that are closely matched to that of the bath, is glued to the outside surface of the cylinder. The control thermometer for the feedback is a platinum PT-100 ***resistive temperature device*** (RTD), purchased from Lakeshore. (This thermometer will be referred to, as the *control PRT*). It is placed in a cavity inside the copper cylinder, very close to the surface where the heater is glued. This placement gives very good performance in both the scanning or stepping operational modes.

A copper lid, with a long stainless steel tube in the middle, is mounted with six bolts on top of the bath. A gas tight seal is achieved with an O-ring, set in a circular groove around the top surface of the copper block. The tube allows for the cables to go through as well as the application of vacuum. At the end of the tube a copper extension is placed with a hole in the center, where another platinum RTD, PT-1000, is placed. This second PRT is referred to as the *center PRT*. It is placed very close to the cell and the center of the bath cavity, therefore can measure the bath temperature, T_B, next to the cell, with very good accuracy.

The cell is supported in place by its own heater and thermistor leads, which are soldered to posts. The posts themselves are placed at a plate at the very end of the stainless steel tube. At the other side of the posts are soldered permanently the wires that connect the sample's heater and thermistor to the break-out box, and from there to the Keithley DMM.

3.1.4.3 Electronic Circuitry

Fig. 3.6 gives a block diagram of the electronics employed and the way the system is connected. The whole experiment is controlled via a pentium PC, operating under Windows 98 ©. The program that controls the data acquisition and preliminary analysis was written in C++, and compiled under Borland C++ © (see Appendix A). The communication with the instruments is done through a PCI-GPIB interface card from National Instruments, Inc. [32]. All the instruments are connected to the experiment via a breakout box, which facilitates a very clean cable configuration, and also gives more versatility to the system.

A 12 pin, vacuum proof, Amphenol [33] connector is placed in the other end of the stainless steel tube. Permanent electrical cables that run through the tube

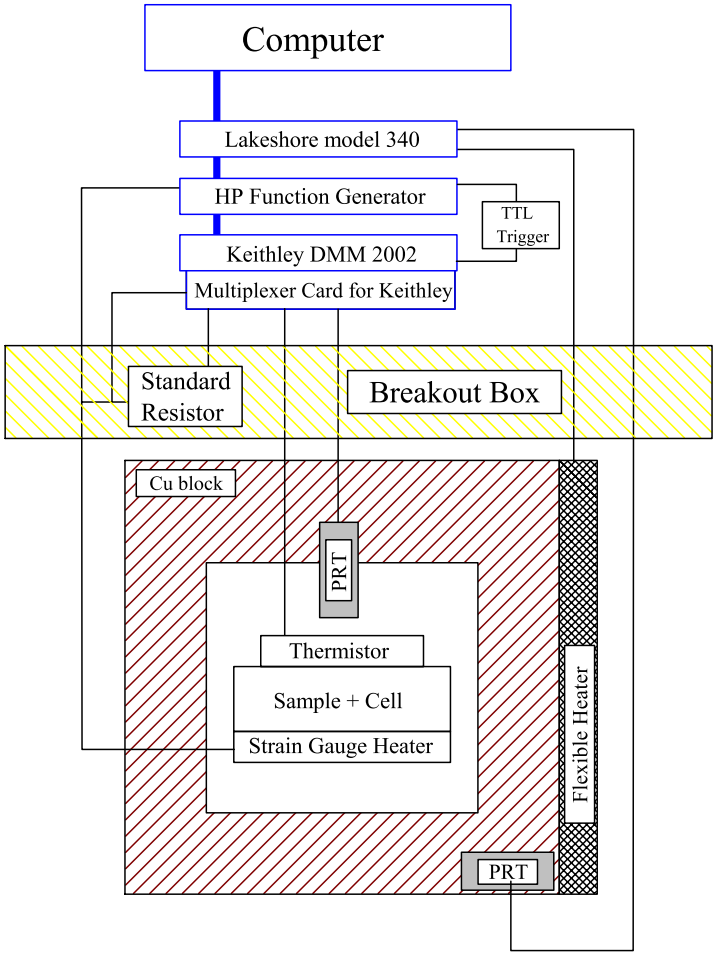

Figure 3.6. Block diagram of Calor A and B, showing all the connections to the instruments. The whole control and data acquisition is computer controlled through a GPIB interface.

connect the connector to the terminal posts inside the bath (see Fig. 3.5). On the other side of these posts are connected the strain-gauge heater, the thermistor leads from the cell and the center PRT leads.

The system makes full use of the Keithley DMM, model 2002, with $8\frac{1}{2}$ digits of resolution, a 128 kB on board memory card, and a multiplex scanner card model 2001-SCAN [34]. The scanner card gives the possibility to completely automate the measurements, since all the parts are permanently connected to the DMM. The card can be configured to do 4-wire or 2-wire measurements. The resistance measurements of the center PRT and the thermistor are configured as 4-wire, while the voltage and resistance measurements, across the strain-gauge heater and

the standard resistor, are configured as 2-wire measurements [3]. The latter two measurements are needed in order to accurately determine the ac power applied at the cell, as will be explained in more detail in the next section.

When measuring the resistance of the PRT thermometers, care is taken to minimize the self heating that comes as a consequence of current passing through the resistance from the measurement itself. This was seen to be very small and furthermore, would remain almost constant during the measurement. Thus it can safely be neglected as a correction to the temperature of the bath.

The electrical power dissipated in the strain-gauge heater is provided by an Hewlett Packard Function Generator/Arbitrary Waveform Generator, model HP 33120A [35]. The strain-gauge is connected in series with a high precision standard resistor, of resistance R_{STD}, which is placed in the breakout box. The purpose of this resistor is two fold. First it reduces the voltage across the strain gauge heater, and secondly, it is used to accurately measure the current through the heater, since $I_{HTR} = I_{STD}$ (by virtue of the series connection).

As already mentioned, the bath temperature is controlled by the Lakeshore model 340 temperature controller. The cables for the heater and the control PRT pass through a hole at the top of the Lauda bath directly to the Lakeshore terminals.

3.1.4.4 Thermometry

The accurate determination of temperature is one of the most important aspects of any thermodynamic measurement, and more so for the study of phase transitions. Two types of ***Resistive Temperature Devices*** (RTDs) were used in this work, platinum, and carbon flake thermistors. RTDs change the resistance as a function of temperature, i.e., there is a function f that describes this dependence: $R = f(T)$ or $T = f^{-1}(R) = g(R)$. Platinum RTDs, or short PRTs, have an almost linear function with a positive temperature coefficient ($\partial R/\partial T \simeq const > 0$). They are

[3] In the 4-wire measurement two of the wires supply the current while the other two measure the voltage drop across the resistance; this way only the value of the resistance of interest gets measured, without adding the lead's resistance. In the two-wire measurement the same line that applies the current, does the voltage measurement, therefore the resistance of the connecting leads is added to the resistance of interest. This can be a source of error especially if small resistances are to be measured.

generally very stable and very reproducible even for different thermometers; therefore they are good for calibration and control. Carbon flake thermistors, on the other hand, can be made very small, and very sensitive, i.e., their resistance changes substantially with a small temperature change. Their resistance-temperature dependence is highly nonlinear with a negative temperature coefficient ($\partial R/\partial T < 0$). The nonlinearity of the dependence used to be a problem, but the use of computers makes it very easy to convert the resistance to temperature, or vice versa. Their main drawback is that they are not quite stable, thus not very reproducible.

Empirically the dependence of the resistance of the PRT on the temperature can be described by:

$$R = R_0 \left(1 + aT + bT^2\right) \tag{3.20}$$

where, R_0, is the resistance at $0°C$, and a, b are calibration constants. It is straight forward to invert Eq. (3.28), to get the temperature as a function of the resistance. Converting the readings of the resistance of the center PRT, before and after the sample temperature digitizing (R_b^{PRT}, R_a^{PRT}), to the respective temperatures, (T_b^{PRT}, T_a^{PRT}), allows for the calculation of the bath temperature by linear interpolation, or simple averaging (Remember, the temperature is always, either fixed or linearly ramped). So:

$$T_{bath} = \frac{T_b^{PRT} + T_a^{PRT}}{2} \tag{3.21}$$

For the thermistor, the relation between temperature and resistance, is more complicated due to the stronger temperature dependence. Usually, the temperature dependence on resistance ($g(R)$), is well described by the following form:

$$\frac{1}{T} = a_0 + a_1 \log\left(\frac{R}{R_0}\right) + a_2 \left[\log\left(\frac{R}{R_0}\right)\right]^2 \tag{3.22}$$

where a_0, a_1, a_2 are constants, and R_0 is the resistance at some temperature. We fix $R_0 = 10k\Omega$ for all calculations. Since the coefficients will drift slightly with time, recalibration of the thermistor against the PRT at the end of each run is required.

Experimentally, the amplitude ΔR, the average thermistor resistance R_{th}, and the phase φ_R, of the resistance oscillation, is found from the fit of the digitized

waveform. From Eq. (3.22), the temperature of the thermistor T_{th}, can be easily calculated. From the amplitude ΔR, since the amplitude of the oscillations is very small, we can find T_{AC}, (the corresponding amplitude of temperature oscillations), by using the approximation:

$$T_{AC} \approx \left|\frac{dT}{dR}\right| \Delta R \tag{3.23}$$

T_{AC} is needed in the calculation of C^* (see Eq. (3.26))). From Eqs. (3.22) and (3.23), T_{AC} is then calculated by:

$$T_{AC} = T_{th}^2 \frac{\Delta R}{R_{th}} \left[a_1 + 2a_2 \log\left(\frac{R_{th}}{R_0}\right)\right] \tag{3.24}$$

The fit of the digitized wave will return the amplitude and phase, for each frequency. If the voltage is set on purpose with some offset, there will be signal also in the voltage frequency. This gives the possibility of doing a simultaneous measurement of $C_p(\omega/2)$, and $C_p(\omega)$. See appendix A.2 for details.

3.1.4.5 Data Acquisition

The data acquisition is achieved with software written in C++, and compiled under Borland C++. The program is written in multi-threaded fashion. This enables an efficient split of the temperature control task from the data collection task. The main thread collects the data, does the preliminary analysis and the storage and printing of the results, while the second thread controls the temperature. Both threads communicate with synchronizing signals when needed.

Before starting the program, the user is required to modify the configuration file *Acp_All.ini*, which holds the values of the temperature, the rates, the frequency and amplitude of the voltage for the strain-gauge heater, as well as some basic settings that control the instruments. A typical *Acp_All.ini* configuration file is given in appendix A.3. After saving this file the user starts the program which reads the *Acp_All.ini* file, displays the information on the screen and asks the user permission to continue. If the answer is "yes" the program will check for possible error input. If there are no errors the experiment proceeds without further user intervention. The input configuration file is saved in the parameter output file

(*.par), which stores the fit parameters.

Firstly, the power dissipated at the strain gauge heater gets measured. This is done by "digitizing" [4] the voltage across the standard resistor and then the heater. The amplitude of the power dissipated at the cell is calculated from the formula:

$$P_0 = I_H V_H = I_{STD} V_H = \frac{V_{STD}}{R_{STD}} V_H \tag{3.25}$$

where,V_{STD}, V_H, are the voltage amplitudes at the heating frequency and R_{STD} is the resistance of the standard resistor. From the waveform the phase of the power oscillations $\varphi_{_P}$ is also extracted. For more details on how this is done refer to the appendix A.1.

After the power measurement the temperature controlling thread (TCT) is started. The data collection, starts after the TCT has signaled the main thread to Start Digitizing. The data collection continues as follows:

1. Record the average resistance of the center PRT, R_b^{PRT}, before the Digitizing. This corresponds to the temperature of the bath before Digitizing, T_b.

2. Digitize the thermistor readings for several heating periods. Fit the waveform to find the amplitude ΔR_{th} and phase $\varphi_{_R}$ of the resistance oscillations. These correspond respectively to the amplitude of the temperature oscillations, ΔT_{AC}, and the phase of the temperature oscillations, $\varphi_{_T}$. From the fit one gets also the values of the fit quality, χ^2, and the average thermistor resistance R_{th}. See appendix A.1 for the details.

3. Record the average resistance of the center PRT, R_a^{PRT}, after the Digitizing. This corresponds to the temperature of the bath after Digitizing, T_a.

4. Convert the resistance values to corresponding temperature values. See section 3.1.4.4 for more details.

[4] The DMM is set to do a specified number of measurements at equally spaced time intervals. For each measurement the time elapsed and the measured value get stored in the internal memory. After the specified number of measurements is carried out, the data are then downloaded at the computer. The digitizing gets triggered by the TTL trigger of the HP, which happens at every zero crossing of the voltage.

5. Calculate C^*, the relative phase shift φ between the temperature and the power, and the temperature of the bath with the formulas:

$$C^* = P_0/(\omega T_{AC}) \quad (3.26)$$

$$\varphi = \varphi_R - \varphi_P \quad (3.27)$$

$$T_{PRT} = (T_b + T_a)/2 \quad (3.28)$$

6. Save to the data file (*.dat) the C^*, φ, T_{PRT}, T_{AC}, as well as the average resistance of the thermistor, R_{th} and χ^2 from the fit.

7. Signal the TCT that it is Done with Digitizing.

8. Check to see if the TCT has signaled that the temperature has reached the end of one scanning zone or the end of all zones. If none is signaled, repeat again from step 1. If the Zone Has Ended, continue to the next zone. If the TCT has signaled that it is Done With All Zones, end TCT, end communication with instruments, and finish the program.

The temperature control thread when it starts it does the following:

1. Starts the Loop that goes through all the zones.

2. Determine the type of zone, i.e., if it is *TIME*, *STEP*, or *RAMP*[5]. Call the appropriate function to handle the temperature control. If all zones are done, continue to step 3.

   The called function does the following:

   (a) Equilibrate the temperature at the starting temperature of the zone, and then signal the main thread to Start Digitizing.

   (b) Control the temperature with the given specifications until the end of the zone.

[5]In a *TIME* zone, the temperature is maintained constant at the specified value for a certain amount of time. In a *STEP* zone, the temperature is stepped between a specified start temperature and end temperature with a specified stepsize. In a *RAMP* zone, the temperature is ramped between a specified start temperature and end temperature, with a specified ramprate.

(c) Wait until the ongoing Digitizing ends; then signal the main thread that the Zone Has Ended, and return to step 2.

3. End communication with temperature controller; Signal the main thread that TCT is Done With All Zones.

3.2 Non Adiabatic Scanning Calorimetry

3.2.1 Introduction to NAS Calorimetry

In section 3.1, we discussed AC calorimetry. There it was mentioned that the AC method is not accurate in determining the latent heat of the transition. Non Adiabatic Scanning (NAS) calorimetry is a calorimetric method that is directly sensitive to enthalpy. This method suits us very much, because we can run the NAS experiment in the exact same calorimeter that is running the AC calorimetry experiment, without any change in its configuration. Furthermore, even the cell designs for AC calorimetry are suitable for the NAS method. The only difference is the software to control and analyze the data.

In traditional relaxation calorimetry, instead of putting a sinusoidal power into the system, one can switch on a small but constant power, P_0 at $t = 0$. The sample's temperature is digitized as it relaxes exponentially to a temperature T_{high}, that is higher than that of the bath. Then, if the power is switched back off, the system will relax exponentially to the bath temperature T_b which is kept constant during this whole process. Because the bath is a huge thermal reservoir, the small power input to the system does not bring any noticeable change in the regulated bath temperature.

NAS is a modified version of the traditional relaxation calorimetry. Here the power is not stepped, but instead, is linearly ramped up, from 0 to a maximum value P_0. It is kept constant at P_0 for a certain amount of time, to allow the sample to equilibrate at T_{high}. Then the power is linearly ramped down from P_0 to 0. The temperature response of the sample is measured during this whole time. The process gets repeated again at another temperature, T_B of the bath, until all the desired temperature range is covered.

3.2.2 Theory of Operation

For an infinitesimal process at constant pressure the first law of thermodynamics can be written as:

$$dW_e = Pdt = dH - đQ \tag{3.29}$$

where, dW_e is the nonmechanical work done on the system (electrical in our case), P is the electrical power, dH is the enthalpy change of the system, and $đQ$ is the heat flow between the system and the bath. The latter is given otherwise by Newton's law:

$$-\frac{đQ}{dt} = \frac{T - T_B}{R_e} \tag{3.30}$$

From Eqs. (3.29) and (3.30) one can directly find that:

$$dH = \left(P - \frac{T - T_B}{R_e}\right) dt \tag{3.31}$$

and the change in enthalpy can be found simply by integrating Eq. (3.31))

$$\delta H = \int dH = \int_{t_1}^{t_2} \left(P - \frac{T - T_B}{R_e}\right) dt \tag{3.32}$$

On the other hand the enthalpy can be expressed as

$$dH = \left(\frac{\partial H}{\partial T}\right)_p dT + d(\Delta H) = C_p dT + d(\Delta H) \tag{3.33}$$

where, the latent heat, $d(\Delta H) = 0$, if the system is outside the two-phase coexistence region. Substituting Eq. (3.33) into Eq. (3.31) it is easy to find that:

$$C_p \left(\frac{dT}{dt}\right) = P - \frac{T - T_B}{R_e} - \frac{d(\Delta H)}{dt} \tag{3.34}$$

Eqs. (3.32) and (3.34) are the basic equations used in the calculation of C_p, H and latent heat (ΔH), for the NAS method.

Outside the two-phase coexistence region, or in second order phase transitions,

where $d(\Delta H) = 0$, the heat capacity is given by:

$$C_p = \frac{P - (T - T_B)/R_e}{dT/dt} \tag{3.35}$$

As seen from Eq. (3.35), in order to calculate C_p, one needs to know R_e and its temperature dependence, and more important, must perform the numerical differentiation dT/dt. This accentuates the noise present in the data, thus making $C_p(NAS)$ generally noisier than $C_p(AC)$. Also, as mentioned before, the width of the two-phase coexistence region can be determined accurately from the AC method, but there is no way to determine it from the NAS data.

Inside the two-phase coexistence region, where the release of the latent heat occurs, the interesting quantities to measure are again C_p, H and the latent heat of the transition (ΔH). H again can be measured using Eq. (3.32). Here we introduce the idea of an effective heat capacity, which can be measured from the derivative of enthalpy:

$$C_{eff} = \frac{dH}{dT} = \frac{P - (T - T_B)/R_e}{dT/dt} \tag{3.36}$$

Comparing Eq. (3.36) to Eq. (3.33), we see that:

$$C_{eff} = C_p + \frac{d(\Delta H)}{dT} \tag{3.37}$$

from which is evident that C_{eff} and C_p are identical outside the two-phase coexistence region. From Eq. (3.37) immediately follows that:

$$(\Delta H) = \int_{T_1}^{T_2} (C_{eff} - C_p) dT \tag{3.38}$$

where T_1 and T_2 are the temperatures that abut the two-phase coexistence region.

Here a legitimate question arises: "*What do we take as C_p?*" The answer is simple: "*We should take the heat capacity that would had been observed in the absence of the phase conversion.*" A reasonable assumption would be a linear interpolation between the C_p values just before and just after the two-phase coexistence region, i.e.:

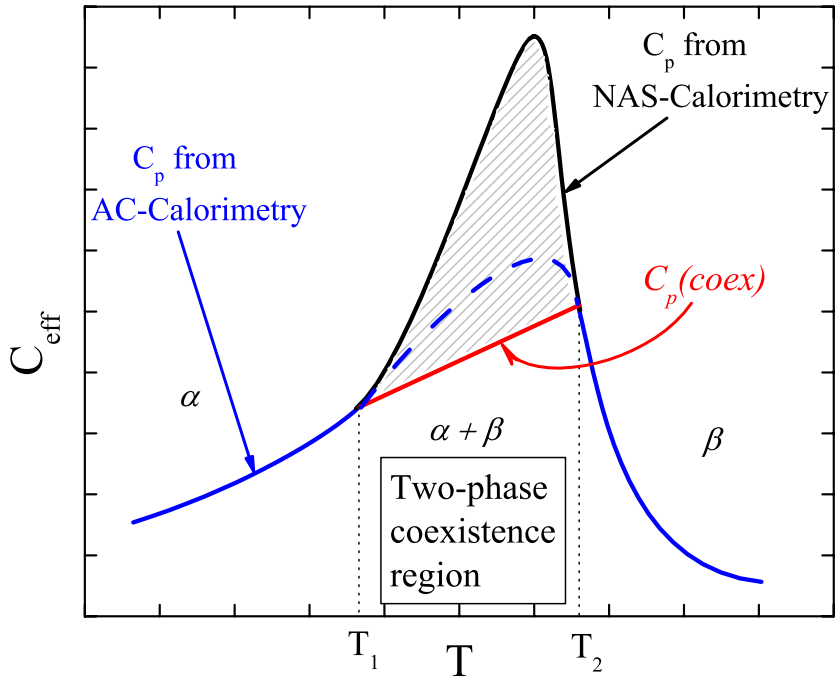

Figure 3.7. Schematic draw of the typical behavior of C_{eff} for a first order transition. Below T_1 the sample is in the α phase and above T_2 in the β phase. The shaded area represents the latent heat of the transition.

$$C_p(coex) = C_p(addendum) + X_\alpha C_p(\alpha) + X_\beta C_p(\beta) \tag{3.39}$$

where, X_i is the mass fraction of phase $i = (\alpha, \beta)$, and $C(i) = C_{eff}$ - $C_p(addendum)$ just before entering the two-phase coexistence region. So the latent heat of transition is given by:

$$\Delta H = \int_{T_1}^{T_2} [C_{eff} - C_p(addendum) - X_\alpha C_p(\alpha) - X_\beta C_p(\beta)]dT \tag{3.40}$$

In order to find the latent heat one measures first the C_{eff} and then integrates the area between the C_{eff} and $C_p(coex)$. See Fig. 3.7.

3.2.3 Data Acquisition

The data acquisition is achieved with software written in C++, and compiled under Borland C++. In order to have linearly ramped power over time, i.e., $P = At$, the

voltage should change as $V = \sqrt{At}$. For this, a wave form with a functional form $V_n = \sqrt{n/15000}$, for n = 0-15000, has been preloaded on the memory of the HP arbitrary function generator. Similarly, for the linear ramp down the voltage has the form $V_n = \sqrt{1 - n/15000}$, for n = 0-15000.

The data collection goes as follows:

1. The user specifies the power P_0 and the time to do the ramp, as well as the stepsize for the bath temperature.

2. The temperature of the bath is equilibrated.

3. The temperature of the sample and the bath are measured by the DMM ($T = T_{bath}(1)$).[6]

4. The HP generator starts a linear power ramp. At the same time start the digitizing of the temperature of the sample $T(t)$ with the DMM.

5. The HP outputs a constant DC power P_0. After waiting for full relaxation measure the temperature of the sample T_{high} and that of the bath $T_{bath}(2)$.

6. The HP starts to ramp the power linearly down, from P_0 to 0. At the same time the DMM digitizes the temperature of the sample $T(t)$.

7. The HP generator outputs no power ($P = 0$). After waiting for full relaxation to equilibrium measure the temperatures of the sample and bath again $T = T_{bath}(3)$.

8. Calculate the average bath temperature, $\overline{T}_B = \frac{1}{4}\left(T_{bath}(1) + 2T_{bath}(2) + T_{bath}(3)\right)$, and $R_e = P_0/(T_{high} - \overline{T}_B)$. Save all the digitized, $T(t)$, data into a separate file.

9. The bath temperature gets the next value and the process gets repeated from the second step, until all the temperature range of interest has been covered.

[6]The DMM actually measures the resistance of the thermistor and of the center PRT. Then these values are converted to temperature from their respective calibration curves. See section 3.1.4.4 for more details.

10. Reanalyze all files after the run in order to do the calibration of the thermistor temperature and the differentiation dT/dt. Then calculate C_{eff} according to the Eq. (3.36).

3.3 Light Scattering

3.3.1 Introduction to Light Scattering

Calorimetry cannot directly measure the correlation lengths and structure. It can only deduce them through scaling analysis. Light scattering instead can directly measure the correlation lengths and also extract structural information relatively easy of submicron or larger size. The light scattering methods of interest in this work are *Turbidity*, *Integrated Low Angle Light Scattering (ILALS)* and *Optical Microscopy*, which coherently combine to allow for an accurate determination of the onset of the nematic state. Interestingly enough, there is a simple and very profound relation between the calorimetric and light scattering measurements. The part of the enthalpy that can be found from the difference of the enthalpies, as measured by NAS and AC calorimetry, turns out to be proportional to the fractional of the Isotropic converted into Nematic, ϕ_N, which can be measured optically through the two-phase coexistence region. The next two sections will describe the basic theory of the turbidity and ILALS techniques.

First, let's introduce the two main quantities that can be measured by light scattering, namely the ***Birefringence***, Δn, and the ***Nematic Correlation Length***, ξ_N. As mentioned before, because of its anisotropic orientation of molecules, the nematic phase in general, shows anisotropic optical properties. A measure of this is the birefringence, Δn, which is defined as:

$$\Delta n = n_{\parallel} - n_{\perp} \tag{3.41}$$

where, $n_{\parallel}$ and $n_{\perp}$ are respectively, the refractive indices parallel and perpendicular to the nematic director $\hat{n}$ [7]. $n_{\parallel}$ and $n_{\perp}$ are often called respectively as, extraordi-

[7] Most of LCs are uniaxial, however there exists biaxial molecules which have three indices of refraction. In the case of biaxial systems the birefringence is defined as the difference between the largest and the smallest indices of refraction.

nary and ordinary indices of refraction. For uniaxial nematic LCs, if $\Delta n > 0$, the systems are referred to as positive uniaxial, and if $\Delta n < 0$, the system are referred to as negative uniaxial. The birefringence is a temperature dependent quantity and is related to the magnitude of the order parameter [3]. The two indices of refraction in a nematic LC equal the square root of the corresponding relative dielectric permittivities. Therefore the square of the birefringence, $(\Delta n)^2$, or the quantity $n_{\parallel}^2 - n_{\perp}^2$, are often used to get an estimate of the order parameter.

Another characteristic of the nematic phase is the *Nematic Correlation Length*, ξ_N, which is the characteristic distance over which the nematic director $\hat{n}$ remains correlated. ξ_N is defined as one-third of the correlation length for the director autocorrelation function $g(R)$ which is **assumed** to be exponential [36]:

$$g(R) = \left\langle \hat{n}(\vec{r}) \cdot \hat{n}(\vec{r} + \vec{R}) \right\rangle_{\vec{r}} \propto \exp\left(-\frac{R}{3\xi_N}\right) \tag{3.42}$$

where, $\hat{n}(\vec{r})$ is the nematic director at the position $\vec{r}$, $R = |\vec{R}|$, and the brackets $\langle\,\rangle_{\vec{r}}$ indicate an average over the position $\vec{r}$. When the system undergoes a transition from isotropic to nematic this quantity grows as the nematic domains grow inside the predominantly isotropic sample. So, this also is a temperature dependent quantity. The value of the nematic correlation length can't be measured directly, but it can be extracted by turbidity measurements. A typical configuration of the light scattering experiment is shown in Fig 3.8.

3.3.2 Turbidity

Turbidity is a measure of how opaque a system is, i.e., relates the intensity of the transmitted light at some solid angle $d\Omega$ and wave vector $\vec{q}$, to the incident intensity, I_0. If one defines the differential diffusion cross section as:

$$\frac{\partial \sigma}{\partial \Omega} = \frac{I_s(\vec{q}) R^2}{I_0} \tag{3.43}$$

then turbidity, τ, is defined as the total diffusion cross section per unit volume:

$$\tau = \frac{1}{V} \int \frac{\partial \sigma}{\partial \Omega} d\Omega = \frac{\int I_s(\vec{q}) R^2 d\Omega}{I_0 V} \tag{3.44}$$

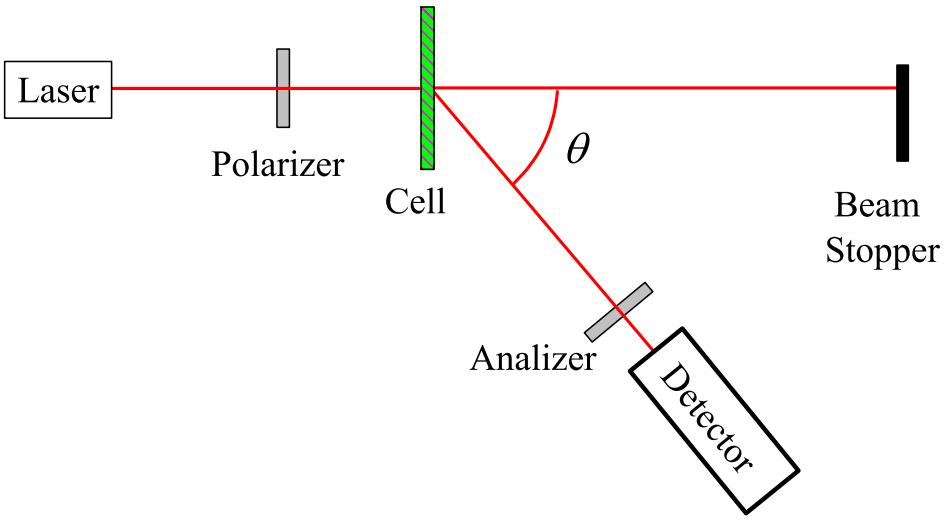

Figure 3.8. Typical configuration of the light scattering geometry.

where,V is the scattering volume, R is the distance between the scattering volume and the detector, $I_s(\vec{q})$ is the intensity of the scattered light at wave vector $\vec{q}$ corresponding to solid angle $d\Omega$, and I_0 is the incident intensity.

Experimentally one can measure the turbidity, τ, by simply measuring the transmitted intensity, $I_t(\theta)$, through a pin-hole at some angle θ with the direction of the incident light, and considering the extinction equation:

$$I_t(\theta) = I_0 * e^{-\tau d} \tag{3.45}$$

where d is the thickness of the sample and I_0 the incident intensity.

The nematic correlation length, ξ_N, can be extracted from the turbidity data of aerosil disordered liquid crystals, based on the model proposed by Bellini et al. [36]. In this model for the aerosil disordered LC it's assumed that:

1. The nematic correlation function decays exponentially, and thus the nematic correlation length, ξ_N, can be described by Eq. (3.42)).

2. The orientation of the nematic director presents spatial fluctuations with a scalar order parameter which is constant throughout the sample, i.e., the scattering medium is a uniaxial material having continuous but random distortions of the optical axis.

3. The main contribution to scattering comes from the large spatial fluctuations introduced by the quenched disorder, whereas thermal fluctuations can be neglected.

4. The local birefringence of the $LC + SIL$ in the nematic phase is equal to the bulk Δn, calculated at ΔT_{IN}. This assumption is very reasonable since the director distortions are on a length scale much larger than the molecular size.

Using the Ralyleigh-Gans approximation, which requires that $\Delta n \ll 1$, and $\xi_N \Delta n \ll 1$, then it is found that:

$$\tau = \frac{\Delta n^2 \left[\left(1 + 4k_o^2\xi_N^2 + 28k_o^4\xi_N^4\right) 4k_o^2\xi_N^2 - \left(1 + 6k_o^2\xi_N^2 + 8k_o^4\xi_N^4\right) \ln\left(1 + 4k_o^2\xi_N^2\right)\right]}{90 \langle n \rangle^2 k_o^2 \xi_N^3 \left(1 + 4k_o^2\xi_N^2\right)} \tag{3.46}$$

where, $\langle n \rangle$ is the average refractive index of the LC, Δn the birefringence of the nematic LC, and k_0 the incident wavevector amplitude. In the limit $\xi_N k_0 \gg 1$, this expression can be simplified into:

$$\tau = \frac{14k_o^2 \cdot \xi_N \cdot \Delta n^2}{45 \langle n \rangle^2} \tag{3.47}$$

In the two-phase coexistence of the $I - N$ transition, not all of the material is in the nematic phase. We denote by $\phi_N(T) = m_N/M$, the mass fraction of the sample that has undergone the transformation to the nematic phase, m_N, to the total mass of the sample, M. Of course, $\phi_N(T)$ is temperature dependent and takes values between 0 and 1 in the two-phase coexistence region. In the nematic phase $\phi_N(T) \equiv 1$. Furthermore, the nematic correlation length is strongly temperature dependent close to the isotropic phase, since there is growth of nematic domains, inside the isotropic rich phase. Taking these facts into account, Eq. (3.47) is modified into:

$$\tau = \frac{14k_o^2 \cdot \xi_N(T) \cdot \Delta n^2(T) \cdot \phi_N(T)}{45 \langle n \rangle^2} \tag{3.48}$$

Eqs. (3.47) and (3.48) are the basic equations that describe the relation between the turbidity τ and the nematic correlation length $\xi_N(T)$, the birefringence Δn and the nematic fraction $\phi_N(T)$. Note that in Eq. (3.48) we have written the

temperature dependence explicitly.

3.3.3 Integrated Low Angle Light Scattering (ILALS)

The ILALS technique consists of collecting into an integrating sphere all the depolarized light scattered within a cone, limited by the scattering vector $q = |\vec{q}|$. Selecting depolarized light suppresses the largest part of transmitted light and of the light scattered by the silica structure. This simple technique, though less precise than the direct measurement of $I(\vec{q})$, still permits a reliable measurement of the director correlation length ξ_N in the single scattering regime.

In the model proposed by Bellini [36], in the single scattering regime and the Raleigh-Gans approximation, the scattered intensity $I(\vec{q})$, as a function of the scattering vector $\vec{q}$, is given by:

$$I(\vec{q}) = \frac{2I_0 k_0^4 \Delta n^2 V \xi_N^3}{45\pi L^2 \langle n \rangle^2} \cdot \frac{7 - \sin^2\theta \cos^2\phi}{(1 + q^2\xi_N^2)^2} \tag{3.49}$$

where, $k_0 = \frac{2\pi}{\lambda}\langle n \rangle$ is the incident wave vector amplitude (λ is the wavelength of the incident light), I_0 is the total incident intensity, θ and ϕ are the angles of the direction of the scattered light, and $q = 2k_0 sin\frac{\theta}{2}$ is the scattering vector amplitude. Integrating Eq. (3.49) over the possible ϕ angles we obtain:

$$I(q) = \frac{2I_0 k_0^4 \Delta n^2 V \xi_N^3}{45\pi L^2 \langle n \rangle^2} \cdot \frac{\pi\lambda^4(27 + cos2\theta)}{(1 + q^2\xi_N^2)^2} \tag{3.50}$$

In this equation the term $cos2\theta$ can be neglected. Thus the intensity profile $I(q)$ can be well approximated by a squared Lorentzian function:

$$I(q) = \frac{A}{(1 + q^2\xi_N^2)^2} \tag{3.51}$$

where A is the appropriate proportionality constant.

Although most of the transmitted light and that scattered by the silica gets suppressed, some of it "finds" the way into the detector. To take care of this effect, in the fitting procedure we add to Eq. (3.52) an additive constant P_1, which accounts for the collection of some transmitted light. So the obtained data has

been fitted with the *area* weighted integral of Eq. (3.51) which has the form:

$$P(q) = P_1 + \frac{P_2 q^2}{(1 + \xi_N^2 q^2)} \tag{3.52}$$

where P_1, P_2 and ξ_N are fitting parameters. Fitting the dependence of the area weighted intensity from q to Eq. (3.52) enables the extraction of the nematic correlation length value ξ_N.

3.4 X-Ray Diffraction

3.4.1 X-Ray Diffraction Setup at NSLS-BNL

The *N-SmA* transition for a series of different density dispersion of SIL in the LC, $8OCB$ were studied by x-ray diffraction. The high-resolution x-ray diffraction measurements were carried out at the X20A beam-line at the National Synchrotron Light Sources. Detailed description of the beam line can be found in Ref. [37]. This is a bending magnet beam-line and in this case the energy (wavelength) was chosen to be 8 keV (~ 1.54 Å) [8].

Fig. 3.9 shows a schematic diagram of the x-ray scattering geometry. The monochromatic incident beam was collimated using slits, while the diffracted beam was collimated using slits and the (111) reflection off a Ge single crystal. The measurements were quasi-elastic. The reflection corresponding to the smectic fluctuations occurs at $2\theta \sim 3^o$; hence care has to be taken to avoid parasitic scattering from the through beam. The diffracted intensity was recorded using a Bicron NaI scintillation detector. The $LC + SIL$ dispersion has a random isotropic distribution of *liquid crystallites*. Smectic fluctuations give rise to a ring of scattering. The resolution along the radius of the ring was $\Delta 2\theta \sim 0.02^o$.

The sample environment for the x-ray measurements comprised a single stage oven within a dry nitrogen environment. The sample temperature was controlled via a resistive heater. The temperature was stabilized by a proportional and integral controller to better than ± 0.05 K. The diffraction measurements were carried out in transmission geometry. The sample was sandwiched between two Kapton

[8] The angles of the monochromator and analyzer crystals are fixed once the energy is selected.

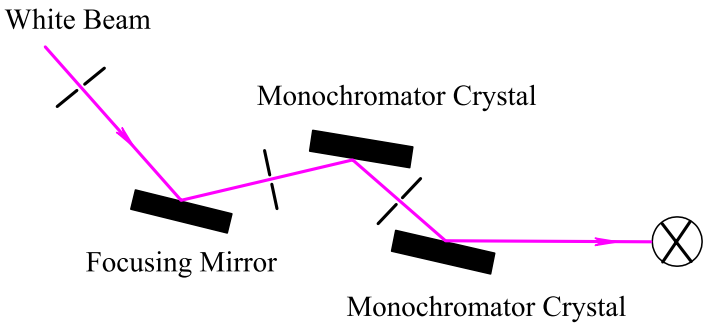

(a) Outside the hutch

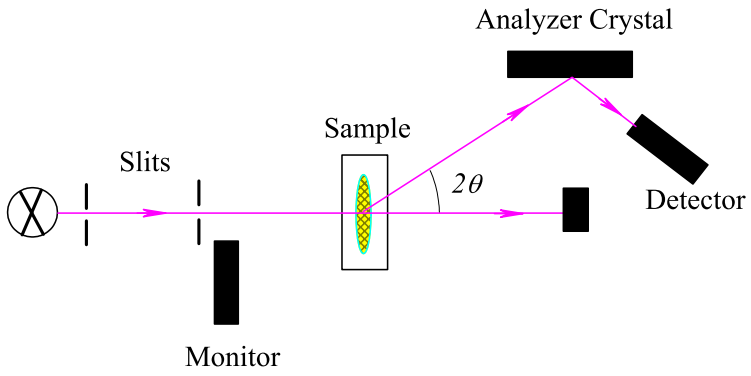

(b) Inside the hutch

Figure 3.9. Typical configuration of x-ray diffraction geometry.

windows and had a diameter of $\sim$ 5 mm and a thickness of $\sim$ 1 mm. Care was taken that the sample remained in the smectic phase as it was transferred to the diffractometer.

Prior to taking data, each sample was held in the isotropic phase for several hours to allow the gel to equilibrate in the holder. The number of scans of intensity as a function of 2θ was kept limited and the counting time low in order to minimize the amount of x-ray damage. The sample thickness was varied with density in an effort to insure that approximately one absorption length of material was in the beam. This was done to improve measurement statistics and decrease the effects of beam damage. Measurements were made on cooling at a rate ≤ 1 K h^{-1}.

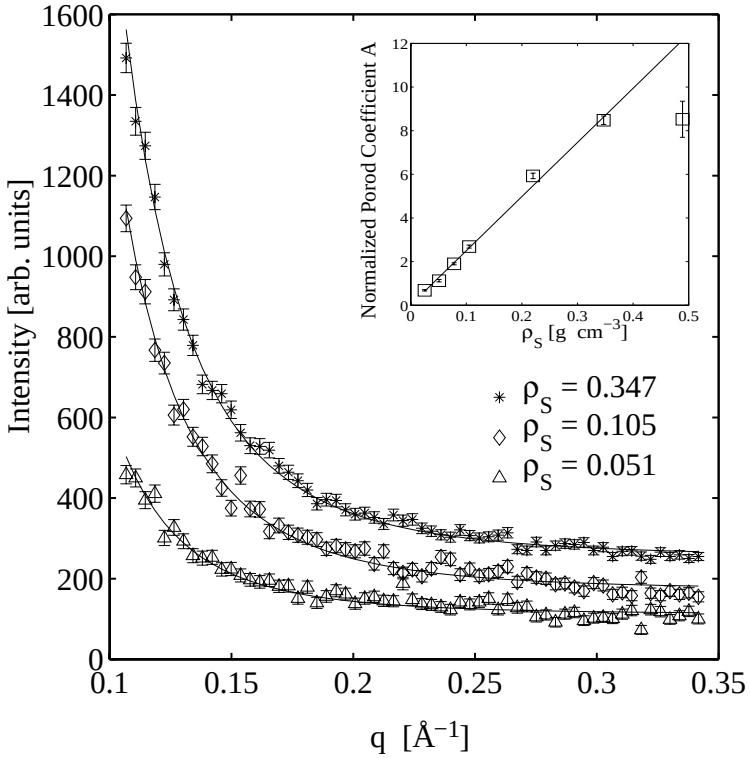

Figure 3.10. X-ray scattering intensity as a function of wave-vector transfer for three $8OCB$+aerosil dispersions at 353 K, which is $\sim$ 13 K above the *N-SmA* transition temperature T^o_{NA} and just above the *I-N* transition temperature T^o_{IN} in pure $8OCB$. The scattering is predominantly due to the aerosil particles and corresponds well to Porod's law: $I(q) = A/q^4 + B$. Inset: A plot of the q^{-4} coefficient A, corrected for absorption and normalized to the volume of liquid crystal, against ρ_S, the mass of aerosil per volume of liquid crystal.

3.4.2 Characterization of background scattering

In addition to studying the smectic correlations as a function of temperature, measurements were made of the small angle background scattering and of the absorption in the sample. The small angle background scattering primarily results from the aerosil network. The intensity as a function of wave-vector transfer is plotted in Fig. 3.10 for a range of aerosil densities. These measurements were made at 353 K to minimize the contribution of smectic correlations to the scattering intensity. The wave-vector dependence of the intensity is well modeled by the Porod law [38, 39]:

$$I(q) = \frac{A}{q^4} + B \; . \tag{3.53}$$

The parameter A is proportional to the surface area of the scattering objects. The density ρ_S is the mass of aerosil per volume of liquid crystal and is also proportional to the surface area of aerosil particles. The values of the parameter A can be related to ρ_S values by correcting for absorption, dividing by the volume of liquid crystal, and then finding the optimum proportionality constant using a least-squares fit; in this form they are listed in Table 3.2. The fit results are shown in the inset of Fig. 3.10. The experimental ρ_S values and the values ρ_P determined from the Porod law fits are in good agreement. The relationship breaks down for the highest density sample. In this case, the sample is no longer in the dilute regime where the model of Eq. (3.53) is applicable.

ρ_S	ρ_P	$I/I(0)$	d
0.025	0.027 ± 0.001	0.46	1.46
0.051	0.045 ± 0.002	0.65	0.70
0.078	0.076 ± 0.003	0.54	0.87
0.105	0.108 ± 0.004	0.37	1.28
0.220	0.238 ± 0.008	0.34	0.97
0.347	0.341 ± 0.011	0.22	1.06
0.489	0.343 ± 0.034	0.41	0.51

Table 3.2. Sample parameters for seven 8OCB+aerosil dispersions studied with x-rays. Shown are the densities ρ_S and ρ_P in grams of SiO_2 per cm^3 of 8OCB, the ratio of the transmitted to incident beam intensity $I/I(0)$, and the thickness of each sample d in mm.

Also listed in Table 3.2 are the ratios of the transmitted to the incident intensity and the thickness of the sample derived from this ratio. The ratio was determined by measuring the straight-through beam intensity $I(0)$ in the absence of the sample and the straight-through beam intensity I with the sample in place. The sample thickness for which each photon scatters, on average, once is optimal for accurate measurements and for reducing x-ray damage. In this case, the ratio $I/I(0) \sim e^{-1}$; for our samples $I/I(0)$ values are scattered around 0.4, indicating close to optimal thickness.

3.5 X-Ray Intensity Fluctuation Spectroscopy

3.5.1 Introduction to XIFS

Photon correlation spectroscopy is one of the most used techniques in the study of dynamic phenomena in soft condensed matter. Recently this method was introduced to x-ray wavelengths, mainly because of the technological developments made in the generation of very high flux and very brilliant x-rays at synchrotron facilities around the world. This technique is known by the name of X-ray Intensity Fluctuation Spectroscopy, or for short, XIFS [40, 41, 42, 43, 44]. It is the equivalent of the widely used and very well established technique of Dynamic Light Scattering (DLS) [45], which is used in the visible region of the spectrum. The source of light for DLS is generally a laser, and thus the properties of the incident light are very high spatial and temporal coherence, as well as very good polarization, depending on the source. Unfortunately, so far there are no lasers that operate in the x-ray region of the spectrum. To make a coherent x-ray beam one has to chop and throw away most of the incoherent light that is part of the synchrotron x-ray beam and thus waste most of the flux in this process. This is the reason that the XIFS method has become available only recently, parallel to the development of new techniques and instrumentation for x-ray generation and optics.

One of the most important advantages that comes with XIFS is the possibility of accessing dynamic phenomena down to atomic length scales, in contrast to DLS which can not probe dynamics on length scale smaller than about 200 nm. Furthermore, the most severe limitation of DLS, multiple scattering, is non existent for the XIFS method because of the very small wave length. These two factors make XIFS a very exciting new technique that will give the possibility to research complex fluids and bio-systems in much smaller length scales than before. However, the feasibility of XIFS has been demonstrated mainly on systems displaying slow and ultra-slow dynamics, $\sim 1s$ time scale. Many biological and complex fluid systems display fast dynamics, exhibit particle interactions or may scatter very weakly. Performing XIFS in these cases is very challenging due to intensity limitations, the non perfect coherence properties of the XIFS beam and the pulsed nature of synchrotron sources. In general, the need is for higher flux in order to

study the weak scattering systems, as well as have better photon statistics which will make possible the determination of the autocorrelation function with higher statistical accuracy. The increasing flux and the detection of faster dynamics will require faster detectors with higher dynamic range and lower noise.

The availability of high flux coherent x-ray beams will also open up dramatic opportunities to other techniques that use coherent flux, such as scanning x-ray microscopy and x-ray interferometry.

3.5.2 X-Ray Beam at APS-ANL

The experiments were conducted on the SRI-CAT, 2-ID-B undulator beamline at the Advanced Photon Source ANL, using a coherent x-ray beam in the transmission geometry. Fig. 3.11 shows the x-ray optics setup outside the experiment chamber. Outside the hutch, the focusing mirrors, the monochromator and the Entrance (ENS) and Exit Slits (EXS) achieve the task of focusing the x-ray beam down to micron size as well as a good degree of coherence. The typical coherence length during the experiment was $\sim 25\ \mu m$. This could be improved by further closing the entrance and exit slits, but at the expense of the flux of photons available

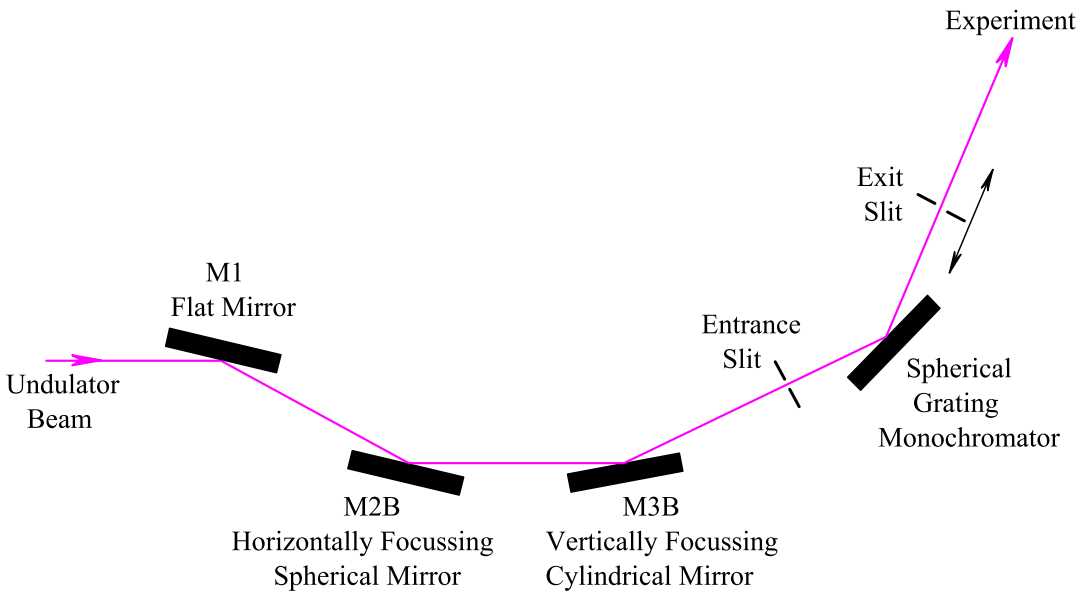

Figure 3.11. Schematic diagram of the optical path at the 2-ID-B beamline outside the hutch.

[46]. The exit slit can move upstream or downstream to track the monochromator settings. Typical slit opening settings during the experiment were ENS/EXS = 200/50 (μm).

The coherent X-rays enter the experiment chamber through a 10 μm pinhole. Figure 3.12 shows the scattering inside the hutch and the positioning of the knife

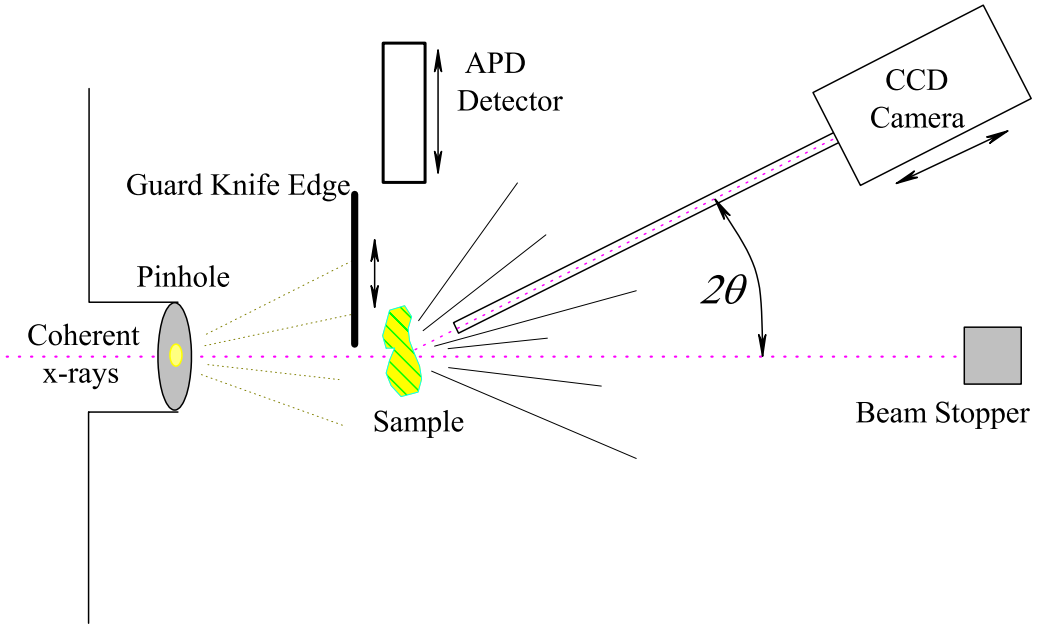

Figure 3.12. Schematic diagram of the optical path at the 2-ID-B beamline inside the hutch.

edge, Avalanche Photo Diode (APD) detector, and the CCD camera. The knife edge is used to block parasitic scattered x-ray from the pinhole. Several times during the experiment the knife edge would move into the path of the direct beam scattering the x-ray beam. This came as a result of very small thermal motions of the motors controlling the edge, or because of possible changes in beam steering that comes from the sub-micron thermal mirror motion. The APD has a very high saturation limit and is used to measure the intensity of the direct beam as well as record the absorption image of the sample. This is used to determine the best possible position in the sample that gives a high speckle contrast. Experimentally it was found that regions which had $\sim 25\%$ absorption gave the best speckle contrast. The sample is located at the center of the 2θ circle of the goniometer and could be moved parallel and perpendicular to the beam via a piezoelectric stage. The

total distance from the pinhole to the sample is less than 2 cm, reducing the air absorption of the x-ray beam and possible scattering from air molecules.

The sample holder is made of two copper plates which can be screwed together. A small hole is drilled on each of them, and on top of it is glued a very thin silicon nitride [47] substrate with a $0.7 \times 0.7\ mm^2$ window for the x-rays. A thin layer of sample is spread over one of the silicon nitride windows and is sealed by the similar plate on the other side. Care should be shown while spreading the sample because the window is very thin and breaks easily. The alignment of the windows was done carefully under the microscope to get the maximum possible area exposed to x-rays. The sample holder was mounted in a copper stage that can be temperature controlled through a recirculating water bath. In order not to agitate the sample mechanically, the temperature controller was turned off, thus the experiments were carried out at room temperature (301.75±1 K), which corresponds to the smectic

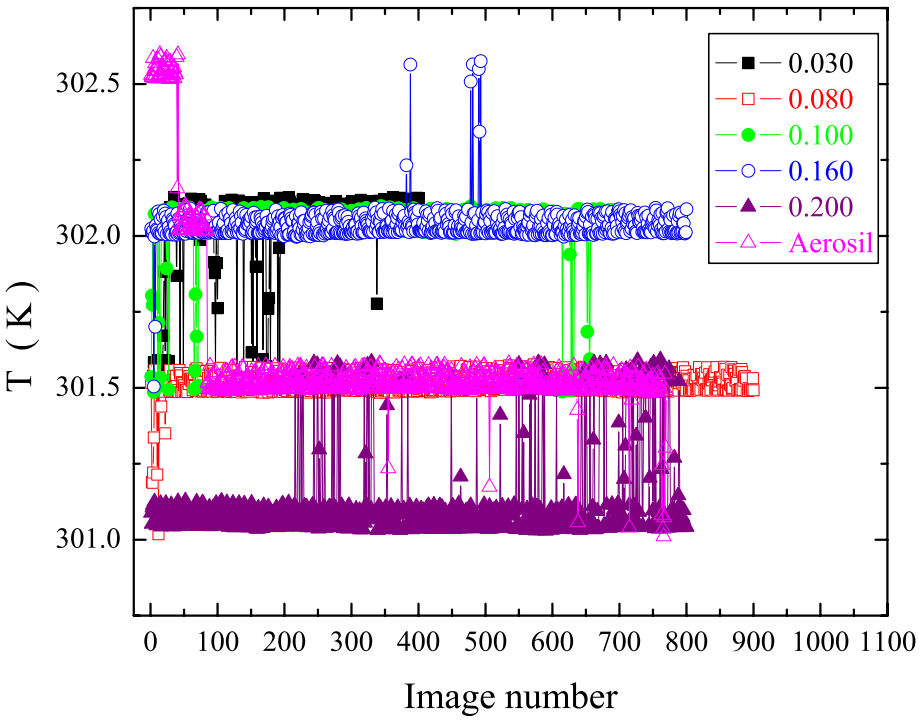

Figure 3.13. Temperature of the stage as a function of the image number. The spurious jumps are probably errors in the thermocouple reading and not real room temperature changes.

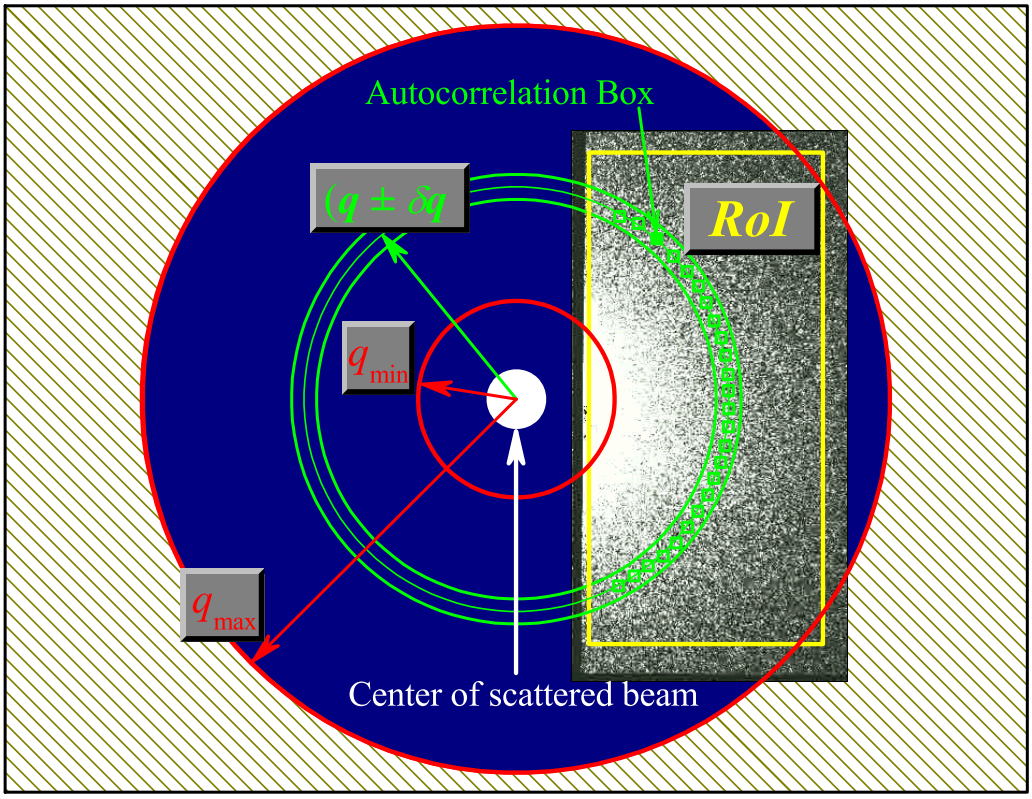

Figure 3.14. Schematics of CCD setup and the ROI definition.

phase of 8CB. During the experiment the temperature of the stage was measured with a thermocouple. The sample temperature as a function of the image number is shown in Figure 3.13. The temperature stability could easily be improved by using a resistive heater and a PID temperature controller.

The scattered light from the sample gets collected from a CCD camera mounted at the arm of the goniometer, at a distance of 950 mm from the center, and at angle $2\theta = 0.82$ degrees from the direct beam. The CCD we used was a 16 bit, Princeton Instruments CCD chip, 1024×1024 pixels 25×25 mm^2 size, cooled to liquid nitrogen temperature. It covered momentum transfer (q) ranges from 0.02 to 0.2 nm^{-1}. Fig. 3.14 represents the positioning of the CCD with respect to the center of the scattered beam. In the analysis which is done off-line, the user can specify the *Region of Interest* (*ROI*), the minimum and maximum range of q to be

included in the analysis, as well as the size of the autocorrelation box. The region that is between q_{min}, q_{max} and inside the ROI is the one for which the analysis gets done. We call it the *Analysis Region* (AR).

In order to achieve good speckle contrast from the SIL we chose the x-ray energy to be 1.830 keV, just below the Si K-absorption edge [48]. Time series of CCD images of $\sim$ 30 s exposure and $\sim$ 6.4 s between images were recorded for each sample, for about 4 to 9 hours. The radiation dose received by the sample was very small to notice any apparent damage on the samples. For each density, clearly fluctuating speckles were observed.

3.5.3 Data Reduction and Analysis

Images of the series were stored in the "*.HDF" format, together with some of the most important settings at the time of the image acquisition. The other data (called metadata) include among others, the absolute time when the image was recorded, the current of the synchrotron ring, the temperature of the sample, as well as the settings for the mirrors and slits, the position of the sample the CCD the guard knife edge, etc. The data reduction and calculation of the temporal autocorrelation function, $G^{(2)}(q, \Delta t)$ followed the scheme suggested by Lumma et. al. [49], including corrections for the storage ring current, the total intensity of the image, and the dark noise of the CCD. This was done effectively with a GUI, IDL [50] program, written for this purpose (See Appendix B for more details).

Care was taken to correct all images for the dark readout noise of the CCD as well as for damaged or high noise pixels in the CCD. This is particularly important for the high q region of the CCD where the signal is not very strong. A *Master Dark* image is created as an average of a time series of dark images which were taken without the x-ray beam going through the sample (shutter at the "OFF" position). For each sample run, a single dark image is recorded just before the run. The Master dark image scaled to the intensity of the single dark image is subtracted, to give the Dark corrected image. All the pixels of the n-th image of the series are scaled to the ring current and the total intensity of the first image of the series in a pixel by pixel basis. The ring current and total intensity dependence on the image number are plotted in Fig. 3.15. This type of scaling

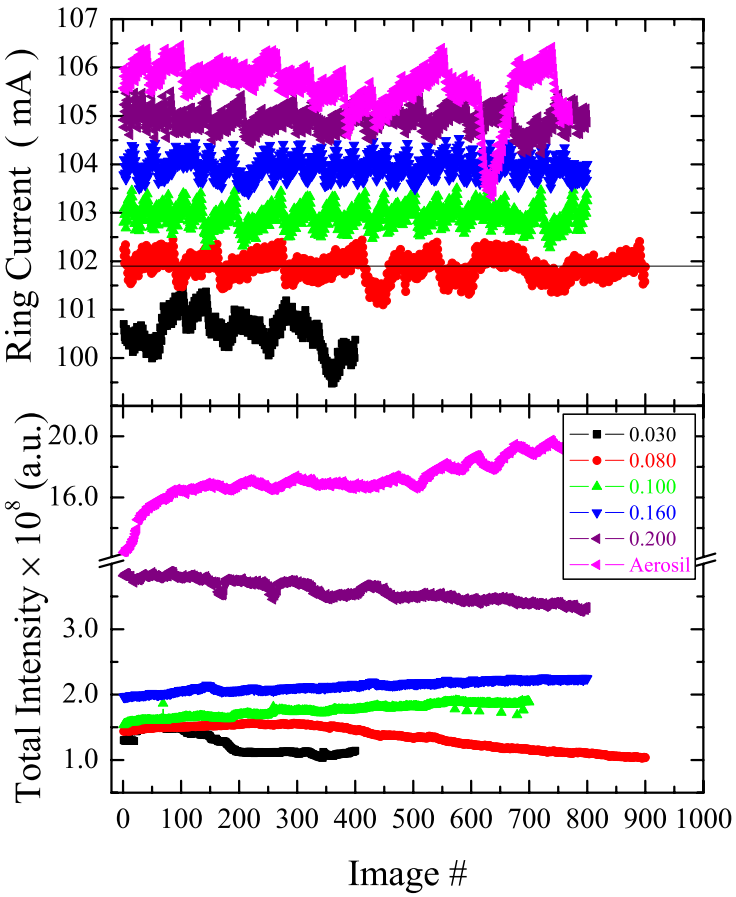

Figure 3.15. Upper Panel: Dependence of the Ring Current Intensity on the image number. Curves are shifted for easier viewing. The line represents the average ring current for all runs. Lower Panel: Dependence of the Total Image Intensity on the image number.

reduces the possible instability in the intensity of the beam that may come from the ring current changes, as well as other factors that can change the position or the intensity of the beam at the sample.

Preliminary analysis needs to be done to create the master dark image and to find the size of the autocorrelation box. The size of the autocorrelation box is set by the user at the beginning of the IDL program and should be similar to the average speckle size. The average speckle size was calculated from the average

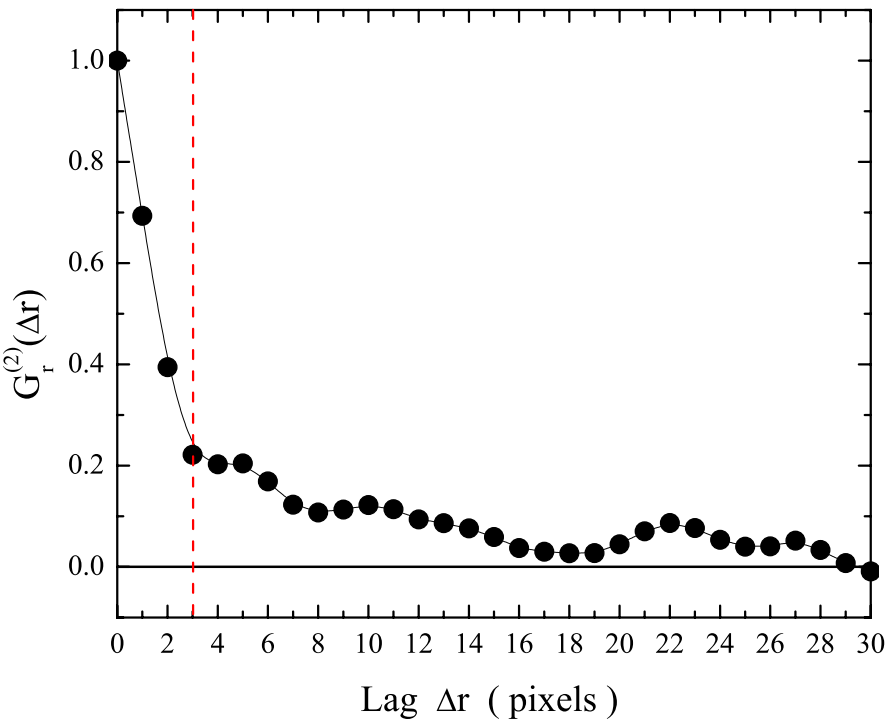

Figure 3.16. Average spatial intensity autocorrelation function. The autocorrelation function has decayed almost 80% at the 3 pixels radius which was chosen as the average speckle radius.

spatial autocorrelation function of several images

$$G_r^{(2)}(\Delta r) = \frac{\langle I(r)\ I(r+\Delta r)\rangle_r}{[\langle I(r)\rangle_r]^2} - 1 \tag{3.54}$$

and it was found to have a radius of ~ 3 pixels as can be seen in Fig. 3.16.

In the IDL program, the user specifies the q range (q_{min}, q_{max}), the ROI in which the data analysis should be performed, the size of the autocorrelation box, as well as the path to the location of the images to be included in the analysis. The data analysis program calculates the position of the autocorrelation boxes which cover all the AR. Then the dark image is subtracted from each image and the scaling gets done in a pixel by pixel basis. For a box centered at the position (q, θ, t), where t is the time when the image was acquired, the average intensity of all the pixels $I(q, \theta, t)$ inside that box gets calculated.

The temporal intensity autocorrelation function gets calculated for each box (from the same position in the image) in the time series of images. This effectively

gives one autocorrelation function for each box. Then a second reduction can be done by calculating the average time autocorrelation function from the boxes which lie in the same $q \pm \delta q$ range. This is the autocorrelation for the specific q. All the autocorrelation functions are saved into a file and can be displayed through the IDL program.

To improve the statistical accuracy, the multi-tau method with the symmetric normalization scheme was adopted [51, 52, 53]. See Appendix B for the details of the IDL program that was written for the data analysis.

3.6 Sample Preparation

All samples were prepared in our lab at WPI [9]. The liquid crystals were obtained from Aldrich and Merck, and were used without any further purification. The SIL was obtained by Degussa Corp. [54]. Prior to use, the SIL was dried at $\sim 200°C$ overnight to remove any adsorbed water. The preparation procedure was followed strictly for each sample, thus all samples were exposed to the same conditions prior to the data acquisition. This way, effects that might come from different aging times or history are reduced to a minimum.

3.6.1 Calorimetry Sample Preparation

- ***Batch Sample Preparation***

  The preparation method starts with adding the appropriate amounts of silica powder and LC together so that the desired SIL density is achieved. Then the mixture is dissolved with spectroscopic grade acetone and mixed, first mechanically and then in a sonic bath for about 2 hours. This allows a microscopically uniform dispersion of the SIL spheres throughout the mixture. The sample is then placed on a hot plate at temperature $\sim 50\ °C$ to allow the acetone to evaporate slowly and for the gelation to occur. After most of the acetone has evaporated the sample is then placed under vacuum at $10^{-3}\ Torr$ and at elevated temperatures, $\sim 65 - 90°C$ for about 2.5 hours,

[9] Except for the $CCN47$ batch sample, which was prepared in the lab of Prof. T. Bellini. See the following section, for the batch sample preparation method.

in order to remove any remaining solvent. This part is the same for all samples, regardless of their T_{IN}, and will be referred to as the *batch sample preparation*.

The sample is then transferred to the cell, *making sure that it does not crystalize at anytime*. The cell gets mounted in the calorimeter after it is closed and the heater and thermometer are mounted on opposite sides.

- ***In-Situ Preparation Method for High Transition Temperatures (8OCB and $\bar{8}$S5)***

  In order to have a randomly dispersed gel, without any anisotropy, the mixing and gel formation happens best in the isotropic phase of the liquid crystal. Furthermore, crystallization of LC can possibly damage the fragile aerosil gel, especially for low silica densities. At room temperature, $8OCB$ and $\bar{8}$S5 are a crystalline solid even in the presence of high aerosil density. Their isotropic transition temperature is well above $50°C$. It was almost impossible, due to the small heat capacity of the cell + sample arrangement, to keep the sample from crystalizing while mounting it. Therefore, a special procedure was followed after the batch mixing for these two samples.

  The sample was introduced into the cell and allowed to cool. The cell was then crimped and the heater and thermometer were attached. A constant current was placed across the heater to maintain the cell temperature well above T_{IN}. The filled cell was then placed in an ultrasonic bath to remix the sample. After remixing for about 2 hours, the cell was mounted in the calorimeter, while constantly applying the current. This sample preparation protocol also allows a controlled entry into the crystal phase. However, since the cell is sealed, the in situ remix could not be inspected and so some small dispersion inhomogeneity may remain.

3.6.2 Light Scattering Sample Preparation

This experiment was performed in Prof. Bellini's lab at Universita di Milano, Milano, Italy. The details of the light scattering cell are described in detail in Ref. [36, 55, 56].

3.6.3 X-Ray Diffraction Sample Preparation

At room temperature, $8OCB$ is a crystalline solid even in the presence of high densities of aerosils. It was imperative to avoid crystallization of the $8OCB$ once an aerosil dispersion is formed, since this was observed to give rise to phase separation in the sample. For the x-ray studies, this was accomplished by maintaining the temperature of the mixture while the solvent was evaporating above the bulk crystallization temperature, and then quickly transferring the sample to the x-ray oven which was at a similar temperature. So there is a small difference in the sample preparation between calorimetry and x-ray methods. Prior to taking data, each sample was held in the isotropic phase at ~ 353 K for six hours to allow the gel to equilibrate in the holder.

3.6.4 XIFS Sample Preparation

To study the gel dynamics, we prepared 6 different dispersions of SIL in $8CB$ with the following densities ρ: 0.030, 0.080, 0.100, 0.160, and 0.200 g cm^{-3} (grams of silica per cm^3 of total volume) and a pure SIL sample of unknown density. (We will drop the units from here on.) Each sample was dissolved in very high purity acetone and sonicated for more than 1 hour to produce a microscopically dispersed mixture. The acetone was slowly evaporated allowing gelation and then the sample was dried under vacuum for more than 2 hours at elevated temperature.

A thin layer of sample of varying thickness was spread on a 0.7 x 0.7 mm silicon nitride [47] substrate attached to a copper plate (with a window to allow x-rays), and sealed with a similar plate on the other side. This sample holder was mounted in a copper stage that can be temperature controlled through a recirculating water bath. In order not to agitate the sample mechanically the temperature controller was turned off. Thus the experiments were carried out at room temperature (301.75$\pm$1 K), which corresponds to the smectic phase of 8CB. During the experiment the temperature of the stage was measured with a thermocouple. The pure SIL sample was prepared by sprinkling a thin layer of SIL on the silicon nitride window and sealed. The SIL was held there by pure electrostatic forces.

3.7 General Characteristics of Aerosil Gels and Bulk LC's

This section presents the main characteristics of the bulk liquid crystals used in this work, as well as the characteristics of the aerosil gel structure. The procedure regarding the $LC + SIL$ sample preparation has been already described in section 3.6.

3.7.1 Characteristics of the Aerosil Gel

We prepared several samples of LC with quenched random disorder (QRD) incorporated into them. QRD in LCs requires the inclusion of fixed random solid surfaces at all possible length-scales up to the sample size. This was achieved by "dissolving" type 300 aerosil (SIL) into the host LC. The SIL is comprised of SiO_2 (silica) spheres of diameter about 7 nm, coated with (-OH) hydroxyl group. The coating enables the spheres to hydrogen bond and form a thixotropic[10], fractal gel, in an organic solvent, through a diffusion limited aggregation process. Although the details of the aggregation process for the SIL are not very well known, the gel structure appeared uniform under the microscope or simple eye inspection, and held its shape even at elevated temperatures well above the T_{IN} of the LC. The fact that aerosil forms a fractal gel structure, which appears to hold its shape even in the isotropic phase of the LC, is crucial, because the analysis and interpretation of the optical and calorimetric data is based on the hypothesis that the restructuring process of the aerosil structure plays no role during the experiments. In fact, the XIFS study of the SIL dynamics shows that, there are no significant dynamics in the experimental relevant time scales [57].

A cartoon of the SIL gel and LC molecules, drawn to scale, is shown in Fig. 3.17. The gel can be thought of as randomly crossing long silica chains with very high pore volume fraction and no preferred orientation, as was shown by light scattering [55] and small angle x-ray scattering (SAXS) studies [58]. However, the SAXS studies showed that the basic aerosil unit consists of a few of these spheres fused together during the manufacturing process [58]. This picture of the gel is

[10]The term thixotropic stands for structures that can cut and reform within a short time scale, so that the overall structure holds its shape.

also confirmed by the electron microscope picture, shown in Fig. 3.18. The specific surface area of the type 300 SIL is $a \approx 300\ m^2 g^{-1}$ as determined by a Brunauer-Emmett-Teller (BET) adsorption isotherm as specified by the manufacturer.

The gelation threshold for the SIL is for a density $\rho \approx 0.015\ g/cm^3$. The molecules of the LC anchor to the solid SIL surface homeotropically. This pins the local director very close to it. Since the orientation of the SIL surfaces is fixed and completely random, these surfaces provide the desired QRD effect. The strength of the QRD provided by the gel, should increase with increasing silica density,

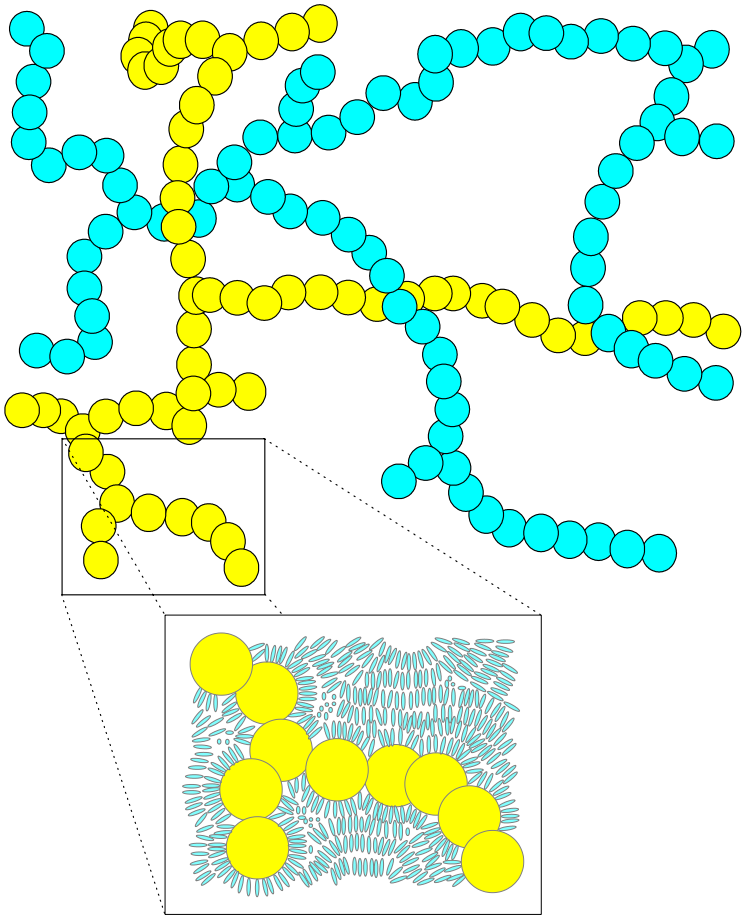

Figure 3.17. Cartoon of an aerosil gel formed by diffusion limited aggregation. The SIL forms long necklace like chains that interconnect randomly and percolate to form a fractal gel at densities above $\sim 0.015\ gcm^{-3}$. The LC molecules anchor homeotropically to the surface of the SIL spheres. The zoomed region shows a cartoon of a distorted Smectic-A phase by the presence of the SIL gel.

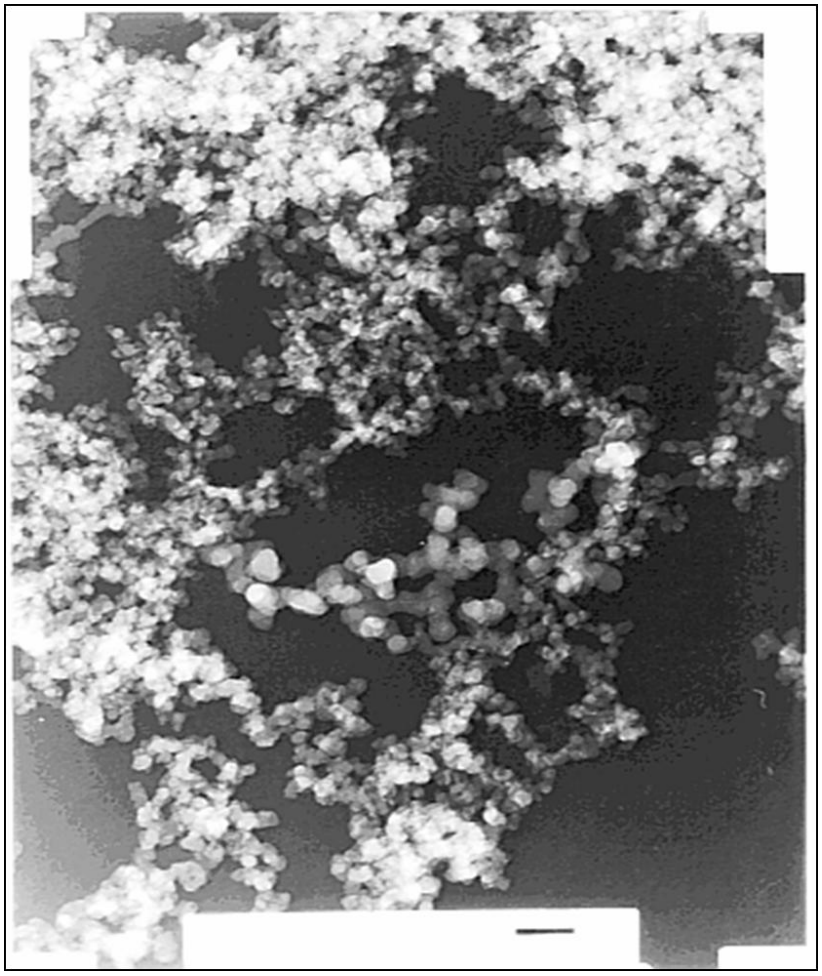

Figure 3.18. Electron microscope picture of the fractal gel formed by the aggregation of aerosil particles. The black length bar corresponds to $50nm$

but the exact relation between the two is not known so far. Furthermore, the dimensional distribution of the voids containing liquid crystal is dependent on the SIL density. It is expected that, with increasing silica densities, the confinement of the host LC will play an increasingly important role in the transition, which will interplay with QRD effects [59].

3.7.2 Characteristics of $8CB$

$8CB$ is the abbreviated name of the LC octylcyanobiphenyl. It is one of the most well known and probably the most studied LC. $8CB$ has a typical rod-like molecule, with a rigid biphenyl core, to which are attached an aliphatic tail and

a polar cyano head group. Its molecular weight is $M_w = 291.44$ g mol^{-1}. The molecular structure is shown in Fig. 3.19. Pure $8CB$ undergoes a weak first-order

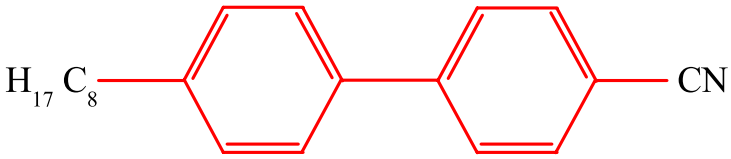

Figure 3.19. Molecular structure of the $8CB$ molecule.

isotropic to nematic transition, at $T^o_{IN} = 313.98$ K, and a continuous nematic to smectic-A transition, at $T^o_{NA} = 306.97$ K. Below 290 K $8CB$ crystalizes via a first order transition. The 1-atm phase sequence for $8CB$ is (in kelvin) [58, 60]

$$\text{Crystal} \xrightarrow{\sim\ 290} SmA_{\text{d}} \xleftrightarrow{306.97} N \xleftrightarrow{313.98} I$$

3.7.3 Characteristics of $8OCB$

The $8OCB$ molecule is another typical rod-like liquid crystal molecule. It has a rigid biphenyl core, to which are attached an aliphatic tail via an oxygen link, and a polar cyano head group. Its molecular weight is $M_w = 307.44$ g mol^{-1}. The oxygen link constitutes the sole molecular difference between $8OCB$ and $8CB$ as can be seen in Fig. 3.20. At ~ 353 K, there is a weak first-order transition

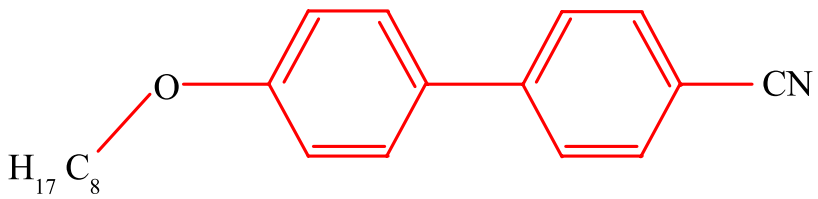

Figure 3.20. Molecular structure of the $8OCB$ molecule.

from the isotropic to an orientationally ordered nematic phase. At $T^o_{NA} \simeq 340$ K a

continuous transition occurs from the nematic to a partial bilayer smectic-A phase. The 1-atm phase sequence for $8OCB$ is (in kelvin) [61]

$$\text{Crystal} \xrightarrow{\sim\ 327.9} SmA_{\text{d}} \xleftrightarrow{340.27} N \xleftrightarrow{353.39} I$$

where the reproducible Crystal-SmA melting temperature is given. As usual, the SmA phase can be supercooled substantially below this melting temperature. Due to coupling between the nematic and smectic order parameters as well as couplings involving their fluctuations, the N-SmA transition is not a simple member of the 3D-XY universality class. Rather, it exhibits complex anisotropic critical behavior [20].

This material has stronger smectic interactions than 8CB as evidenced by the higher transition temperature and the larger bare correlation lengths for smectic interactions [62]; additionally, $8OCB$ is more sensitive to changes in density. This final point is illustrated by the reentrant nematic phase which $8OCB$ exhibits at high pressures or when diluted with a shorter homolog [63, 64].

3.7.4 Characteristics of $\bar{8}$S5

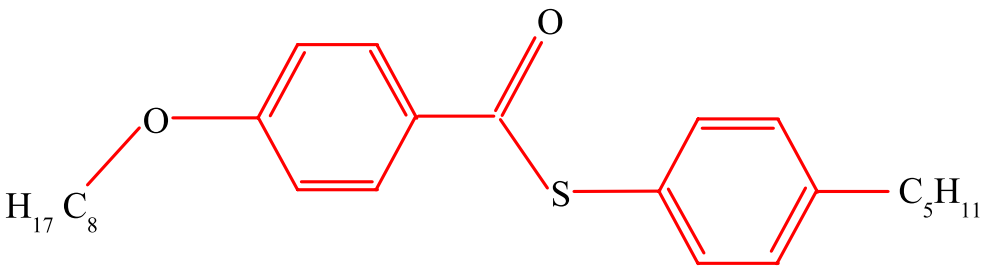

Figure 3.21. Molecular structure of the $\bar{8}$S5 molecule.

$\bar{8}$S5 is the abbreviated name of the LC 4-n-pentylphenylthiol-4'-n-octyloxybenzoate. The liquid crystal $\bar{8}$S5, synthesized at Kent State University, was used after degassing in the isotropic phase for two hours. The best literature reported transition temperature values in the bulk for this liquid-crystal molecule ($M_w = 412.64$ g mol^{-1})

are $T^o_{IN} \cong 359.6$ K for the weak first-order isotropic to nematic (I-N) transition, $T^o_{NA} \cong 336.58$ K for the XY-like continuous nematic to smectic-A (N-SmA) transition, and $T^o_{AC} \cong 329.35$ K for the monotropic Landau tricritical smectic-A to smectic-C (SmA-SmC) transition [65]. At lower temperatures on cooling, a monotropic smectic-C to smectic-B (SmC-SmB) transition occurs at $T^o_{CB} \sim 304$ K. The strong first-order Crystal-SmC (Cr-SmC) transition occurs reproducibly on heating at $T^o_{CrC} \sim 332$ K and can be supercooled down to 293 K. The measured transitions temperatures for our bulk material occur at $T^o_{NA} \cong 336.64$ K, $T^o_{AC} \cong 328.96$ K, and $T^o_{CrC} \sim 331.0$ K, which are in reasonable agreement with the literature bulk values. The 1-atm phase sequence for our bulk $\bar{8}$S5 is (in kelvin)

$$Crystal \xleftarrow{\sim 293} SmB \xleftarrow{\sim 304} SmC \xleftrightarrow[\sim\ 331.0]{} SmA \xleftrightarrow{336.64} N \xleftrightarrow{353.39} I$$

However, $\bar{8}$S5 is known to age and its transition temperatures continuously shift downward with time, especially when heated into the isotropic phase [65, 66]. Fortunately, the N-SmA and SmA-SmC transitions remain relatively sharp, well defined, and consistent during the sample aging, as will be discussed in sections 5.3 and 6.1. Although the aging of this LC is unavoidable, the bulk LC and LC+aerosil samples studied here experienced the same preparation method and thermal history, thus the relative evolution of these transitions with aerosil disorder should be preserved.

The bulk $\bar{8}$S5 and all $\bar{8}$S5+aerosil samples experienced the same thermal history after mounting; six hours in the isotropic phase to ensure homogeneous gelation, then a slow cool into the smectic phase at $\sim$ 320 K before beginning the first detailed heating scan to $\sim$ 345 K, followed immediately by a detailed cooling scan over the same range. Tests on bulk $\bar{8}$S5 with various thermal histories in the isotropic phase reveal an aging of the material. There are progressive shifts of the transition temperatures downward with increased time at high temperature. However, other than an increase in the rounding of the C_p peaks and the downward shift of the transition with time, the critical character remains essentially unchanged.

3.7.5 Characteristics of $CCN47$

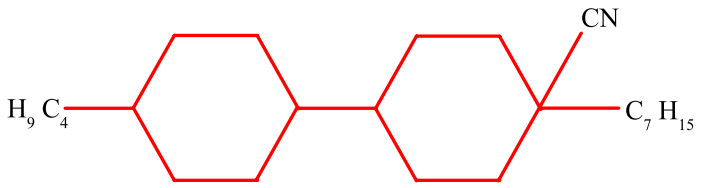

Figure 3.22. Molecular structure of the $CCN47$ molecule.

$CCN47$ is the abbreviated name of the liquid crystal 4'-transbutyl-4-cyano-4-heptyl-bicyclohexane, in which the biphenyl group has been replaced by saturated hydrocarbon rings, as can be seen from its molecular structure shown in Fig. 3.22. This change yields a very low birefringence, about 1/10 that of cyanobiphenyls. This very attractive feature of $CCN47$, allows the measurement of the bulk birefringence (Δn) throughout its nematic phase and even through the $I-N$ and N-SmA transitions. The bulk birefringence temperature dependence is needed in order to extract the nematic correlation length ($\xi_{\hat{n}}$), from turbidity and ILALS measurements. (See sections 3.3.2 and 3.3.3 for a description of these experimental methods.)

$CCN47$ features a wide range nematic phase between the isotropic and smectic-A phases. According to our data, it undergoes a weak first-order transition from the isotropic to an orientationally ordered nematic phase, at $\sim$ 330.41 K, and another very weak first-order transition occurs from the nematic to the smectic-A phase at $T^{o}_{NA} \simeq 301.93$ K in agreement with previous investigations [67]. The 1-atm phase sequence for $CCN47$ is (in kelvin)

$$\text{Crystal} \xrightarrow{\sim\ 297.16} SmA_{\text{d}} \xleftrightarrow{301.93} N \xleftrightarrow{330.41} I$$

Its molecular weight is $M_w = 345.617$ g mol^{-1}. Measurements of the bulk birefringence Δn_B by birefringence compensation at the microscope can be described by

$$\Delta n_B = \Delta n^{**} + A(T^{**} - T)^{\beta}, \tag{3.55}$$

where $\Delta n^{**} = 0.0085$, $A = 0.0096$, $T^{**} - T_{IN} \approx 0.14$ K, and $\beta \cong 0.28$, consistent with typical values for nematics [68]. The bulk specific heat capacity and birefringence dependence on temperature are shown in Fig. 4.7. Characterization of the

I-N transition by calorimetry reveals a weak first-order character, with a latent heat $\Delta H \approx 1.55$ J g^{-1} and a total transition enthalpy (including the pretransitional contribution δH) $\Delta H_T = \delta H + \Delta H \approx 5.65$ J g^{-1}.

Chapter 4

Isotropic to Nematic Phase Transition in Aerosil Disordered Liquid Crystal

4.1 Introduction

This chapter describes the effect of quenched random disorder due to a dispersed thixotropic aerosil gel on the weakly first-order isotropic to nematic (I-N) phase transition. At the I-N transition, the orientational order has a finite correlation length and is established in three dimensions, which is described by a symmetric and traceless $2nd$ rank tensor Q_{ij} [3] (as such, it possesses only five independent components). Thus, nematic order belongs, in principle, to a $d = 3$, $n = 5$ Heisenberg class. However, by ignoring any biaxial character and aligning the orientation axis with a principle axis of a local frame, this tensor can be split into a scalar order parameter (S) measuring the magnitude of orientational order about the orientation axis, and a "headless" vector called the nematic director, $\hat{n}$ ($\hat{n} = -\hat{n}$), describing the spatial orientation of this axis. In this simplified view, nematic order is described on short length scales by S and on longer length scales by $\hat{n}$, which is useful in describing the elastic properties of the nematic structure. These measures of nematic order are related to the quadrupolar nematic order parameter by $Q_{ij} = \frac{1}{2}S(3\hat{n}_i\hat{n}_j - \delta_{ij})$.

In principle, the effect of the aerosil gel network on the orientational order of the nematic phase is two fold. The silica gel firstly dilutes the liquid crystal and secondly creates a preferred local orientation [69, 70]. In addition, the first-order transition from the isotropic to the nematic phase necessitates the formation of interfaces between coexisting domains/phases, which must occur within the available void spaces. The latter effect is the classic result of quenched random disorder; a distribution of transition temperatures due to the nucleation of ordered domains within voids having some size distribution. This leads to short-range order (SRO), a rounding of the transition, and suppression of the first-order character of the transition [71]. The contribution of a random preferred local orientation effect to the total Hamiltonian can be represented as:

$$\mathcal{H}_{RF} = -\sum_i g_2(\vec{h}_i \cdot \hat{n}_i)^2 \tag{4.1}$$

where, $\hat{n}_i$ is the orientation of the molecules over some small region where the orientation is approximately constant, and $\vec{h}_i$ is the random influence of the silica surface. The variance of this random field $\langle(\vec{h})^2\rangle$ should be proportional to the density of solids dispersed in the LC medium. This term is squared due to the effective inversion symmetry of the molecules in the nematic phase. Since the nematic order parameter is quadratic in $\hat{n}_i$ due to the same inversion symmetry [3], Eq. (4.1) is also linear in the order parameter and hence constitutes a random field (RF) interaction. Recently, Eq. (4.1) has also been interpreted as a random-anisotropy (RA) interaction [70], but this seems only applicable to systems described by a pure vector $n = 3$ order parameter. The formation of interfaces and the resulting surface energy penalties places restrictions on the effects of $\langle(\vec{h})^2\rangle$, depending on the elasticity of the nematic. Light scattering measurements have shown that the nematic phase in liquid crystal and aerosil dispersions breaks up into large (micron size) but finite-size domains [36]. In addition, more extensive optical studies focussing on the nature of the nematic director structure well below the *I-N* transition have shown that the director correlation length $\xi_{\hat{n}}$ decays exponentially with distance, which is a hallmark of short-range order [55, 56]. These features are consistent with an RF interaction for nematics with QRD. The bulk transition exhibits significant pretransitional fluctuations and is very close to a

tricritical point [72]. Both aspects are nontrivially affected by random disorder.

To date, the most thoroughly studied $LC + SIL$ system is the dispersion of type-300 aerosil in octylcyanobiphenyl ($8CB$), denoted $8CB + SIL$. Detailed calorimetric [73, 58, 74], x-ray scattering [75, 76], x-ray intensity fluctuation spectroscopy [77, 57], static and dynamic light-scattering [36, 55, 56], and deuterium NMR [78] studies on the nematic to smectic-A (N-SmA) and the isotropic to nematic (I-N) phase transitions of this system have shown that there are clear quenched random-field characteristics, as well as finite-size scaling effects [59].

Calorimetry measurements on $8CB + SIL$ samples have been particularly useful in yielding detailed information on both the I-N and the N-SmA phase transitions [58]. The results for both transitions show a complex dependence of the transition temperature on the aerosil density. While the N-SmA heat capacity peak remains sharp and evolves towards 3D-XY behavior with increasing silica density, the I-N behavior is more complicated. For silica densities below $\rho_S \sim 0.1$ g cm^{-3}, two heat capacity peaks, closely spaced in temperature, were observed. At higher aerosil densities, the heat capacity peaks for both the I-N and the N-SmA transitions displayed highly smeared and non-singular features. Deuterium NMR measurements on deuterated $8CB + SIL$ dispersions, which were carried out over a wide range of silica densities, showed that the magnitude of the orientational order S below the I-N transition temperature was essentially unchanged from bulk behavior [78]. The amount of liquid crystal reorientation for field-cooled samples upon rotation within the DNMR field is small and decreases continuously with silica density up to $\rho_S = 0.094$ g cm^{-3} (the units will be dropped hereafter), confirming distinct low and high ρ_S behavior. X-ray intensity fluctuation spectroscopy (XIFS) studies have found evidence of aerosil gel dynamics in $8CB + SIL$ dispersions, (See chapter 7 for more details) indicating an elastic coupling between the gel and LC [77, 57]. The optical, calorimetric, DNMR, and XIFS results all appear to be consistent with a model in which director fluctuations are suppressed with increasing aerosil density.

4.2 *I-N* Transition in $8OCB$

In this section we focus on a different liquid crystal – octyloxycyanobiphenyl, $8OCB$, – having dispersed in it the same type of aerosil over a comparable range of silica densities as the well-studied $8CB + SIL$ system. This liquid-crystal has several important differences from the closely related $8CB$. The liquid-crystal $8OCB$ has stronger smectic and nematic interactions than $8CB$ as evidenced by the higher transition temperatures, the larger bare correlation lengths for smectic interactions [62], and the larger elastic constants. More specifically, $8OCB$ has a 17% larger bend, 36% larger twist, and 10% larger splay nematic elastic constants than $8CB$ (in the single elastic constant approximation, $8OCB$ has a $\approx$ 20% greater K_N than $8CB$ with an overall uncertainty of 5%) [79]. Thus, comparison of behaviors between $8CB+SIL$ and $8OCB+SIL$ systems allows for the isolation of general quenched random-disorder (QRD) effects from material specific effects; in this case the elasticity of the liquid-crystal host medium.

4.2.1 General Description

The heat capacity of the pure $8OCB$ liquid-crystal is in good agreement with previously published results [61, 80]. For our pure $8OCB$ material the transition

ρ_S	T_{IN}	T^*	ΔT_N	δT_{IN}	δT_{2p}	δH^*_{IN}	$\delta H''_{IN}$
0	352.47	339.52	12.95	0.10	–	6.57	0.25
0.036	352.56	339.64	12.92	0.11	–	6.69	0.19
0.051	352.75	340.22	12.56	0.32	–	7.17	0.24
0.078	351.03	338.61	12.42	0.27	–	6.88	0.10
0.105	351.02	338.51	12.51	0.18	–	7.03	0.12
0.220	351.16	338.61	12.55	0.27	0.09	7.08	0.12
0.347	352.30	338.85	13.45	0.46	0.11	6.96	0.08
0.489	352.17	338.05	14.12	0.70	0.22	6.77	0.04
0.647	351.09	337.30	13.79	1.20	0.54	6.22	0.01

Table 4.1. Summary of the calorimetric results for $8OCB+SIL$ samples. Shown are the sample density (ρ_S in grams of aerosil per cm^3 of $8OCB$) as well as the *I-N* (T_{IN}) and the *N-SmA* (T^*) phase transition temperatures, the nematic range ($\Delta T_N = T_{IN} - T^*$), the width of the *I-N* coexistence region (δT_{IN}), and the difference in temperature between the two $\Delta C_p(IN)$ peaks (δT_{2p}) all in kelvins. The *I-N* transition ac-enthalpy (δH^*_{IN}) and the integrated imaginary specific heat ($\delta H''_{IN}$) in J g^{-1} are also tabulated.

temperatures were $T^o_{IN} = 352.53$ K and $T^o_{NA} = 339.52$ K. The *I-N* two-phase coexistence width was ≈ 95 mK wide, and the *N-SmA* transition enthalpy was $\delta H^o_{NA} = 0.42$ J g^{-1}. These thermal features indicate that the $8OCB$ liquid-crystal used in this study was of reasonably good quality. A summary of the calorimetric results for pure $8OCB$ and $8OCB + SIL$ samples is given in Table 4.1.

In order to determine the excess heat capacity associated with the phase transitions, an appropriate background was subtracted. The total sample heat capacity over a wide temperature range had a linear background, C_p(background), subtracted to yield

$$\Delta C_p = C_p - C_p(\text{background}) \tag{4.2}$$

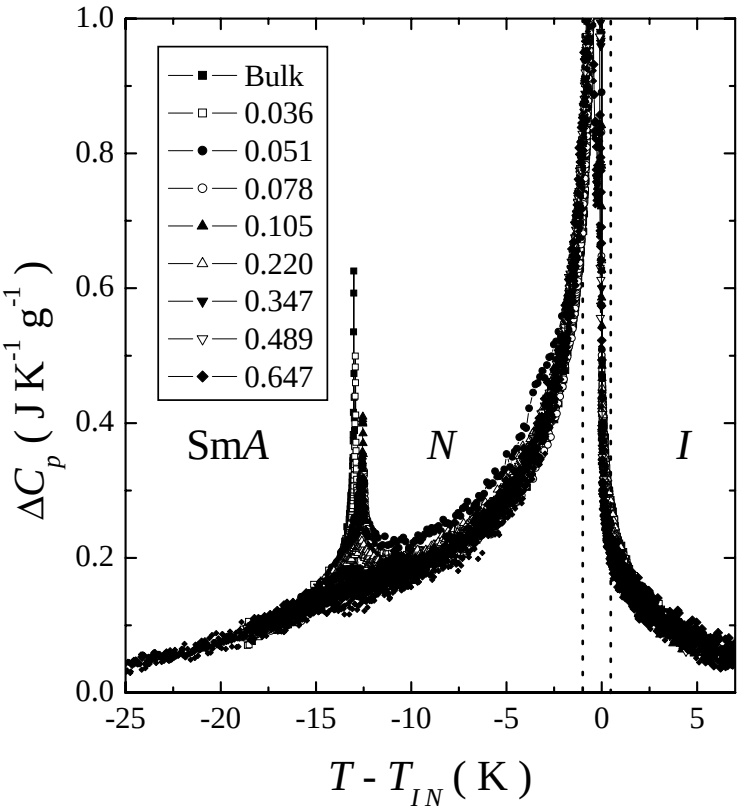

Figure 4.1. Excess specific heat, ΔC_p, as a function of temperature about T_{IN} for bulk $8OCB$ and $8OCB + SIL$ samples from $\rho_S = 0.036$ to 0.647 grams of silica per cm^3 of liquid crystal. See figure inset for definition of symbols. The vertical dashed lines indicate the *I-N* transition region expanded in Fig. 4.2.

as the excess C_p due to the *I-N* and *N-SmA* phase transitions. The resulting ΔC_p data are shown for pure $8OCB$ and all $8OCB + SIL$ samples in Fig. 4.1 over a wide temperature range about T_{IN}, where the units are J K^{-1} per gram of *liquid crystal*. The transition temperature, T_{IN}, is determined as the highest temperature where any nematic phase is present and corresponds to the highest temperature peak in C''_{filled}.

As seen in Fig. 4.1, the ΔC_p values away from the *N-SmA* transition and the $I+N$ coexistence regions overlap with bulk behavior independent of silica concentration. The detailed variations of ΔC_p associated with the *N-SmA* transition with ρ_S has been reported in Ref. [81], and will be described in section 5.2. The deviations of some of the $\rho_S = 0.05$ points in the nematic phase is likely a consequence of sample inhomogeneity. The ΔC_p "wings" of the *I-N* transition are associated with short-range fluctuations of nematic order. Given the simplification of the nematic order parameter, the short-range fluctuations in bulk nematics are mainly composed of thermal fluctuations of the scalar part S. For the $8OCB + SIL$ system, the temperature dependence of $\Delta C_p(IN)$ being independent of ρ_S suggests that thermal fluctuations of S are independent of disorder over the whole range of ρ_S studied in this work. The $\Delta C_p(IN)$ wing behavior shown here for $8OCB + SIL$ is completely consistent with similar results for $8CB + SIL$ [58] and low-density $8CB$+aerogel samples [82].

In stark contrast to the behavior of ΔC_p in the one-phase regions, the two-phase coexistence region of the *I-N* transition exhibits strong effects of silica concentration, as shown in Fig. 4.2. From 1 K below to 0.4 K above T_{IN}, the $\Delta C_p(IN)$ peaks for the pure $8OCB$ and the $\rho_S = 0.036$ sample are essentially the same [83]. Upon increasing silica density, the peak in $\Delta C_p(IN)$ is substantially lower in temperature relative to the peak in C''_{filled} and considerably broader than for the bulk or the $\rho_S = 0.036$ sample. See the upper panel in Fig. 4.2. In addition, there is a small and very broad shoulder below the main specific heat peak, also seen in bulk, which moves toward the main peak with increasing ρ_S. The nature of this subsidiary feature is not known. It is likely, given the similarity of the materials used here with the $8CB + SIL$ system, that the percolation threshold for type-300 aerosil in $8OCB$ is essentially the same at $\rho_P \approx 0.018$ [58]; so a true gel should be present for all samples studied in this work. This is supported by

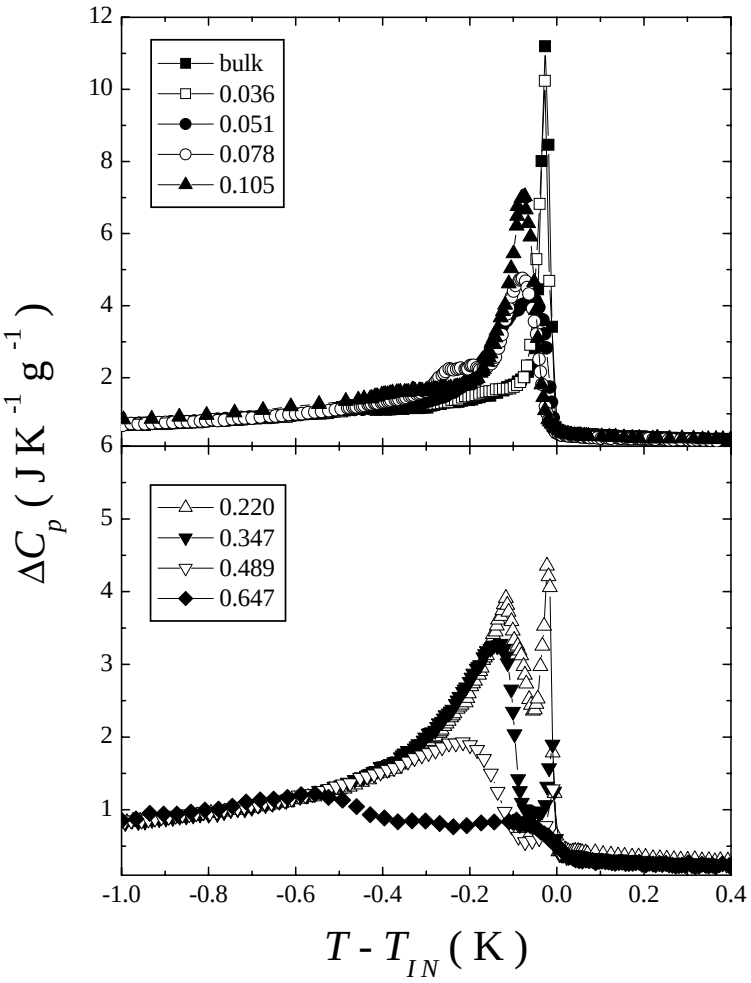

Figure 4.2. Expanded view of the excess specific heat about the *I-N* transition as a function of temperature. See figure insets for definition of symbols. The samples have been separated into two groups; the upper panel appears to indicate inhomogeneity induced broadening for samples with $\rho_S \lesssim 0.1$; the lower panel depicts the evolution of ΔC_p for $\rho_S > 0.1$ and shows two distinct features, one sharp and one broad feature consistent with those seen in $8CB + SIL$ systems [58].

a visual inspection of these samples holding their shape above the crystal melting temperature. The *I-N* transition regions shown in Fig. 4.2 for $\rho_S \lesssim 0.1$ appear to be quite sensitive to small inhomogeneities in the silica gel dispersion and so, are grouped together. Given the dominance of a large, broad, specific heat peak and relatively erratic transition temperature shifts, discussed below, the effect of the silica gel on the *I-N* phase transition is strongly dependent on the quality of the

dispersion.

Beginning with the $\rho_S = 0.22$ sample and for increasing silica content there is a systematic variation of the excess heat capacity, which is shown by the lower panel in Fig. 4.2. At $\rho_S = 0.22$, a double heat capacity feature is observed with a sharp high-temperature peak ΔC_p^{HT} corresponding closely to (but very slightly below) a sharp peak in C''_{filled}, followed at lower temperature by a broader peak ΔC_p^{LT} also having an associated broad peak in C''_{filled}. Clearly, both are first-order signatures and are separated by ≈ 0.1 K. For the $\rho_S = 0.347$ and 0.489 samples, the ΔC_p^{HT} feature remains sharp but decreases in magnitude, while the ΔC_p^{LT} feature becomes increasingly rounded and moves to lower temperature relative to ΔC_p^{HT} by 0.15 and 0.2 K, respectively. For the $\rho_S = 0.647$ sample, both heat capacity features are rounded and separated now by ~ 0.5 K. Over this entire range of silica density, the size of the C''_{filled} peak decreased monotonically with increasing ρ_S. Such a double *I-N* heat capacity feature was observed in $8CB + SIL$ samples for silica concentrations up to $\rho_S \approx 0.1$, but ΔC_p exhibited a single, rounded feature above this density [58]. Only a single rounded $\Delta C_p(IN)$ feature was observed for all $8CB$+aerogel samples [82].

4.2.2 The *I-N* Transition Enthalpies

The *I-N* transition enthalpy also exhibits a dependence on aerosil concentration and can be a quantitative measure of the strength of the transition. For a second-order (or continuous) phase transition, the change in enthalpy through the transition is given by

$$\delta H = \int \Delta C_p dT \tag{4.3}$$

where the limits of integration are as wide as possible about the heat capacity peak. However, for first-order transitions the situation is complicated by the presence of a two-phase coexistence region, in this work I+N, as well as a latent heat ΔH. The total enthalpy change through a first-order transition is the sum of the pretransitional enthalpy and the latent heat. In an AC-calorimetric measurement, ΔC_p values observed in the two-phase region are artificially high and frequency dependent due to partial phase conversion during a T_{ac} cycle. The pretransitional enthalpy δH is typically obtained by substituting a linearly truncated

ΔC_p behavior between the bounding points of the two-phase coexistence region into Eq. (4.3), while an independent experiment is required to determine the latent heat ΔH [58]. A direct integration of the observed ΔC_p yields an effective transition enthalpy δH^* and this contains some of the latent heat contributions; thus $\delta H < \delta H^* < \Delta H_{total} = \delta H + \Delta H$.

For our analysis, the observed $\Delta C_p(IN)$ was directly integrated over a wide temperature range of -25 K below to $+5$ K above T_{IN} for all bulk and $8OCB{+}SIL$ samples where the *N-SmA* transition enthalpy contribution was subtracted. This will be referred to hereafter as the ac-enthalpy and denoted as δH^*_{IN}, as it represents only a part of the total transition enthalpy. Integration of the $\Delta C_p(IN)$ data, shown in Fig. 4.1, (with linear truncation in the two-phase coexistence region) over a similar a similar range yields a pretransitional enthalpy $\delta H_{IN} = 5.13$ J g^{-1} that is independent of aerosil density. Integration over a similar temperature range yielded a pretransitional δH_{IN} value of 5.43 J g^{-1} for $8CB + SIL$ samples, also independent of silica density [58]. In addition, the integration of the imaginary heat capacity given by Eq. (3.15) and normalized to the LC mass, defines an imaginary transition enthalpy, referred to as im-enthalpy and denoted as $\delta H''_{IN}$, which is an indicator of the first-order character of the transition. Although $\delta H''_{IN}$ is a measure of the dispersive component of the complex enthalpy, it is only approximately proportional to the transition latent heat due to the fixed-ω ac-technique employed in this work. As the silica content changes, the two-phase conversion rate may change and so alter the proportionality between $\delta H''_{IN}$ and ΔH_{IN}; thus a detailed frequency scan for each sample would be needed to fully characterize the relationship. This was done for a few samples and the frequency employed in this work is sufficiently close to the static limit that this effect should be minimal.

The results of both the ac- and im-enthalpy for $8OCB + SIL$ samples are shown in Fig. 4.3 as a function of the silica density. There is a slight variation (first increasing for increasing ρ_S up to 0.220 then decreasing for larger ρ_S) of the ac-enthalpy due mainly to changes in ΔC_p values within the two-phase coexistence range, since the heat capacity wings away from the transition are ρ_S independent (except for $\rho_S = 0.051$, which is systematically high for $T - T_{IN}$ from -3 K to -10 K). Given the fixed-ω aspect of the technique, any variation observed in the ac-enthalpy in the two-phase region can be attributed to changes in either

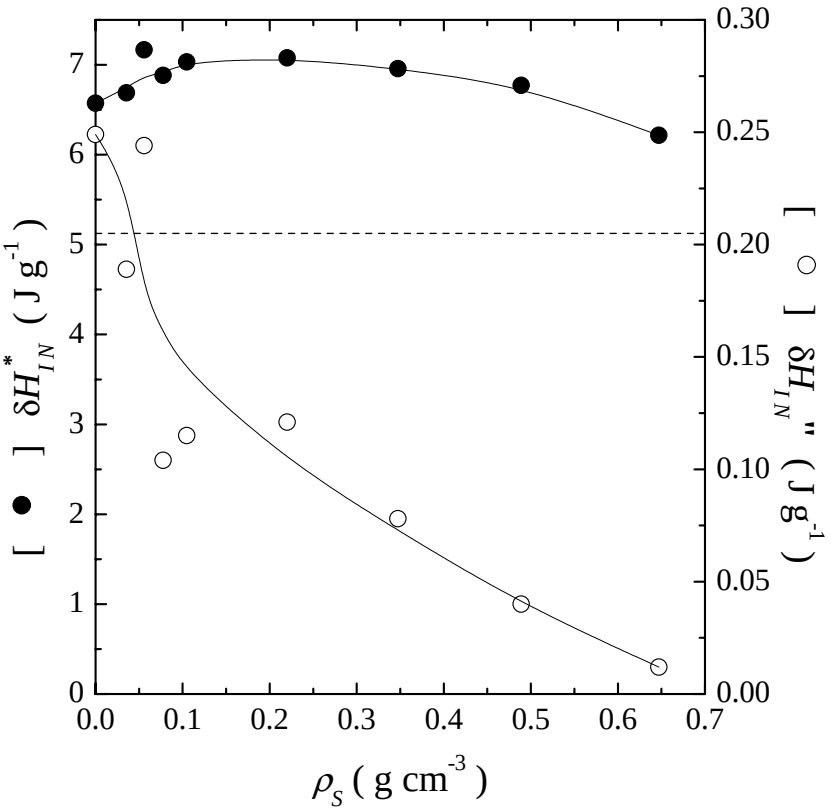

Figure 4.3. The real (solid symbol, left axis) and imaginary (open symbol, right axis) *I-N* transition enthalpy are shown as a function of ρ_S. The effective enthalpy δH^*_{IN} is weakly dependent on silica content, indicating only minor changes to the latent heat conversion dynamics occur relative to the ac-frequencies employed in this work. The monotonic decrease in the imaginary component is evidence that the first-order character of the *I-N* transition decreases with increasing quenched disorder. Solid lines are guides to the eye while the horizontal dotted line represents the total pretransitional enthalpy $\delta H_{IN} = 5.13$ J g^{-1}, which is independent of ρ_S. See text for details.

the dynamics or magnitude (or both) of the latent heat evolution. The small non-monotonic variation of δH^*_{IN} for $8OCB + SIL$ samples is in contrast to the systematic decrease of δH^*_{IN} with increasing ρ_S for $8CB + SIL$ samples. This may reflect a difference in the phase conversion dynamics between $8CB$ and $8OCB$ and how they are modified by the presence of aerosils.

The interpretation of the im-enthalpy is more straight-forward as it is closely related to the latent heat of the transition. With increasing ρ_S, the im-enthalpy appears to monotonically decrease to almost zero for $\rho_S = 0.647$. See Fig. 4.3. This

suggests that for the highest ρ_S sample studied, the *I-N* latent heat has become nearly zero. Similar trends were observed for $8CB + SIL$ [58] where a continuous *I-N* transition is estimated to occur near $\rho_S \approx 0.8$. Also, a nearly continuous *I-N* transition was reported for $7CB$+aerosil for silica densities near $\rho_S \approx 1$ [84]. The above observations are consistent with the general view that with increasing QRD, first-order transitions are driven continuous [71].

4.2.3 Transition Temperatures

The *I-N* transition temperature, defined here as the peak in C''_{filled} for the highest temperature feature, for the $8OCB + SIL$ samples as well as those for the $8CB + SIL$ system taken from Ref. [58] are shown in Fig. 4.4 as a function of silica density. For the $8OCB + SIL$ system, T_{IN} is essentially unchanged up to $\rho_S = 0.051$, then decreases sharply by ~ 1.5 K at $\rho_S = 0.078$, 0.105, and 0.220. It then rises strongly for $\rho_S = 0.347$, nearly recovering the bulk value. Upon further increase in ρ_S, T_{IN} decreases monotonically (with a concave downward character) until it is again about ~ 1.5 K below T^o_{IN} for the $\rho_S = 0.647$ sample. The non-monotonic evolution of T_{IN} with silica content for the $8OCB + SIL$ system is similar to that seen in the $8CB + SIL$ system. This suggests that the initial depression of T_{IN}, recovery, then continued depression, is a general phenomena of quenched random disorder on nematics while the specific ρ_S dependence is liquid crystal material dependent. Over this same range in silica density, the width of the two-phase coexistence region δT_{IN} also has a non-monotonic dependence on ρ_S, as seen in Table 4.1. However, δT_{IN} is sensitive to local inhomogeneities of the aerosil dispersion that may account for its variation when $\rho_S < 0.1$. Beginning at $\rho_S = 0.105$, δT_{IN} increases monotonically by a factor of ~ 6.7, while ρ_S increases by a factor of ~ 6. The observed broadening of the two-phase coexistence width in nearly direct proportion with increasing QRD is generally consistent with the behavior of first-order transitions with quenched disorder [71].

4.2.4 Effect of Crystallization

The calorimetric results on the *I-N* transition temperature described above suggest the importance of sample homogeneity. As a test of the fragility of the silica gel,

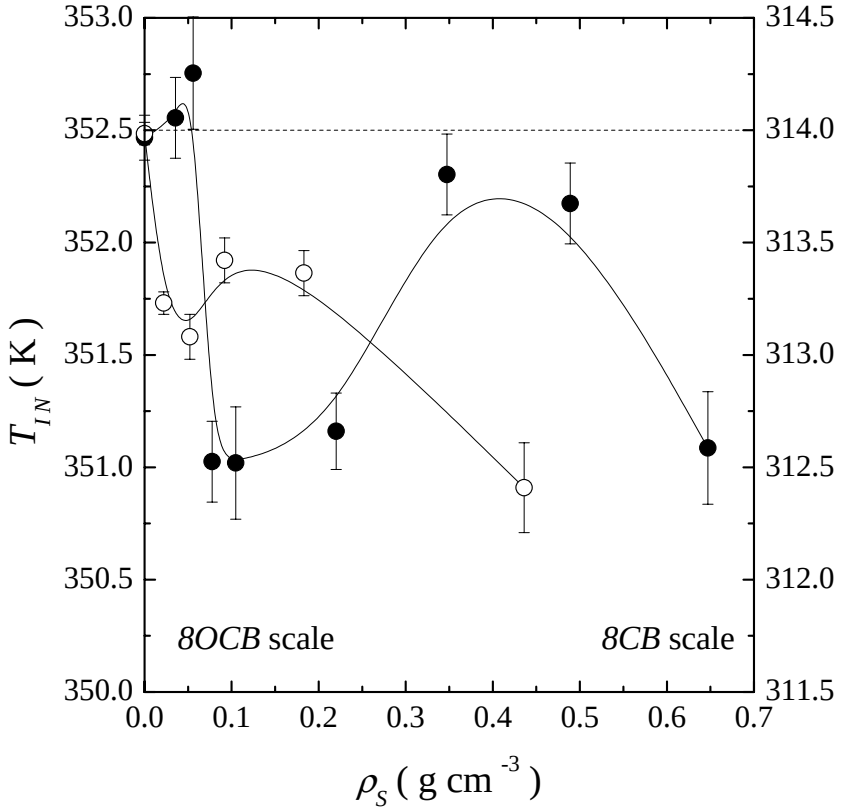

Figure 4.4. Dependence on ρ_S of the *I-N* transition temperature, T_{IN}, for $8OCB+SIL$ (solid circles and left axis, $T^o_{IN} = 352.47$ K) and $8CB+SIL$ (open circles and right axis, $T^o_{IN} = 313.99$ K) samples. Data for $8CB+SIL$ samples taken from Ref. [58]. Note that both the left and right axes span 3 K in temperature. The solid lines are guides to the eye.

heat capacity scans were performed on a low and high density $8OCB+SIL$ sample immediately before and after crystallization of the *LC*. Such a thermal cycle for the $\rho_S = 0.051$ sample is shown in Fig. 4.5 and for the $\rho_S = 0.220$ sample in Fig. 4.6 as a function of $\Delta T = T - T_{IN}$ in order to suppress hysteresis effects of the *I-N* transition. The effect of crystallization on the $\rho_S = 0.051$ sample is striking, revealing significant distortion of the ΔC_p signature at both the *I-N* and *N-SmA* transitions. The appearance of an additional broad ΔC_p feature beginning ~ 0.9 K below T_{IN} as well as a broadened feature over the *N-SmA* transition region after crystallization may indicate increased sample inhomogeneity, presumably caused by the local expulsion of silica particles as *LC* crystallites form. However, there are two puzzling aspects; (1) the shift in T_{IN} is *downward* by ~ 0.7 K and (2) the

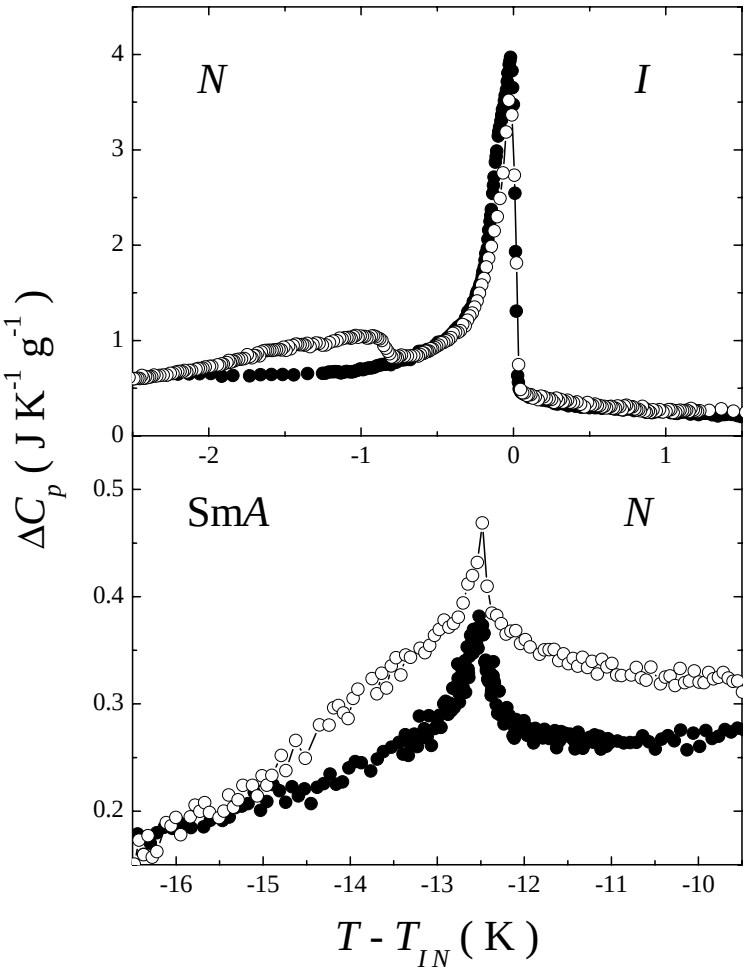

Figure 4.5. Behavior of the *I-N* and *N-SmA* excess specific heat of the $\rho_S = 0.051$ sample as a function of temperature relative to T_{IN} before (solid circles, $T_{IN} = 352.76$ K) and after (open circles, $T_{IN} = 352.07$ K) sample crystallization. Both are heating scans made under identical *AC* calorimetry conditions. Note the excess enthalpy for the *N-SmA* transition and the second feature near the *I-N* transition as well as a ~ 0.7 K shift *downward* of T_{IN} observed after crystallization. See text for details.

specific distortion seen in ΔC_p about T^* reveals an *increased N-SmA* transition enthalpy. The first aspect is counter-intuitive as the expulsion of impurities upon crystallization should have moved the system closer to bulk behavior by increasing the size of pure *LC* domains (regions where no silica is present). The second aspect is particularly puzzling as the *N-SmA* transition enthalpy after crystallization surpasses the *N-SmA* transition enthalpy for *bulk* $8OCB$ ($\Delta H_{NA}(before) = 0.334$,

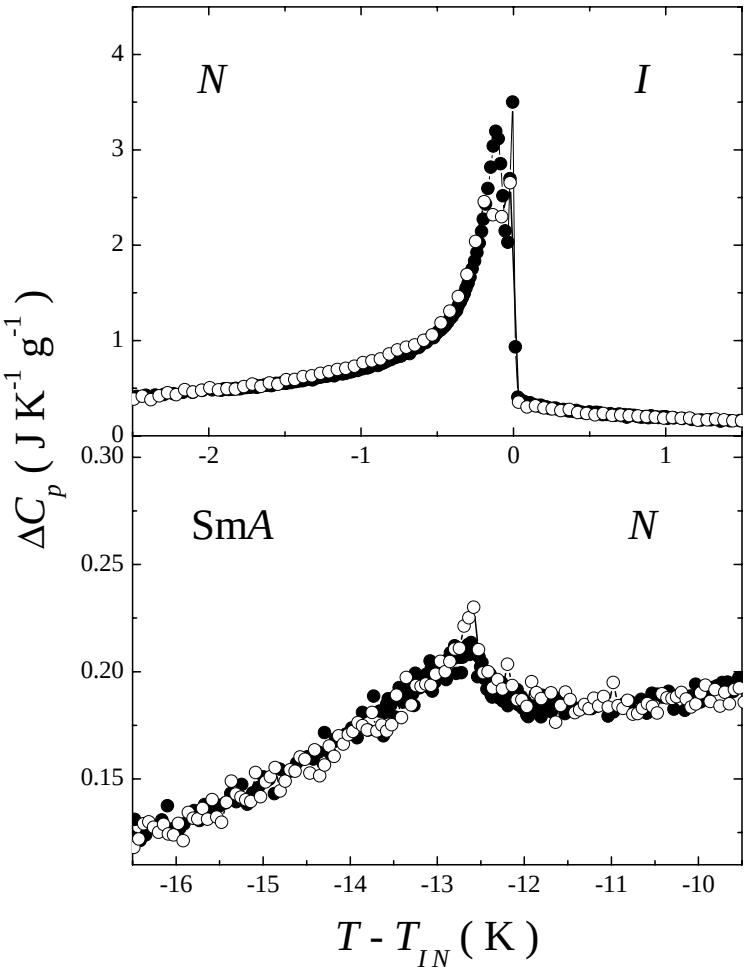

Figure 4.6. Behavior of the *I-N* and *N-SmA* excess specific heat of the $\rho_S = 0.220$ sample as a function of temperature about T_{IN} before (solid circles, $T_{IN} = 351.02$ K) and after (open circles, $T_{IN} = 351.23$ K) sample crystallization. The after scan used the same ac-input power but a faster temperature scan rate than the scan before crystallization; both are heating scans. Note the nearly perfect reproducibility of ΔC_p with a T_{IN} shift *upward* of ~ 0.2 K observed after crystallization. See text for details.

$\Delta H_{NA}(after) = 0.65$, and $\Delta H_{NA}(bulk) = 0.42$ all given in units of J g^{-1}). Visual inspection of the sample immediately after the first crystallization revealed no obvious inhomogeneities. A recent Raman spectroscopy study of $8CB$ crystallizing within a gel matrix provides evidence of new solid and semi-solid phase at low temperature [85]. The additional enthalpy observed here could indicate new solid phases for $8OCB+SIL$ samples. These results are only observed upon initial

crystallization of a freshly dispersed $8OCB+SIL$ sample. Bulk $8OCB$ behavior is eventually approached upon repeated thermal cycling through the crystallization transition. Clearly, at these low silica densities the silica gel is, at least locally, quite fragile, and short range restructuring of the gel can strongly affect the liquid-crystal.

The results of initial cycling through the crystallization transition for the $\rho_S = 0.220$ sample shown in Fig. 4.6 do not reveal any significant changes. Aside from a very small, sharp, additional heat capacity feature at the *N-SmA* transition, the ΔC_p curves are almost perfectly reproducible. The shift in T_{IN} after the initial crystallization is small and upward by ~ 0.2 K, as expected by the expulsion of impurities. This indicates that for higher silica densities, the gel is robust and well behaved. Note that there is no appreciable change in the nematic range, as seen in both Fig. 4.5 and 4.6.

4.3 *I-N* Transition in $CCN47$

4.3.1 General Description

In this section we will focus on the *I-N* transition in the liquid crystal $CCN47$, in which we dispersed the same type of aerosil 300 as in all the samples studied in this thesis. As with all the other $LC+SIL$ systems studied so far, the heat capacity of the $CCN47$ shows the well known double feature at the *I-N* transition for low and intermediate SIL densities [58, 86]. $CCN47$ in contrast to the very well studied cyano-biphenyls, is not a very widely studied liquid crystal. Our interest in it arose because of its very low birefringence Δn, which allows the measurement of Δn not only through the *I-N* transition, but also very deep in the nematic phase and the *N-SmA* transition, *without running into a severe multi-scattering regime.* This very attractive property of $CCN47$ will allow us to study the *I-N* transition via the Turbidity, ILALS, Confocal Microscopy, as well as *AC*-calorimetry. This joint project required very well calibrated thermometry on experiments that were to be carried on in two different labs, in different continents, one ocean apart. This was done by jointly calibrating two similar PT-102 platinum thermometers, but it was ultimately refined by the study of the bulk $CCN47$ as it is shown in Fig. 4.7

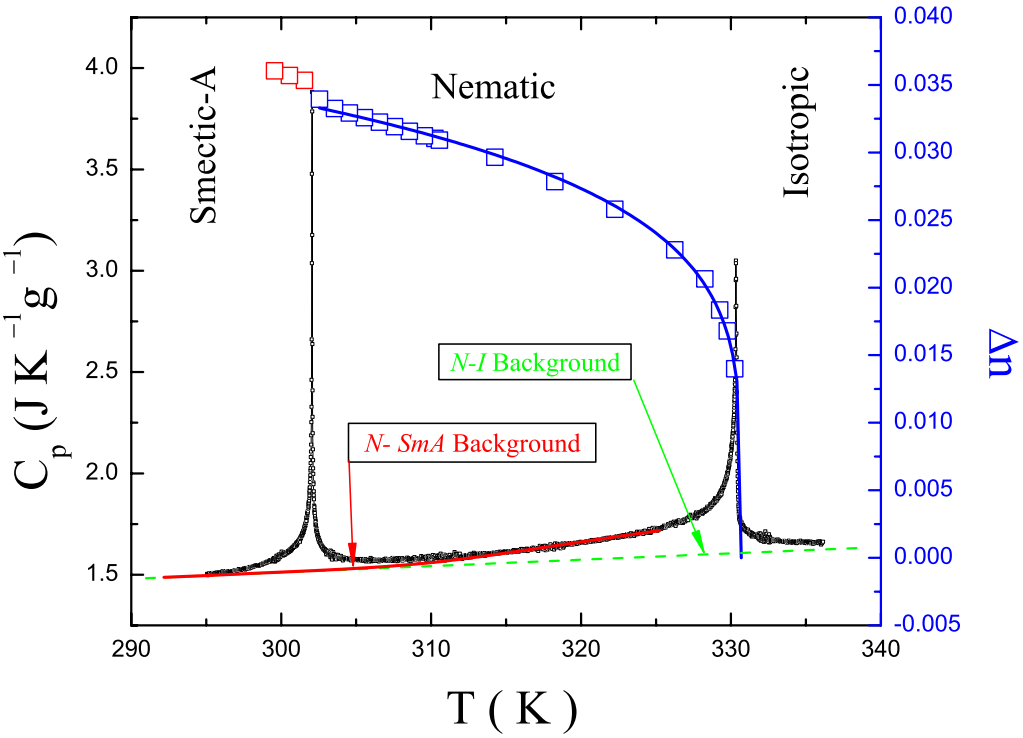

Figure 4.7. Temperature dependence of the specific heat capacity C_p (left y-axis) and the birefringence Δn (right y-axis) for bulk CCN47. The solid line going through the bulk birefringence Δn, is a fit with Eq. (3.55). Note the choices for the *I-N* (dashed line) and *N-SmA* (solid line) backgrounds.

and it was discussed in section 3.7.5.

Previous investigations have shown that the measurement of the transmitted light intensity of highly turbid $LC+SIL$ samples as a function of temperature (T) and optical wavelength (λ) can determine, respectively, the nematic correlation length and the shape of the nematic correlation function [36, 55]. The use of turbidity (τ) measurements instead of scattered intensity ($I(\vec{q})$), was motivated by the large scattering cross section of $LC+SIL$ samples and by the unavoidable use of samples significantly thicker than the nematic correlation length. Indeed, when cyanobiphenyl $LC+SIL$ samples are used, transmittance larger than 10% cannot be obtained without excessive thinning of the cells.

The use of a very low birefringence material enables a better optical characterization both through the study of $I(\vec{q})$ in the single scattering regime - where

the nematic (director) correlation length ξ_N can be extracted - and through the measurement of $\tau(T)$ in the Rayleigh-Gans regime, in which the turbidity is a simple function of the relevant properties of the local nematic, namely $\tau(T) \propto \phi_N(T)\Delta n^2(T)\xi_N(T)$ as given from Eq. (3.48) in Sec. 3.3.2, where ϕ_N is the nematic volume fraction. We have thus undertaken a combined T-dependent optical and calorimetric investigation of $CCN47$, $LC + SIL$ samples through the I-N transition over a range of silica densities displaying the double I-N transition peak. This work offers compelling evidence that the I-N transition with weak quenched random disorder proceeds via a two-step process in which random-dilution is followed by random-field interactions on cooling from the isotropic phase. This previously unrecognized phenomena should be ubiquitous to first-order transitions with sufficiently weak quenched random disorder.

Since heat capacity measures the entire spectrum of energy fluctuations ranging from short range molecular interactions to fluctuations in long-range order (S and $\hat{n}$ for nematics), direct comparisons with other experiments are sometimes difficult. In particular, optical studies naturally probe nematic order of submicron size and larger. For a quantitative comparison, the contribution to C_p related to optical length scales, i.e. in a bulk-like manner, is required. Typically for studies of first-order transitions, $C_p(AC)$ is truncated through the two-phase coexistence region then subtracted from $C_p(NAS)$ which is then integrated to determine the transition latent heat ΔH as described in Sec. 3.2.2. The two techniques are completely consistent outside the two-phase coexistence region. However, disorder can seriously alter the dynamics and T-width of the two-phase conversion region allowing $C_p(AC)$ to sense a significant fraction of the transition latent heat. By foregoing the usual truncation of $C_p(AC)$, we extract $\Delta C_B = C_p(NAS) - C_p(AC)$, which can be associated with domain conversions slower than the ac cycle. Since our ac cycle is quite slow ($\sim 15mHz$), these domains should be large. Its integration gives the enthalpy $\Delta H_B(T, \rho_S) = \int \Delta C_B dT$, which we propose to be directly proportional to the fractional conversion of I into N as optically measured through the two-phase coexistence region.

For this study we prepared 5 calorimetric and light scattering cells from the same batch samples. Their respective densities (ρ_s) were 0.050 gcm^{-3} (grams of SIL per cm^3 of LC), 0.075 gcm^{-3}, 0.100 gcm^{-3} and 0.200 gcm^{-3} and a pure bulk

sample. We will drop the units hereafter. A summary of the calorimetric results for pure $CCN47$ and $CCN47 + SIL$ samples is given in Table 4.2

4.3.2 Calorimetry Results

The AC and NAS calorimetric data were acquired on Calor B, the details of which were described in Chap. 3. Outside the very close vicinity of the I-N transition, $(\pm 1K)$, the ΔC_p wings match very closely with the bulk ΔC_p. This suggests that the short-range fluctuations, which are mainly composed of the thermal fluctuations of the scalar nematic order parameter, are very similar to bulk fluctuations and the disorder does not affect them very strongly. Remember that theoretically the order parameter fluctuations are simplified by considering two quantities separately, the scalar S, and the director $\hat{n}$. This behavior is consistent with all previously studied samples and seems to be a general rule for aerosil disordered LCs. Inside the I+N coexistence region, the excess specific heat capacity data show clearly the double feature for the samples with low SIL densities, while the 0.200 sample shows a rounded overall peak with a very small hint of the sharp peak remaining, as can be seen in the upper panel of Fig. 4.8.

The second wider peak is at lower temperature and seems to "ride up" the shoulder of the first sharp peak. It is interesting to note that this peak approaches the I-N transition temperature with increasing SIL density up to the 0.100 gcm^{-3} sample. Similar behavior for similar densities was observed even in the I-N tran-

ρ_S	T_{IN}	T^*	ΔT_N	δT_{IN}	δT_{2p}	δH^*_{IN}	$\delta H''_{IN}$
0	330.41	301.93	28.49	0.29	–	2.28	0.048
0.050	329.23	300.70	28.53	0.35	0.18	2.52	0.087
0.075	329.34	300.52	28.81	0.32	0.16	2.66	0.048
0.100	329.74	301.47	28.27	0.25	0.10	2.80	0.039
0.200	330.32	301.93	28.40	0.35	–	2.63	0.024

Table 4.2. Summary of the ac-calorimetric results for $CCN47 + SIL$ samples. Shown are the sample density (ρ_S in grams of aerosil per cm^3 of $CCN47$) as well as the I-N (T_{IN}) and the N-SmA (T^*) phase transition temperatures, the nematic range ($\Delta T_N = T_{IN} - T^*$), the width of the I-N 2-phase coexistence region (δT_{IN}), and the distance in temperature between the wide peak and T_{IN} (δT_{2p}) (only where the 2-nd peak can be distinguished) all in kelvins. The I-N transition ac-enthalpy (δH^*_{IN}) and the integrated imaginary specific heat ($\delta H''_{IN}$) in J g^{-1} are also tabulated.

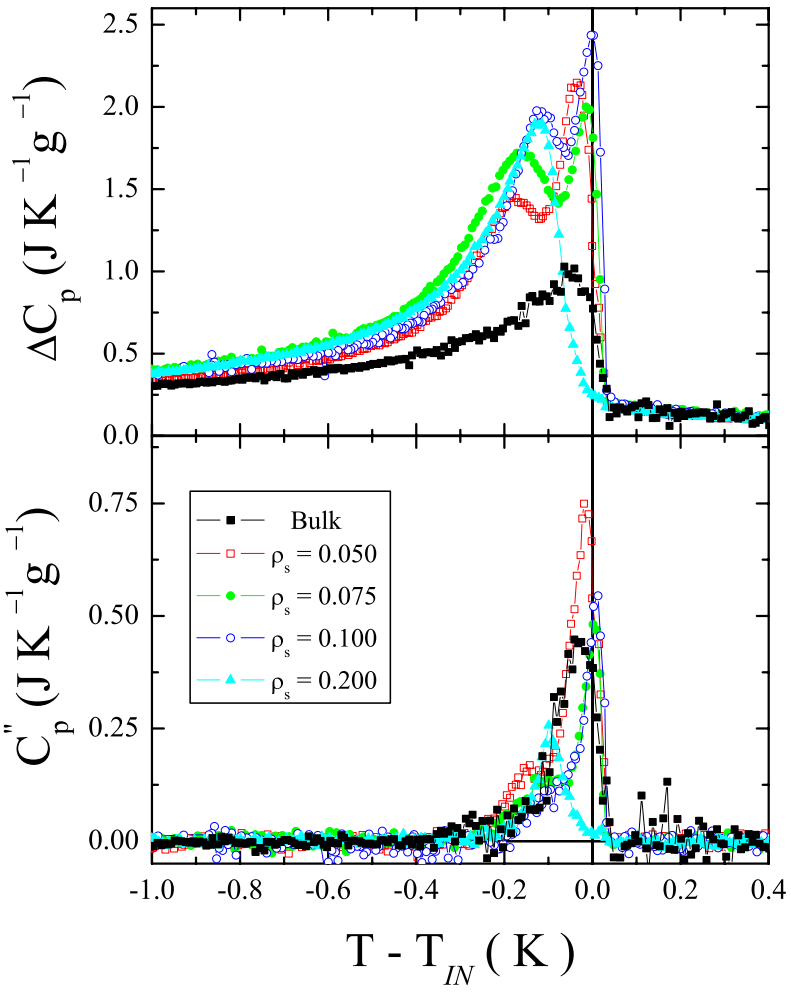

Figure 4.8. a- Upper panel: Close view of the excess specific heat ΔC_p, for cooling scans, about the *I-N* transition, as a function of the *I-N* transition temperature T_{IN}.
b- Bottom panel: Close view of the imaginary specific heat C_p'', about the *I-N* transition as a function of the *I-N* transition temperature T_{IN}.
Curves on both panels show cooling scans on $CCN47 + SIL$ samples and are labelled by density. The symbols defined in the figure inset are the same for both panels.

sition in $8OCB$, although the δT_{2p} was more erratic. At higher densities, above 0.100 gcm^{-3} the two peaks are indistinguishable, and form a broad round feature. This is similar to the behavior of the $8CB$, while for $8OCB$ the two peaks remained separated and the direction of the δT_{2p} was reversed. The differences in the behavior of $CCN47$ and $8CB$ compared to those of $8OCB$ should be attributed to the

higher transition temperatures and elastic constants of $8OCB$. Furthermore, the in-situ mixing of $8OCB$ can not be checked and thus probable inhomogeneities are to blame for the erratic behavior at low SIL densities. These characteristics seem to be LC dependable and elasticity seems to be the main factor in the differences.

The double feature can be seen even in the imaginary specific heat C_p'', which is shown in the lower panel of Fig. 4.8. This is a clear indication that the release of the latent heat is affected by the disorder, and follows a two-step process. The existence of the imaginary heat capacity is directly linked to the first order nature of the transition and the release of the latent heat. Furthermore, its magnitude is related to the magnitude of the latent heat and the dynamics of its release. Disorder seems to affect both the magnitude and the dynamics of the latent heat release. Unfortunately the fixed frequency, AC calorimetry method is only sensitive to the release of latent heat that is in phase with the heat applied to the sample. An AC

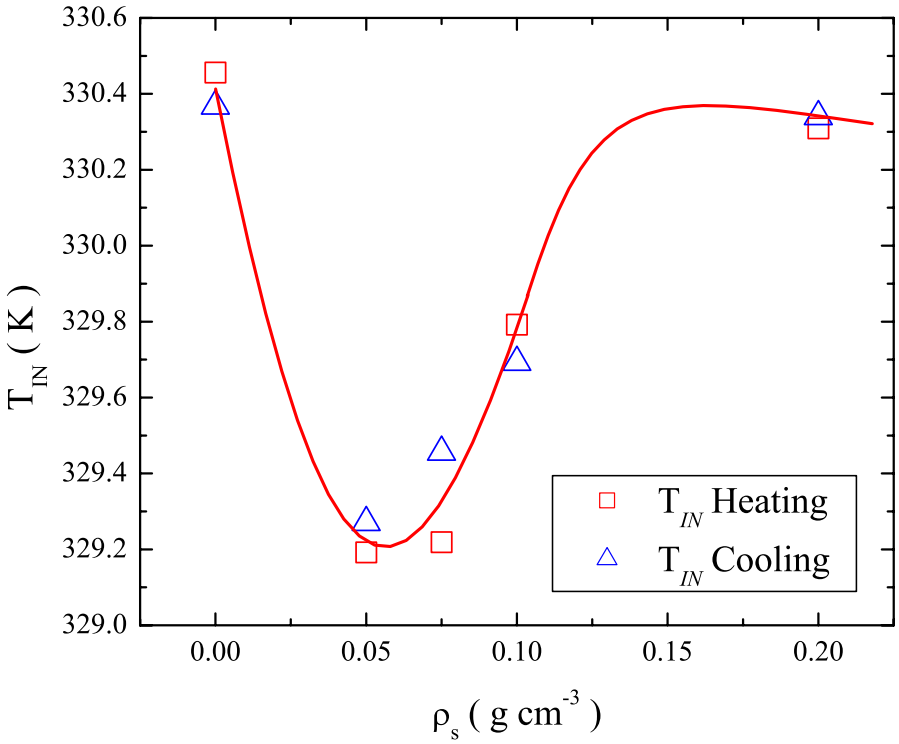

Figure 4.9. Density dependence of the I-N transition temperature T_{IN}, of $CCN47$ for heating and cooling scans. See figure inset for definition of symbols. The solid line is a guide to the eye.

calorimetric spectroscopy method, sensitive to a wide band of frequencies, would give better information about the dynamics of the phase conversion and the release of the latent heat.

The *I-N* transition temperature, T_{IN}, is defined as $40mK$ below the temperature at which the system enters the two-phase coexistence from the isotropic phase. This is very close to the peak in the C_p'' for the high temperature feature. With this choice the nematic and isotropic wings have an almost perfect overlap, for all samples. This choice was consistently done for all samples in heating and cooling, and the does not affect the results by more than $50mK$. The T_{IN} evolution as a function of the silica density is shown in Fig. 4.9. It shows "*the very well known behavior*", a sharp decrease by $\sim$ 1.2K at low densities up to $\rho_s = 0.050$, followed by a sharp recovery to almost the bulk value, at the $\rho_s = 0.200$ density sample. It is expected that for higher SIL concentration the temperatures will evolve downward, as it was the case for all the other LCs + SIL studied so far [58, 86].

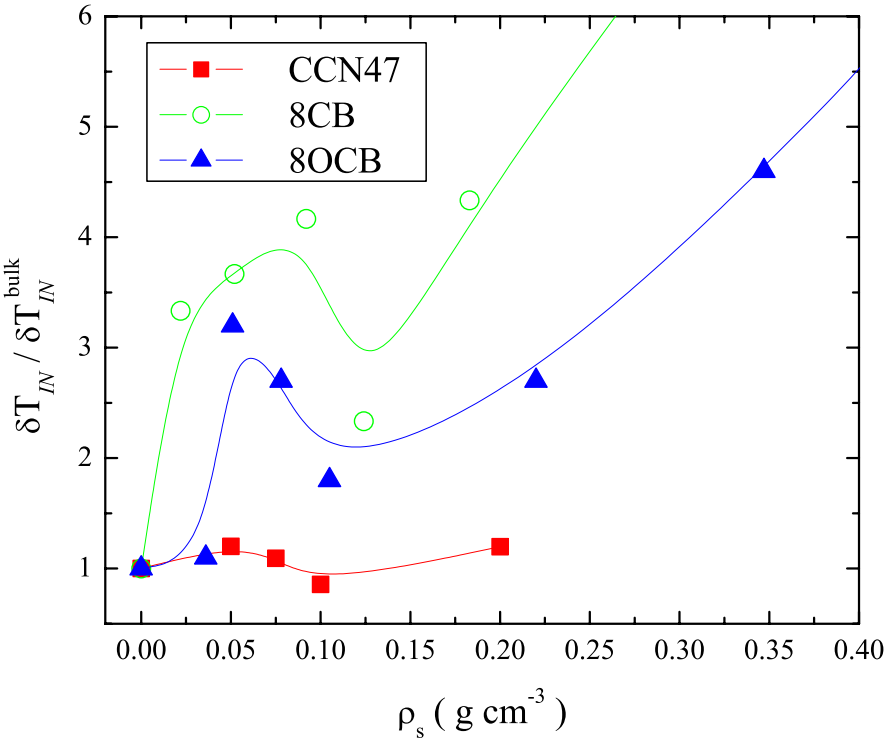

Figure 4.10. Density dependence of the *I-N* two-phase coexistence region, scaled to the bulk values for three liquid crystals, $8CB$, $8OCB$ and $CCN47$. Solid lines are guides to the eye. See figure inset for symbol definitions

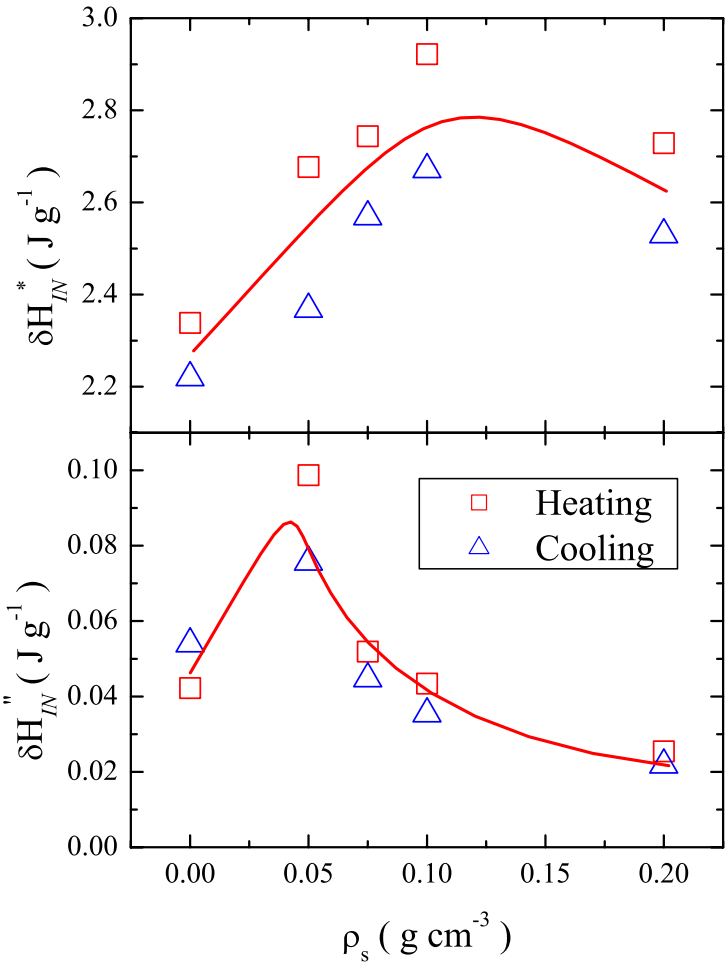

Figure 4.11. a- Upper panel: Density dependence of the *I-N* excess transition enthalpy δH^*_{IN}, as measured by *AC* calorimetry.
b- Bottom panel: Density dependence of the *I-N* imaginary transitional enthalpy $\delta H''_{IN}$. Solid lines are guide to the eye. The symbols defined in the figure inset are the same for both panels.

The density dependence of the width of the two-phase coexistence region is shown in Fig. 4.10. δT_{IN}, for $CCN47$, shows the same qualitative behavior as the other $LC + SIL$, although it is affected much less by the disorder than the $8OCB$ and $8CB$, at least in the range of densities studied in this work. This might be a consequence of the wide two-phase coexistence region to begin with in the bulk, $\sim 0.3K$. As it was the case in the $8OCB + SIL$ study, there is evidence that δT_{IN} increases dramatically for SIL densities above 0.100. The evolution at smaller densities is increasing slightly first, and then, decreasing until

the 0.100 density sample. This behavior is "inversed" with respect to the T_{IN} density dependence. The non-monotonic variation at small SIL concentrations was attributed to possible inhomogeneities, in the $8OCB + SIL$ study. There is growing evidence that this dependence might be a real evolution and not just scatter of the data that comes from micro-scale inhomogeneities in the samples. A single monotonic behavior was observed for all aerogel studied samples.

The *I-N* transition enthalpy δH^*_{IN}, is also strongly dependent on the SIL concentration as can be seen in the upper panel of Fig. 4.11. Again the integration limits are as wide as possible about the heat capacity peak, -20K to +5 K in our case. The behavior of the transitional enthalpy closely resembles that of the $8OCB + SIL$ samples, where the enthalpy increases first and then decreases above some density. This behavior can be explained by an interplay of effects that come from changes in the magnitude of the latent heat, as well as the dynamics of its release. Thus the behavior of δH^*_{IN} from the silica density is LC dependent, since the dynamics of the latent heat release is strongly related to molecular interactions. It also is very sensitive to small perturbations that may come from the presence of small amounts of impurities.

The imaginary enthalpy $\delta H''_{IN}$, shows the same non-monotonic behavior but it peaks at a lower density, as can be seen in the lower panel of Fig. 4.11. As expected for higher silica concentration the trend is downward, which is consistent with the observation that, with increasing disorder first order transition are driven continuous.

4.3.3 Light Scattering Results

The turbidity $\tau(T)$ was measured by spatially filtering in the forward direction the light transmitted through a $LC + SIL$ sample [55]. Fig. 4.12 shows the temperature dependence of the turbidity for three different samples. Fitting the turbidity data in a wide temperature range, starting from 0.5 K below T_{IN}, allows the determination of the nematic correlation length ξ_N. The fits were performed with Eq. (3.47), where the only free parameter is ξ_N, while the birefringence temperature dependence is assumed to be the same with bulk, as given from Eq. (3.55). The temperature dependence of the turbidity shows that practically the nematic

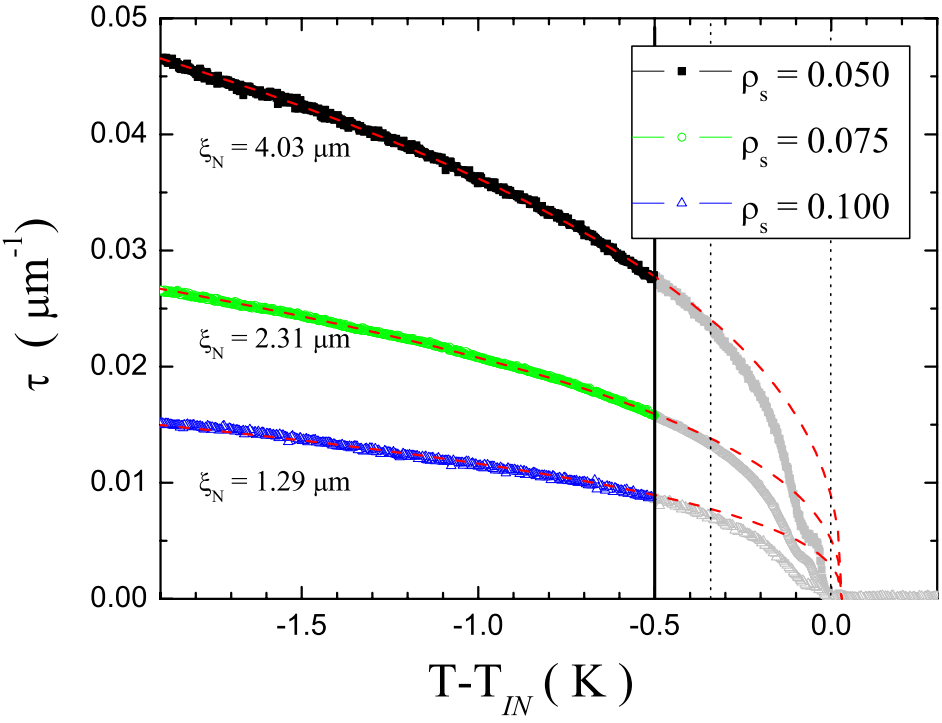

Figure 4.12. Temperature dependence of the turbidity τ for different silica densities. The values of the nematic correlation length ξ_N were extracted by fitting the turbidity with Eq. (3.47) and Δn fixed to the bulk dependence. Only data below solid vertical line, which corresponds to $\sim -0.5K$ below T_{IN}, were included in the fit. The dotted vertical lines mark the approximate two-phase coexistence region.

correlation length does not change appreciably in the nematic phase, fact that is supported from other studies in similar samples [36]. An analogous matching is found, over the same T region, between the ΔC_p measured for the bulk and the $LC + SIL$ $CCN47$ samples, that was reported in the calorimetric study, and is completely consistent with data reported in Ref. [58]. Furthermore, since the fits work very well, by considering only that the birefringence temperature dependence is that of the bulk, is another argument in support of a constant ξ_N throughout the fitting range. This confirms that outside the immediate two-phase coexistence region of the transition, the T dependence of $LC + SIL$ systems is entirely expressed by the variation of a bulk-like local order parameter S, with no director or silica restructuring.

Fig 4.13 shows the dependence of the extracted correlation lengths ξ_N from the silica density ρ_S in a log-log scale (filled circles). ξ_N decreases with increasing

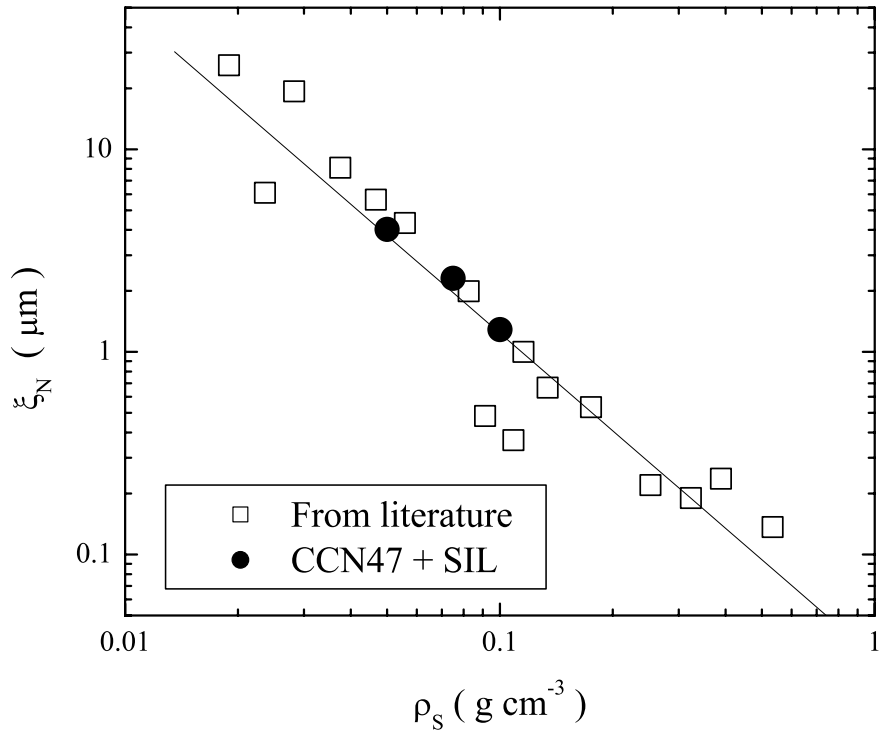

Figure 4.13. *Log − log* plot of the ρ_S dependence of nematic correlation length ξ_N (solid circle). Open squares: ξ_N values taken from Ref. [36]. The solid line is a fit of the $CCN47$ data, with a power law of the form $\xi_N \propto \rho_S^{-Y}$, where $Y = 1.6 \pm 0.2$.

disorder density with a dependence that can be described by a power-law, $\xi_N \propto \rho_S^{-Y}$, where the exponent $Y = 1.6 \pm 0.2$. This dependence is consistent with the dependence found by Bellini et. al. [36] for other $LC + SIL$ samples. The data from Ref [36] are shown in Fig 4.13 with open squares.

Closer to T_{IN}[1] the fits can not be performed, since there is no prior knowledge of the temperature dependence of the nematic fraction $\phi_N(T)$ and $\xi_N(T)$ inside the two phase coexistence region. The fits break down in a narrow temperature region, close to the two-phase coexistence region, where the fact that the fit overestimates the data is a clear indication that the measured turbidity depends on $\phi_N < 1$. The shapes of τ and ΔC_p inside the two-phase coexistence region, suggest a strong

[1]In the light scattering experiments, T_{IN} is defined as the temperature of entering the two-phase coexistence region from the isotropic phase. This definition does not alter any of the arguments that will be discussed latter. It is only a more convenient definition in this case.

connection between the calorimetry double peak and the light scattering data.

In order to measure ξ_N inside the two phase coexistence region, we used the $ILALS$ technique which was described in detail in Sec. 3.3.3. The data have been obtained in a 48 μm thick sample, in which the fraction of the collected light resulting from a single scattering process is in the plotted range always larger than 71%. ξ_N was extracted with an uncertainty of at least $\sim 0.1\mu m$ in our measurements [87], by fitting the $q-$dependence of the collected intensity with Eq. (3.52). In order to take care of the double scattering effect a correction to the extracted ξ_N is needed. This correction was performed, but did not alter the results appreciably, as can be seen in Fig. 4.14. The corrections become increasingly relevant farther below from T_{IN}, since the double scattering becomes more relevant

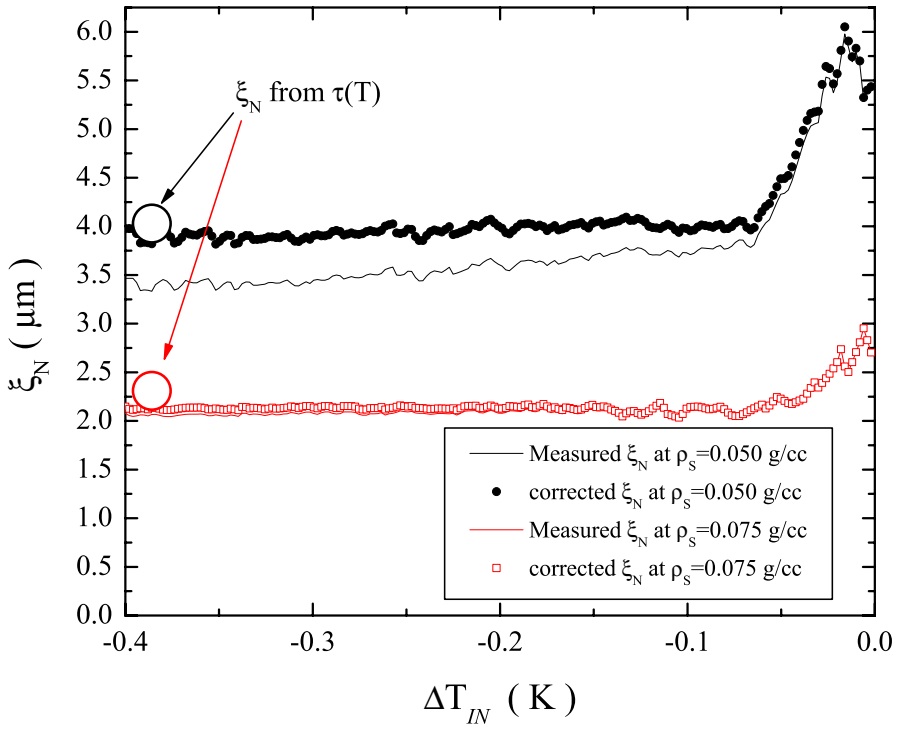

Figure 4.14. Plot of the temperature dependence of the nematic correlation length $\xi_N(\Delta T)$ in the two-phase coexistence region as extracted from the $ILALS$ experiment. Note that the double scattering correction has a small effect on the uncorrected results, but it increases at lower temperatures. In the plot are also shown the $\xi_N(\Delta T)$ values extracted from the turbidity measurements, outside the two-phase coexistence region. See figure inset for symbol definitions.

deeper in the nematic phase. The $ILALS$ experiment was performed only on the 0.050 and 0.075 samples. For the 0.100 and 0.200 samples the nematic correlation value was assumed to be temperature independent inside the two-phase coexistence region, similar with the value obtained from the turbidity measurements.

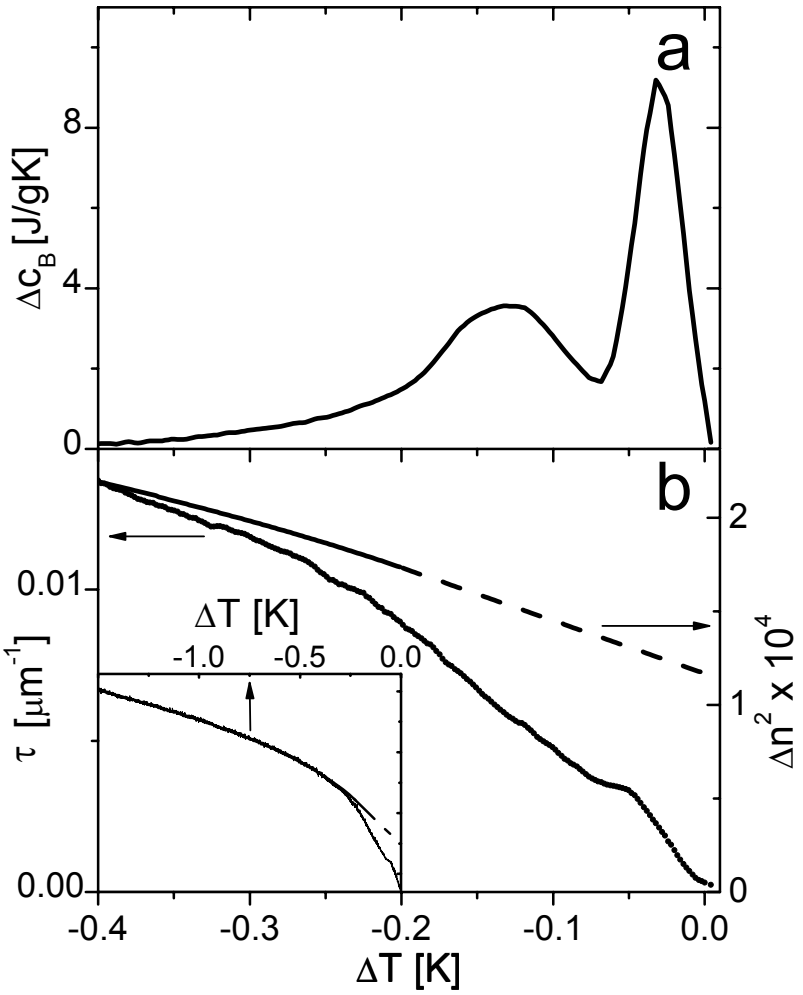

Figure 4.15. Excess specific heat ΔC_B (a) and turbidity τ (b-left axis) measured as a function of the temperature shift ΔT within the two-phase coexistence region for the $CCN47 + SIL$ $\rho_S = 0.075$ sample. Also shown, the bulk birefringence squared Δn^2 (b-right axis): measured values (solid line) and linear extrapolation (dashed line). Inset: τ and Δn^2 over a wide ΔT range.

4.3.4 Connection of Light Scattering with Calorimetry

The $\Delta C_B(T)$ variation for $\rho_S = 0.075$ is shown in Fig. 4.15 as a function of the temperature shift $\Delta T = T - T_{IN}(\rho_S)$ where $T_{IN}(\rho_S)$ is the temperature of the first appearance of nematic in $LC + SIL$ samples. The double calorimetric feature is thus evident here as it was for other LCs [58, 86]. Figure 4.15 also shows, for the same sample, $\tau(T)$ (left axis) together with the bulk behavior of $\Delta n^2(T)$ (right axis). The match between $\tau(T)$ and $\Delta n^2(T)$ extends over a large T interval at lower temperature (inset Fig. 4.15b), indicating that, outside the transition region, ξ_N is constant, as previously reported [36], and it was discussed in the previous section.

In the I+N coexistence region, because of the distributed local transition temperatures, the determination of the Δn^2 for the N-fraction, with which to interpret τ, is more difficult. In what follows, we have adopted the simplest view and assume that the value of Δn^2 for the coexisting nematic fraction is given by a linear extrapolation of the bulk Δn^2 (dashed line in Fig 4.15b). This is supported by NMR data on $LC + SIL$ indicating that in the coexistence region the local S has a weaker T dependence than bulk [78]. The $\xi_N(T)$ extracted from $ILALS$ data is shown again in Fig. 4.16 in order to view side by side the T evolution of both ΔC_B and ξ_N. As shown in the figure, first-order correction (double scattering - open dots) has a negligible effect on ξ_N. From the optically measured τ, Δn^2, and ξ_N we extract $\phi_N(T)$, which is shown in Fig. 4.17. The calculation of $\phi_N(T)$ was done according to Eq. (3.48), while for the calorimetry was calculated by the normalized to one integral of ΔC_B.

As Fig. 4.17 demonstrates, both calorimetric and optical measurements indicate that the double peak must be entirely due to a two-step transformation of the LC from the isotropic to the nematic state. The results from the calorimetric and optical techniques display remarkable agreement. The relative size of the two processes is plotted for samples having different ρ_S in the inset of Fig. 4.17. Apart from the 0.050 sample, which may suffer from the separation of bulk LC from the $LC + SIL$ during the thin cell preparation, the agreement is very good. To interpret the double transition process, a key observation is the smoothness and the limited decrement of ξ_N data, which unambiguously demonstrate that the transition doubling *cannot* be attributed to a bimodal distributed porosity in the silica gel. However, the decrease of ξ_N as T decreases, which has been confirmed

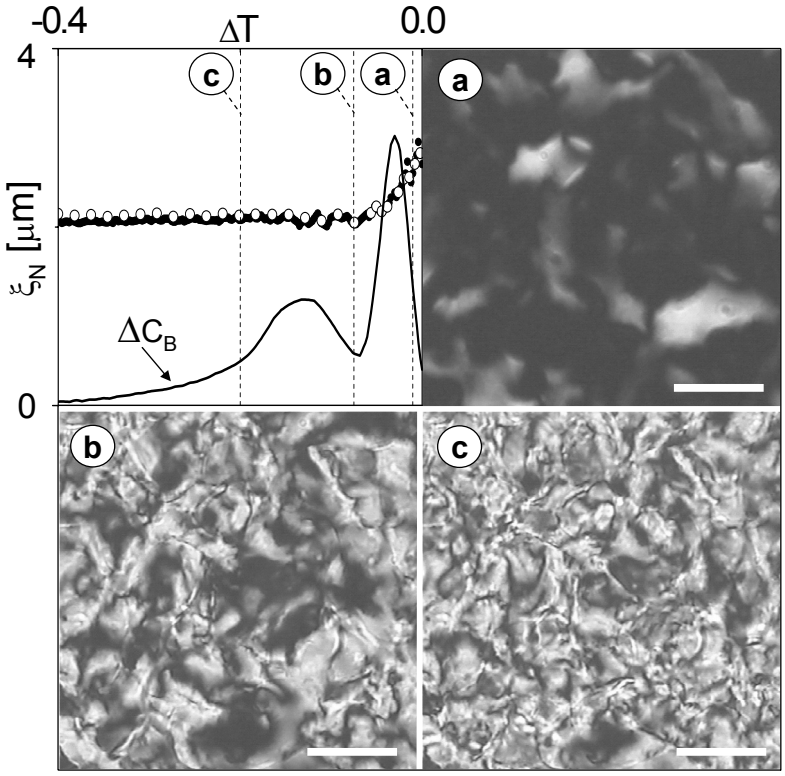

Figure 4.16. Upper Left Panel: Nematic correlation length ξ_N raw data (solid dot) and double scattering corrected (open dot) and ΔC_B (arbitrary scale) for the $\rho_S = 0.075$ sample measured as a function of ΔT. Panels (a), (b), (c): Optical cross-polarized microscope pictures taken at a ΔT of -0.033 (a), -0.07 (b), and -0.2 (c) indicated by the vertical dotted lines in the upper left panel. Bar corresponds to 10 μm.

by direct optical microscopy observations shown in Fig. 4.16, offers an important clue for interpreting the observed behavior. Figures 4.16a-c show a sample in cross-polarized microscopy at three different temperatures corresponding to the first appearance of the N phase, to a point in between the C_p peaks, and to a low T state (see upper left panel of Fig 4.16). The nematic first appears as isolated regions with approximately uniform director alignment. As T decreases through the region of the higher-T C_p peak, the domains grow in number, distort and exhibit recognizable defect lines, an indication of an increased coupling of the director with the silica surfaces. As this distortion proceeds, the transition slows and, for a narrow interval between the C_p peaks, no new nematic domains appear. As T decreases further, the nematic growth manifests itself in a different way. New volumes undergo the *I-N* transition, but no changes in the director is observed:

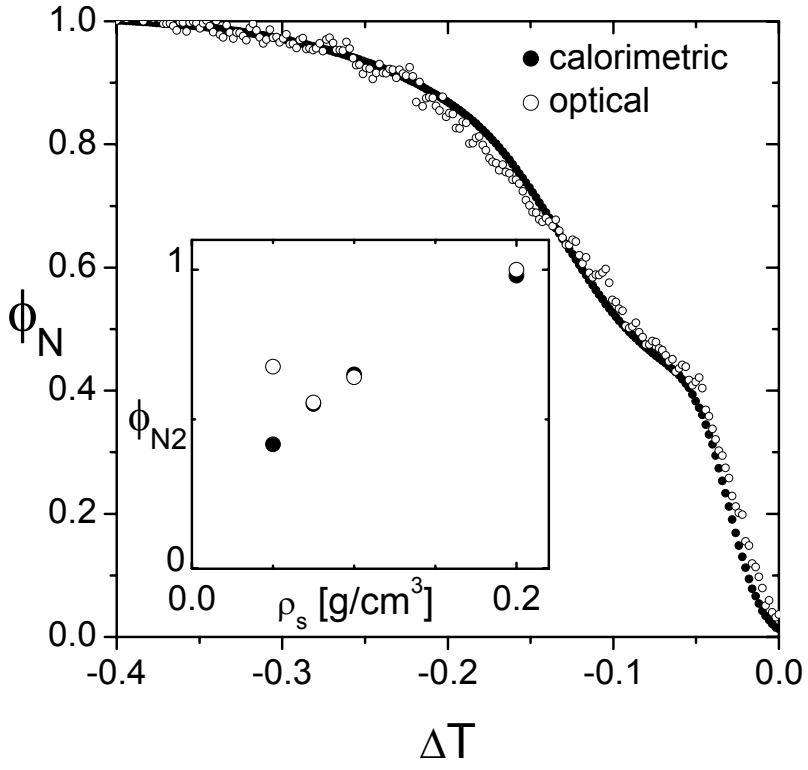

Figure 4.17. Nematic volume fraction ϕ_N obtained from the integral of $\Delta C_B(0.075)$ (solid dots) and deduced from optical measurements $\phi_N \propto \tau/(\Delta n^2 \xi_N)$ (open dots) as a function of ΔT through the two-phase coexistence region. Inset: N volume fraction ϕ_{N2} converted through the low temperature C_p peak, as a function of ρ_S.

domains appear with their "final" low T distorted structure. This is consistent with an essentially constant correlation length thereafter. Thus, the combination of microscope observations and the ξ_N data suggest that the two processes differ in the *strength* of the coupling with the silica matrix.

We argue that this observation leads to an explanation of the nature of the double C_p peak. Incorporation of solids in a spontaneously ordering media has different effects on the phase behavior and, in particular, on the shift and distribution of transition temperatures. The simplest expected - and, in some cases, observed [88] - effect comes from dilution, weakening of the mean molecular field. At the mean field level, this effect downshifts T_{IN} by the total reduction of the molecular coordination, provided by the contact with the solid-LC interface area. The disorder broadening of the transition can be most simply modelled by a distribution in ΔT_{IN} within the two-phase coexistence region linear in the local disorder (silica)

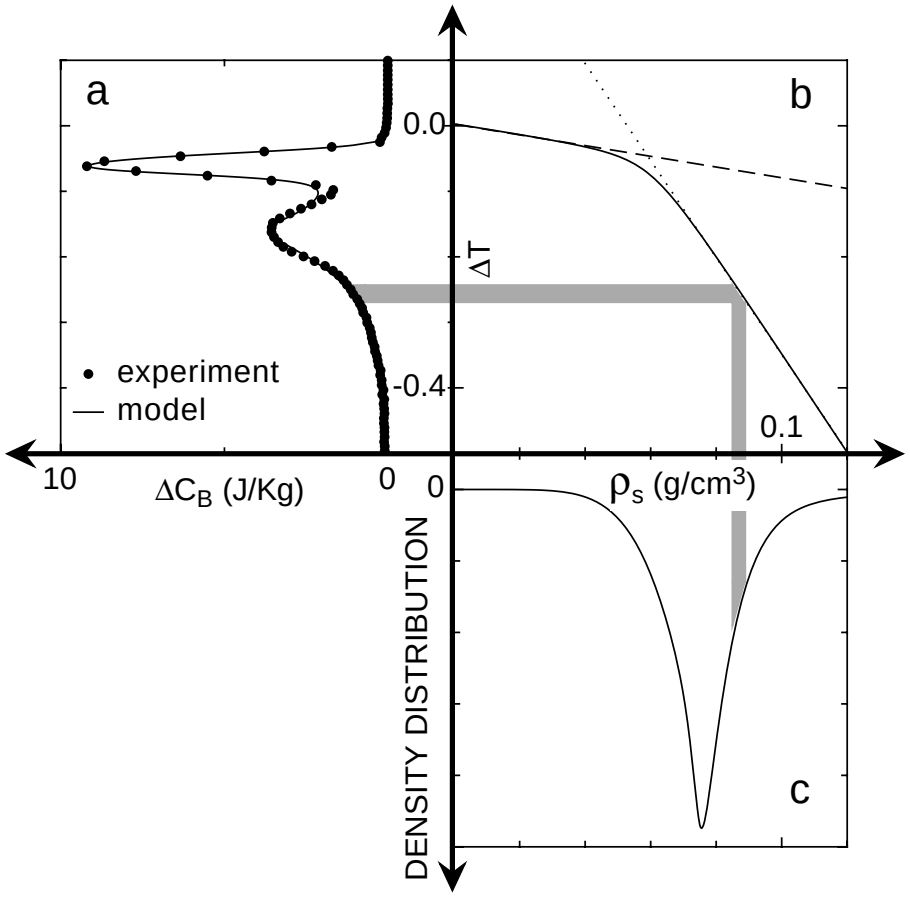

Figure 4.18. Proposed interpretation. Panel (a): Model (continuous line) and ΔC_B (full dots) versus ΔT for the $\rho_S = 0.075$ sample. Panel (b): distribution of transition temperatures ΔT within the two-phase coexistence region (solid line) versus disorder density (ρ_S) crossing over from random dilution effects (dashed line) to random field effects (dotted line). Panel (c): Local density distribution versus disorder density which successfully reconstructs ΔC_B.

density (dashed line in Fig. 4.18b). If this was the only mechanism, the amount of material undergoing the *I*-*N* transformation in a given interval within the two-phase range would simply be an image of the disorder density distribution function, possibly averaged by a suitable nucleation length, in analogy to that described in other phase transitions [89]. However, as the data indicate, the disorder distribution is not bimodal and there appears at lower T a stronger coupling, resulting in stronger distortions and the appearance of topological defects, a situation of random orientational pinning not accounted for by random dilution. We suggest that this cross-over is the result of the progressive thinning of a sheath of disordered

LC, which screens - for a penetration length - the silica surface. As the temperature is lowered further, the disordered LC surface layer converts to a defected nematic and the random dilution turns into a random field coupling, described by some other, certainly steeper, distribution of $\Delta T_{IN}(\rho_S)$ behavior (dotted line in Fig. 4.18b). This cross-over is proposed here to be the origin of the observed double peak. A simple disorder density distribution (Fig. 4.18c) transforms, by virtue of the transfer function in Fig. 4.18b, into a double peaked $d(\phi_N(T))/dT$ (line in Fig. 4.18a).

In this approach, a rather featureless disorder distribution and a simple transfer function were chosen so as to yield an overlap with the $\Delta C_B(0.075)$ data, demonstrating that these few ingredients can reproduce the observed doubled transition. This model does not address the observed [58] complex $T_{IN}(\rho_S)$ shifts, which requires a more detailed study. Nevertheless, our description of a random-dilution to random-field cross-over should be a generic effect at first-order phase transitions with quenched random disorder.

4.4 Discussion

Results have been presented from high-resolution ac-calorimetric experiments on $8OCB+SIL$ dispersions with emphasis on the weakly first-order I-N phase transition. These results for $8OCB+SIL$ dispersions have been compared with existing results for $8CB+SIL$ dispersions [58, 59] and reveal new aspects of the effect of quenched random disorder on liquid crystal phase transitions. In particular, these two $LC+SIL$ systems are very similar except for the relative elasticity of the LC material. The material $8OCB$ is elastically stiffer, having an effective (single) nematic elastic constant K_N larger by approximately 20%, than $8CB$. This is reflected by the higher transition temperatures for the nematic, smectic, and crystal phases. Thus, aspects that are LC material dependent and those that are general to quenched random disorder can be distinguished.

From the very good overlap of the ΔC_p wings away from the I-N two-phase coexistence region and from direct NMR studies on $8CB+SIL$ [78], a general feature of LC+aerosils is that the magnitude of the nematic order, S, is essentially the same as in the bulk LC. Thus, the main effect of QRD is on the director

structure with the elasticity of the LC and the kinetics of the ordered phase growth as likely important factors. This is supported by the differences seen between $8OCB + SIL$ and $8CB + SIL$ systems; in particular, the different ρ_S dependence is likely connected to the difference in elasticity for the two liquid-crystals.

The effect of quenched random disorder on first-order phase transitions is substantially different than that on continuous phase transitions. First-order transitions have an additional energy penalty for the formation of interfaces between coexisting phases, which complicates random-field type theoretical approaches. In the classical treatment first developed by Imry and Wortis [71], the QRD effect on first-order transitions is that a quenched random-field creates domains having a randomly shifted transition temperature. This would have the effect of smearing the overall transition, a monotonic decrease in the transition latent heat and temperature with increasing QRD, and a low-temperature phase possessing only short-range order for arbitrarily weak QRD. These predictions are generally consistent with the behavior of nematic in aerogels [82]. For nematics in aerosils, the transition latent heat appears to decrease monotonically with increasing disorder as well as the transition becoming apparently continuous for high disorder strength. These features are generally consistent with the classical picture. However, the character of the transition and the non-monotonic transition temperature shifts and the width of the coexistence region do not appear to be consistent with this view. More strikingly, the *I-N* transition in aerosils in some range of ρ_S, appears to proceed via two transitions. This could only occur in the classical view if a bimodal distribution of the random-field variance $\langle h^2 \rangle$, connected to a bimodal distribution in ρ_S, is present. This is not supported by SAXS studies, which revealed the fractal-like nature of the aerosil gel structure [58], nor the behavior at the *N-SmA* transition [90, 91, 58]. However, nematics are very "soft" materials and the QRD imposed by aerosils appears to be much weaker than that of aerogels, thus elasticity of the LC (and possibly the gel) can play an important role.

In LC+aerosil systems, $\langle h^2 \rangle$ is thought to depend on the given concentration of silica and interaction with the LC, whereas the LC elasticity K_N is strongly temperature dependent (being proportional to S^2) near and below T_{IN}. Since the aerosil gel is thixotropic and formed in the isotropic phase, any high energy strains or deformations that may exist are likely quickly annealed. Thus the anisotropy

of the gel should be fixed and essentially zero, especially for rigid gel structures like aerogels. However, the disordering nature of the gels may evolve with thermal history of the LC in aerosil gels. As seen by the result of cycling through crystallization presented here as well as the DNMR [78] and electro-optical [55, 56] studies, the gel can be compliant with respect to distortions in the director structure for a range of silica densities. Note that the quantity T_{IN} differs by at most 10% between $8CB$ and $8OCB$; thus the energy scales are similar while the twist elastic constant differs by 36%.

The features described above suggest a possible physical scenario for the origin of the double ΔC_p feature at the *I-N* (or any "soft" first-order [92]) transition in LC+aerosil systems. As the nematic elastic constant strongly increases with decreasing temperature for $T \lesssim T_{IN}$, a "skin" of low nematic order (due to the undulations of the aerosil strands) may coat the silica strands. The thickness of this paranematic boundary layer would be strongly temperature dependent, shrinking with decreasing T below T_{IN}. The presence of such a layer would serve to partially decouple the disordering (or field) effect of the silica gel from the void nematic (acting as a kind of "lubricant"). Once the layer thickness reaches its minimum value (roughly equivalent to a molecular length) the elasticity of the void nematic becomes strongly coupled to that of the aerosil gel. This would effectively increase, for a given ρ_S, the disorder strength. This cross-over is proposed here to be the origin of the observed double peak. A simple disorder density distribution (Fig. 4.18c) transforms, by virtue of the transfer function in Fig. 4.18b, into a double peaked $d(\phi_N(T))/dT$ (line in Fig. 4.18a).

A consequence of this speculation for a first-order transition induced change in disorder strength (through the onset of coupling between the director fluctuations and gel) would be the alteration of the gel dynamics (i.e., vibrational modes). This would be consistent with large changes in the relaxation times of aerosil gels observed by dynamic x-ray studies on $8CB + SIL$ near T_{IN} [77]. In addition, this coupling should dampen director fluctuations and could account for the variation in the critical behavior seen at the *N-SmA* transition for $LC + SIL$ samples. Another consequence of this view is that the director correlation length $\xi_{\hat{n}}$ (the relevant aspect of nematic order) would jump to a large isotropic value at the first transition and upon further cooling cross a second transition into a more strongly disordered

state having a *smaller* correlation length, as was confirmed by the detailed optical studies of $\xi_{\hat{n}}$ through the two transition peaks in the $CCN47 + SIL$ samples.

The different silica density dependence of T_{IN} and the temperature distance between the two C_p peaks (δT_{2p}) between $8OCB+SIL$ and $8CB+SIL$ would also be consistent with the difference in the nematic elasticity of the two liquid-crystals. A stiffer silica gel (higher ρ_S) would be required to influence a stiffer LC, thereby stretching the shift in T_{IN} with respect to ρ_S, as seen between the $8OCB + SIL$ and $8CB + SIL$ systems. The ρ_S dependence in the high-density regime of δT_{2p} for $8OCB + SIL$ (see Table 4.1) compared to the nearly constant $\delta T_{2p} \sim 0.1$ K seen only in the low density regime of $8CB + SIL$ [58] would be compatible with a transition induced increase in the variance of the gel disorder strength. The liquid-crystal $8CB$ being much softer would only be able to stress a very weak (low ρ_S) gel, while the much stiffer $8OCB$ would be able to distort a wider range of gels. Since the ρ_S dependence of the critical behavior for the *N-SmA* transition is quite similar between $8CB + SIL$ and $8OCB + SIL$ [81], these observations suggest that the effects observed at the *I-N* transition are not directly connected to those at the *N-SmA*.

The unexpected behavior of the low silica density sample when initially cycled through the crystallization transition is not fully understood. The expulsion of silica impurities by the strongly first-order crystallization transition seems to lead to a *more* disordered system. One possibility to explain this phenomena is that the initial crystallization causes the expulsion of the silica particles locally and transforms the flexible fractal structure into a more rigid, foam-like, gel. The depression of T_{IN} is then a consequence of the greater elastic distortions imposed by the new gel arrangement. Repeated cycling through crystallization would continue to expel impurities, eventually destroying the foam-like structure. Once the silica has been compacted sufficiently, percolation is no longer possible and free-floating silica particles would represent an annealed disorder. The gels formed in the high silica density samples are more robust and would not be expected to change significantly when the LC crystallize. This view can be directly tested with a detailed structural study by small-angle x-ray scattering where the thermal history is carefully controlled. The increase in the enthalpy of the *N-SmA* transition after the initial crystallization to a value greater than the bulk LC value remains a puzzle.

Note that the speculations presented here for the double *I-N* transition peaks and the unusual hysteresis behavior are intended to motivate future experimental and theoretical studies.

Finally, the $CCN47 + SIL$ calorimetric results were in-line with the data obtained from the $8CB + SIL$ and the $8OCB + SIL$ samples. The ρ_S evolution of the transition temperatures and the enthalpies was similar to that observed in the previously studied samples. Furthermore the study of $CCN47 + SIL$ samples made possible the understanding of the double peak observed in the *I-N*, weak first-order transition as a crossover from the random dilution, where the random field is barely coupled to the nematic phase, to random disorder, where the random field couples strongly to the nematic phase.

Chapter 5

Nematic to Smectic-A Phase Transition in Aerosil Disordered Liquid Crystal

5.1 Introduction

Recent studies of the nematic (N) to smectic-A (SmA) phase transition in octyl-cyanobiphenyl ($8CB$) + aerosil dispersions by Park and coworkers using x-ray scattering [75, 76], and by Iannacchione and coworkers using calorimetry [58], have shown that this system has clear quenched random-field characteristics and that the finite ordered domain size creates finite-size scaling effects [59]. Here, we present a complimentary study of three different liquid crystals $8OCB$, $CCN47$, and $\bar{8}$S5 - in which the same type of aerosil is dispersed over a comparable range of silica densities. The measurements will enable us to further test our understanding of liquid crystal - aerosil dispersions, as well as identify LC characteristic behaviors.

The effect of quenched random disorder on phase transition behavior can be profound. The modification of transitions depends on the aspect of the system which is effected by the disorder, on the dimensionality, and on the number of components to the order parameter. Of interest here is quenched random disorder which couples linearly to the order parameter. We have studied the effect of

this type of apparent random-field due to a dispersed thixotropic aerosil gel on the nematic to smectic-A (*N-SmA*) phase transition in the liquid crystals 8*OCB*, *CCN*47, and $\bar{8}$S5. At the *N-SmA* transition, translational invariance is broken along one dimension [3]. The smectic order parameter involves the amplitude and the phase of a one-dimensional density wave; thus, this phase is a member of a three-dimensional, two-component order parameter system (3D-XY).

The effects of random fields on single-component order parameter magnetic transitions have been studied for many years [93]. This has been carried out using the Fishman-Aharony trick: a random-field Ising ferromagnet (RFIM) can be created by applying a magnetic field to a diluted Ising antiferromagnet [1]. However, it is not possible to use this technique on systems having a multicomponent order parameter. For a multicomponent order parameter, the applied field will always result in a uniaxial random-field and not the required continuous-symmetry random-field. Common physical realizations of multicomponent order parameter random-field systems are pinned vortices in type-II superconductors and pinned charge-density waves. In both of these systems, the disorder strength is substantially more difficult to control than the applied field in the RFIM system.

The nematic to smectic-A translational behavior in pure liquid crystals has been studied extensively using high-resolution x-ray diffraction and *AC* calorimetry. An attractive feature of studying the effect of disorder on liquid crystal ordering is the precision with which the pure system structure factor and thermal fluctuations are known. High-resolution studies have demonstrated that the smectic correlations in the nematic phase are described by an anisotropic Lorentzian structure factor [94]. The results clearly show that a fourth-order correction term is required, which diminishes as the transition is approached. Although this behavior is well characterized empirically, it is not yet fully understood.

The study of the nematic to smectic-A transition in a random-field presented here is important because it is a multicomponent order parameter system for which the disorder strength can be easily controlled. The quenched random-field is created by a dispersed gel of aerosil particles and the variance of the field strength is varied by changing the density of aerosils in the dispersion. See section 3.7.1 for characteristics of the aerosil gel. Studies have previously been carried out by various groups on liquid crystals in an aerogel medium [95]. Because of the fused

silica nature of the aerogel structure, the aerosil gel provides a weaker and more easily controlled perturbation, and thus opens up a physically interesting regime. The aerosil or aerogel surfaces pin both the direction of the layer normal and the position of the layers. Small angle x-ray studies have shown that the aerosil gel dispersion has a fractal structure and no preferred orientation [58]. The random surfaces provide a random pinning field for smectic ordering, which overcomes the intrinsic problem found in random-field multicomponent order parameter systems.

At the *N-SmA* transition, the orientationally ordered phase becomes modulated in density along the long axes of the molecule. To understand the effect of the aerosil network on this transition, it is necessary to first consider how the disorder disrupts the nematic phase. The aerosil network dilutes the nematogens and additionally creates a preferred local orientation [69, 70]. This latter effect appears to be the most important and can be represented as

$$H_{RF} = -\sum_i g_2(\vec{h}_i \cdot \hat{l}_i)^2 \tag{5.1}$$

where $\hat{l}_i$ is the orientation of the molecules and $\vec{h}_i$ is the random influence of the silica surface. This term is squared due to the effective inversion symmetry of the molecules in the nematic phase. Since the order parameter is quadratic in $\hat{l}_i$, this term is also linear in the nematic order parameter and hence constitutes a random field. In support of this conjecture, light scattering measurements show that the nematic phase in liquid crystal - aerosil dispersions breaks up into large but finite-size domains [36]. As the sample is cooled further, smectic correlations develop within finite-size nematic domains. The free-energy of the liquid crystal close to the *N-SmA* transition can be written as the sum of the de Gennes free-energy, the Frank free-energy for director fluctuations, and the contribution due to the influence of the aerosil. The latter can be expressed as [69, 96]

$$F_{RF} = \int d^3r(-g_2(\vec{h} \cdot \hat{n})^2 - V\Psi - V^*\Psi^*) \; . \tag{5.2}$$

Here, $\hat{n}$ is the nematic director while Ψ is the complex smectic-A order parameter. The first term is the influence of the aerosil surface on the molecular orientations. This interaction limits the ability of the smectic correlations to increase the nematic

order. It also modifies the relationship between the nematic and smectic phases and, as a result, allows the system to behave more like a standard 3D-XY system [58]. The second pair of terms represent the influence of the aerosil environment on the position of the smectic layers. This term is linear in the smectic order parameter Ψ and is likely to create the observed random field behavior. The pinning of the layer position at the *N-SmA* transition is similar to the pinning of the phase of a charge-density wave by random impurities.

It has been observed in 8*CB*+aerosil samples that the smectic domains which form are very much smaller than the nematic domains which precede them [75, 76] (the nematic correlation length $\xi_N \geq 20\bar{\xi}$, where $\bar{\xi}$ is the mean smectic-A correlation length at low temperatures). This strongly suggests that it is some effect other than orientational disorder that is disrupting the growth of smectic ordered regions. Our results support the idea that the pinning of the phase is the dominant effect while the orientational disorder creates subsidiary modifications.

8*CB*+aerosil dispersions have been studied previously using high-resolution x-ray diffraction [75, 76]. The structure factor used to analyze the scattered intensity as a function of wave-vector transfer was motivated by analogy with the behavior of magnetic random field systems. This appears to support the idea that the aerosil gel network creates a quenched random pinning field. The correlation length for the smectic fluctuations was observed to saturate at a finite value which was density dependent. Thus, no true *SmA* phase exists in aerosil samples. However, there is an *effective N-SmA* transition temperature T^*, below which static quenched-random effects dominate and above which they are close to negligible and thermal fluctuations dominate. Here, we build upon this 8*CB*+aerosil work by showing that the dependence of the correlation length on silica surface area is in line with theoretical predictions. We will argue that the surface area is a good measure of the disorder strength. Additionally, we study the variation of the scattering peak intensity and associated specific heat peak as a function of silica surface area.

Other studies have been carried out on liquid crystals with an aerosil gel dispersion using a variety of techniques. Calorimetry measurements on 8*CB* with an aerosil dispersion have yielded detailed information on both the isotropic to nematic(*I-N*) and the *N-SmA* transition [58]. The results for both the *I-N* and *N-SmA* transitions show a complex transition temperature dependence on the aerosil

density, while the ΔC_p(NA) heat capacity evolves towards 3D-XY behavior with increasing silica density. At high aerosil densities, the heat capacity measurements show a ΔC_p(NA) feature which is highly smeared and non-singular. Deuterium NMR measurements have also been made on deuterated $8CB$ with an aerosil dispersion [78]. Here, studies were carried out for a wide range of silica densities, but the requirement of an applied magnetic field makes this work somewhat different from the calorimetry and the x-ray studies described below. In an intermediate density range of interest here, the samples were cooled in a 4.7 T field and the DNMR spectra were observed in the nematic phase before and after rotating in the field direction through 90^o. The molecular configuration established by cooling in the field is stabilized by the silica filaments. The amount of liquid crystal reorientation upon field rotation is small and decreases continuously with silica density up to $\rho_S = 0.094$ g cm^{-3}. Both calorimetry and DNMR results are consistent with a model in which the nematic susceptibility decreases with increasing aerosil density.

Promising results have been obtained concerning the dynamic behavior of $8CB$+aerosil dispersions using x-ray intensity fluctuation spectroscopy [48, 57]. Measurements of the aerosil gel dynamics were carried out with x-ray energies just below the Si absorption edge and in a q range sensitive to large silica aggregate structure. The results show that the silica motions are damped by the liquid crystal elastic medium, and that the relaxation time constant increases substantially at the *N-SmA* phase transition. This coupling of two elastic media is the likely mechanism for the decreasing nematic susceptibility with silica concentration.

5.2 *N-SmA* Transition in $8OCB$

5.2.1 Calorimetric Results

The heat capacity of the pure $8OCB$ liquid crystal used in making the $8OCB$+aerosil samples for both x-ray and calorimetry studies was determined in order to make quantitative comparisons with aerosil data. The excess heat capacity associated with the pure *N-SmA* transition, shown in Fig. 5.1, is in good agreement with previously published results [61, 80]. We find for our pure $8OCB$ material the

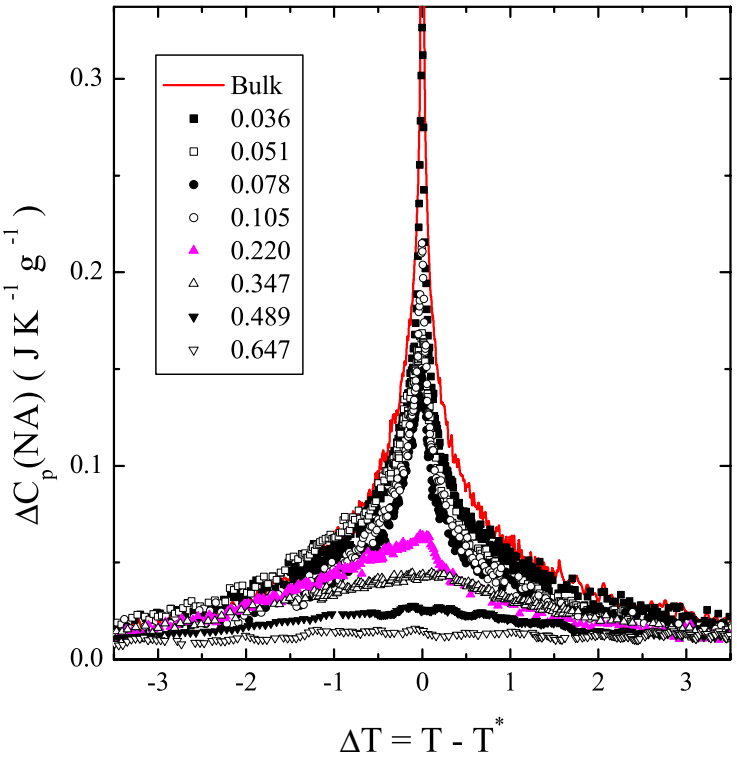

Figure 5.1. Specific heat due to the *N-SmA* phase transition, ΔC_p(NA), as a function of temperature about T* for bulk 8*OCB* and 8*OCB*+aerosil samples from $\rho_S = 0.036$ to 0.647 grams of silica per cm^3 of liquid crystal. See figure legend for definition of symbols.

transition temperatures $T^o_{NI} = 352.53$ K and $T^o_{NA} = 339.52$ K. The *I-N* two-phase coexistence width was $\approx$ 95 mK wide, and the *N-SmA* transition enthalpy was $\delta H^o_{NA} = 0.42$ J g^{-1}. These thermal features indicate that the 8*OCB* liquid crystal used to make up both x-ray and calorimetric studies was of reasonably good quality. A summary of the calorimetric results for pure 8*OCB* and 8*OCB*+aerosil samples is given in Table 5.1. Except for the additional $\rho_S = 0.036$ and 0.647 samples, the samples studied with calorimetry were from the same batches as those studied by x-rays. However, as explained in Sec. 3.6.1 and 3.6.3, the sample handling differed slightly.

In order to determine the excess heat capacity associated with the *N-SmA* transformation shown in Figure 5.1, two backgrounds were subtracted. The total

sample heat capacity over a wide temperature range had a linear background, C_p(background), subtracted to yield

$$\Delta C_p = C_p - C_p(\text{background}) \tag{5.3}$$

as the excess C_p due to the *I-N* and *N-SmA* phase transitions. The excess C_p due to the *N-SmA* transition, $\Delta C_p(NA)$, was found by subtracting a mimic function (a simple power-law C^{NI}_{power}) depicting the low-temperature $\Delta C_p(NI)$ wing variation:

$$\Delta C_p(NA) = \Delta C_p - C^{NI}_{power} \tag{5.4}$$

The parameters for each 8*OCB*+aerosil sample of the empirical low-temperature C^{NI}_{power} wing were determined by fitting ΔC_p after removing a $T^* \pm 5$ K wide window of data related to the *N-SmA* contribution. See Fig. 1 given in Ref. [58] and accompanying text there for additional details about obtaining $\Delta C_p(NA)$. The resulting $\Delta C_p(NA)$ data are shown for pure 8*OCB* and all 8*OCB*+aerosil samples in Fig. 5.1, where the units are J K^{-1} per gram of *liquid crystal*. The *N-SmA* transition enthalpy is then given by

$$\delta H_{NA} = \int \Delta C_p(NA) dT \tag{5.5}$$

ρ_S	T_{NI}	T^*	ΔT_{nem}	δH_{NA}	h_M
0	352.53	339.52	13.01	0.420	-
0.036	352.53	339.64	12.89	0.385	0.326
0.051	352.79	340.22	12.57	0.334	0.167
0.078	351.08	338.61	12.47	0.268	0.146
0.105	351.02	338.51	12.51	0.284	0.213
0.220	351.20	338.61	12.59	0.230	0.100
0.347	352.31	338.85	13.46	0.202	0.044
0.489	352.05	338.05	14.00	0.149	0.027
0.647	351.41	337.30	14.11	0.050	0.014

Table 5.1. Summary of the calorimetric results for the 8*OCB*+aerosil samples. Shown are transition temperatures for the *I-N* (T_{NI}) and the *N-SmA* (T^*) phase transitions in Kelvin, the nematic temperature range $\Delta T_{nem} = T_{NI} - T^*$, the *N-SmA* transition enthalpy δH_{NA} in J g^{-1}, and heat capacity maximum (value at T^*) $h_M \equiv \Delta C_p^{max}(NA)$ in J K^{-1} g^{-1} units.

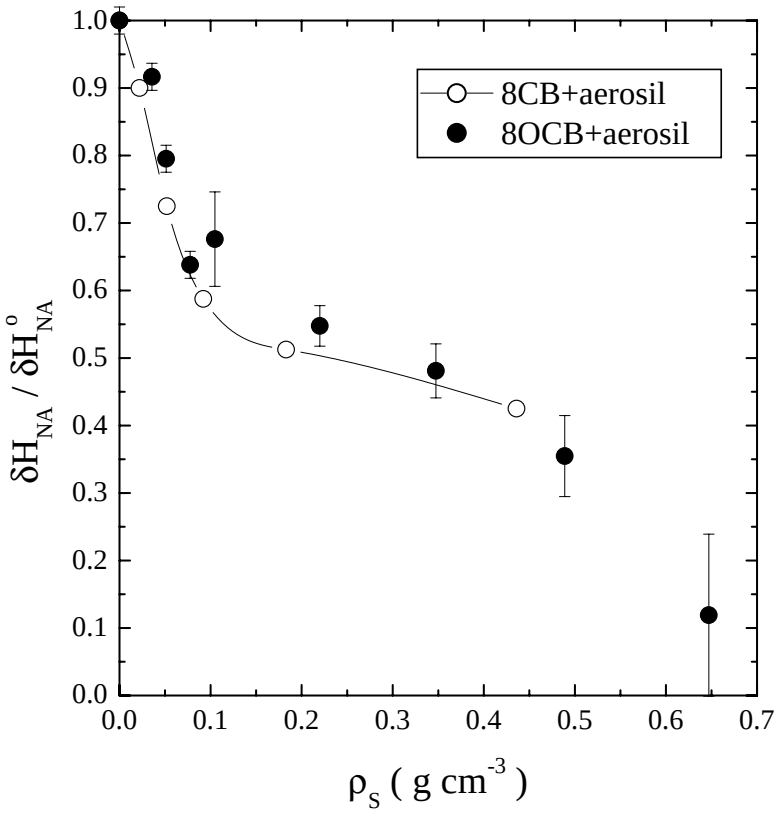

Figure 5.2. The ρ_S dependence of the *N-SmA* pseudo-transition enthalpy $\delta H_{NA} = \int \Delta C_p(\mathrm{NA}) dT$, scaled by the transition enthalpy of pure $8OCB$, $\delta H^o_{NA} = 0.42$ J g^{-1} for $8OCB$+aerosil samples. Also shown are $\delta H_{NA}/\delta H^o_{NA}$ for $8CB$+aerosil samples taken from Ref. [58] using $\delta H^o_{NA} = 0.80$ J g^{-1} for the pure $8CB$ *N-SmA* transition enthalpy. The solid line for the $8CB$+aerosil samples is a guide to the eye.

where consistent limits of the integration, ± 5 K about T*, were used for all samples.

The behavior of $\Delta C_p(NA)$ as a function of temperature for various aerosil density is shown in Fig. 5.1. The *N-SmA* C_p peak remains sharp for aerosil densities up to $\rho_S = 0.105$. Above this aerosil density, $\Delta C_p(NA)$ becomes significantly rounded. The increasingly asymmetric shape of $\Delta C_p(NA)$ with increasing ρ_S, observed for $8CB$+aerosils [58], is also observed for $8OCB$+aerosils though to a weaker extent. Since the change in shape for $\Delta C_p(NA)$ has been interpreted as a disorder-driven crossover toward the underlying 3D-XY critical behavior [97] (having $\alpha_{\mathrm{3D-XY}} = -0.013$), the more subtle change for $8OCB$+aerosil is not surprising as the bulk critical exponent for $8OCB$ ($\alpha_{8OCB} = 0.20$) is lower than that for $8CB$ ($\alpha_{8CB} = 0.30$) [20]. In this light, the $8OCB$+aerosil system has less room to vary

ρ_S	T_c	α	A^+	A^-	D^+	D^-	B_c	χ^2_ν
0	339.519	0.18	0.103	0.101	1.871	2.253	−0.264	1.017
0.036	339.639	0.17	0.087	0.082	0.874	1.643	−0.189	1.147
0.051	340.215	−0.04	−1.321	−1.367	−0.179	−0.470	1.098	1.098
0.078	338.612	0.14	0.081	0.089	−0.159	1.371	−0.160	1.257
0.105	338.508	−0.01	−4.979	−4.999	−0.121	−0.161	4.712	1.854

Table 5.2. Results from fitting the excess specific heat $\Delta C_p(NA)$ associated with the *N-SmA* pseudo-transition of the 8*OCB*+aerosil samples with Eq. (5.6). T_c values are in kelvin, $A^\pm$ and B_c are in J K^{-1} g^{-1}, while $D^\pm$ values are dimensionless. Note the odd behavior for the 0.078 sample indicating inhomogeneity of that dispersion.

in order to achieve the 3D-XY fixed point.

To characterize the change in shape of these $\Delta C_p(NA)$ data, a traditional power-law form [20] in terms of the reduced temperature $t = \mid T - T^* \mid /T^*$ is used to analyze the experimental specific heat data associated with the *N-SmA* phase transition:

$$\Delta C_p(NA) = A^\pm t^{-\alpha}(1 + D^\pm t^{\Delta_1}) + B_c \ , \tag{5.6}$$

where the critical behavior as a function of reduced temperature t is characterized by an exponent α, amplitudes $A^\pm$ above and below the transition, a critical background term B_c, and corrections-to-scaling terms characterized by the coefficients $D^\pm$ and exponent $\Delta_1 \simeq 0.5$. An increasing temperature gap of excluded data about the $\Delta C_p(NA)$ peak with increasing ρ_S was required to perform the fitting. These fit results are presented in Table 5.2 and show a systematic evolution of the effective critical exponent α toward the 3D-XY value consistent with previous studies on 8*CB*+aerosil samples [58]. The exception is the $\rho_S = 0.078$ 8*OCB*+aerosil sample which exhibited an exponent closer to the pure *N-SmA* value and is likely an indication that this sample was an inhomogeneous dispersion.

The *N-SmA* pseudo-transition temperatures T^* scaled by the bulk transition temperature T^o_{NA} for $8OCB + SIL$ and $8CB + SIL$ systems are shown in Fig. 5.3. The pattern of fractional changes in the T^* is essentially the same for both $LC + SIL$ systems with an initial rapid depression, recovery, then more gradual decrease with a total change of less than 1% from T^o_{NA}. The primary difference with the $8CB + SIL$ system is that this behavior is "stretched" in ρ_S for the $8OCB + SIL$

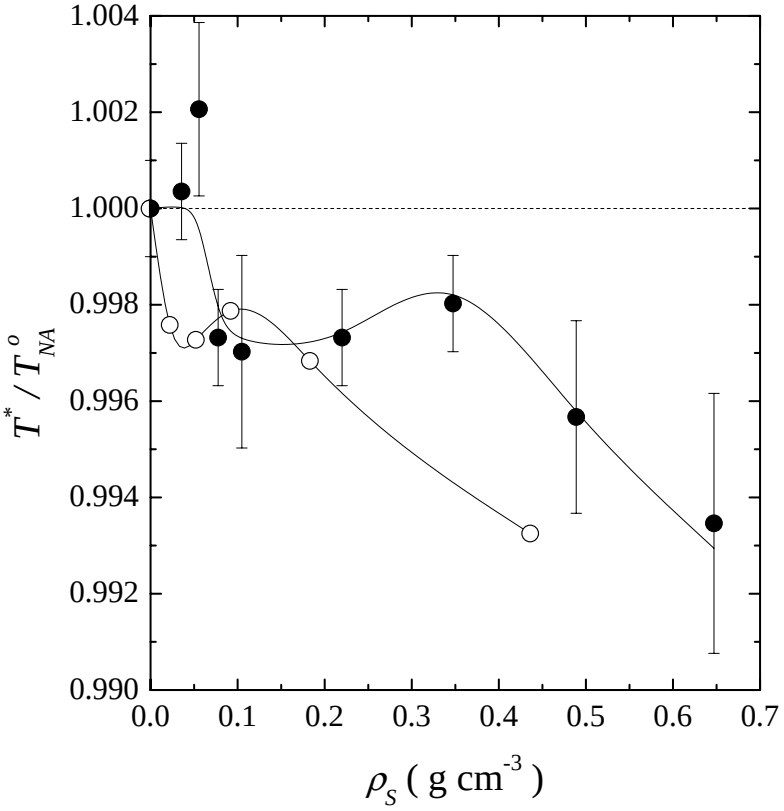

Figure 5.3. Dependence on ρ_S of the pseudo-transition *N-SmA* temperature, T^* scaled by the bulk value for $8OCB+SIL$ (solid circles, $T^o_{NA} = 339.52$ K) and $8CB+SIL$ (open circles, $T^o_{NA} = 306.97$ K) samples. Data for $8CB + SIL$ samples taken from Ref. [58]. The solid lines are guides to the eye.

samples. This is consistent with the evolution seen of T_{IN} shown in Fig. 4.4 and described above.

The nematic phase temperature range, $\Delta T_N = T_{IN} - T^*$, normalized by the bulk nematic range $\Delta T^o_N = T^o_{IN} - T^o_{NA}$, is shown in Fig. 5.4. While the individual transition temperature changes reflect the absolute stability limit of the nematic and smectic phases, ΔT_N reflects the relative stability of both phases. For $8CB + SIL$, a decrease of $\sim 1\%$ in ΔT_N was seen up to $\rho_S \approx 0.5$, corresponding to the the local maximum of $T_{IN}(\rho_S)$ and $T^*(\rho_S)$. This was originally thought to be scatter in the data of Ref. [58]. For $8OCB + SIL$ samples, a similar and far more pronounced 4% decrease in ΔT_N is seen from $\rho_S = 0.051$ to 0.220. This decrease in ΔT_N reflects a greater depression of T_{IN} than T^* and indicates that in this range of silica density, the disorder primarily effects nematic (orientational) ordering. Upon

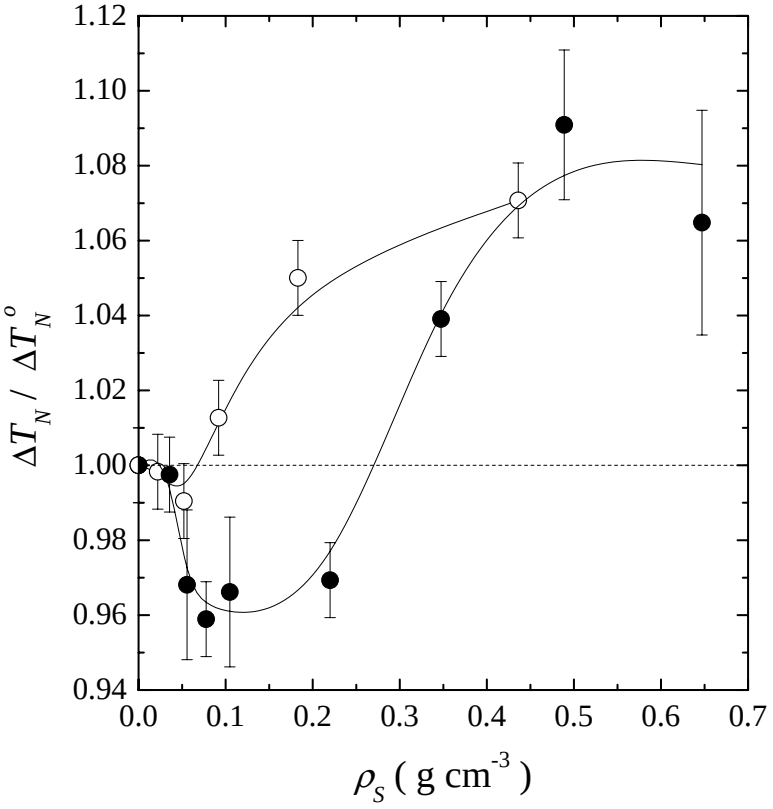

Figure 5.4. The nematic phase temperature range $\Delta T_N = T_{IN} - T^*$ scaled by the bulk value for $8OCB + SIL$ (solid circles, $\Delta T_N^o = 12.95$ K) and $8CB + SIL$ (open circles, $\Delta T_N^o = 7.01$ K) samples. Data for $8CB + SIL$ taken from Ref. [58]. The solid lines are guides to the eye.

further increasing ρ_S, the nematic range begins to increase and appears to saturate at an 8% increase similar to that seen in the $8CB + SIL$ system. This growth in the nematic range occurs because of the greater suppression of T^* relative to T_{IN} and so, reflects that above $\rho_S \gtrsim 0.2$, the effect of the silica gel is to mainly disorder smectic (1D-translational) ordering.

The *I-N* and *N-SmA* transition temperatures, the nematic temperature range $\Delta \mathrm{T}_{nem}$, the *N-SmA* transition enthalpy $\delta \mathrm{H}_{NA}$, and the heat capacity maximum $h_M \equiv \Delta \mathrm{C}_p^{max}(NA)$ are tabulated along with ρ_S in Table 5.1 for the $8OCB$+aerosil dispersions studied by calorimetry. The *N-SmA* pseudo-transition temperature T^*, and the transition enthalpy δH_{NA} can be normalized by the corresponding bulk values, T_{NA}^o and δH_{NA}^o respectively, in order to make quantitative comparison with the results for the previously studied $8CB$+aerosil system [58].

The *N-SmA* transition enthalpy, as determined from Eq. (5.5), for the $8OCB+SIL$ samples is sensitive to the changes in shape of the $\Delta C_p(NA)$ peak and complements the power-law analysis of the evolving critical behavior. Here, we take $\delta H^o_{NA} = 0.42$ J g^{-1} for our bulk $8OCB$ *N-SmA* transition enthalpy. These enthalpy results, again scaled by the pure liquid crystal value, are shown versus ρ_S in Fig. 5.2 for $8OCB + SIL$ and $8CB + SIL$ samples. Note that the same fractional change in the *N-SmA* enthalpy occurs for both $8OCB + SIL$s and $8CB + SIL$s as a function of ρ_S. Two ρ_S regimes are clearly evident. For $0 < \rho_S \lesssim 0.1$, there is a rapid drop in δH_{NA}, while for ρ_S values greater than ~ 0.1 the decrease is more gradual. For the $\rho_S = 0.647$ sample, δH_{NA} has nearly disappeared indicating that the *SmA* absolute stability limit must be near this aerosil density for $8OCB$ + aerosils.

Figure 5.5 depicts the normalized *N-SmA* pseudo-transition temperatures for $8OCB$+aerosils and those for $8CB$+aerosils taken from Ref. [58]. Here we take $T^o_{NA} = 339.52$ K for our bulk $8OCB$ *N-SmA* transition temperature. The estimated error bars shown represent the reproducibility of T^* found by repeating measurements on a few samples having the same ρ_S. Note that typically T^* for a given sample scan is known within ± 5 mK. The observed variation in T^* for a given ρ_S is likely due to the incomplete remixing by the method employed for the calorimetry sample preparation. For $8OCB + SIL$s, there is a slight increase in T^* up to $\rho_S = 0.051$ which is not understood. However, above this aerosil density, a sharp drop in T^* is observed on the order of that seen for the $8CB + SIL$ system. Also, the recovery and subsequent slower decrease in T^* for $\rho_S \gtrsim 0.1$ appears broader in ρ_S as compared to $8CB + SIL$. As seen in Fig. 5.5, the maximum recovery of T^* for $8OCB + SIL$ occurs at $\rho_S \approx 0.3$ as compared to ≈ 0.1 for $8CB$+SIL. The *I-N* transition temperatures track the same trend as was discussed in Sec. 4.2.3. (See Fig 4.4 and Table 5.1). Recall that the shape of ΔC_p(NA) for the 80CB+aerosil samples evolves in the same way as that for $8CB+SIL$ samples, having a critical behavior moving towards 3D-XY with increasing ρ_S then becoming smeared for $\rho_S \gtrsim 0.1$. The difference in the ρ_S dependence of T^* between these two systems then indicates that a liquid crystal specific mechanism, such as their relative elasticity, is playing a dominate role in determining the *N-SmA* transition temperature shift with silica concentration.

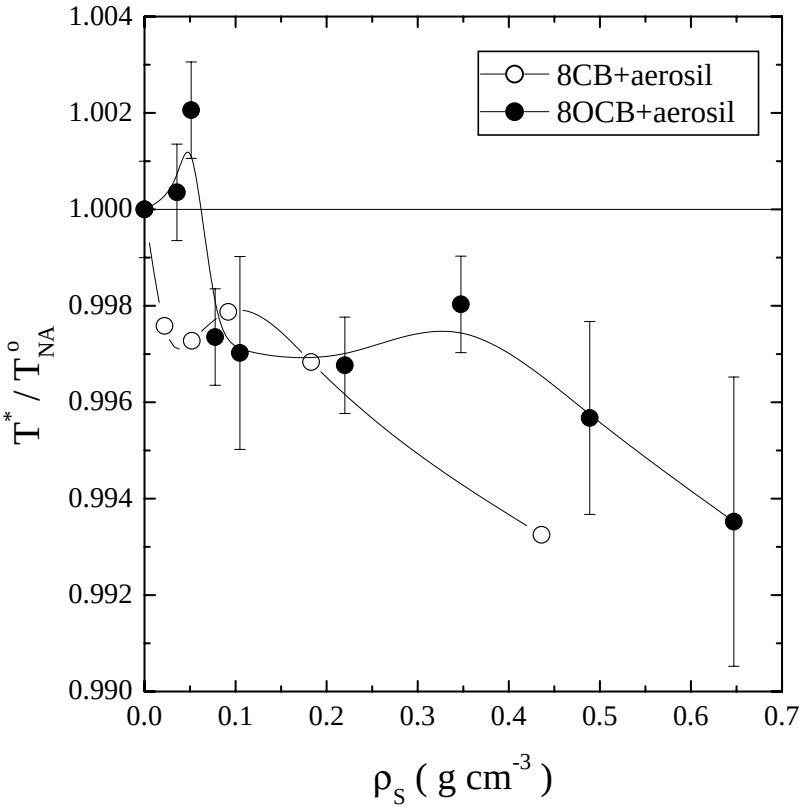

Figure 5.5. Dependence on ρ_S of the pseudo-transition *N-SmA* temperature, T* scaled by the pure $8OCB$ *N-SmA* transition temperature, $T^o_{NA} = 339.52$ K, for $8OCB$+aerosil samples. Also shown are T^*/T^o_{NA} for $8CB$+aerosil samples taken from Ref. [58] and uses $T^o_{NA} = 306.97$ K for pure bulk $8CB$ *N-SmA* transition temperature. The solid lines are guides to the eye.

The heat capacity maximum at the pseudo-transition is an indication of the finite-size effects that are inherent in such studies. Figure 5.6 depicts a log-log representation of the heat capacity maximum as a function of ρ_S for $8OCB$ and $8CB + SIL$ samples, where again the error bars indicate reproducibility. Since the mean distance between silica surfaces scales as ρ_S^{-1}, the construction presented in Fig. 5.6 should reveal a straight line having a slope equal to $\alpha/\nu_\parallel$ for finite-size scaling effects based on simple power-laws. For pure $8OCB$, $\alpha/\nu_\parallel = 0.28$ [20] whereas the slope for the $8OCB + SIL$ samples varies from 0.75 for $\rho_S < 0.1$ to 1.77 for $\rho_S > 0.1$. However, as described in detail for the $8CB + SIL$ system [59], corrections-to-scaling terms play a significant role and alter the expected finite-size behavior.

A more complete finite-size scaling (FSS) analysis should begin with the power-law form of the excess specific heat given in Eq. (5.6) and the power-law form describing the correlation length of the ordered phase taken as

$$\xi_{\parallel} = \xi_{\parallel o} t^{-\nu_{\parallel}}. \tag{5.7}$$

For smectic liquid crystals, the parallel correlation length is always larger than the perpendicular, and so our analysis uses this length scale for the definition of the minimum reduced temperature. Defining the maximum possible correlation length as ξ_M, one solves Eq. (5.7) for the *minimum* reduced temperature above T* as $t_m^+ = (\xi_M/\xi_{\parallel o})^{-1/\nu_{\parallel}}$. It is not possible to define a similar minimum reduced temperature below the transition since the critical correlation length behavior below T* is not known. Substituting t_m^+ into Eq. (5.6) gives the relationship for the heat capacity maximum h_M at the *N-SmA* transition as a function of the cutoff correlation length as

$$h_M = A^+ \left(\frac{\xi_M}{\xi_{\parallel o}}\right)^{\alpha/\nu_{\parallel}} \left(1 + D^+ \left(\frac{\xi_M}{\xi_{\parallel o}}\right)^{-\Delta_1/\nu_{\parallel}}\right) + B_c \,. \tag{5.8}$$

Because of the importance of corrections-to-scaling for the analysis of $\Delta C_p(NA)$, a log-log plot of $h_M - B_c$ versus ξ_M would not yield a straight line of slope $\alpha/\nu_{\parallel}$. The FSS effect on the *N-SmA* transition enthalpy is obvious since it involves replacing the singular $\Delta C_p(NA)$ peak between t_m^+ and t_m^- by h_M and thus decreasing the integral of $\Delta C_p(NA)$ over T.

Plotted on Fig. 5.6 are FSS trends given by Eq. (5.8) for 8CB+aerosil and 8OCB+aerosil samples using the *bulk N-SmA* 8CB and 8OCB critical parameters respectively and the mean distance between silica surfaces (mean void size) $l_o = 2/a\rho_S$, where a is the specific surface area, for the cutoff correlation length ξ_M. This closely follows the procedure laid out in Ref. [59]. The result for 8CB+aerosil samples are in very good agreement despite the change in the apparent critical behavior of the specific heat. However, this interesting result is not seen in the 8OCB+aerosil samples where the *bulk* finite-size scaling analysis is everywhere lower than that observed. Despite the uncertainty in the 8OCB+aerosil results, the agreement seen between FSS using the bulk critical parameters and the 8CB+aerosil samples must be regarded as accidental. Also, the change in

)

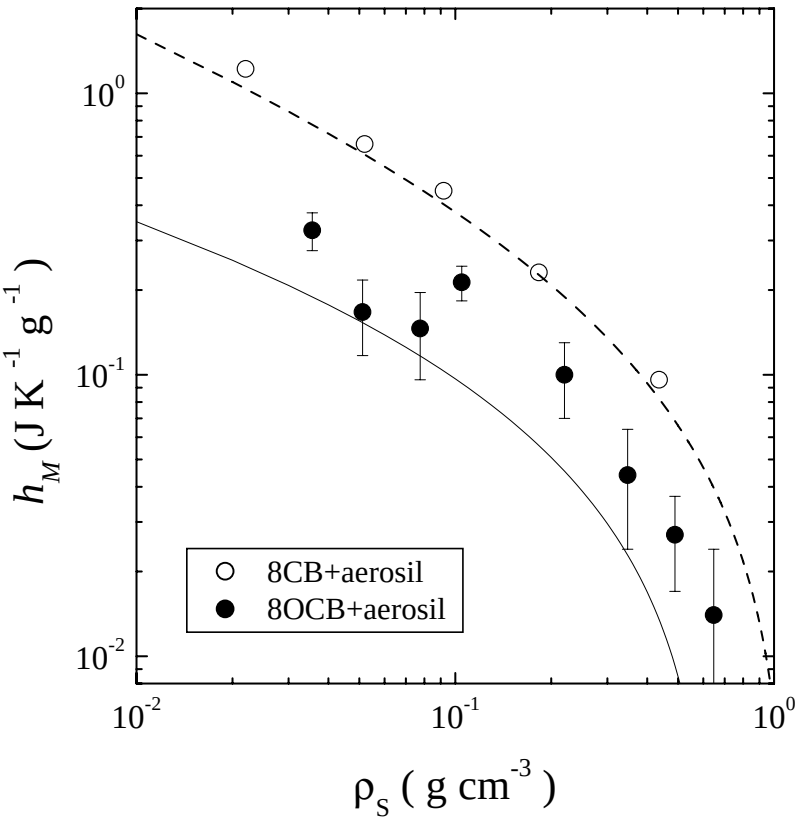

Figure 5.6. Behavior of the *N-SmA* heat capacity maximum $h_M = \Delta C_p^{max}(NA)$ at T* as a function of ρ_S for the $8OCB$+aerosil samples and for the $8CB$+aerosil samples studied in Ref. [58]. The dashed and solid line indicate a FSS model using the bulk critical parameters for the respective liquid crystal and the mean void size as the cutoff correlation length, $\xi_M = l_o$. See text for details.

shape of $\Delta C_p(NA)$ described by the changing fit parameters given in Table 5.2, is more important than FSS for the enthalpy variation with ρ_S as shown in Fig. 5.2.

5.2.2 X-Ray Scattering Results

High-resolution x-ray diffraction measurements were carried out on $8OCB$ samples having silica densities listed in Table 5.3 over the temperature range 353 to 315 K. Figure 5.7 shows the scattering intensity as a function of wave-vector transfer for three different aerosil densities. The displayed results are for the lowest temperature studied ($T^o_{NA} - 25$ K). The resolution width, determined from the profile of the straight-through beam, is indicated by a horizontal line. The addition of

ρ_S	a_2/σ_1^{LT}	$\xi_\parallel$	T*
0.025	–	–	340.02 ± 0.03
0.051	0.042 ± 0.010	3670 ± 10	340.04 ± 0.07
0.078	0.022 ± 0.010	3290 ± 10	339.81 ± 0.10
0.105	0.026 ± 0.007	2995 ± 10	336.06 ± 0.10
0.220	0.273 ± 0.056	965 ± 5	338.24 ± 0.06
0.347	0.429 ± 0.131	820 ± 5	337.67 ± 0.47
0.489	5.25 ± 1.82	410 ± 5	337.30 ± 1.61

Table 5.3. Sample parameters for seven $8OCB$+aerosil dispersions studied with x-rays. Shown are the densities ρ_S, the ratio of the random-field amplitude a_2 to the thermal amplitude σ_1 at low-temperatures in units of 10^{-5} Å^3; see text. The low-temperature parallel correlation lengths $\xi_\parallel$ are in Å, and the temperatures of the pseudo-transition T* are in Kelvin.

aerosil particles leads to peak broadening beyond the resolution limit of the instrument even at the lowest temperature studied. Unfortunately, at the lowest density studied ($\rho_S = 0.025$ g cm^{-3}), any peak broadening is unresolvable for the straight-through beam profile available. At higher densities of aerosils, the scattering peaks are broader than the resolution and thus smectic correlation lengths are finite even at the lowest temperatures. There is a clear qualitative change in the reflection profile with increasing density. The solid lines are fits to a model of the x-ray scattering structure factor, which will be discussed below.

For each aerosil density, the reflection lineshape evolves as the temperature is reduced. Figure 5.8 shows the x-ray scattered intensity as a function of wave-vector transfer at two temperatures at the same aerosil density. At high temperatures (e.g., 338 K), short range smectic fluctuations are evidenced by a broad peak in the scattered intensity. The reflection becomes narrower and sharper at lower temperatures. Again, the solid lines are the best fits with the model x-ray structure factor given below.

The x-ray structure factor for smectic thermal fluctuations has been studied extensively. The most commonly used expression is [94]

$$S^T(\mathbf{q}) = \frac{\sigma_\mathbf{1}}{\mathbf{1} + \xi_\parallel^\mathbf{2}(\mathbf{q}_\parallel - \mathbf{q_o})^\mathbf{2} + \xi_\perp^\mathbf{2}\mathbf{q}_\perp^\mathbf{2} + \mathbf{c}\xi_\perp^\mathbf{4}\mathbf{q}_\perp^\mathbf{4}} \ . \tag{5.9}$$

This is an anisotropic Lorentzian with a fourth-order correction, where $\xi_\parallel$ ($\xi_\perp$) is the correlation length parallel (perpendicular) to the smectic layers; q_o ($2\pi/d$, where

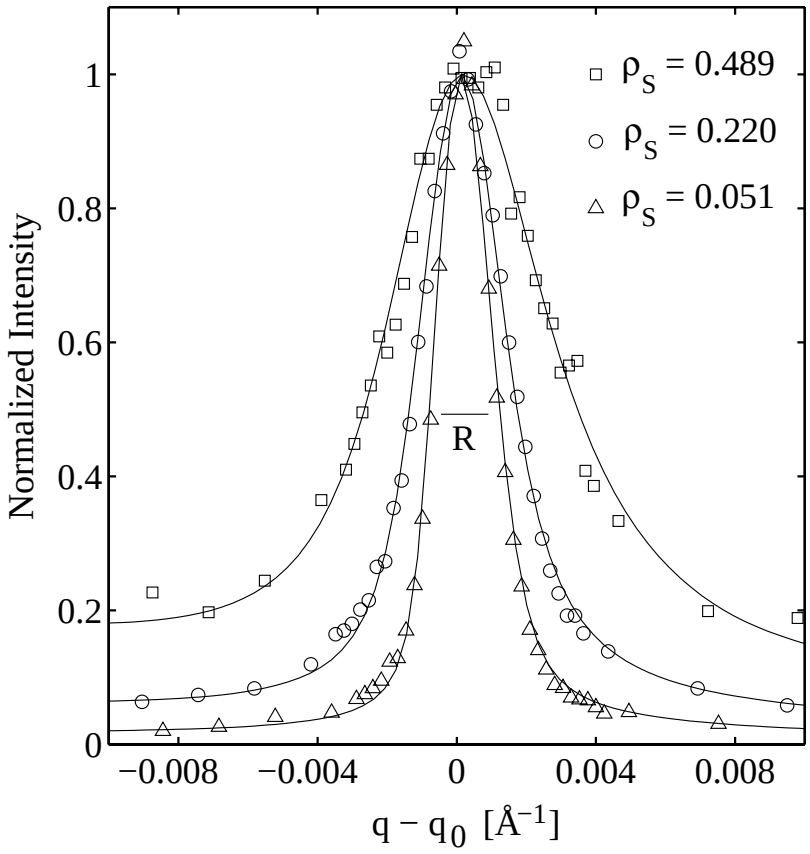

Figure 5.7. Normalized x-ray scattering intensity of $8OCB$+aerosil dispersions due to short-ranged smectic-A order at low temperatures (approx. $T^o_{NA} - 25$ K) as a function of wave-vector transfer. The broadening of the lineshape due to increasing disorder is evident. The solid lines through the data points are fits to a model of the x-ray scattering structure factor described in the text. The resolution was determined from the profile of the straight-through beam. The full width at half maximum intensity of the resolution function is indicated by the horizontal line labelled R. The value of q_o at such low temperatures is ~ 0.1998 Å^{-1} for all three samples.

d is the smectic layer thickness) is the wave-vector corresponding to the peak in the reflected intensity; σ_1 is related to the thermal fluctuation susceptibility; and c gives the scale of the fourth-order correction. The coefficient c has the value ~ 0.25 at high temperatures, hence the perpendicular profile is then a Lorentzian squared intensity distribution. The parameter c tends to 0 as the transition is approached. This lineshape has been used to analyze x-ray scattering from pure $8OCB$ and many other smectic liquid crystals. The reduced temperature dependence of the fourth-order correction and the ratio $\xi_\perp/\xi_\parallel$ are consequently well known for $8OCB$

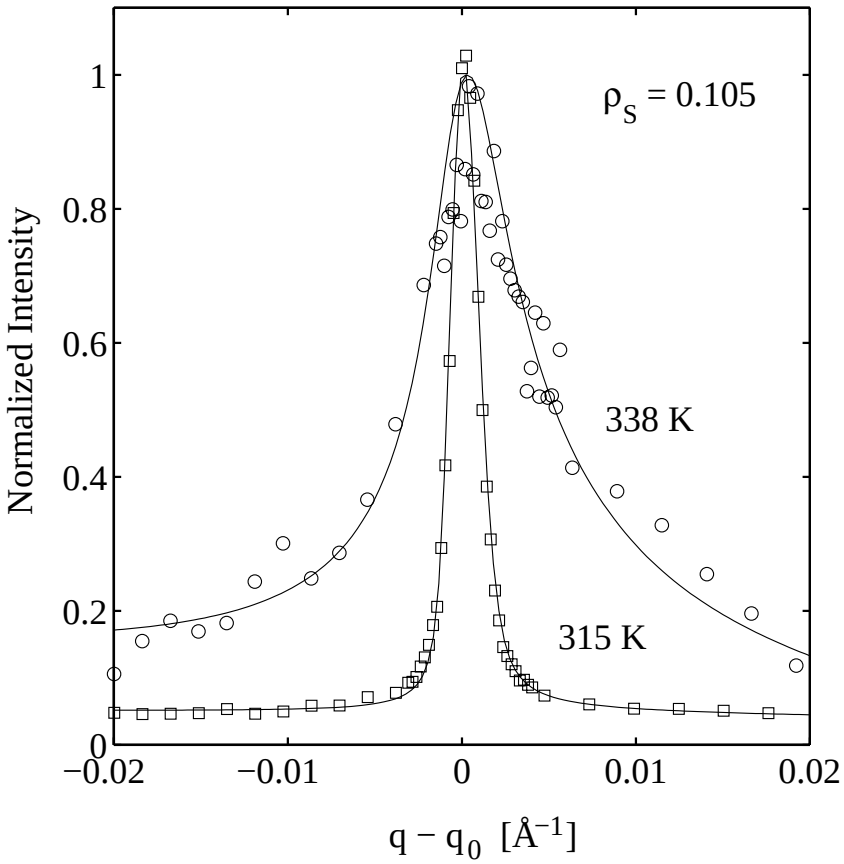

Figure 5.8. Normalized x-ray scattering intensity due to short-ranged smectic-A order for a typical 8OCB+aerosil dispersion with $\rho_S = 0.105$ as a function of wave-vector transfer. Open circles are for T = 338 K = T* − 1.88 K while open squares are for T = 315 K = T* − 24.5 K. There is a clear change in the lineshape as a function of temperature. Fits with the structure factor given in Eq. (5.14) to these data are shown as solid lines.

[62, 63].

The x-ray structure factor used to analyze the scattering from the 8OCB+aerosil dispersions is motivated by studies of random field magnets. A random field gives rise to fluctuations of the ordered state with a different wave-vector dependence than that for the thermal fluctuations. Theoretical and experimental studies [98, 93] support the idea that random-field spatial fluctuations behave as thermal fluctuations with the lower marginal dimensionality shifted up by two. This leads

to the structure factor

$$S^{RF}(\mathbf{q}) = \frac{\sigma_{\mathbf{2}}}{[\mathbf{1} + \xi_{\|}^{\mathbf{2}}(\mathbf{q}_{\|} - \mathbf{q_o})^{\mathbf{2}} + \xi_{\perp}^{\mathbf{2}}\mathbf{q}_{\perp}^{\mathbf{2}} + \mathbf{c}\xi_{\perp}^{\mathbf{4}}\mathbf{q}_{\perp}^{\mathbf{4}}]^{\mathbf{2}}} \ . \tag{5.10}$$

The denominator is the square of the thermal fluctuation denominator. The numerator σ_2 is related to the disconnected susceptibility. Smectic correlations in the $8OCB$+aerosil samples are influenced by both thermal and random field fluctuations. Aharony and Pytte [99] have shown that for a random field system the structure factor should have the low temperature scaling form

$$S(q, \xi) = \xi^d \overline{S}(q\xi) \ . \tag{5.11}$$

For smectic liquid crystal fluctuations, there are different correlation lengths in the directions parallel and perpendicular to the smectic layer normal. We assume by analogy with the isotropic result that the liquid crystal structure factor should have the scaling form

$$S(q_{\|}, \xi_{\|}, q_{\perp}, \xi_{\perp}) = \xi_{\|}\xi_{\perp}^2 \overline{S}(q_{\|}\xi_{\|}, q_{\perp}\xi_{\perp}) \ . \tag{5.12}$$

Comparison of this form to Eq. (5.10) leads to the conclusion that, for a random field system, the amplitude can be written as

$$\sigma_2 = a_2(\xi_{\|}\xi_{\perp}^2) \ , \tag{5.13}$$

where a_2 is the integrated area $\int S^{RF}(q)dq$ when c is small, as it is for $8OCB$+aerosil samples at low temperatures.

The total structure factor thus consists of two terms:

$$S(q) = S^T(q) + S^{RF}(q) \ . \tag{5.14}$$

The thermal structure factor dominates at high temperatures, while the random field structure factor dominates at low temperatures. There is a concurrent change in the reflection lineshape as the balance between these two structure factors changes. In order to compare this model with the data, it is necessary to perform

a powder average and then convolve the resulting lineshape with the resolution function. The powder average involves integrating over the random directions of the smectic domains. The resolution function is measured as the profile of the straight-through beam. The powder average procedure and the handling of the resolution function are discussed in detail in Ref. [76]

The powder average of the structure factor in Eq. (5.14) has been fitted to the measured wave-vector transfer dependence of the scattered intensity. The background intensity was taken to be a straight line

$$S^{Bk}(q) = Mq + C \ , \tag{5.15}$$

over the limited $q - q_o$ range of the smectic scattering. The free parameters over which the fit is optimized are M, C, q_o, $a_1(= \sigma_1/\xi_\parallel \xi_\perp^2)$, a_2, and $\xi_\parallel$. The values of $\xi_\perp(\xi_\parallel)$ and $c(\xi_\parallel)$ are assumed to retain the same behavior as they exhibit in pure $8OCB$ and so are taken here as functions of $\xi_\parallel$. This assumption is physically reasonable for the weak disorder imposed by the aerosil gel and was also used for the $8CB$+aerosil study [75]. An initial fitting of the data was made with all six parameters free. Subsequently, M and C were fixed at their average low-temperature values for each sample to remove any unphysical fit noise. The remaining four parameters; q_o, a_1, a_2, and $\xi_\parallel$, were then redetermined. The temperature and density dependence of q_o, σ_1, a_2, and $\xi_\parallel$ are discussed below. The low temperature limiting values of the parameters a_2/σ_1 and $\xi_\parallel$ are shown in Table 5.3. Examples of the correspondence between this structure factor and the measurements are given in Fig. 5.7 for different densities, and in Fig. 5.8 for different temperatures. The agreement between the data and the model is observed to be good.

Other forms for the background were also tried. The resulting values for the fit parameters q_o, a_1, a_2, and $\xi_\parallel$ were very similar. However, the straight-line given by Eq. (5.15) yielded the lowest χ^2 values and thus has been used throughout this analysis.

The peak position q_o and its weak temperature dependence displays little variation between samples for all densities except the highest studied. For $\rho_S = 0.489$, q_o is slightly but consistently lower (by ~ 0.0007 Å^{-1}). The robust value of the peak position for low disorder is surprising. Pure $8OCB$ exhibits a partial

bilayer smectic-A phase, hence the ordering wave-vector is incommensurate with the molecular length. Since the balance of interactions in a liquid crystal system is likely to be altered by the silica. it might have been anticipated that the peak position would change for even the lowest ρ_S sample. The independence of q_o(T) on ρ_S up to 0.347 demonstrates that the partial bilayer smectic in $8OCB$+aerosil dispersions, although not long range, has the same local packing as in the pure $8OCB$.

Figure 5.9 presents the results for the peak amplitudes. The temperature dependence of the random-field fluctuation term given in Eq. (5.10) is equivalent to the development of a Bragg peak in a pure liquid crystal. The integrated intensity of $S^{RF}(q)$ can be equated with the order parameter squared for the transition in a random-field. The parameter a_2 is close to this integrated intensity, which is a_2 multiplied by a c-dependent correction. The temperature dependence of the S^{RF} integrated intensity is shown in Fig. 5.9(a) for three $8OCB$+aerosil samples. The values of the pseudo-transition temperature T* is taken as the onset temperature for the random-field contribution to the structure factor and are given in Table 5.3.

The thermal fluctuation term given in Eq. (5.9) would also occur in a pure liquid crystal. It is assumed that at high temperatures the behavior is unchanged, only being modified as the correlation lengths become comparable to the void sizes of the medium. The observed behavior of σ_1 is shown in Fig. 5.9(b). It was not possible to make sufficient measurements to fully explore the high temperature behavior without subjecting the sample to excessive x-ray beam damage. Three densities are shown in Fig. 5.9(b), and in general the amplitude rises to a maximum near the pseudo-transition temperature before settling to a constant low temperature plateau value. The maxima near T* are perhaps the remnants of the divergent susceptibility at the pure *N-SmA* transition or a consequence of the turning on of the random-field contribution.

At high temperatures, the scattering is dominated by the thermal fluctuations while the random field fluctuations dominate as T falls below T*. It has been shown in Ref. [76] that the temperature dependence of a_2 can be represented by an effective power-law $a_2 \sim (\mathrm{T}^* - \mathrm{T})^x$, where T* marks the temperature above which the integrated intensity of the random-field component S^{RF} is essentially zero, as shown in Fig. 5.9(a). With both $8OCB$+aerosil and $8CB$+aerosil [75, 76]

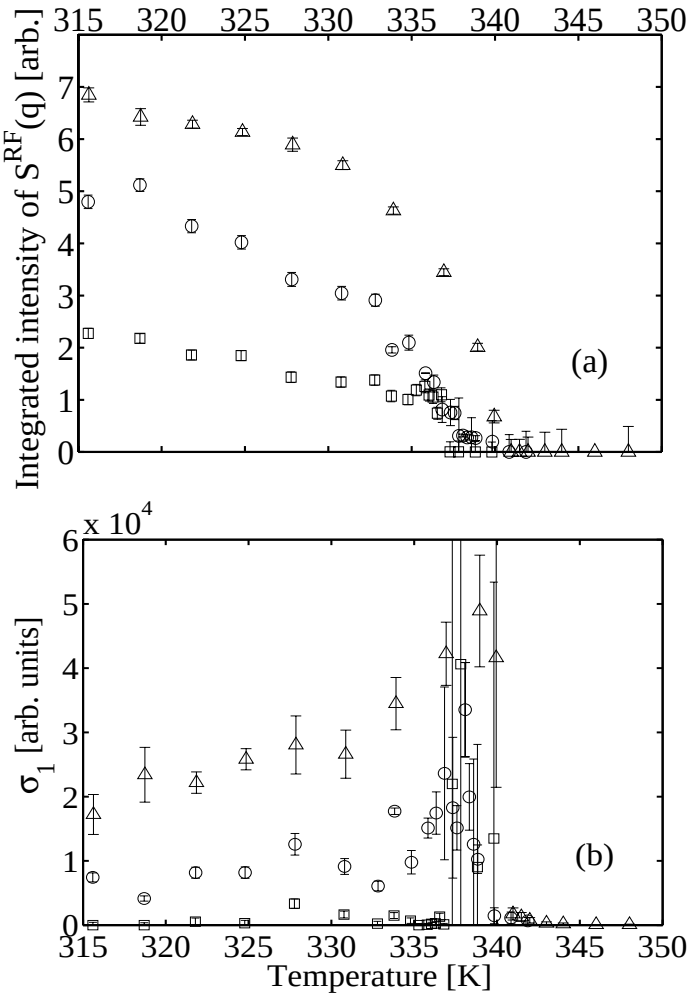

Figure 5.9. Plots showing intensities as a function of temperature. (a) Integrated intensity of the random field term $S^{RF}(\mathbf{q})$ for $\rho_S = 0.051$ (open triangles), 0.220 (open circles), and 0.489 (open squares); this can be thought of as the order parameter squared for this pseudo-transition. (b) The amplitude of the thermal contribution to the scattering. The peak near T* is perhaps the remnant of the diverging susceptibility for the pure system. The $\rho_S = 0.220$ values have been multiplied by 2 and the $\rho_S = 0.489$ values have been multiplied by 20 for clarity.

studies, the number of scans of scattered x-ray intensity was kept limited in order to minimize damage to the sample. For the $8CB$+aerosil samples, it was possible to make measurements down to $\sim$ 15 K below T* and hence the data are somewhat focused around the pseudo-transition. With the $8OCB$+aerosil samples, x-ray measurements were made down to $\sim$ 23 K below T*. This has the advantage that the lineshape can be characterized well below the pseudo-transition, and the

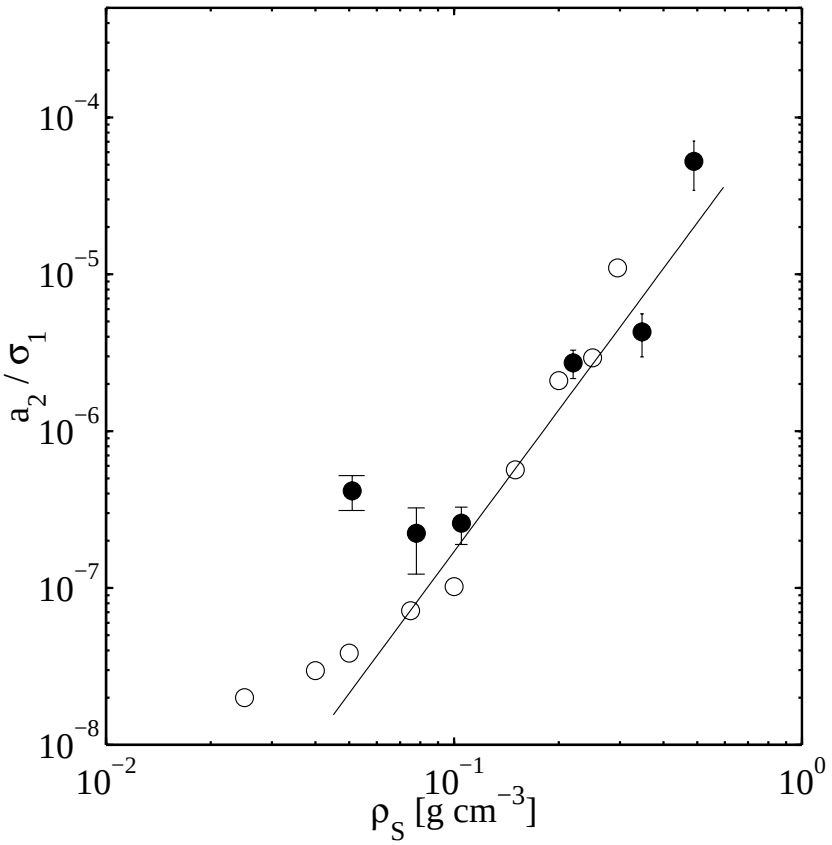

Figure 5.10. Variation of a_2/σ_1^{LT} for $8OCB$+aerosil as a function of ρ_S. The full circles are for $8OCB + SIL$ while the open circles are for $8CB + SIL$. For $8OCB$ a_2 and σ_1 are the average values for $T < 320K$, i.e., $\Delta T = T - T^* \sim -21K$. The data points show larger scatter but are roughly consistent with results for $8CB$+aerosil [76] and with expectations for a random field system if the random field strength $h \sim \rho_S$. The slope of the solid line is 3.

disadvantage that there are fewer scans around the pseudo-transition region itself. As a result, the present $8OCB$+aerosil data are too sparse to yield a good set of values for the exponent x as a function of ρ_S; however, they can be used to determine T* values which are given in Table 5.3.

The ratio of the amplitude of the random-field term to the thermal amplitude far below T* is predicted to be related to the variance, Δ, of the strength of the random-field h where $\Delta = |h|^2$ [99]. It has been shown [59] that the relationship can be written as $a_2/\sigma_1 \sim \Delta^3$. Note that the quantity a_2/σ_1 is independent of the normalization of the intensities. The low-temperature ratio a_2/σ_1 is taken where both parameters are their average values for T $<$ 320 K, i.e. ΔT = T -

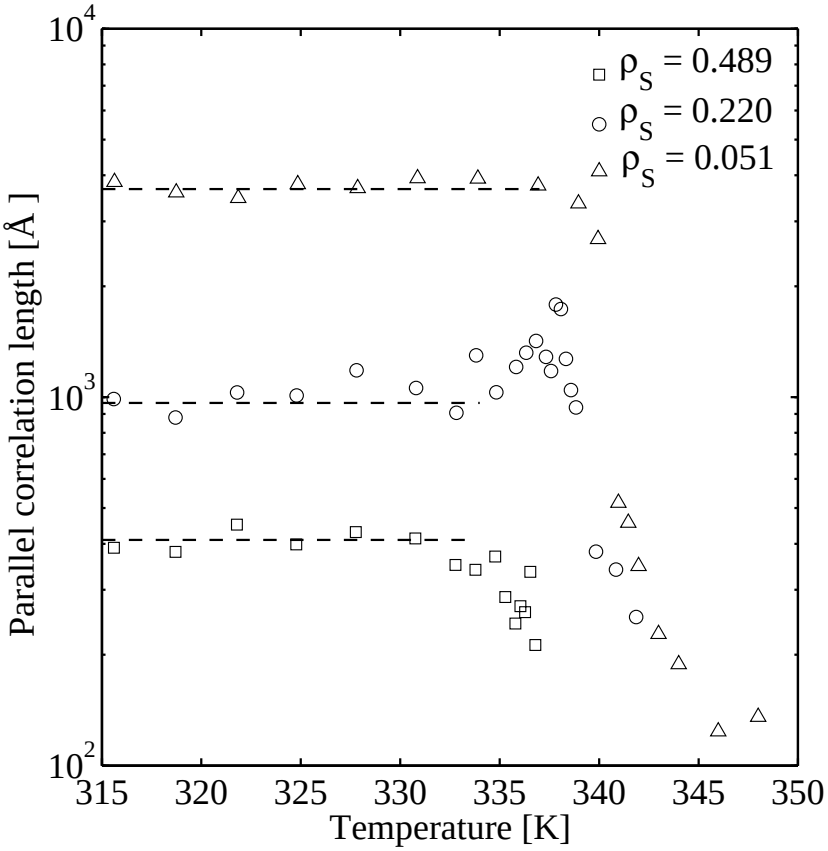

Figure 5.11. Parallel correlation lengths for smectic order as a function of temperature for three $8OCB$+aerosil samples. The values saturate rather than diverge as would be expected for a pure liquid crystal. Four points have been suppressed for the highest density at high temperature, where poor statistics gave rise to substantial errors.

$T^* \sim -21$ K. These ratio values, given in Table 5.3 and displayed in Fig. 5.10, show qualitative agreement with the relation $a_2/\sigma_1 \sim \rho_S^3$.

The nematic to smectic-A transition is characterized by two correlation lengths: one parallel and one perpendicular to the nematic director. Only the parallel smectic correlation length $\xi_\parallel$ was taken as a free parameter; the relationship between $\xi_\parallel$ and $\xi_\perp$ was assumed to be the same as that for the pure $8OCB$ liquid crystal. The fit $\xi_\parallel$ values for three densities are shown in Fig. 5.11. The correlation length is observed to grow sharply on cooling towards T^*, but rather than diverging as in a pure material, the value saturates and remains roughly constant at low temperatures. The saturation value decreases monotonically with increasing ρ_S similar to that observed for the $8CB$+aerosil system [75, 76]. For high density samples,

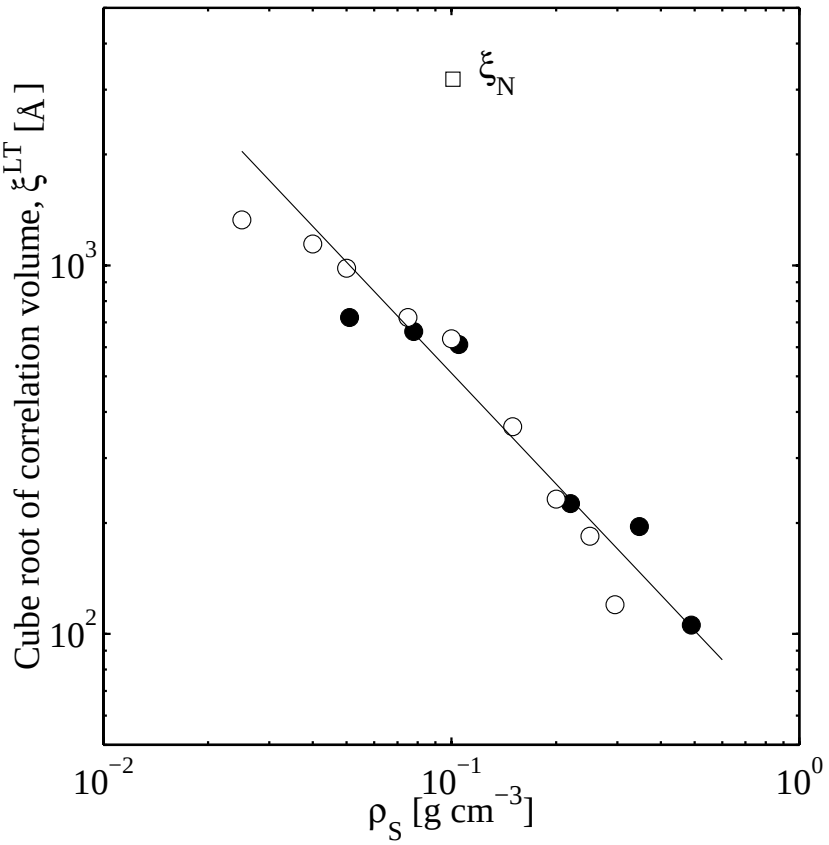

Figure 5.12. Plot of the low-temperature mean correlation length for smectic order $\bar{\xi}^{LT} = (\xi_{\|}\xi_{\perp}^2)^{1/3}$ as a function of ρ_S. The full circles are for $8OCB+SIL$, while the open circles are for $8CB + SIL$ [59]. The power-law shown by the line, which is $\bar{\xi}^{LT} \sim \rho_S^{-1}$, is expected for a random field system if $h \sim \rho_S$. The $\rho_S = 0.025$ reflection profile is the same width as the resolution function and no meaningful smectic correlation length can be obtained for that sample. The open square is the nematic correlation length ξ_N for $8CB + SIL$ [56].

where the scattering intensity was smallest, there was occasional difficulty extracting an unambiguous correlation length near T*. This can be observed in Fig. 5.11 as the slight peak for $\xi_{\|}$ close to T* for the $\rho_S = 0.220$ sample; the associated error bars (not shown) for the correlation lengths are large. The equivalent feature for the $\rho_S = 0.486$ g cm^{-3} sample has been removed from Fig. 5.11 for clarity. The average low temperature (below 323 K) $\xi_{\|}$ values are listed for each aerosil density in Table 5.3 and are shown as dashed lines in Fig. 5.11. Many models of the effects of disorder on phase transition behavior apply to systems where the correlation volume is isotropic. In order to make quantitative comparisons we as-

sume that the cube root of the correlation volume gives the extent of *SmA* order. The values $\bar{\xi}^{LT} = (\xi_{\parallel}\xi_{\perp}^2)^{\frac{1}{3}}$ have been plotted in Fig. 5.12. With the exception of the $\rho_S = 0.025$ sample, the dependence of $\bar{\xi}^{LT}$ on ρ_S can be well described by the power-law $\bar{\xi}^{LT} \sim \rho_S^{\zeta}$ with the exponent $\zeta = -0.9 \pm 0.1$ in good agreement with previous measurements on $8CB$+aerosil [76, 59].

5.3 *N-SmA* Transition in $\bar{8}$S5

The present section focusses on the effect of QRD induced by a nano-colloidal dispersion of hydrophilic type-300 aerosil forming a mass-fractal gel within the liquid crystal 4-*n*-pentylphenylthiol-4'-*n*-octyloxybenzoate ($\bar{8}$S5). This study closely follows the reported x-ray studies of Ref. [100]. High-resolution calorimetry has been

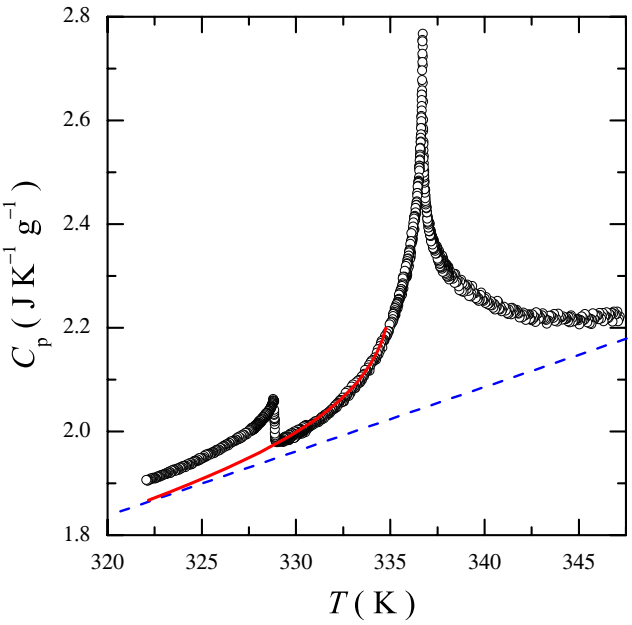

Figure 5.13. The specific heat of bulk $\bar{8}$S5 on cooling spanning the nematic, smectic-*A*, and smectic-*C* phases. The dashed line represents the linear C_p(background) used to extract the excess C_p associated with the *N-SmA* transition, $\Delta C_p(NA)$. The solid line represents the low-temperature wing of the *N-SmA* transition and is used to extract the excess C_p associated with the *SmA-SmC* transition, $\delta C_p(AC)$.

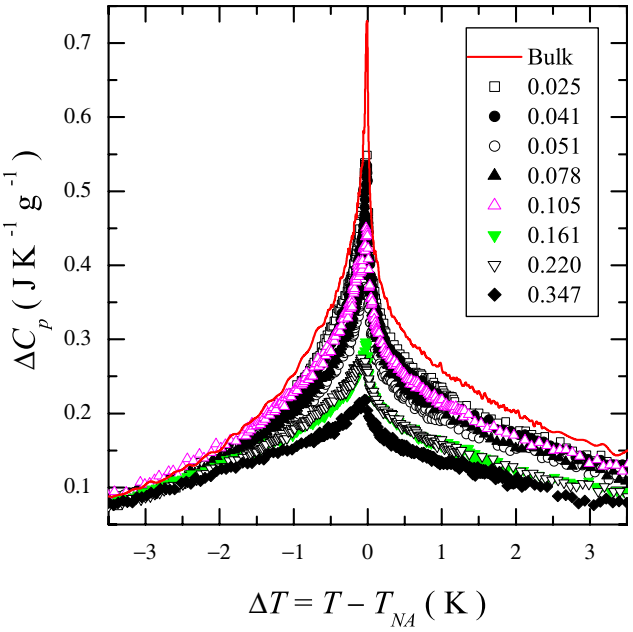

Figure 5.14. Excess specific heat ΔC_p of the *N-SmA* transition ±3.5 K about T_{NA} for bulk $\bar{8}$S5 and $\bar{8}$S5+aerosil samples. The inset lists the ρ_S for each data set shown. The temperature range shown corresponds approximately to $\pm 10^{-2}$ width in reduced temperature.

carried out on these $\bar{8}$S5+aerosil dispersions as a function of aerosil concentration and temperature spanning the smectic-*C* to nematic phases. This liquid crystal possesses two continuous XY phase transitions of interest. The first is a fluctuation dominated nematic to smectic-*A* characterized by a heat capacity exponent $\alpha \lesssim 0$. The critical character of the *N-SmA* transition remains unchanged with the introduction of the quenched random disorder, while its enthalpy and heat capacity maximum decreases in a manner consistent with finite-size scaling without any obvious crossover from soft to stiff gel seen on other *LC*+aerosil systems. The stability of the heat capacity critical behavior for this system with QRD represents the strictest test yet of the Harris criteria. The second is a mean-field Landau tricritical smectic-*A* to smectic-*C* phase transition which will be described in section 6.1.

The specific heat on cooling for a bulk sample of $\bar{8}$S5 is shown in Fig. 5.13.

Clearly visible are the XY-like *N-SmA* phase transition at 336.71 K and a Landau mean-field *SmA-SmC* at 328.82 K. These are in good agreement with Ref. [65]. The excess specific heat due to the *N-SmA* transition ΔC_p for the bulk and *LC*+aerosil samples is obtained by subtracting from the specific heat C_p a linear background as

$$\Delta C_p(NA) = C_p - C_p(\text{background}) \ , \tag{5.16}$$

where C_p(background) is shown as the dashed line in Fig. 5.13. The resulting $\Delta C_p(NA)$ for all samples studied are shown in Fig. 5.14 over a ± 3.5 K temperature range about T_{NA}.

The fluctuation dominated *N-SmA* transition enthalpy may be sensibly defined as

$$\delta H_{NA} = \int \Delta C_p dT \ , \tag{5.17}$$

where consistent limits of the integration of ± 5 K about T_{NA} were used for all samples. The relevant thermal characteristics for both phase transitions of $\bar{8}$S5+aerosils as a function of ρ_S are given in Table 5.4.

As seen in Fig. 5.14, the *N-SmA* C_p peak remains sharp for all aerosil densities

ρ_S	l_o	T_{NA}	T_{AC}	ΔT_A	δH_{NA}	h_M	δC_{AC}^{Step}
0	∞	336.626	329.009	7.617	2.136	0.726	0.044
0.025	2636	336.073	328.836	7.237	1.985	0.541	0.043
0.041	1636	336.524	329.136	7.388	1.897	0.530	0.034
0.051	1303	336.315	329.124	7.191	1.780	0.377	0.025
0.078	859	336.519	329.527	6.992	1.834	0.487	0.032
0.105	636	336.676	329.210	7.466	1.952	0.444	0.027
0.161	414	336.573	329.456	7.117	1.573	0.302	0.014
0.220	303	336.865	329.915	6.950	1.561	0.284	0.013
0.347	192	336.505	329.621	6.884	1.404	0.231	0.003

Table 5.4. Summary of the calorimetric results for $\bar{8}$S5+aerosil samples. Shown are the conjugate silica density (ρ_S in grams of aerosil per cm^3 of $\bar{8}$S5), the mean-void length within the gel in Å, the *N-SmA* (T_{NA}) and the *SmA-SmC* (T_{AC}) phase transition temperatures, and the smectic-A temperature range ($\Delta T_A = T_{NA} - T_{AC}$) all in kelvins and averaged between heating and cooling scans. These are followed by similarly averaged enthalpy (δH_{NA}) in J g^{-1} and specific heat maximum $h_M \equiv \Delta C_p^{max}$ in J K^{-1} g^{-1} values for the *N-SmA* phase transition. The final column tabulates the specific heat step in J K^{-1} g^{-1} of the *SmA-SmC* phase transition δC_{AC}^{Step} averaged between heating and cooling scans and taken as the value of the excess specific heat -6 K below T_{AC}.

up to the maximum studied of $\rho_S = 0.347$, with no abrupt truncation marking a transition from soft to stiff gel behavior seen in $8CB$+aerosil and $8OCB$+aerosil systems [58, 81]. The $\Delta C_p(NA)$ wings on both sides of the transition decrease with increasing ρ_S in contrast with that found for $8CB$+aerosils, which found significant reduction of the high-temperature $\Delta C_p(NA)$ wing [58]. Qualitatively, the $\Delta C_p(NA)$ peak shape remains remarkably stable with increasing ρ_S. For the $\bar{8}$S5+aerosil system, the most striking effect of the aerosils is the strong decrease in the heat capacity maximum at the transition, $h_M = \Delta C_p^{max}(NA)$, and the transition enthalpy δH_{NA} with increasing ρ_S. In addition, the evolution of $T_{NA}(\rho_S)$ also displays very little sensitivity to the aerosils even when the aging of the $\bar{8}$S5 is taken into account.This is in stark contrast to the non-monotonic downward shifts found for nearly all other LC+aerosil systems [58]. See Table 5.4.

5.3.1 The XY-like *N-SmA* scaling analysis

The shape of the experimental $\Delta C_p(NA)$ data as a function of aerosil content is characterized by a traditional power-law form [20] in terms of the reduced temperature t given by Eq (5.6) where the critical behavior as a function of reduced temperature t is characterized by an exponent α, amplitudes $A^{\pm}$ above and below the transition, a critical background term B_c, and corrections-to-scaling terms having an amplitude $D^{\pm}$ and exponent $\Delta_1 \simeq 0.5$. An increasing temperature gap of excluded data about the $\Delta C_p(NA)$ peak with increasing ρ_S was required to perform the nonlinear least-squares fitting. These fit results for the sets of heating and cooling scans for bulk $\bar{8}$S5 and $\bar{8}$S5+aerosil are presented in Tables 5.5 and 5.6, respectively. In addition to fits with the effective critical exponent α_{eff} free, fits were also performed with α_{eff} fixed to the 3D-XY value of $\alpha_{\rm XY} = -0.013$. The bulk $\bar{8}$S5 results are of good quality for both heating and cooling and consistently give a very small and negative α_{eff} that is not significantly different from fixing α_{eff} to $\alpha_{\rm XY} = -0.013$ as indicated by χ^2_ν. This indicates that the *N-SmA* critical heat capacity for the bulk LC behaves essentially as a clean XY transition consistent with the literature [101, 58]. As ρ_S increases, the fits for both heating and cooling are all of good quality even up to the highest density studied. These fits show that the critical character of the *N-SmA* transition remains unchanged for

ρ_S	T_C	α_{eff}	B_C	A^+	A^-	D^+	D^-	$t_{min} \times 10^{-5}$	χ^2_ν
0	335.220	-7×10^{-5}	1023.600	-1023.760	-1023.630	0.0002	0.0022	+1.80/-12.3	1.266
	335.222	[-0.013]	6.053	-6.260	-6.122	0.0026	0.3712		1.319
0.025	334.712	-1×10^{-4}	536.893	-536.971	-536.845	0.0007	0.0045	+3.50/-29.9	1.073
	334.711	[-0.013]	4.757	-4.880	-4.741	0.0450	0.5234		1.027
0.041	335.111	-1×10^{-4}	383.615	-383.643	-383.536	0.0016	0.0060	+2.56/-14.2	1.287
	335.110	[-0.013]	4.124	-4.194	-4.076	0.1117	0.5715		1.307
0.051	334.938	-2×10^{-4}	154.089	-154.083	-154.025	0.0045	0.0086	+11.4/-49.2	1.134
	334.937	[-0.013]	3.228	-3.249	-3.186	0.1954	0.4153		1.137
0.078	335.123	-1×10^{-4}	376.628	-376.688	-376.614	0.0010	0.0036	+3.08/-14.9	1.163
	335.123	[-0.013]	4.049	-4.146	-4.064	0.0628	0.3348		1.183
0.105	335.297	-1×10^{-4}	259.368	-259.267	-259.171	0.0049	0.0095	+3.63/-19.3	1.076
	335.297	[-0.013]	2.767	-2.698	-2.593	0.4513	0.9716		1.084
0.161	335.162	-7×10^{-4}	18.744	-18.608	-18.580	0.0655	0.0615	+5.67/-42.3	1.036
	335.161	[-0.013]	1.335	-1.212	-1.181	1.0162	0.9862		1.037
0.220	335.498	-4×10^{-4}	10.314	-10.099	-10.048	0.1651	0.1875	+3.59/-57.5	1.004
	335.496	[-0.013]	0.630	-0.428	-0.373	3.9745	5.2388		1.004
0.347	335.145	-6×10^{-4}	6.892	-6.724	-6.703	0.1839	0.1400	+0.27/-85.1	1.056
	335.144	[-0.013]	0.573	-0.414	-0.391	3.0646	2.4651		1.056

Table 5.5. Heating scan summary of the results of fitting Eq. (5.6) to the excess specific heat peak ΔC_p of the *N-SmA* phase transition on $\bar{8}$S5+aerosil samples. The transition temperature T_C is given in kelvins, while the parameters B_C and $A^\pm$ are given in J K^{-1} g^{-1}. The parameters $D^\pm$ are dimensionless. All scans were fit from $t_{max} = 10^{-2}$ to $\pm t_{min}$. All parameters were free to vary in the fit except when the exponent was fixed to $\alpha_{\rm XY} = -0.013$ (denoted by the square brackets).

$\bar{8}$S5+aerosil for all ρ_S even above the $\rho_S = 0.1$ where previous studies found no critical behavior [ref]. Apparent from the fits are that the increasing temperature gap ($\pm t_{min}$) is dominated by rounding on the low-temperature side of the $\delta C_p(NA)$ peak.

The finite-size scaling (FSS) analysis follows that of reference [59] by using the correlation length power-law to equate the cut-off length scale (maximum correlation length) ξ_M to a minimum reduced temperature as given by Eq (5.7).

The finite-size induced rounding of the transition is estimated, since the Eq. (5.7) is defined only for $T > T^*$, in terms of the minimum reduced temperature on the

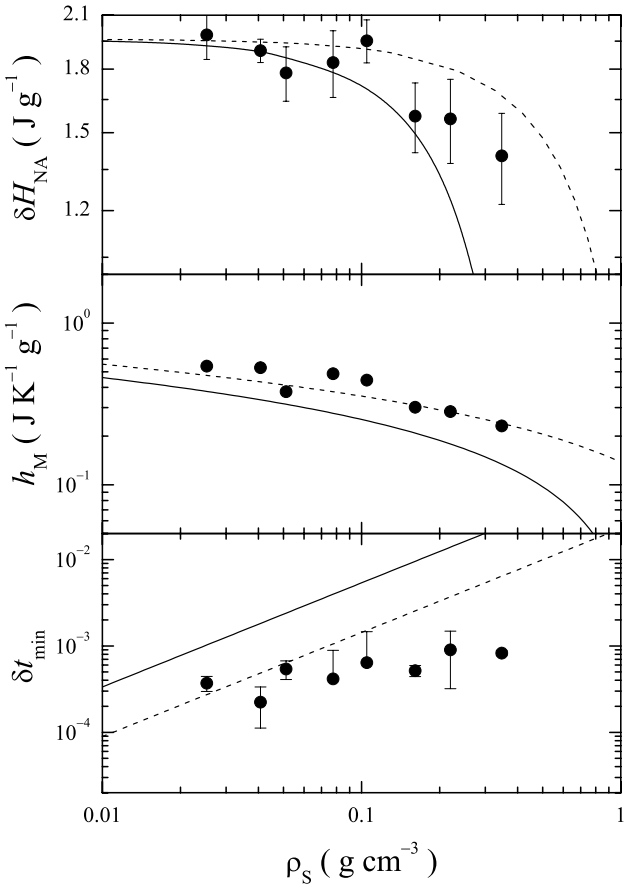

Figure 5.15. Finite-size scaling analysis of the *N-SmA* phase transition in $\bar{8}$S5+aerosil (solid circles) on log-log scales. Top Panel: Transition enthalpy δH_{NA}. Middle Panel: Excess specific heat maximum $h_M = \Delta C_{NA}^{max}$. Bottom Panel: Transition rounding in reduced temperature $\delta t_{min} = |t_{min}^-| + |t_{min}^+|$. The bulk finite-size scaling predictions are given by Eqs. (5.8) and (5.18) where the mean-void length l_o is used as the cut-off length scale (solid lines) or $3l_o$ (dashed lines).

high-temperature side of the transition t_m^+, as given by the form

$$\delta T^*/T^* \approx 2t_m^+ = 2\left(\frac{\xi_M}{\xi_{\|o}}\right)^{-1/\nu_\|} = 2\left(\frac{\xi_{\|o}}{2n}a\rho_S\right)^{1/\nu_\|} , \tag{5.18}$$

where the cut-off length scale is written in terms of n, the number of mean-void lengths l_o. The heat capacity maximum at the transition h_M is given by substituting t_m^+ into Eq. (5.16) and is also explicitly defined for the $T > T^*$. The explicit form for h_M is given by Eq (5.8).

Finally, the FSS transition enthalpy δH_{NA} is determined by using t_m^+ to truncate the integration of Eq. (5.16) both above and below the transition T^*.

Plotted on Fig. 5.15 are FSS trends for the *N-SmA* transition of $\bar{8}$S5+aerosil samples using the *bulk N-SmA* $\bar{8}$S5 critical parameters. Two choices for the cut-off length scale are shown. The first choice uses the mean distance between silica surfaces (mean void size) $l_o = 2/a\rho_S$, where a is the specific surface area, for the cutoff correlation length ξ_M. The second choice allows ξ_M to vary as some multiple of l_o, i.e. $\xi_M = nl_o$. The results for $\delta T^*/T^*$, h_M, and δH_{NA} for $\bar{8}$S5+aerosil samples are in very good agreement using the second choice of $\xi_M \equiv 3l_o$, which closely matches the measured saturated smectic correlation length [100].

ρ_S	T_C	α_{eff}	B_C	A^+	A^-	D^+	D^-	$t_{min} \times 10^{-5}$	χ^2_ν
0	335.198	-7×10^{-5}	1047.600	-1047.800	-1047.670	-0.0001	0.0019	+3.42/-9.91	1.463
	335.197	[-0.013]	6.565	-6.826	-6.688	-0.0499	0.2870		1.532
0.025	334.632	-1×10^{-4}	474.449	-474.466	-474.327	0.0012	0.0060	+7.86/-32.8	1.159
	334.630	[-0.013]	4.422	-4.484	-4.334	0.0956	0.6721		1.176
0.041	335.108	-3×10^{-4}	141.506	-141.494	-141.395	0.0056	0.0167	+4.37/-23.5	1.203
	335.108	[-0.013]	3.844	-3.868	-3.760	0.1782	0.6412		1.207
0.051	334.845	-1×10^{-4}	216.789	-216.692	-216.619	0.0047	0.0091	+11.0/-36.4	1.134
	334.843	[-0.013]	2.611	-2.541	-2.462	0.3824	0.8130		1.138
0.078	335.057	-2×10^{-4}	195.069	-195.050	-195.018	0.0050	0.0069	+32.6/-32.7	1.188
	335.055	[-0.013]	3.800	-3.809	-3.775	0.2461	0.3545		1.192
0.105	335.179	-0.0043	11.848	-11.888	-11.823	0.0425	0.1152	+37.0/-68.2	1.145
	335.178	[-0.013]	4.239	-4.301	-4.232	0.1061	0.3208		1.145
0.161	335.123	-4×10^{-4}	48.578	-48.455	-48.427	0.0192	0.0211	+16.4/-39.1	1.151
	335.121	[-0.013]	1.647	-1.538	-1.508	0.6025	0.6853		1.152
0.220	335.458	-3×10^{-4}	33.646	-33.468	-33.415	0.0363	0.0481	+19.7/-99.6	1.032
	335.455	[-0.013]	1.205	-1.043	-0.985	1.1714	1.6754		1.032
0.347	335.14	-3×10^{-4}	9.953	-9.734	-9.706	0.1367	0.1229	+5.65/-74.2	1.129
	335.14	[-0.013]	0.332	-0.119	-0.088	11.6406	14.1668		1.129

Table 5.6. Cooling scan summary of the results of fitting Eq. (5.6) to the excess specific heat peak ΔC_p of the *N-SmA* phase transition on $\bar{8}$S5+aerosil samples. The transition temperature T_C is given in kelvins, while the parameters B_C and $A^\pm$ are given in J K^{-1} g^{-1}. The parameters $D^\pm$ are dimensionless. All scans were fit from $t_{max} = 10^{-2}$ to $\pm t_{min}$. All parameters were free to vary in the fit except when the exponent was fixed to $\alpha_{XY} = -0.013$ (denoted by the square brackets).

5.4 *N-SmA* Transition in $CCN47$

The *N-SmA* transition in $CCN47$ is in contrast to what might be expected from McMillan's theory [16] a very weak first-order transition. Our calorimetric data show clearly that there is an imaginary component to the heat capacity at the *N-SmA* transition of bulk $CCN47$. As it was discussed in Sec. 3.7.5, the *N-SmA* transition in the bulk $CCN47$ is about 28.5 K below the *I-N* transition; therefore, according to McMillan, the *N-SmA* transition should be a second order transition. For other *LC*s, $8CB$ for instance, T_{NA} is just 7 K below T_{IN}, but the *N-SmA* transition is continuous. However this is not the case for $CCN47$, and this can be attributed to effects of the elasticity and couplings between the full smectic and nematic order parameters as it was discussed in Sec. 2.1.2. The bulk transition exhibits significant pretransitional fluctuations and is very close to a tricritical point. Because this is a very weak first order transition, (weaker then the *I-N* transition), the contribution of fluctuations in the transition is big compared to the amount of the latent heat released. The latent heat is released in a very narrow temperature range; as such the anomaly in the heat capacity data is limited to a very narrow two-phase coexistence region, especially for the heating scans. These facts as well as the high quality of the C_p data will allow us to attempt fits of this peak.

Despite the complication of the first order transition the results of the fits are very interesting. The transitional enthalpy gets suppressed by the presence of the gel with increasing ρ_S, because of finite size effects. Therefore with increasing ρ_S the transition is approaching the tricritical point where it becomes second-order, which is estimated to be somewhere around the 0.200 density sample. Furthermore, with increasing ρ_S, the effective heat capacity exponent α_{eff} decreases, approaching the 3D-XY value, which is the underlying behavior of the *N-SmA* transition. A similar evolution has been observed in second order *N-SmA* transitions, and was a clear manifestation of the Harris criterion. The bulk sample shows clearly an $\alpha = 0.5$ which is the tricritical value from the Landau mean field theory, but fluctuations are big on both sides of the transition and very symmetric, at least in heating. The evolution of the transition above the tricritical point is not clear, because we did not study higher density samples. However the fits to this high aerosil

densities are really difficult to perform, because of the rounding of the transition from the finite size effects caused by smaller voids of the silica gel.

5.4.1 Calorimetric Results

In this section we will describe the calorimetric results on the*N-SmA* transition in $CCN47$. The sample preparation and data followed the procedure described in detail in Sec. 3.6, while the calorimetric data were acquired on calor B, which has been described in detail in Sec. 3.1. The appropriate background for all samples, which mimicked closely the low-temperature nematic wing of the *I-N* transition, was subtracted to yield the excess specific heat capacity data. This background is practically linear, since the *I-N* transition is $\sim$ 28.5 K higher than the *N-SmA* transition.

A narrow view, $\pm 0.4K$, of the excess specific heat capacity data for all samples is shown in the upper panel of Fig. 5.16. This corresponds to the boxed region of the wider view of the same data ($\pm 6K$), which is shown in the inset of the upper panel. In the lower panel of Fig. 5.16 is shown the corresponding $\pm 0.4K$ narrow region of the imaginary specific heat capacity. The heat capacity peak doubling that was seen in all the weakly first order *I-N* transitions, here is seen only for the 0.050 sample. At higher densities a single peak is observed. The fact that this feature can be seen only on the 0.050 sample, can be explained by an interplay of several factors. First the fact that this transition is very weakly first order, and weaker than the *I-N* transition. The same increase of the disorder density affects it relatively stronger than the *I-N* transition. Also the character of the transition is different from the *I-N* transition; it is described by a different order parameter to say the least. For the second order *N-SmA* transition there was no sign of double peak, in all the $LC + SIL$ samples studied so far. Furthermore the elasticity of the LC plays a very important role in the existence and range where it is observed this transition doubling. As can be easily seen in the narrow view the high temperature peak is smaller than the low temperature one. This feature makes it resemble to some of the high density samples in $8OCB$, (see Fig 4.2, lower panel, densities above 0.220), and is very easily supported by a similar double peak in the imaginary heat capacity. The similarities of this feature with those observed

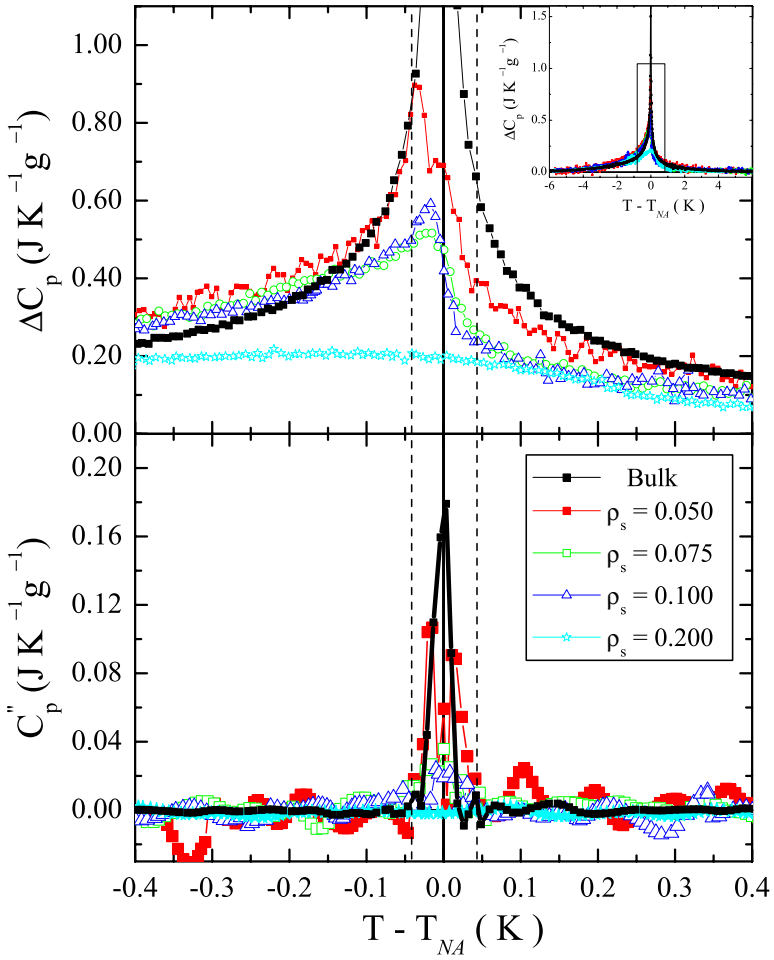

Figure 5.16. Excess specific heat capacity and imaginary heat capacity of the *N-SmA* transition in $CCN47$, about T_{NA}, for heating scans. Dashed vertical lines represent the approximate two-phase coexistence region.
Inset Upper Panel: Wide view ($\pm 6K$) of the excess specific heat capacity around the *N-SmA* transition in $CCN47$. The boxed region is expanded in the upper panel.
Upper Panel: Narrow view $\pm 0.4K$ of the excess specific heat capacity. Note the doubling of the transition for the 0.050 sample, which is similar to the *I-N* first order transition.
Lower panel: corresponding narrow view of the Imaginary heat capacity. Note the similar doubling for the 0.050 sample which is a sign that the release of the latent heat proceeds in two steps. All data are labeled by density, as can be seen in the figure inset in the lower panel.

at first order *I-N* transitions, strengthen the belief that the peak doubling is a characteristic feature in any first order transition, not just *I-N* transitions with low quenched random disorder density. The character of the doubling and its density dependence, of course, depend on the character of the transition as well as the specific *LC* characteristics, like elasticity.

The existence of a peak in the imaginary heat capacity is a clear sign that this transition is first order. The very weak first order character makes the determination of the two-phase coexistence width less accurate than for stronger transitions. Furthermore, the heating runs showed always sharper and higher transition peaks than the cooling scans, i.e., the width of the two-phase coexistence is wider in cooling scans. This type of hysteresis is characteristic of first order transitions. Despite these two complications, the width of the two-phase coexistence region increased monotonically with increasing SIL density, for the densities that were studied. The width of the two-phase coexistence region for the heating scans, δT_{NA}, is given in Table 5.7, and an average value is indicated in Fig. 5.16, by the dashed vertical lines.

There was a striking difference between heating and cooling scans. The peaks observed in heating scans were generally higher and sharper than the cooling scans. This is illustrated in the upper panel of Fig. 5.17, where the maximum specific heat capacity, $h^{max}_{ReC_p}$, is plotted as a function of ρ_S. $h^{max}_{ReC_p}$ for the heating scans, showed a very strong density dependence. It decreased sharply up to $\rho_s = 0.075$, and than decreased at a slower rate at higher densities. In contrast, the cooling scans show a very slight increase of the heat capacity maximum with density, up to $\rho_S = 0.100$, and then a decrease that is exactly the same with heating scans. This behavior is very interesting because it hints for general differences in the dynamics of the latent heat release in the sample. It seems that the latter is dynamically different in heating and cooling scans, but with increasing disorder, above 0.100, the dynamics become similar. We do not understand the effect that disorder has on the dynamics of phase conversion, except that in general it slows it down. The imaginary heat capacity maximum, plotted at the lower panel of Fig. 5.17, shows also this very peculiar behavior.

Although the peak heights differed a lot between the heating and cooling scans, the transition enthalpies were generally very similar. The transition enthalpy,

which is a quantitative measure of the strength of the phase transition was calculated by integrating the ΔC_p data, in a wide temperature range, ± 6 K around T_{NA}, for all aerosil + $CCN47$ samples and the bulk $CCN47$. As already discussed for first order transitions, the total enthalpy change is the sum of the pretransitional enthalpy and the latent heat. The pretransitional enthalpy is a measure of the strength of the fluctuations, while the latent heat is a measure of the first order character of the transition. The amount of the latent heat released in the *N-SmA* transition is much smaller than that released in the *I-N* transition, thus the *N-*

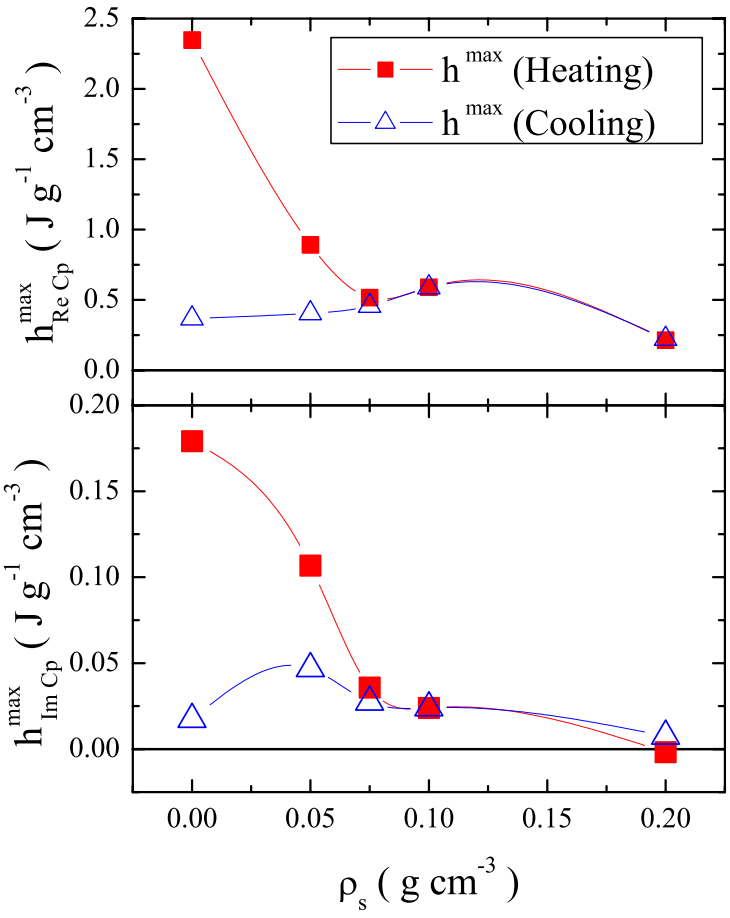

Figure 5.17. a- Upper panel: Density dependence of the *N-SmA* heat capacity peak maximum $h^{max}_{ReC_p}$, for $CCN47 + SIL$ samples as measured by *AC* calorimetry.
b- Bottom panel: Density dependence of the *N-SmA* imaginary transitional enthalpy $h^{max}_{ImC_p}$ for $CCN47 + SIL$ samples.
Solid lines are guide to the eye. The symbols defined in the figure inset are the same for both panels.

SmA transition is fluctuation dominated. For the bulk sample for instance, the pretransitional enthalpy is, $\delta H_{NA}(pretransitional) \simeq 0.8$, while the total enthalpy as measured by *AC* calorimetry is $\delta H^*_{NA} \simeq 0.88$. Although the *AC* method can not measure the total enthalpy, it can represent a very significant portion of it. Thus the latent heat makes up for only $\sim$ 10%-20% of the pretransitional enthalpy.

The total *N-SmA* transitional enthalpy is less than $\sim 900\ mJg^{-1}$, and shows a strong dependence on the aerosil density, as can be seen in the upper panel of Fig. 5.18. Initially, the enthalpy remains almost constant with increasing ρ_S, up to 0.050, and is followed by a sharp decrease at higher ρ_s, with a concave downward behavior. This is the expected behavior, since with increasing disorder the transition gets suppressed, and at some density will become second order. We believe that this transition occurs somewhere in the vicinity of the $\rho_s = 0.200$. This is supported from the imaginary enthalpy, $\delta H^{"}_{NA}$, which is the area under the imaginary heat capacity. The imaginary enthalpy is directly related only to the latent heat release. As such is a direct measurement of the strength of the first order character of the transition. Of course even in this case the dynamics of the latent heat release play an important role on the amount of $\delta H^{"}_{NA}$ that can be sensed from the fixed AC method. The ρ_s dependence of $\delta H^{"}_{NA}$ is shown in the lower panel of Fig. 5.18. It shows a similar behavior with the transitional enthalpy, remaining almost constant at $\rho_s < 0.050$, followed by a sharp decrease for higher ρ_s, to a value that is essentially zero for $\rho_s = 0.200$.

ρ_S	T_{IN}	T_{NA}	ΔT_N	δT_{NA}	δH^*_{NA}	$\delta H^{"}_{NA}$
0	330.412	301.923	28.490	0.055	0.876	4.73
0.050	329.232	300.674	28.558	0.076	0.906	4.58
0.075	329.338	300.503	28.835	0.117	0.817	2.13
0.100	329.743	301.437	28.306	0.151	0.847	1.34
0.200	330.325	301.861	28.464	-	0.667	0.06

Table 5.7. Summary of the calorimetric results for *CCN*47+aerosil samples. Shown are the conjugate silica density (ρ_S in grams of aerosil per cm^3 of *CCN*47), the *I-N* (T_{IN}) and the *N-SmA* (T_{NA}) phase transition temperatures, and the nematic temperature range ($\Delta T_N = T_{IN} - T_{NA}$) all in kelvins and averaged between heating and cooling scans. The fifth column shows the width of the two-phase coexistence region (δT_{NA}) for the heating scans in kelvin. In the last two columns are given the heat and cooling averaged real enthalpy (δH^*_{NA}) in J g^{-1} and imaginary enthalpy ($\delta H^{"}_{NA}$) in mJ g^{-1} respectively.

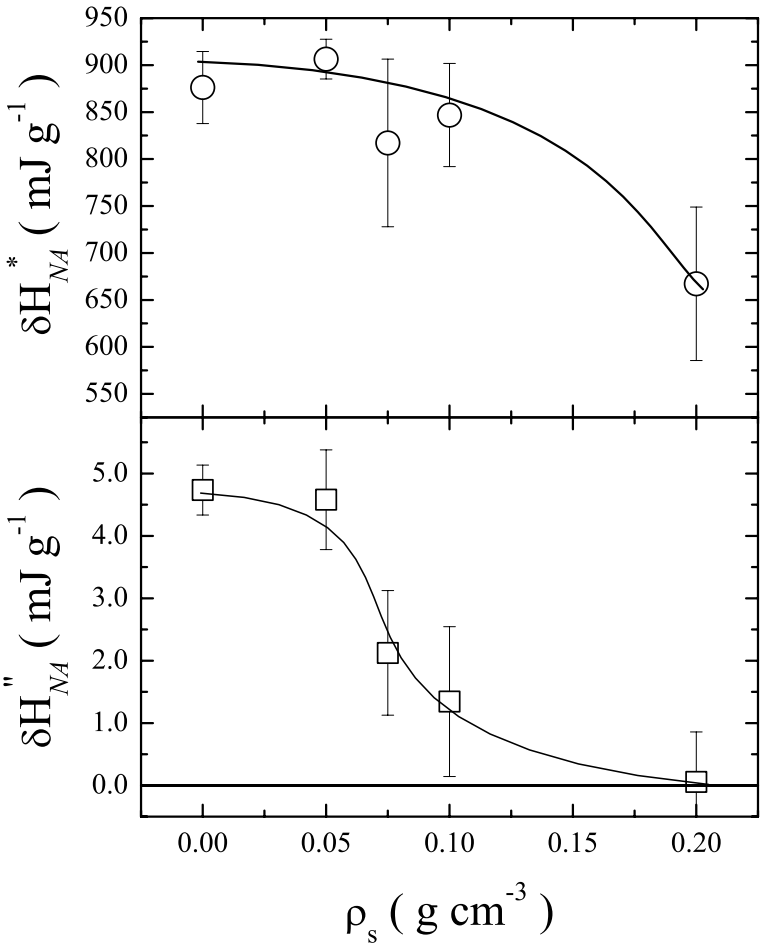

Figure 5.18. a- Upper panel: Density dependence of the *N-SmA* excess transition enthalpy δH^*_{NA}, for $CCN47 + SIL$ samples, as measured by *AC* calorimetry.
b- Bottom panel: Density dependence of the *N-SmA* imaginary transitional enthalpy $\delta H''_{NA}$ for $CCN47 + SIL$ samples.
Solid lines are guide to the eye. The error bars are equal to the difference between heat and cooling scan enthalpies.

The *N-SmA* transition temperature was calculated as the average of the heating and cooling scans. Since this is a first order transition there is some hysteresis because of superheating and super cooling effects, which will not affect the qualitative description in any way, since the changes in temperature are much larger than the uncertainty. However they will effect the clear determination of the nematic temperature range, since the uncertainty in determining the transition temperature is somewhat large, on the order of $\pm$ 0.2 K. The density dependence of the *N-SmA* transition temperatures, T_{NA}, is shown in the upper panel of Fig. 5.19, left y-axis.

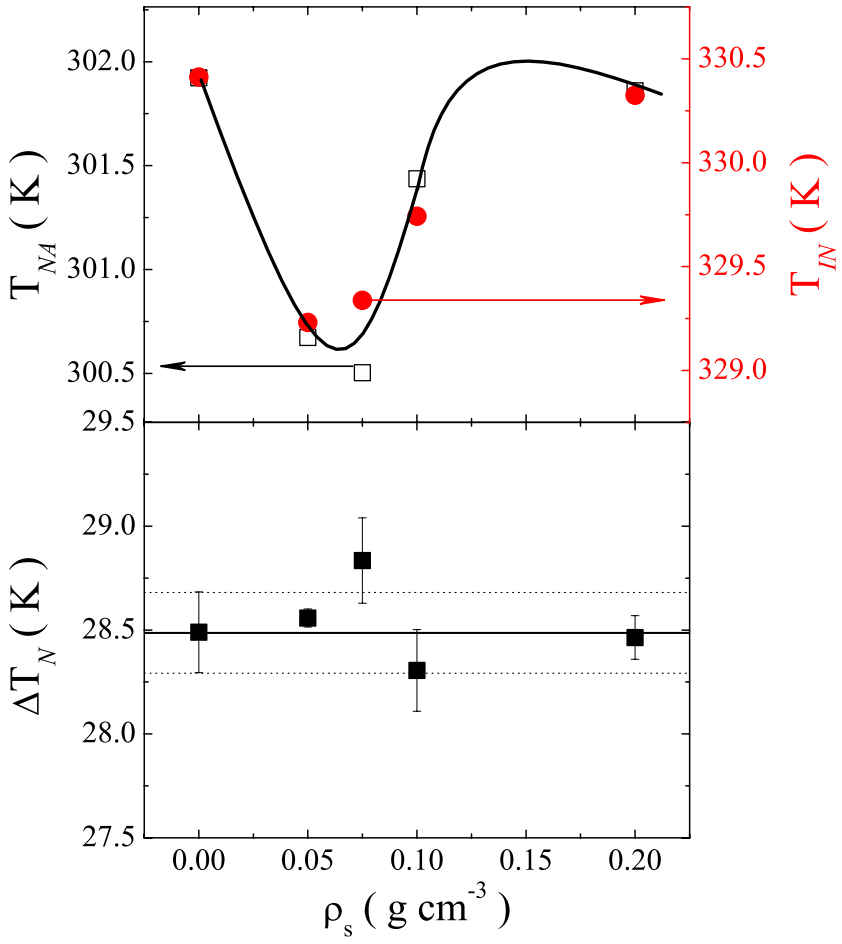

Figure 5.19. a- Upper panel: Density dependence of the T_{NA} and T_{IN}, transition temperatures for $CCN47+SIL$ samples. Left axis and open squares are the T_{NA} values while on the right axis and filled circles are the T_{IN} values, as indicated by the arrows. Both left and right scales span a 2 K range. b- Bottom panel: Density dependence of the nematic range, for $CCN47+SIL$ samples, $\Delta T_N = T_{IN}$- T_{NA}. Solid lines are guides to the eye.

For easy comparison we plot on the right y-axis the *I-N* transition temperature, T_{IN}, with the same axis range span of 2 K. As can be seen the transition temperatures for both transitions follow closely the same qualitative behavior. T_{NA} decreases significantly, to almost $\sim$ 1.5 K below the bulk transition temperature in the intermediate densities with $\rho_S < 0.075$. This is followed by a strong increase in T_{NA}, for $\rho_S > 0.075$, recovering to almost the bulk value at the $\rho_S = 0.200$ sample. We did not study any higher densities than the 0.200, but, judging from the behavior that was observed in all the other $LC + SIL$ samples studied, we

expect a monotonic decrease of T_{NA} with increasing ρ_S, above 0.200. The solid line which is a guide to the eye indicates this type of behavior.

Although qualitatively T_{IN} and T_{NA} behave the same, quantitatively there are differences. The density dependence of the nematic phase temperature range, $\Delta T_N = T_{IN} - T_{NA}$, shown in the lower panel of Fig. 5.19, is a measure of these differences. Furthermore, while the individual transition temperature changes reflect the absolute stability limit of of the nematic and smectic-A phases, ΔT_N reflects the stability limit of both phases. The behavior of ΔT_N for the $CCN47$ $+SIL$, does not resemble to that of cyanobiphenyls + SIL samples. If it was not for the $\rho_S = 0.075$ and ρ_S =0.100 samples, we would certainly have stated that the nematic range does not change with density, which is a sign that, both the nematic and smectic-A ordering are affected similarly by the disorder. However, would had been really fortuitous that the behavior of the two phases is affected in the same exact amount. The fact that both transitions are first order will be in favor of similar dependence, i.e., that the nematic range should not change. Unfortunately we can't tell now with certainty, if this is the case or not, without further testing.

ρ_S	α	A^+ $\times 10^{-3}$	A^- $\times 10^{-3}$	B^+ $\times 10^{-3}$	B^- $\times 10^{-3}$	T^+	T^-	t_{min} $\times 10^{-4}$
0	0.501	7.230	10.40	−57.24	−54.41	302.086	302.082	4.27
0.050	0.408	14.10	30.99	−72.62	−142.8	300.933	301.012	2.25
0.075	0.372	15.76	44.12	−78.84	−193.6	300.543	300.679	5.23
0.100	0.322	18.86	60.29	−61.28	−210.4	301.719	301.828	1.01
0.200	0.199	42.08	186.9	−104.6	−396.2	302.220	302.671	17.8

Table 5.8. Results from fitting the excess specific heat $\Delta C_p(NA)$ associated with the heating scans of the N-SmA transition of $CCN47$+aerosil samples with Eq. (5.21). L was held fixed at $L = 0.444$. $T^{\pm}$ values are in kelvin, $A^{\pm}$ and $B^{\pm}$ are in J K^{-1} g^{-1}, while α and t_{min} values are dimensionless. All scans were fitted from $t_{max} \simeq 3 \times 10^{-2}$ to the tabulated t_{min} value.

The shape of the experimental $\Delta C_p(NA)$ data as a function of aerosil content is characterized by a simultaneous fit of both sides of the heat capacity peak with a power-law form [20] in terms of the reduced temperature $t^{\pm}$, given by

$$\Delta C_p(NA) = B_c^{\pm} + A^{\pm}(t^{\pm})^{-\alpha} \ , \tag{5.19}$$

ρ_S	α	A^+ $\times 10^{-3}$	A^- $\times 10^{-3}$	B^+ $\times 10^{-3}$	B^- $\times 10^{-3}$	T^+	T^-	t_{min} $\times 10^{-4}$
0	0.366	14.13	46.59	−61.80	−186.6	301.821	301.874	15.5
0.050	0.399	12.48	27.57	−60.19	−97.10	301.036	301.766	26.0
0.075	0.412	9.66	25.02	−53.66	−106.9	300.767	300.803	5.8
0.100	0.330	21.22	64.48	−80.13	−230.2	301.471	301.675	1.66
0.200	0.200[1]	61.52	177.4	−149.7	−374.1	302.008	302.371	18.6

Table 5.9. Results from fitting the excess specific heat $\Delta C_p(NA)$ associated with the cooling scans of the *N-SmA* transition of $CCN47$+aerosil samples with Eq. (5.21). L was held fixed at $L = 0.444$. $T^{\pm}$ values are in kelvin, $A^{\pm}$ and $B^{\pm}$ are in J K^{-1} g^{-1}, while α and t_{min} values are dimensionless. All scans were fitted from $t_{max} \simeq 3 \times 10^{-2}$ to the tabulated t_{min} value.

$$t^{\pm} = \begin{cases} (T - T^+)/\ T^+ = T/T^+ - 1 & \text{if } T > T^*, \\ -(T - T^-)/\ T^- = 1 - T/T^- & \text{if } T < T^*. \end{cases} \tag{5.20}$$

where the parameters with the + index correspond to the wing above the transition, and those with −, to that below the transition. To take care of linear background terms that were not subtracted correctly a noncritical linear background term was added and thus the fitting equation became

$$\Delta C_p(NA) = Lt + B_c^{\pm} + A^{\pm}(t^{\pm})^{-\alpha}\ , \tag{5.21}$$

where, $t = T/T^* - 1$, and T^* is an arbitrary temperature, usually taken in the middle of the gap of excluded data points. The fits are not sensitive at the choice of T^*.

As seen in Eq. (5.21), the critical behavior of the heat capacity was characterized by the critical amplitudes $A^{\pm}$ and backgrounds, $B_c^{\pm}$, above and below the transition. For second order transitions only one transition temperature and a single background term are needed, since there is no jump in the background and both high temperature and low temperature wing diverge at the same temperature T^*. However for first order transitions one has to allow for the possibility of two different values, T^+ and T^-, which are the diverging temperatures of the above and below wings respectively, as well as a jump in the critical background, by allowing the two terms B^+ and B^-. In most of second order critical fits, corrections-to-

[1]Value of α was held fixed.

scaling terms, with amplitudes $D^{\pm}$ and exponent $\Delta_1 \simeq 0.5$, are needed. Interestingly enough the fits that were tried with the corrections to scaling term "turned ON" did not perform very well, and there was a clear interference between the amplitudes $A^{\pm}$ and $D^{\pm}$. As a result, no corrections-to-scaling terms were included in any of the fits, and the fits were performed with Eq. (5.21), where the linear term L was fixed for all fits to $L = 0.444$.

There was a clear distinction between the non linear least square fits performed for heating and for cooling scans. For cooling scans, the gap of excluded data points

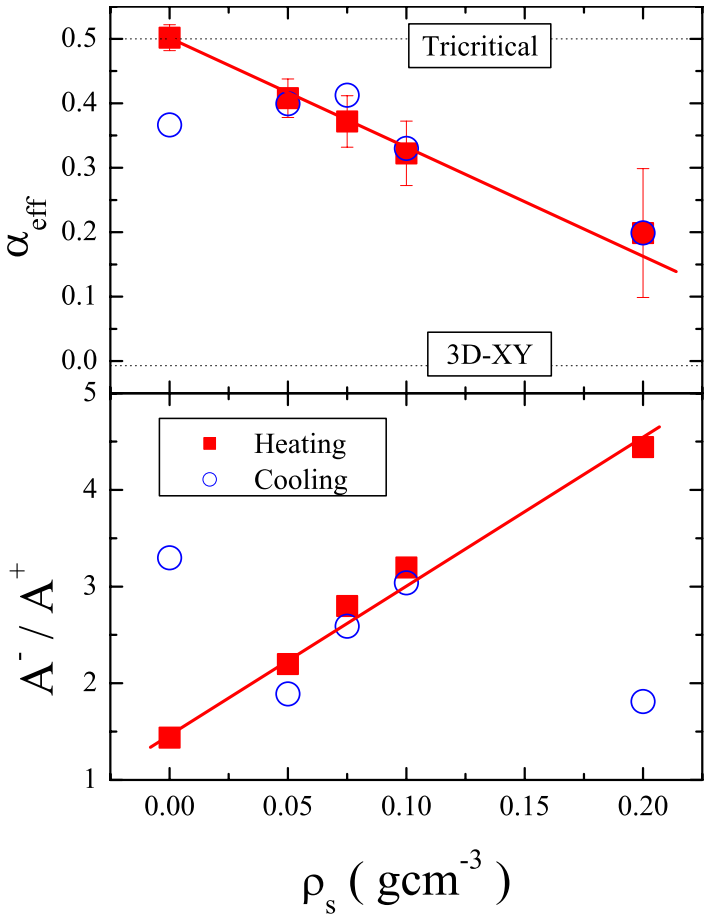

Figure 5.20. a- Upper panel: Density dependence of the effective heat capacity exponent α for heating and cooling scans, for $CCN47 + SIL$ samples. Dotted lines show the theoretical values for the tricritical and 3D-XY universality classes.
b- Bottom panel: Density dependence of the amplitude ratio A^{-}/A^{+} for $CCN47 + SIL$ samples.
Solid lines are guide to the eye. The symbols defined in the figure inset are the same for both panels. Note the scatter of points for the cooling scans.

about the peak was always bigger. This is understandable since the two-phase coexistence region in cooling scans was always wider than that for the same density sample in heating. The wide data gap made the cooling fits less sensitive. Furthermore, the higher C_p peaks for heating made the determination of the exponent α, and amplitudes $A^{\pm}$ more accurate than that of cooling scans. The fit results for the sets of heating and cooling scans for bulk $CCN47$ and $CCN47$+aerosil are presented in Tables 5.8 and 5.9, respectively.

The ρ_s dependence of the heat capacity critical exponent α_{eff}, is plotted in the upper panel of Fig. 5.20. For the heating scans, the bulk exponent is exactly equal to the Gaussian tricritical value $\alpha = 0.5$. With increasing density, the exponent decreases towards the 3D-XY value of α = -0.013. Note that somewhere close to ρ_S = 0.200, the transition becomes second order. The further evolution is unknown since we did not study higher densities. It might continue with a line of second order transitions or become supercritical, i.e., the line of first order transitions stops at the second order transition. If the transition evolves with a second order transition line and fits are possible, than their evolution will be very interesting to follow. However, at this high SIL concentration, the fits are usually very difficult, because of the severe rounding of the peak. The behavior of α for the cooling scans, is more noisy and its density dependence is not as clear as for the heating scans. Note that the exponent for the highest density was fixed to $\alpha \equiv 0.200$. If α was let free the value goes higher than 0.5 to about 0.68, which is closer to a gaussian tetracritical exponent ($\alpha = 2/3$).

Both critical amplitudes for heating showed a monotonic increase starting from similar values. The density dependence of the ratio A^-/A^+ also increased monotonically with ρ_S, meaning that the fluctuations on the lower side of the transition became stronger and the shape of the ΔC_p peak more asymmetric. The cooling scans show a completely different behavior. Both A^- and A^+ decrease initially, with increasing silica up to the $rho_S = 0.075$, and then increase, with increasing ρ_S. Although both A^- and A^+ show the same pattern, their changes are not proportional. This can be seen in the ratio A^-/A^+, for cooling, which is noisy and it is mostly smaller than the bulk ratio.

Of interest is also the density evolution of the temperature gap $T^- - T^+$, and the baseline jump $B^- - B^+$, which are shown in Fig. 5.21. The temperature gap

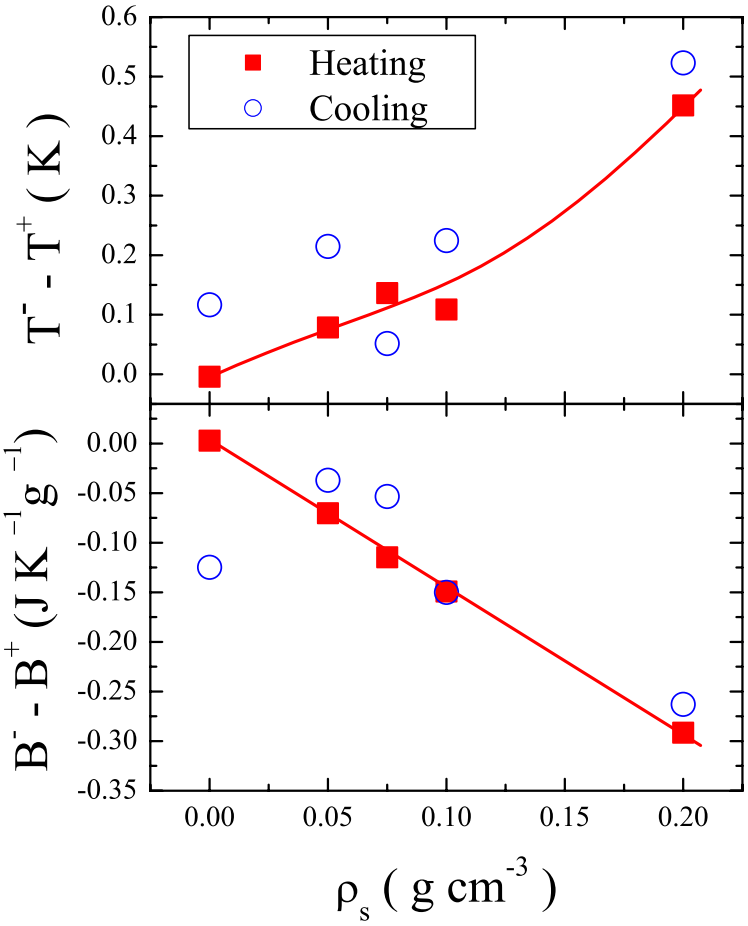

Figure 5.21. a- Upper panel: Density dependence of the temperature gap $T^- - T^+$ from the fit, for $CCN47 + SIL$ samples.
b- Bottom panel: Density dependence of the baseline jump $B^- - B^+$ from the fit, for $CCN47 + SIL$ samples.
Solid lines are guide to the eye for the heating scans. Symbols defined in the figure inset are the same for both panels. Note the scatter of points for the cooling scans.

$T^- - T^+$ shows a monotonic increase with the silica density, while the baseline jump, $B^- - B^+$, becomes increasingly negative. Normally we would expect that with the transition approaching criticality the baseline jump and the temperature gap to asymptotically approach zero. However the effect of disorder clearly disrupts this behavior. The fluctuations seem to evolve toward 3D-XY, while the first order nature of the transition becomes weaker. This added complexity seems to be the source of the unexpected behavior in the temperature gap and baseline jump. shown in Fig. 5.21. Certainly a more detailed study of these samples as well as

better characterization of the ΔC_p peak with a more appropriate fitting function will shed more light towards this very interesting transition. One thing is for sure, that $CCN47+SIL$ samples are very interesting candidates which will open a wide area of possible future studies.

5.5 Discussion

Results have been presented from high-resolution x-ray scattering and AC calorimetric experiments on 8OCB+aerosil dispersions. The x-ray structure factor has been described using a random-field model which accounts well for the data. The correlation length and amplitudes from this model have been presented as a function of the aerosil density ρ_S for each sample. These results for 8OCB+aerosil dispersions are fully compatible with existing results for 8CB+aerosil dispersions [76, 75] and in addition reveal new aspects of quenched random disorder on liquid crystal phase transitions.

Theories of random field behavior predict the relationship between the saturated correlation length and the variance Δ of the strength of the random-field h, which depends on the dimensionality of the system and on its lower marginal dimensionality as a random field system. Since the system is anisotropic, we take the appropriate saturated correlation length to be the low-temperature mean value $\bar{\xi}^{LT}$. For a 3D-XY phase transition, the lower marginal dimensionality, below which long-range order is not possible, is $d_c = 2$. Due to Landau-Peierls instability, the pure N-SmA transition has a lower marginal dimensionality of $d_c = 3$. The pioneering observations of the algebraic decay of smectic correlations, a hallmark of a system at its lower marginal dimension, were in fact made on pure 8OCB [102]. However, on length scales accessible in this work, the SmA phase of pure 8OCB is long-range ordered. Indeed, broadening of the scattering peak beyond the resolution limit of the experiment is unobservable for a 8OCB+aerosil sample with $\rho_S = 0.025$. Thus, the distinction between a 3D-XY and a N-SmA transition is not important on the length scales probed in this work and so, pure smectic ordering can be reasonably thought of as having $d_c = 2$. For the quenched random disordered system, random-field spatial fluctuations are more effective than thermal fluctuations at destroying an ordered state. Theoretical work on a 3D-XY

system has suggested that such random-field fluctuations have the same effect as thermal fluctuations would have in a system with two fewer dimensions [99]. This implies that we should take $d_c = 4$ for the *N-SmA* transition in a random-field. The dependence of the correlation length on the random field strength should then be $\bar{\xi}^{LT} \sim \Delta^{-1/(d_c-d)} = \Delta^{-1}$ [76, 59, 99]. The results presented in Fig. 5.12 agree fairly well with this relation if $\Delta = \rho_S$. In addition, the density dependence of the ratio of the random field and thermal amplitudes, $a_2/\sigma_1 \sim \Delta^3$ [59] supports the idea that $\Delta \sim \rho_S$ (see Fig. 5.10).

In Figures 5.10 and 5.12, the random-field variance Δ is equated with ρ_S. This is a useful parameter since it is proportional to the surface area of the dispersed aerosil and the relation $\Delta \sim \rho_S$ can be understood on physical grounds. For an LC+aerosil system, a smectic region is likely to form away from the aerosil surface due to the surface undulation of the aerosil ("pearl-necklace") strands. These undulations have wavelengths that varies somewhat from strand to strand but are comparable to the 70-Å diameter of an individual aerosil sphere. As the temperature decreases, the smectic order grows toward the aerosil strands. Eventually, a smectic domain will impinge on a particular gel strand. Here, the phase of the smectic mass-density wave becomes perturbed as it attempts to accommodate the particular strand's undulation. Thus, the variance of this perturbation might be expected to scale as the surface area of the gel and so to the density ρ_S. The proportionality between ρ_S and the surface area of the dispersed silica is supported by the analysis of the background scattering presented in this work.

The calorimetry results show that the specific heat peak associated with the *N-SmA* phase transition remains sharp for low-disorder, while evolving in its critical behavior with increasing ρ_S towards the underlying 3D-XY behavior. See Fig. 5.1 and Table 5.2. For higher ρ_S samples, the *N-SmA* transition becomes highly smeared. The decrease in the transition enthalpy, Fig. 5.2, and in the specific heat maximum, Fig. 5.6, with increasing ρ_S is very similar to those observed for the 8CB+aerosil system [59]. However, the shift in the pseudo-transition temperature T* with respect to the pure LC transition temperature between the $8OCB$+aerosil and $8CB$+aerosil samples, while functionally similar, differs in the quantitative dependence on ρ_S. Given the "stiffer" elastic nature of $8OCB$ relative to $8CB$, these results are consistent with the disorder induced by the aerosil gel

disperse altering the coupling between the nematic and smectic phases [59].

The observed break-up into finite sized domains [23] as well as the x-ray lineshape and intensity [99] are consistent with random field behavior. The analysis makes the assumption that the pure system anisotropic lineshape should be retained to describe the thermal fluctuations in the random-field system. The disorder imposed by an imbedded aerosil gel appears to be substantially weaker than that imposed by an aerogel of the same density. This adds further weight to the assumption that some measure of the pure system behavior should be retained for the *LC*+aerosil system.

The suite of characteristics normally associated with random-field behavior leads to the conclusion that the dominant form of disorder is the one which couples linearly to the order parameter. This suggests that it is the smectic layer position pinning in Eq. (5.2) which dominates. This would suggest that the *LC*+aerosil system is closely analogous to charge-density wave materials where the phase of the density wave is pinned by impurities. [103, 104] As outlined in the introduction, the relative domain sizes for the orientational and translational order is an indication that there exists in addition to the orientational disorder another mechanism disrupting the smectic phase.

Radzihovsky and Toner [96] have asserted that the difference between charge-density waves and smectic-A order has a fundamental effect on their response to quenched random disorder. In a charge-density wave material, the orientation of the translational order is selected by the underlying lattice. Impurities then pin the phase of the charge-density wave and this is source for the random-field disorder. At the *N-SmA* phase transition in an *LC*, a density wave is also formed. In this case, there is no underlying lattice which singles out a direction for the modulation. It has been suggested that the orientational disorder, which the aerosil or aerogel surfaces impose, is the most pernicious form of the disorder. This corresponds to the first term in Eq. (5.2). Our results appear to disagree with this view. The correlation lengths observed at low temperatures are very short compared to the *orientational* correlation lengths observed with light scattering on aerosil dispersions in a related liquid crystal 6CB [36]. Below the bulk nematic to isotropic transition temperature, finite range orientational order is established in a *LC*+aerosil sample having a domain size which extends to ~ 1 μm. When smectic

order forms, it extends within these preoriented nematic domains to ~ 0.1 μm. It appears that disruption to orientation is not the primary effect in breaking up smectic domains. Our results suggest that the pinning of the phase of the mass-density wave is the dominate disorder. Intuitively, the difference between the charge-density wave order and the *SmA* order does not appear to be profound. In the charge-density wave case, the orientational order of the density wave is selected by the underlying crystal lattice. In the mass-density wave of a *SmA* phase, the orientation of the density wave is selected by the underlying nematic orientational order. Thus, these results suggests that it is the pinning of the smectic-A layer positions as the dominate disorder to smectic ordering.

The x-ray results for 8OCB+aerosil samples presented here provide an important comparison with both 8CB+aerosil dispersions [75, 76] and 8CB in an aerogel medium [95]. Our x-ray scattering measurements are in good agreement with those on 8CB+aerosil samples. Contrary to predictions [96], the low-temperature correlation length is independent of temperature rather than varying as some power of the pure *LC* layer compression modulus *B(T)*. As discussed for 8CB+aerosil [76], it is surprising that the weaker disorder aerosil seems to resemble the putative smectic Bragg glass *less* than the aerogel system [95]. It has been suggested [105] that the dispersed aerosil gel systems are fundamentally different from aerogel systems. The aerogel is known to be far more rigid than an aerosil gel. The similarity between the $\xi_{\|}(T)$ results for an 8CB+aerosil sample and for 8CB in millipore has been pointed out; compare Fig. 2 in [95] with Fig. 9(b) in [75]. Millipore is a porous cellulose with smooth walls instead of the fractal structure of either aerogel or aerosil gels. The suggestion has been [105] that the aerosil particles are pushed aside by the smectic order until they form the walls of large pores. This suggestion is inconsistent with small-angle x-ray scattering results [58] which show that the aerosil gel retains its fractal structure when thermally cycled through the smectic and nematic phases. The difference between *LC*+aerosil results and *LC*+aerogel results is not yet understood [76, 95, 105].

Results have been presented from a series of high-resolution *AC* calorimetric experiments on $\bar{8}$S5+*SIL* dispersions through the *N-SmA* of aerosil density. In bulk $\bar{8}$S5, the *N-SmA* is not a clean "XY-like" transition. The C_p data show XY character with an $\alpha \lesssim 0$, but the γ and ν_i values are not [20]. Our bulk

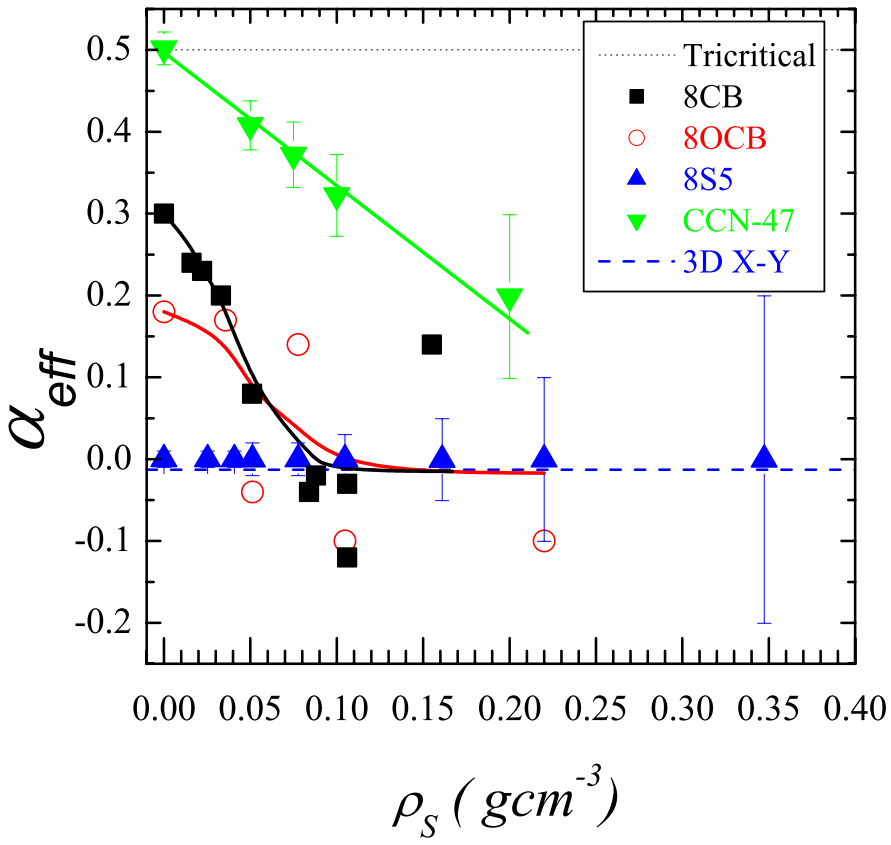

Figure 5.22. Comparison of effective specific heat critical exponent α_{eff} obtained from fitting Eq. (5.6) to the *N-SmA* phase transition between $8CB$, $8OCB$, $\bar{8}$S5 and $CCN47$, + aerosil samples. See the figure inset for symbol definitions. The solid lines are guide to the eye.

measurements are fully consistent with a XY value for α. The introduction of QRD in the $\bar{8}$S5+SIL system allows for the isolation of random-field, finite-size, and elastic strain effects at a pure XY and mean-field transition.

The *N-SmA* transition temperature does not exhibit a sensitivity to the aerosil (and in fact increases slightly) in stark contrast to that seen in nearly all other $LC + SIL$ studies. Although the $\Delta C_p(NA)$ decreases uniformly in size with increasing ρ_S, it remains sharp and is well characterized over the whole range of aerosil concentration. The power-law fits reveal that quasi-critical behavior is preserved and that the exponent α_{eff} remains slightly negative and constant for all ρ_S

studied. See Fig. 5.22. The systematic decrease of the coefficients $A^{\pm}$ but nearly constant ratio A^{+}/A^{-} is a reflection of the uniform decrease in the size of $\Delta C_p(NA)$ (as well as δH_{NA}). This represents the strictest test to date of the Harris criteria, which states that QRD should not alter the critical fluctuations of a transition if the bulk heat capacity critical exponent is negative, i.e. $\alpha < 0$.

Because of the good quality power-law fits available in this study, a detailed finite-size scaling analysis was performed and compared to the heat capacity maximum $h = \Delta C_p^{max}(NA)$, transition enthalpy δH_{NA}, and transition temperature rounding $\delta T^*/T^*$ of the *N-SmA* phase transition. A full FSS analysis using the bulk parameters and an adjustable cutoff length scale ξ_M found excellent agreement for h using $\xi_M(\bar{8}\text{S5+sil}) = 3l_o$ but this does not completely describe the behavior of δH_{NA} nor $\delta T^*/T^*$, especially for $\rho_S > 0.1$. Interestingly, when this FSS analysis is applied to the 8CB+SIL and 8OCB+SIL systems, equally good modelling of h is obtained for $\xi_M(\text{8CB+sil}) = l_o$ and $\xi_M(\text{8OCB+sil}) = 1.5l_o$. Although of unknown significance, it is surprising that such excellent agreement is obtained over the whole range of ρ_S explored for these three LCs despite the apparent violation of the classic expectation of FSS (that is, the truncation of the bulk ΔC_p behavior at the cut-off length-scale).

In this study on $\bar{8}$S5+SIL, it appears that the random-field QRD of the aerosil gel should not play a significant role at the *N-SmA* transition (due to the Harris criteria). It is clear that FSS is present with $\xi_M > l_o$ but it does not appear to play a leading role. How, then, does one understand the evolution of this transition with increasing QRD of aerosil and in light of the other $LC + SIL$ and LC+aerogel results? One possibility is that the aerosil gel, due to its flexibility, is closer to thermodynamic equilibrium with the host LC and so causes the $LC + SIL$ to behave as a stiffer LC as well as provide QRD. The aerosil gel has been shown to exhibit dynamics coupled to the host liquid crystal [77] and recent work has followed its quenching as aerosil density increases [106, 57]. This increase in the effective microscopic elastic stiffness of the LC would be similar to the engineered stiffening of polymer composite materials. A consequence of the stiffening of the nematic phase in $LC + SIL$ systems has already been discussed previously [58, 59, 101] in terms of the decrease in the nematic susceptibility with increasing ρ_S to explain the crossover from tricritical to XY behavior for the *N-SmA* transition.

The present view is to extend this concept to the general stiffening of the LC within the $LC + SIL$.

Finally, high resolution AC calorimetric results were presented for the bulk $CCN47$ and $CCN47 + SIL$ samples. The *N-SmA* transition in bulk $CCN47$ is a very weak first-order transition, which by nature is very close to the tricritical point. The results of the fit to the bulk $CCN47$ *N-SmA* transition showed clearly tricritical-like exponent for the heat capacity, with very symmetrical amplitudes. The introduction of QRD by the aerosil dispersions changed drastically the character of the transition. The ΔC_p decreased differently on both sides of the transition, making it more asymmetric. The size of the heat capacity maximum and enthalpy, both real and imaginary, decreased non-monotonically with SIL density. These results are in perfect agreement with other $LC + SIL$ systems that were studied.

The study of the first order *N-SmA* transition gave us the possibility to further test our understanding of QRD in $LC+SIL$ systems. Being a first order transition it showed the transition doubling, observed at the *I-N* transition, as well as the well documented temperature shifts. On the other hand being very close to a tricritical point, and the very high quality data, it made possible to attempt fitting of this transition peak, despite the complications coming from the first-order character of the transition. The observations on $CCN47+SIL$ further strengthens the believe that these features are general features of weak first-order transitions in presence of the QRD created by aerosil dispersions.

Chapter 6

Smectic-A to Smectic-C Phase Transition in Aerosil Disordered Liquid Crystal

6.1 Introduction

Recently, tilted smectic phases have become the focus of studies on quenched random disorder effects [100, 107]. The smectic-A to smectic-C (SmA-SmC) phase transition involves the breaking of a continuous symmetry and is described by two parameters, the tilt and azimuthal angles. This transition belongs to the 3D-XY universality class but, due to the influence of the smectic layer stiffness (compressibility), the transition is not fluctuation dominated and is typically mean-field. The strong coupling between tilt and layer compression for the SmC phase appears to place the SmA-SmC transition always close to a (Landau) mean-field tricritical point [3]. A consequence of the tilt angle's sensitivity to the layer elasticity is that this transition is much more strongly disordered by perturbations that distort the smectic layers, as in the strong disorder of aerogels, than the N-SmA [108, 109]. For weaker aerosil gel induced disorder, the Landau mean-field heat capacity signature was found to be unaffected by hydrophobic aerosils [90] while a recent high-resolution x-ray scattering study on a different LC in a hydrophilic aerosil found little change in the tilt angle temperature dependence with ρ_S [100]. This

robustness to weak disorder may be a consequence of the mean-field character of the transition, placing it effectively at its upper critical dimension. However, when the transition from the *SmA* phase goes to the chiral analog of the *SmC* phase (*SmC**), the effect of even the aerosil induced disorder is quite strong [107].

6.2 *SmA-SmC* Transition in $\bar{8}$S5

The excess specific heat contribution due to the *SmA-SmC* transition is isolated from $\Delta C_p(NA)$ by subtracting the low-temperature heat capacity wing of the *N*-

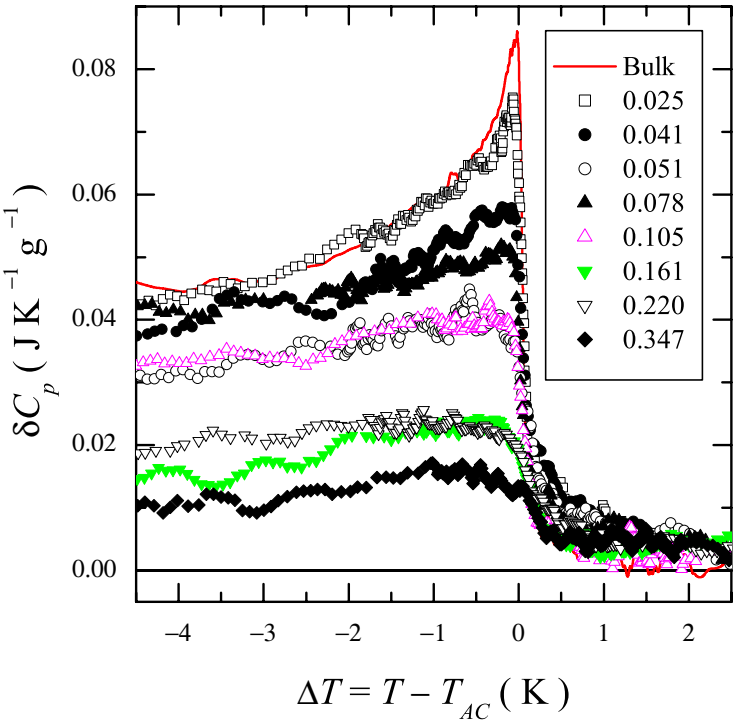

Figure 6.1. Excess specific heat δC_p of the *SmA-SmC* phase transition from +2.5 K above to −4.5 K below T_{AC} for bulk $\bar{8}$S5 and $\bar{8}$S5+*SIL* samples. In the figure inset are listed the ρ_S for each data set shown.

SmA transition as shown in Fig 5.13 with the solid line; i.e.,

$$\delta C_p(AC) = \Delta C_p - \Delta C_p^{wing}(NA) \; . \tag{6.1}$$

The result for all samples studied are shown in Fig. 6.1 over a range +2 K above to −4.5 K below T_{AC}. The bulk sample shows nearly Landau tricritical behavior, which disappears very rapidly at higher SIL densities, changing the transition to a pure step-like mean-field. To characterize this transitions we performed a Landau mean-field analysis, which will be described in the next section. The relevant thermal characteristics for both phase transitions of $\bar{8}$S5+aerosils as a function of ρ_S are given in Table 5.4.

Since this transition is effectively mean-field the definition of a transition enthalpy is not very sensible. A more relevant quantity in this case would be the size of the step for the transition, δC_{AC}^{Step}. This is defined as the value of the excess specific heat −6 K below T_{AC}. The ρ_s dependence of the average between heating

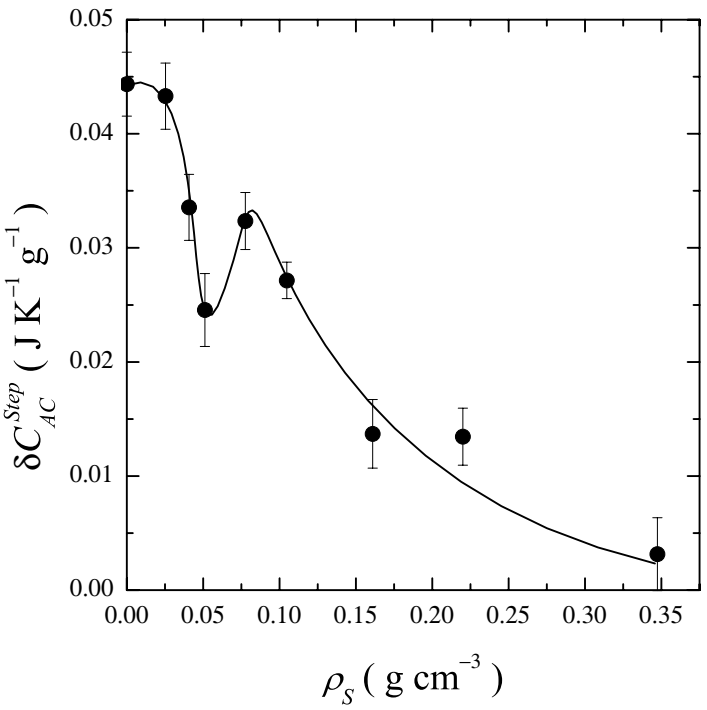

Figure 6.2. The ρ_S dependence of the mean-field specific heat step δC_{AC}^{Step} of the *SmA*-*SmC* phase transition for $\bar{8}$S5+SIL samples. The solid line is guide to the eye.

and cooling scans of δC_{AC}^{Step} is shown in Fig. 6.2. It is clear from Fig. 6.2 that the size of the C_p step decreases with increasing disorder. Although not very clear this decrease appears to be almost monotonic.

The *SmA*-*SmC* heat capacity remains mean-field for all aerosil concentrations studied, with a continuous evolution from the bulk's near tricritical to a simple mean-field step behavior. In particular, the *SmA*-*SmC* heat capacity maximum at the transition scales as $\rho_S^{-0.5}$. The stable mean-field character of the *SmA*-*SmC* with QRD may be a consequence of this transition being effectively at its upper critical dimension. The observed crossover from tricritical to a simple mean-field step behavior for this transition can be understood as a continuous stiffening of the smectic structure with silica density.

6.2.1 The Landau mean-field *SmA*-*SmC* scaling analysis

The bulk SmA-SmC transition is well described by an extended Landau theory [65, 110] given by:

$$\delta C_p(AC) = \begin{cases} 0 & \text{for } T > T_c \\ A\frac{T}{T_c}\left(\frac{T_m - T_c}{T_m - T}\right)^{0.5} & \text{for } T < T_c \end{cases} \tag{6.2}$$

where A is the $\delta C_p(AC)$ maximum at the transition T_c and T_m is the upper stability limit of the SmC phase. Results from fitting Eq. (6.2) to the excess specific heat of the SmA-SmC phase transition δC_p for bulk $\bar{8}$S5 and $\bar{8}$S5+sil samples over the temperatures $T < T_{AC}$ are tabulated in Table 6.1. These results are the average of heating and cooling scan fits. The stability limit of the SmC phase appears to shift upwards from the bulk value by approximately 1.6 K with increasing ρ_S. Although intriguing and indicating a stabilization of the SmC phase with increased ρ_S, given the aging of this particular LC, it is not clear how robust is this result. The fit coefficient A of Eq. (6.2) appears to smoothly decrease with increasing ρ_S. This is consistent with the behavior of the SmA-SmC transition of 7O.4 in hydrophobic aerosil [91]. Although there is no FSS analysis available for this transition, the parameter A is also a measure of the tricritical nature of the SmA-SmC transition. A log-log plot shown in Fig. 6.3 of A versus ρ_S reveals a power-law scaling given by $A \propto \rho_S^{-0.5}$.

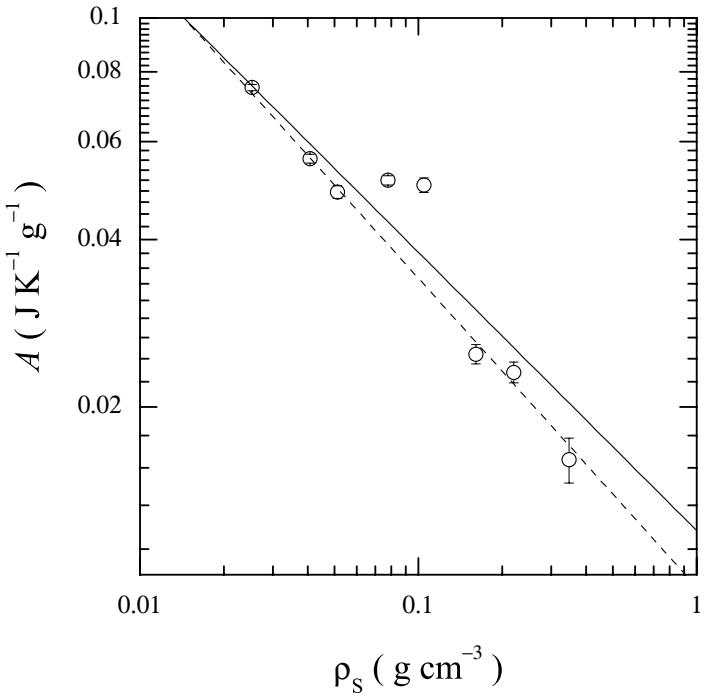

Figure 6.3. Scaling plot of A (δC_p at $T = T_{AC}$), obtain from fitting the excess specific heat of the *SmA*-*SmC* phase transition to Eq. (6.2), against ρ_S. The solid line has a slope of -0.5 while the dashed line a slope of -0.56.

The effect of increasing aerosil concentration on the *SmA*-*SmC* transition heat capacity appears entirely at and below the transition T_{AC}. The $\delta C_p(AC)$ peak smoothly evolves with increasing ρ_S from the bulk tricritical behavior to a simple heat capacity step as shown in Fig. 6.1. Also apparent is the systematic reduction of the step magnitude with increasing ρ_S as shown in Fig. 6.2 and listed in Table 5.4. While there is some rounding of $\delta C_p(AC)$ in the immediate vicinity of T_{AC}, there does not appear any strong effect of the aerosil on the high-temperature δC_p tail. As with the *N*-*SmA* transition, even when aging of the bulk material is taken into account $T_{AC}(\rho_S)$ is not shifted downward with increasing aerosil content but appears to shift slightly upward.

ρ_S	T_C	T_m	A	χ^2_ν
0	328.957	329.26 ± 0.04	0.108 ± 0.001	1.187
0.025	328.706	330.32 ± 0.38	0.075 ± 0.002	1.208
0.041	329.090	330.61 ± 0.36	0.056 ± 0.002	1.328
0.051	329.010	332.23 ± 0.31	0.049 ± 0.003	1.323
0.078	329.495	330.49 ± 0.25	0.051 ± 0.002	1.258
0.105	329.250	331.08 ± 0.40	0.050 ± 0.010	2.317
0.161	329.390	329.97 ± 0.44	0.025 ± 0.002	1.160
0.220	329.860	331.41 ± 0.19	0.023 ± 0.003	1.206
0.347	329.414	330.37 ± 0.47	0.016 ± 0.002	1.211

Table 6.1. Summary of the results of fitting Eq. (6.2) to the excess specific heat peak δC_p of the *SmA*-*SmC* phase transition for $\bar{8}$S5+SIL samples. The fit results have been averaged between heating and cooling scans and were done from ~ -7 K below T_{AC} to a point slightly below the rounded δC_p peak. The transition temperature T_C and the SmC stability limit T_m are given in kelvins while the coefficient A is given in J K^{-1} g^{-1}. No uncertainty is quoted for T_C as it was fixed to this final value for the last fit iteration.

6.3 Discussion

Results have been presented from high-resolution AC-calorimetric experiments on $\bar{8}S5$+aerosil dispersions through the *SmA*-*SmC* phase transition as a function of aerosil density. The calorimetry results show that the mean-field *smA*-*SmC* phase transition temperature exhibits very weak sensitivity to the presence of aerosil (or even increases slightly). This is in stark contrast to that seen for the *SmA*-*SmC* transition in 7O.4+SIL and $\bar{8}$S5 in aerogel [111] as well as the *SmA*-*SmC** transition of CE8+SIL. The heat capacity associated with the *SmA*-*SmC* transition in $\bar{8}$S5+SIL presented in this work exhibit a systematic evolution from a Landau tricritical peak to a simple mean-field step with very little smearing observed for $T > T_{AC}$, and then only at the highest ρ_S. Good quality fits were made using an extended Landau form that found the upper stability temperature increasing with ρ_S consistent with the shift of the observed transition. In addition, the coefficient A, representing the heat capacity maximum at the *SmA*-*SmC* transition, exhibits a scaling with the aerosil conjugate density as $A \propto \rho_S^{-0.5}$, see Fig. 6.3. It is clear that this transition, while evolving in a systematic fashion, remains mean-field over the entire range of ρ_S studied. This may be a reflection of the *SmA*-*SmC* transition behaving as if it were at its upper critical dimension moderating the random-field

disorder produced by the aerosil gel.

In this study on $\bar{8}$S5+SIL, it appears that the random-field QRD of the aerosil gel should not play a significant role at the N-SmA transition (due to the Harris criteria) nor at the SmA-SmC transition (due to the proximity of its upper critical dimension). It is clear that FSS is present with $\xi_M > l_o$ but it does not appear to play a leading role. How, then, does one understand the evolution of these transition with increasing QRD of aerosil and in light of the other LC+SIL and LC+aerogel results? One possibility is that the aerosil gel, due to its flexibility, is closer to thermodynamic equilibrium with the host LC and so causes the LC+SIL to behave as a stiffer LC as well as provide QRD. The aerosil gel has been shown to exhibit dynamics coupled to the host liquid crystal [77] and recent work has followed its quenching as aerosil density increases [106, 57]. This increase in the effective microscopic elastic stiffness of the LC would be similar to the engineered stiffening of polymer composite materials. A consequence of the stiffening of the nematic phase in LC+SIL systems has already been discussed previously [58, 59, 101] in terms of the decrease in the nematic susceptibility with increasing ρ_S to explain the crossover from tricritical to XY behavior for the N-SmA transition. The present view is to extend this concept to the general stiffening of the LC within the LC+SIL.

This effect would serve to explain the evolution of the SmA-SmC transition from Landau tricritical to step in terms of a stiffening of the smectic layer compression modulus B and account for the general stability of the transition temperatures. Note that for $\bar{8}$S5, the nematic and smectic phases are almost fully decoupled in the bulk while there remains significant coupling in the 8CB and 8OCB LCs. It is the latter two LCs that exhibit the strong non-monotonic transition temperature shifts downward with ρ_S and so may be reflecting QRD effects at the I-N transition [112]. It would be expected that twisted (or chiral) phases would be more disordered and smeared due to this general LC stiffening as seen in a recent SmA-SmC^* in aerosil study [107]. Also, if the silica gel is too rigid, then this LC stiffening effect is supplanted by the strong quenched disorder as seen in LC in aerogel and in high density aerosil gel.

Chapter 7

XIFS Study of the Structure and the Slow Dynamics of the Aerosil Nano-Gel Dispersed in Liquid Crystal

7.1 Introduction

The study of the structure and the dynamics of colloidal gels has received a lot of attention in recent papers. This comes from the fact the nano-aggregates can create very fascinating disordered structures, known as fractals, via diffusion or reaction limited aggregation processes. Fractal gels, comprised of a highly disordered network of aggregates that fill all space, are very remarkable materials and possess very interesting properties [113]. Although they are highly disordered their structure can still be very well described through their fractal dimensionality (between 1-3). Contrary to solid structures, they show very complex internal dynamics and related mechanical properties, which depend on the type of aggregates, their density, the temperature etc. A certain class of these gels, the so called thixotropic, have the property of cutting and reforming bonds as they are agitated thermally or mechanically, giving them even more interesting properties. To study the properties of these gels most have used mechanical techniques, which are difficult to use when the gels are very weak and change the structure as soon as a small stress is applied. Light scattering techniques like dynamic light scat-

tering (DLS) [114, 115, 116, 117], become more attractive in this case as long as you do not run in the double scattering regime (optically opaque samples), when the data become difficult to interpret or when the range of the accessible scattering vector (q) is beyond the optical limit. DLS cannot probe the dynamics on a length scale smaller than about 200nm. To overcome these problems we used the recently developed technique of x-ray intensity fluctuation spectroscopy (XIFS) [40, 41, 42, 43, 44], which does not suffer from the double scattering limitations of the DLS. Furthermore, using the high coherent flux available at undulator sources of third generation synchrotrons, XIFS can directly probe the dynamics of disordered systems down to atomic length scales, on time scales down to milliseconds [118, 119, 120, 121]. The use of fast and high dynamic range CCD area detectors extends the possibilities of the XIFS method, since it gives spatial and temporal information in one single experiment. The multispeckle techniques give an obvious advantage in the study of nonergodic and/or slow processes, because the sample does not need rotation [122], improves the quality of the data, and decreases the measurement time to the longest relaxation present in the sample. [117, 49]

In this chapter, we present the results of an investigation of the structure and dynamics of the SIL gel dispersed in the liquid crystal $8CB$ (which plays the role of the organic solvent). Details of the experimental setup and the data reduction and analysis program are given in sections 3.5 and Appendix B respectively. Common sense expects monotonically increasing relaxation times with increasing silica density because of the arrest of motion that comes as a consequence of more random interconnections of the SIL strands. The ultimate limit will be the solidification at very high silica concentrations. We show that this is the case for the aerosil gel. The gel dynamics seem to slow down with increasing SIL density and enters a glass like region for densities $\geq$ 0.100 $g\ cm^{-3}$. This can be confirmed by initial decay as well as pseudo diffusion analysis. The onset of the glass like behavior can be seen in the shape of the temporal intensity autocorrelation function (TICF) of the density 0.080 g cm^{-3} sample, which shows a two-step relaxation (see Fig. 7.4). Interestingly the highest density sample, 0.200 g cm^{-3} shows a different structure and dynamic behavior from the rest of the samples. This can be attributed to normal density dependent evolution, to a structural change in the loading process or to a complex coupling between the SIL gel and the host LC. A similar non-

trivial coupling may explain the "anomalous" density dependence of the transition temperatures in the *I-N* and *N-SmA* phase transitions. Unfortunately we cannot confirm one or the other without further testing. Our samples show, at least in the low density regime, monotonic decrease in the pseudo diffusion coefficient, relaxation rate and contrast of the autocorrelation function as a function of the silica density. Recently, the observation of a crossover behavior in a dispersion of SIL in $8CB$ and other liquid crystals was reported from AC calorimetry and x-ray diffraction studies in the same density region by studying the phase transition behavior of various liquid crystals [58]. This study directly probes the silica structure and dynamics, since the scattering occurs only from the SIL particles and not from the LC molecules. In order to achieve good speckle contrast from the SIL we chose the x-ray energy to be 1.830 keV, just below the Si K-absorption edge [48]. Time series of CCD images of ~ 30 s exposure and ~ 6.4 s between images were recorded for each sample, for about 4 to 9 hours. The radiation dose received by the sample was very small because of the low energy of the x-rays in this study. Clearly fluctuating speckles were observed for each density.

7.2 Structure and Aging

The use of a CCD area detector allows the collection of spatial and temporal information at the same time. Although the q-range in this experiment is rather narrow, limited by the chosen energy and area of the CCD detector, the structure of the scatterers was well characterized for all images by:

$$I(q) \sim q^{-d_f} \tag{7.1}$$

where d_f is the dimensionality. The intensity for all images in a time series, was averaged pixel by pixel and thus an average image was created for each sample. Than an azimuthal average for all pixels on the same q range was taken to find the average scattered intensity as a function of q. So the static light scattering (SLS) is effectively averaged for the duration of the series. Fig. 7.1 shows the dependence of the average intensity on the scattering wave vector, q. The curves are scaled to match at $q = 0.12$ nm^{-1}. At small q values, which correspond to big length scales

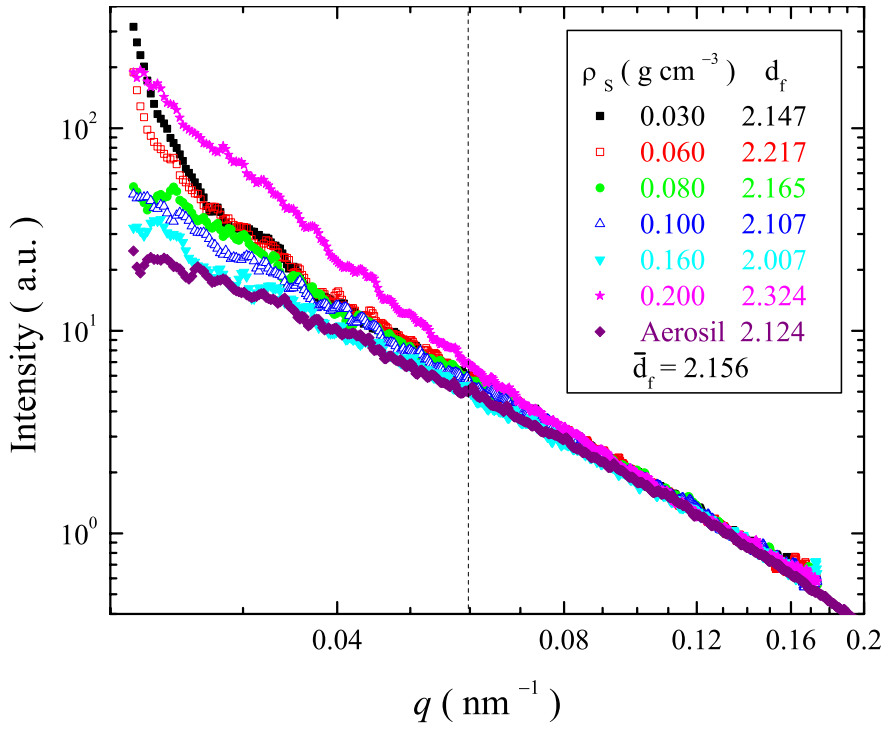

Figure 7.1. Static intensity dependence on the scattering wave vector q. Curves are labeled by density. The high q values of the dimensionality from fits with Eq. 7.1 are shown next to each density. The dotted line represents the cut off q for the fit.

there is a slight upward curvature, for the low silica densities, which is a sign of compacting of the SIL structure at "long" length scales. This compacting might come during the loading of the gel into the XIFS cell, which requires the spreading of a thin layer of sample on the silicon nitride window. At high q's, above 0.06 nm^{-1}, the average dimensionality for all samples is $d_f \approx$ 2.15, a clear sign of the fractal nature of the gel at least at small length scales. This value is consistent with earlier SAXS studies of the same dispersions [58].

To study the aging of the gel a time evolution of the static structure was analyzed by checking the static structure as a function time. The static structure was calculated at regularly spaced images from the time series. A plot of the structure at 1 hour intervals is plotted in Fig. 7.2, for two of the samples. The SLS in this case is the result of five window averaged images at each hour interval. The density 0.080 gcm^{-3} showed the biggest change in intensity, but the structure changed very little with time, as can be seen from the upper panel of Fig. 7.2, where all the graphs are almost parallel to each other. The least changing SLS was

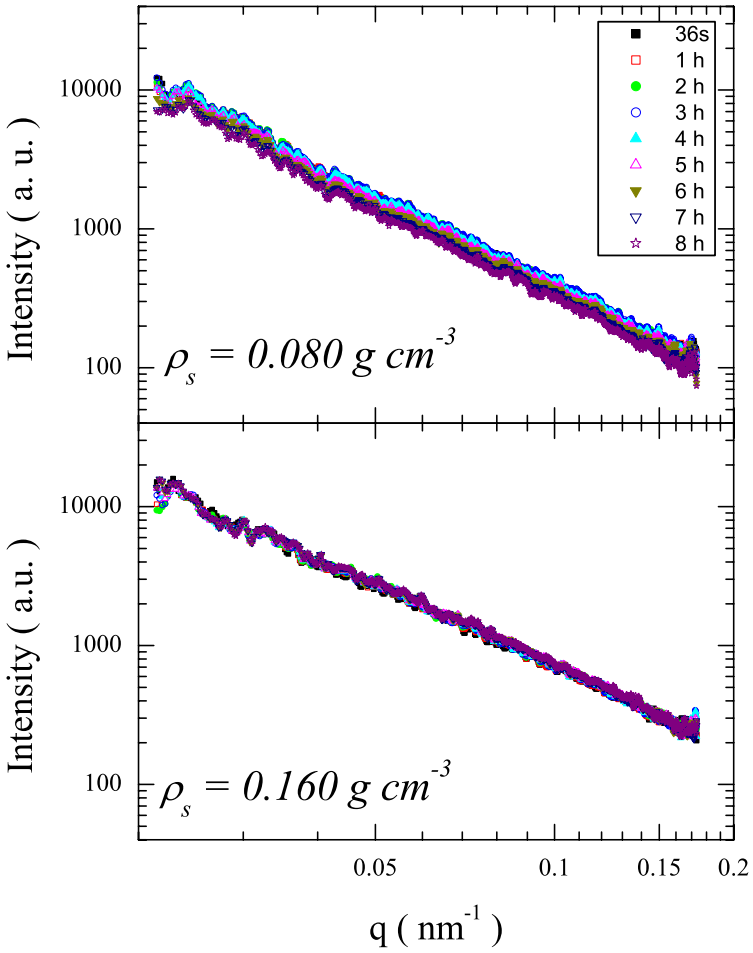

Figure 7.2. Static intensity time evolution for the density 0.080 gcm^{-3} (upper panel) and for the density 0.160 gcm^{-3}, (lower panel). Curves are labeled by the time elapsed since the beginning of the experiment. The structure of the scattered intensity does not change significantly with time even for the bigger change for all samples that is the 0.080 gcm^{-3}.

found to be that of the 0.160 gcm^{-3} density sample, as it can be seen in the lower panel of Fig. 7.2. All the curves are almost on top of each other, suggesting that there is no structuring or aging at all for this sample. Another way to see the aging effect is to plot the time evolution of the average dimensionality. This is shown in Fig. 7.3. Although the 0.030 and 0.080 sample show a very slow decreasing d_f with time, all higher density samples and the pure SIL sample are essentially constant, indicating no significant restructuring. The behavior of the 0.100 sample

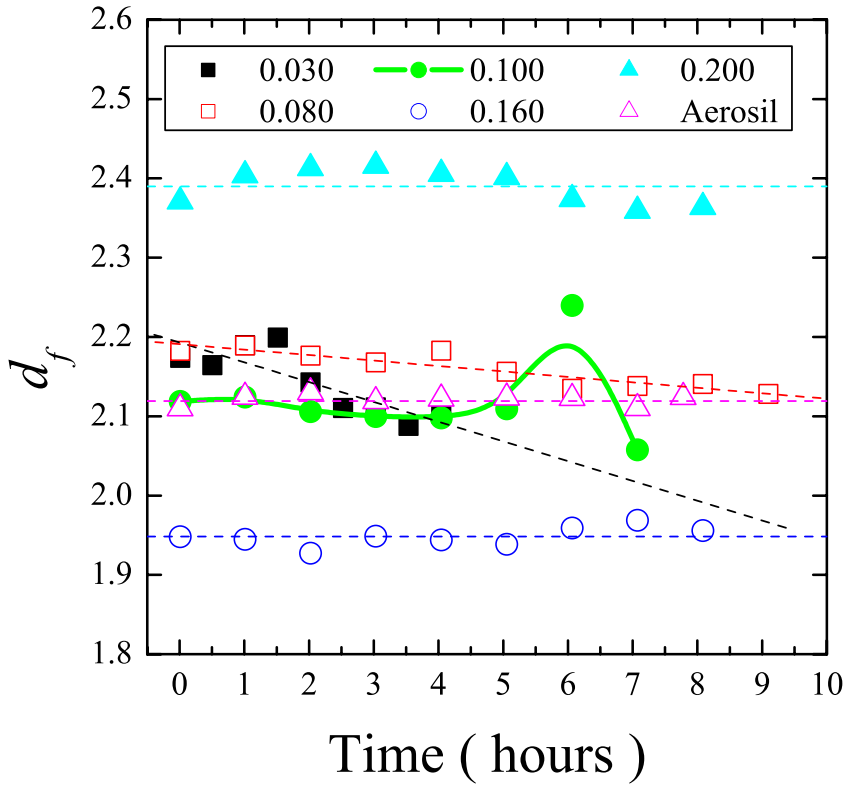

Figure 7.3. Time evolution of the average dimensionality as given by Eq. 7.1. Curves are labeled by density. The dashed lines are linear fits. Note the abrupt change in the evolution of the density 0.100 sample. The solid line is a spline.

is unique and its origin unclear. Until five hours in the experiment it showed very similar behavior with the pure SIL and the 0.160 samples, i.e., with no significant changes in the dimensionality. But in the last two hours it clearly shows a sharp "bump" in the dimensionality, as can be seen in Fig 7.3. This is correlated with a change in the dynamics of this sample (faster dynamics) and it can be very clearly seen in the x-ray movies that were made for each time series; they are part of the CD-ROM accompanying this thesis. The dimensionality of this sample jumps to a high value and comes back to the previous value after almost 1 hour. One possible interpretation is an avalanche of "stuck" states, which compacts the sample temporarily and reveals faster gel dynamics [123]. The gel then comes back to the previous structure in a very slow spring-like effect.

7.3 Dynamics

Fig. 7.4 shows some typical T*emporal Intensity Autocorrelation Functions* (TIAF) at four different q's, ranging from 4.0×10^{-2} nm^{-1} to 10.0×10^{-2} nm^{-1} for all the densities that were studied. One sample, the 0.060 gcm^{-3} had unfortunately visibly bad quality data and its dynamics were not studied. The autocorrelations show low contrast (less than 11%) and long relaxation times (on the order of several 1000s of seconds), remarkable signs of the nonergodic gel dynamics. Furthermore the baseline is not very long. Because of the very long relaxation times and the relatively short baseline, the effect of the finite experiment time on the shape of the autocorrelation function was characterized by analyzing the initial decay of a shifted to 1 autocorrelation as a function of the experiment duration time. This

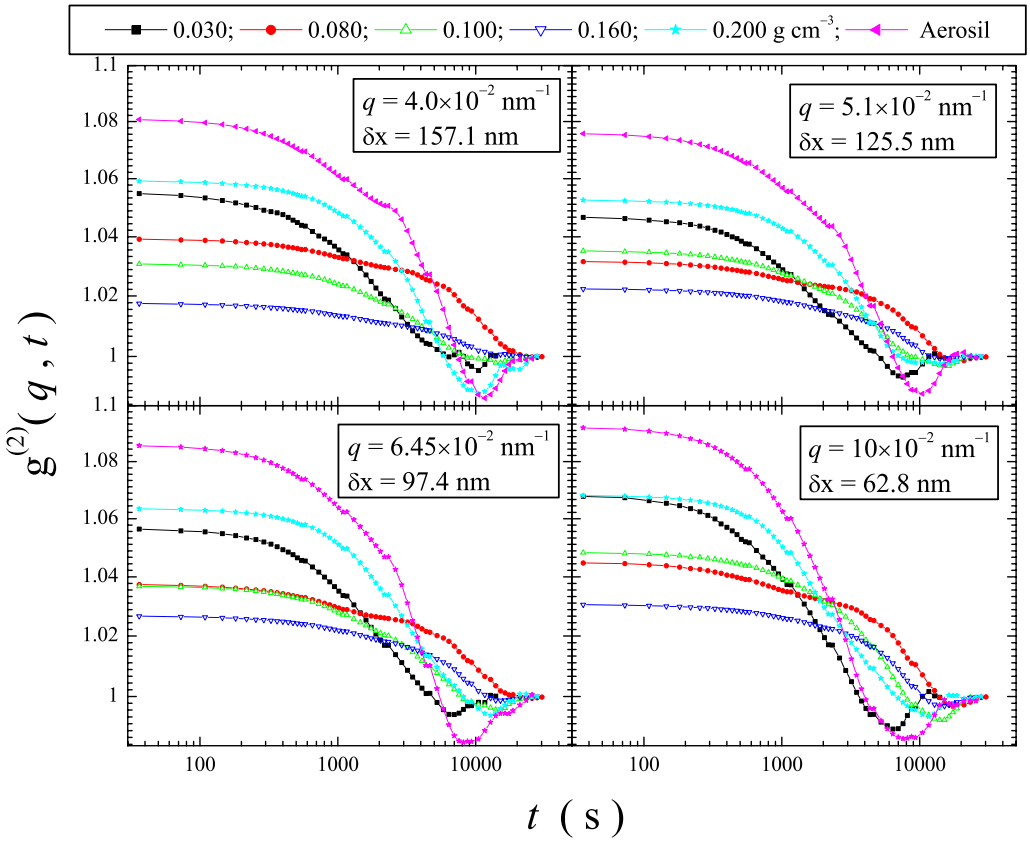

Figure 7.4. Typical intensity autocorrelation functions $g^{(2)}(q,t)$. Curves are labeled by density. In each panel are shown the autocorrelation functions acquired at the q value which is shown in the upper right side box of the respective panel. Shown in each box is also, the corresponding length scale, δx, for the chosen q.

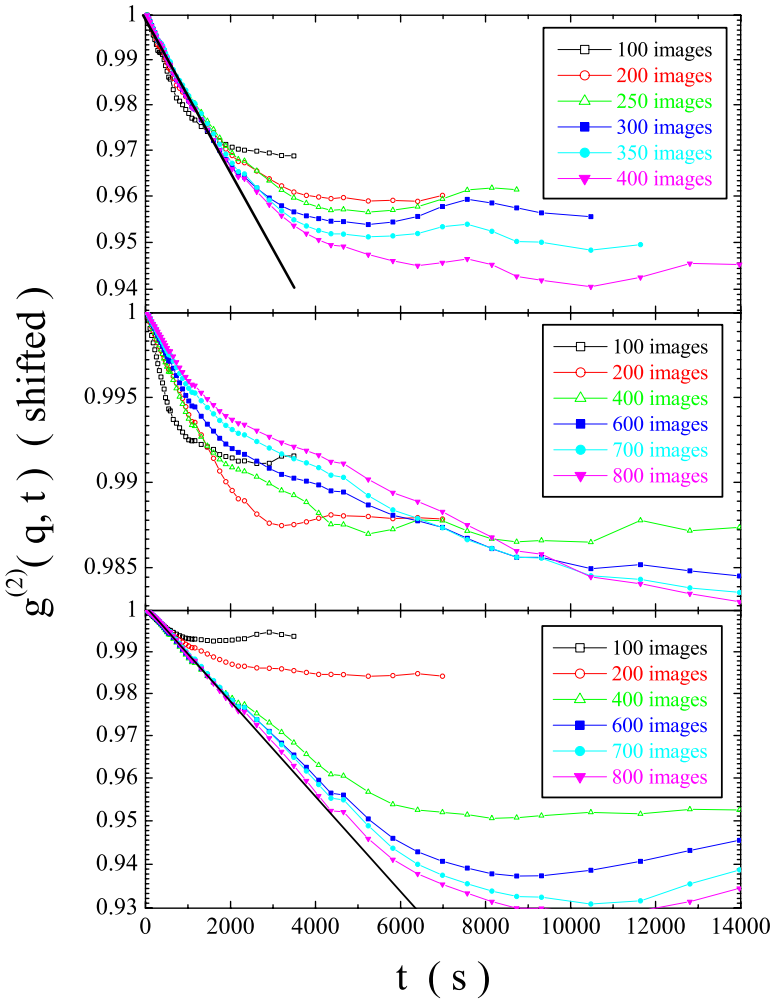

Figure 7.5. Typical semilog plot of the shifted to 1 autocorrelation functions $g^{(2)}(q,t)$ obtained at $q = 4.01{\times}10^{-2}\ nm^{-1}$ corresponding to $\delta x = 156.7\ nm$ length scale. Curves are labeled by the number of images included in the analysis. The straight lines are typical simple exponential decay fits.// Upper panel: autocorrelations for the density 0.030 sample. Middle panel: autocorrelations for the density 0.160 sample. Bottom panel: autocorrelations for the density 0.200 sample.

effectively shows the buildup of the autocorrelation baseline with time. From a first cumulant analysis or simple logarithmic slope of the initial decay, the initial relaxation time dependence on the experiment duration times is determined. At short times compared to the structural relaxation time $\tau(q)$, the decay of $g^{(2)}(q,t)$ can be approximated by an exponential decay with a characteristic decay time

$$\tau_i(q) = -2/\gamma(q) \tag{7.2}$$

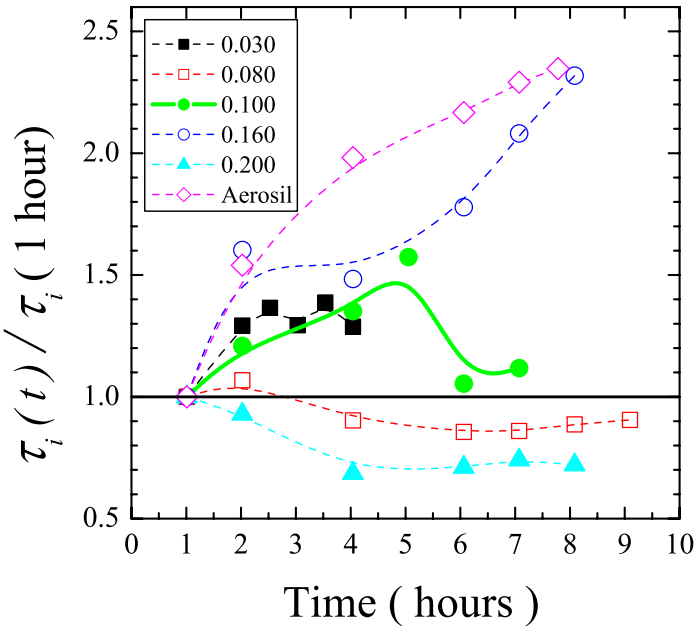

Figure 7.6. Initial decay time dependence on the experiment duration time. The initial times are scaled by the initial time found after 1 hour experiment. Curves are labeled by the *SIL* density. Note the sudden change in the initial decay time of the 0.100 sample, which corresponds to the change in the dimensionality as was shown in Fig. 7.3.

where $\gamma(q)$ is the first cumulant, and $\tau_i(q)$ is the initial characteristic decay time. Fig. 7.5, shows some of the characteristic semilog plots used in the initial decay analysis. As can be seen the samples 0.030 and 0.200 (upper and bottom panels of Fig. 7.5) show a good collapse of the initial part of the autocorrelation function with a very small change after some initial variations, which are understandable from the poor statistics. On the contrary, the 0.160 sample (middle panel of Fig. 7.5) shows no sign of collapse even at very short times. The slope of the lines is increasing with the increasing number of images included in the analysis. The initial decay analysis was done at several wave vectors q and the results were very similar to the ones presented in Fig. 7.5, corresponding to the scattering wave vector $q = 4.01\times10^{-2}\ nm^{-1}$. Fitting the linear part of each curve with a single decaying exponential gives us an estimation of the initial characteristic relaxation time.

The initial relaxation times (scaled to that found for 1 hour experiment duration) are shown as a function of the experiment duration in Fig. 7.6. The initial

decay times for the densities 0.030, 0.080, and 0.200, show some variations at small experiment times, but tend to saturate after approximately 4 hours. Contrary to the above densities, the 0.160 and pure SIL sample show monotonically increasing relaxation times, suggesting that the autocorrelation function for these densities is not sampled even after 8 hours. These samples, display similar speckles with the low and high density samples, but they are much slower, with relaxation times beyond the longest experiment time scales. The 0.100 sample shows an abrupt change in the evolution of the initial decay time. In the last two hours of the experiment it "speeds up," while in the first 5 hours in the experiment was showing a slow down in the dynamics. The behavior of this sample is very strange as can be evidenced by the structural and initial decay analysis. This intermittent type dynamics or avalanche-like processes are now starting to be studied [123]. This dynamics is not very well understood and further experiments with similar samples are needed to clear the situation.

It is interesting to note in the x-ray movies for the 0.100 sample, that its dynamics until the "avalanche" look very similar to those of the low density samples, with small and faster moving speckles. After the avalanche, the sample "behaves" like the higher density samples, with big slow moving speckles. Characteristic of all the speckles for all samples, is that most of them are static, for long periods of time and only small parts in them show changes of intensity. The static part increases with increasing density, which is a clear sign that the sample is becoming more "rigid", and thus is exploring less phase space. If the system gets quenched into a jammed state [124] which by nature is an unstable state, than its evolution is very slow and dependent on a lot of factors including the history of the sample and the depth of the quench. The quenching of our sample might have come during the loading process where a thin layer was spread on the substrate and thus the gel structure might had been severely "changed."

In order to efficiently characterize the q-dependence of the autocorrelation function for all samples over the whole lag time, and for the entire experiment duration, a simple stretched exponential form is used to fit the auto correlation functions

$$G(t) = \Gamma_c \exp\ [-\ (\frac{t}{\tau})^{\beta}\ ] + B\ \ , \tag{7.3}$$

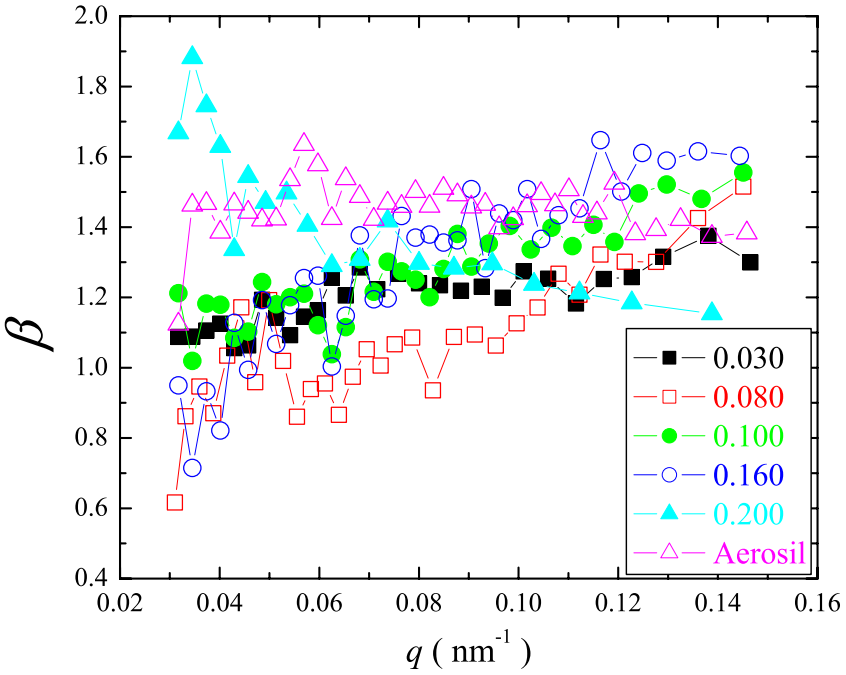

Figure 7.7. q dependence of the stretching exponent β. The curves are labeled by the SIL density.

where the exponent β characterizes the non-exponential nature of the decay, τ is the characteristic decay time, Γ_c is the fluctuation contrast (strength) and B is the baseline. The fit quality is reasonably good for most of the samples except the 0.080 which clearly exhibits a two-step relaxation process. As such $\tau_{0.080}$ is an intermediate decay time between these two relaxations (See Fig. 7.4). In general, the exponent β was bigger than 1, indicating faster than exponential relaxations. Except for the density 0.200, where it decreases with q, the exponent increases slowly with q, as can be seen in Fig. 7.7. This suggests that while the 0.200 sample has nearly as fast dynamics as the 0.030 the character of these dynamics differs. The contrast is a measure of the fluctuation strength. Although the contrast is pretty low (see the upper panel of Fig 7.8), it shows a slight increase with increasing q, which means that on smaller length scales the fluctuations are stronger. This is to be expected since smaller structures should move easier and thus have better contrast.

The characteristic decay times τ, obtained by fitting with Eq. (7.3) with floating or fixed β, were very similar to each other and showed dramatic dependence on

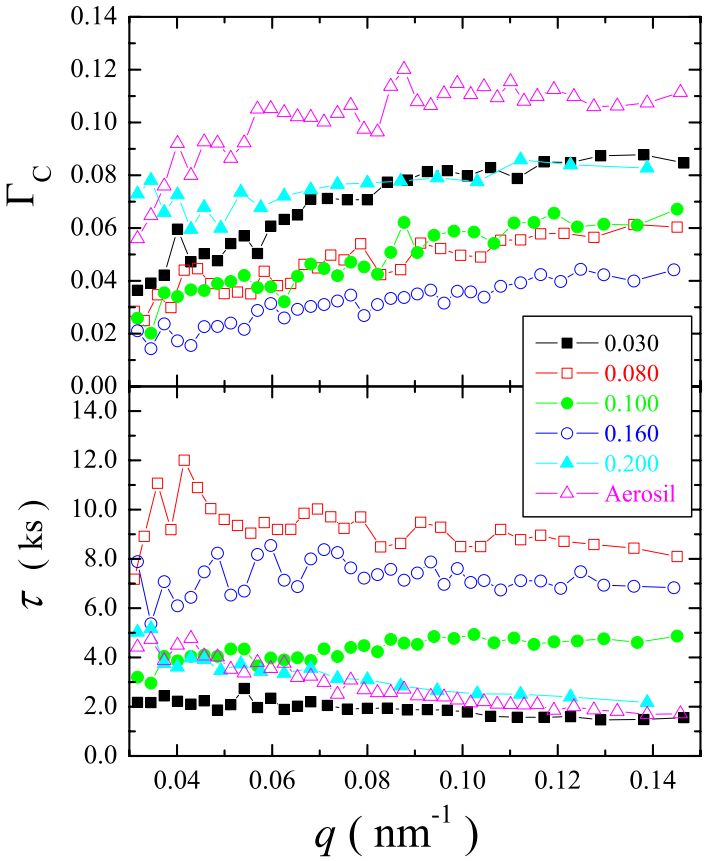

Figure 7.8. Upper Panel: q dependence of the contrast Γ_c from the fit with Eq. (7.3) and β fixed to 1. Lower Panel: q dependence of the characteristic decay time τ from the fit with Eq. (7.3) and β fixed to 1.

the silica density, ranging from $\sim 1600s$ at the lower density to above $7000s$ in the glassy region. At this density region or close to it the characteristic decay time, τ, of $g^{(2)}(q,t)$ is essentially q-independent, in complete contrast with the rest of the samples where it varies considerably, as can be seen from Fig 7.8. This dependence is consistent with a pseudo diffusion or q^{-2} behavior, as can be seen from Fig. 7.9, where we plot the relaxation rate dependence on q^2. The slope of the relaxation rate dependence on q^2 is proportional to the pseudo diffusion coefficient D_p, according to the relation:

$$\tau^{-1} = 2D_p q^2 \quad , \tag{7.4}$$

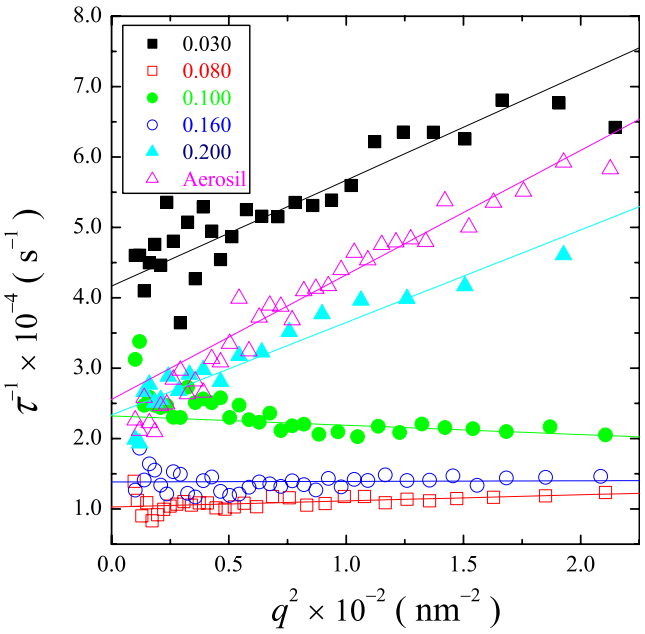

Figure 7.9. Dependence of the relaxation rate, τ^{-1}, on q^2. Data are labeled by the SIL density. Solid lines represent linear fits.

The density dependence of the pseudo-diffusion coefficient is plotted in Fig. 7.10a. It shows a significant decrease of the diffusion coefficient for the 0.080 sample and becomes zero in the glass like region. The pure SIL sample diffusion coefficient is plotted with the dashed line because we have no idea what the real density of this sample was. Recall that the sample was prepared by sprinkling a small amount of aerosil directly onto the silicon nitride substrate. The SIL managed to form a structure even in the absence of the solvent. From the SLS data this structure seems to have the biggest dimensionality overall q range covered by the CCD camera. We do not have confirmation from other methods if this structure is a fractal or is more similar to a foam-like structure with big "blobs" of particles connected loosely by thin strands of SIL. This latter view looks more probable from a closer inspection of the electron microscope picture shown in Fig. 3.18, which was prepared in a similar way. The pseudo diffusion coefficient of the pure SIL sample shows a value higher than all the other samples, which might have been expected, because of the dampening that comes from the very viscous liquid crystal in the smectic phase.

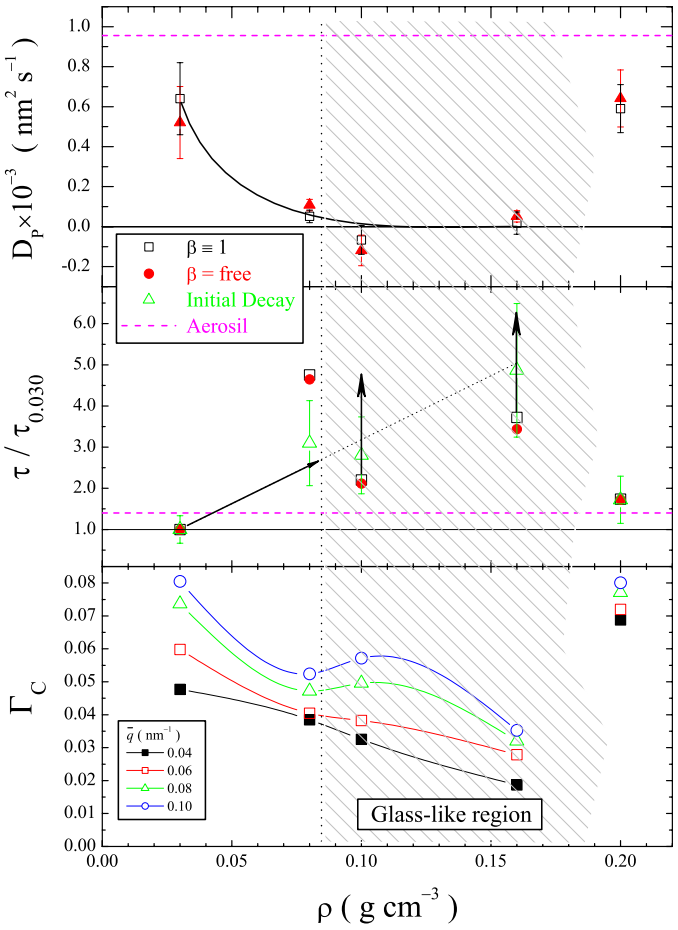

Figure 7.10. a- Upper panel: Dependence of pseudo-diffusion coefficient on silica density. b- Middle panel: Dependence of average decay time (scaled to the 0.030 sample value) on silica density. Note the almost five fold increase in the initial decay time of the 0.160 sample. c- Bottom panel: Dependence of fluctuation contrast on silica density. All lines are guides to the eye. The dashed lines represent the pure *SIL* sample values. Arrows in second panel are to show that exact values can only be $\geq$ than the shown value.

The density dependence of the average decay time is plotted in Fig. 7.10b. The average was taken for all q included in the analysis. The initial decay τ_i shows higher decay times in the glass-like region than the values obtained by the simple exponential and stretched exponential decay analysis. Furthermore their values are beyond the error bars from the analysis and do not overlap as for the rest of the cases. This is a sign that the gel dynamics in this region becomes much slower, and its nature more complex. Since we are not capable of probing the full decay of

the autocorrelation function, in this case, the characteristic decay times can only increase. This is shown in the figure from the arrows pointing upward.

Interestingly the 0.200 sample shows a "revival" of the dynamics which is strange and unexpected. If this behavior is real, it would imply a richer phase diagram for the aerosil samples, with a region of loose, soft and free to move, and another of stiff, cooperating gel strands which are separated by a very slow glass like dynamics region. Another and very interesting possibility is a change in the coupling strength with the host $8CB$. This scenario will fit very well with the data from the phase transition behavior of $8CB + SIL$ samples. A decoupling between the host LC and the SIL gel in the intermediate densities, is to "blame" for the "*strange recovery*" of the transition temperatures. This maybe an effect that comes from the effective disorder being less felt by the LC molecules or as a consequence of the effective elasticity decrease, i.e., the $LC + SIL$ system becoming less stiff.

The fluctuation contrast Γ_c, which is a measure of the fluctuation strength, shows a decrease with increasing density, as can be seen in Fig. 7.10c, where we plot this dependence for several q values. This is another confirmation of the fact that the strength of the fluctuations is smaller in the glass-like region as expected.

7.4 Discussion

In summary, this work has directly probed the behavior of a series of densities of aerosil gel alone and embedded within a liquid crystal, revealing evidence of nonergodic complex, dynamic behavior. More experiments are needed in order to clear the situation at higher densities. Experiments with organic solvents with lower viscosity or at higher temperature will shed light to slightly faster relaxations. Faster acquisition rates of the CCD might also see the first part of the autocorrelation function from 1ms to 30s, as well as improve the uncertainty in the data.

The analysis of the XIFS data was quite a challenge given the many different variables and methods used in the study. We also tried successfully to analyze the data by subtracting the average intensity pixel by pixel. For this a scaled average image of all images in one run was created. (It was scaled by the ring current and the total intensity of the first image.) Subtracting this image from all the scaled images effectively subtracts the background intensity and most of the static

scattered light, leaving only the pure fluctuating part above the static background. Analysis using this approach gave exactly the same results for the decay times and the diffusion coefficients. This increases our confidence in the data analysis and the IDL program used in the analysis.

The multispeckle technique proved to be an indispensable tool in this study. It would be nice to incorporate a preliminary data analysis program in the data taking experiment. This way the user can see in real time the build up of the autocorrelation function. Given the relatively slow rate of the CCD camera, it shouldn't be a problem to do this. Also, including an integrating sphere around the sample that will collect the total scattered intensity or a monitor of the beam intensity right before it gets scattered from the sample, would certainly improve the quality of the scaling that was done in this analysis. Improvement of the temperature controlling and better vibration isolation certainly would not hurt.

Chapter 8

Concluding Remarks

In general, this work reveals a non-monotonic silica density dependence of the *I-N* and *N-SmA* transition temperatures similar to that observed for $8CB$+aerosil but occurring over a larger ρ_S range for $8OCB + SIL$. The calorimetric results presented here for the *I-N* transition reveal the onset of a double transition peak for $\rho_S > 0.1$ with a ρ_S dependence on the temperature distance between the two heat capacity peaks. Evidence is presented that the first-order character of the *I-N* transition continuously decreases with silica content, becoming approximately zero for at high enough silica densities. Over the entire range of ρ_S studied here, the heat capacity temperature dependence away from the immediate vicinity of the transition region is bulk-like and independent of silica content.

We showed strong evidence from the calorimetry and light scattering experiments, that the variance of the disorder $\langle h^2 \rangle$ may change through a first-order transition for nematics to account for these observations. Such a variation of the disorder strength may be due to the silica surfaces introducing a low-order, paranematic-like, boundary layer initially screening the remaining liquid crystal material. The thickness of this boundary layer is strongly temperature dependent in the immediate vicinity of the *I-N* transition and as it shrinks, the screening becomes weaker. This effectively explains the nature of the double peak in the weak first-order transitions in nematics.

High-resolution x-ray diffraction and *AC* calorimetric experiments were carried out on aerosil dispersions in the liquid crystal octyloxycyanobiphenyl (8OCB). The measurements were made over a temperature range around the bulk nematic to

smectic-A transition temperature. The random gel leads to observable broadening of the x-ray reflection from the smectic layers. The structure factor is well described by modeling the effect of the aerosils as a quenched random-field. Dispersed silica surfaces are thought to pin both the direction of the translational ordering and the position of the smectic layers. The latter appears to have the greatest effect on the x-ray lineshape. We showed that the aerosil gel surface area, as verified by small angle scattering, equates to the variance of the random field. Calorimetric results reveal substantial changes to the specific heat peak associated with the nematic to smectic-A transition. As the concentration of the aerosil increases, the specific heat peak remains sharp yet deceases in magnitude and shifts in temperature in a non-monotonic fashion. Above a certain aerosil concentration, the specific heat peak becomes highly smeared and begins to shift smoothly to lower temperatures. The heat capacity exponent α_{eff} decreases toward the 3D-XY value (-0.013), for systems that have $\alpha > 0$ in the bulk, but remains unchanged for those with $\alpha < 0$. This is a clear manifestation of the Harris criterion.

The XIFS experiments complemented the study of the behavior of the LC+SIL systems by shedding light on the other side of the coin, the behavior of the SIL gel. This study found clear evidence of very slow, nonergodic, complex dynamics, which are non-monotonic in SIL density. We speculate that there is a connection between the nonmonotonic density dependency of the SIL dynamics and the LC phase transition temperatures. Certainly more experiments are needed to clarify this puzzle. These experiments should be done at either the isotropic phase of the LC, where the viscosity is lower, and/or using other nonpolar organic hosts.

8.1 Future Directions

As for the future my humble opinion is that there are several things that might be improved in the experiments conducted in the lab:

1. Improve the sensitivity of the AC, and especially the NAS method, by finding the source or a filtering solution for the "high frequency noise" intermittently appearing in the digitized waves.

2. Develop a new calorimeter that utilizes the best of the experience accu-

mulated so far in the lab, and the best available equipment, like the AC resistance bridge.

3. Further develop and improve the AC Continuous Concentration Scanning Calorimetry $AC - CCSC$, because of the great possibilities it opens in the study of biological and other very interesting micellar or complex systems.

4. Develop a true calorimetric spectroscopy method that can simultaneously collect data at several frequencies in parallel, or in a band of frequencies.

5. Improve the current and build a new low temperature AC calorimetric system.

6. Improve and understand better theoretically the behavior of the newly developed RF calorimetry system.

7. Try to integrate all the methods that were developed in the lab, i.e., study the feasibility of building a very complex calorimeter that can perform the AC, NAS, $CCSC$, RF as well as the Dielectric Spectroscopy.

8. Try new cell designs and ways to improve the frequency scan profile of the AC calorimetric cells. Try new models that represent better the cell geometries.

9. Catch up with the new developments in AC calorimetry in order to have the possibility of measuring simultaneously the heat capacity and the thermal conductivity of samples.

10. Use the experience we gained from the XIFS experiment to build a new light scattering experiment, that uses the multispeckle technique.

11. Improve or build a new state of the art microscopy lab.

Appendix A

AC Calorimetry Control Program

A.1 Fitting the wave-form

In reality, the HP gives a voltage wave that has a very small dc component: $V = V_0 \cos(\omega t) + \delta V$, so the power applied will be:

$$P = P_0 + P_\omega \cos(\omega t + \varphi^p{}_\omega) + P_{2\omega} \cos(2\omega t + \varphi^p{}_{2\omega}) \tag{A.1}$$

where, P_0, is the dc component of the power, P_i is the amplitude of the power, $\varphi^p{}_i$ is the phase of the power and $i = \omega,\ 2\omega$, denoting the voltage and heating frequency respectively. The phase shift $\varphi^p{}_i$ is due to the delay between the zero crossing of the voltage and the time the first point is measured(for example, this might come by the finite integration time of the DMM).

The digitized data are fitted with the functional form:

$$\begin{aligned} Y = (a + bt + ct^2) \ + \ A^s{}_\omega \sin(\omega t) \quad + \quad A^c{}_\omega \cos(\omega t) \\ + \ A^s{}_{2\omega} \sin(2\omega t) \quad + \quad A^c{}_{2\omega} \cos(2\omega t) \end{aligned} \tag{A.2}$$

where, the first parenthesis contains the background terms and the rest contains the oscillating terms at the voltage frequency ω and the heating frequency 2ω. The background contains higher order terms because this same equation is used to fit the resistance of the thermistor, and also, it takes care of the case when the temperature scan is not linear. From the fit, the amplitude A, and phase φ, for

each frequency can be calculated:

$$A_i = \sqrt{(A^s{}_i)^2 + (A^c{}_i)^2} \quad \text{(A.3a)}$$

$$\varphi_i = \arctan(\frac{A^s{}_i}{A^c{}_i}) \quad \text{(A.3b)}$$

where $i = \omega,\ 2\omega$. These amplitudes enter in the equation 3.25, to calculate the power dissipated at ω and at 2ω. The values of the fit parameter (a,b,c, $A^s{}_\omega$,$A^c{}_\omega$,$A^s{}_{2\omega}$,$A^c{}_{2\omega}$) as well as the power amplitude (P_ω,$P_{2\omega}$) and the power phase ($\varphi^p{}_\omega$,$\varphi^p{}_{2\omega}$) are saved to the parameter file.

A.2 Calculation of C_p and φ when using double frequency heating.

The calculation is provided in the attached CD-R, as part of the AC calorimetry control program *Acp_All.EXE*, in the *Calc_Cp.cpp* file.

A.3 Typical Configuration File (*Acp_All.ini*)

```
***************  ACP_ALL.INI  ********************
Filename.........=  S5_075_2c1
Filemode(w/a)....=  w
nzones(30).......=  8
-----------------------------------------------------
Zone    Start_T     End_T       Rate;Step;Time
Type_____(K)_________(K)______(mK/h);(mK);(Hours)____

Time    300                         5
Ramp    300         305             200
Ramp    305         306             50
Step    306         306.1           5
Ramp    306.1       307             50
Ramp    307         312             200
Time    320                         10
Ramp    320         280             3000
-----------------------------------------------------

Number_of_Heating_Periods.......=  8
Aperture_of_digitizer(nplc).....=  10
Number_of_points_to_filter......=  12
Filter_type..(MOV/REP)..........=  MOV

V_freq(mHz).....................=  15.625
V_amp(V)........................=  2.3
V_offset(V).....................=  0.0

Equilibration_time(s)...........=  100
Equilibration_bounds(mK)........=  5
Control_loop(A=inside,B=outside)=  b

Save_Raw_Data_for_ChiSq........>=  100
-------------------------------------------------
Thermistor_Coeficients
a[0]=   2.27e-3
a[1]=   1.89887E-4
a[2]=   3.75094E-6
-------------------------------------------------
********************
```

```
Begin User Notes.
*******************
***********************************************
EXPERIMENT STARTED ON  09/05/04 at 15:11:06 .
Calculated experiment time ~105.2 hours.
```

A.3.1 Notes On How To Use The *Acp_All.ini* File.

The program will read all the fields up to the last thermistor coefficient. Below that is yours to write any notes you want. In order for the program to read correctly the ini file the following rules should be kept in mind:

1- **Do not** change any of the header or separating lines

2- Make sure that the **number of zones is equal to the actual entries** in the temperatures.

3- **Do not** leave any spaces before the equal sign

4- **Leave at least one space after any equal sign**

5- Make sure to **write the full name for the zone type** i.e. ***TIME*** for time scan, ***RAMP*** for ramping scan, ***STEP*** for stepping the temperature. The input can be in UPPER or lower case.

6- **For time scan** do not input any number at the end temperature. Just input the start temperature and the time to stay at that temperature in the TIME column.

7- **For step scan** input the start, the end and the step size in the $START\_T$, END_T and $STEP$ columns respectively. Same for a ramp scan.

8- There is no need to input negative rates for cooling scans as in *Acp_Ramp.exe*. The program will determine that from the start and end temperatures for each zone.

9- The 'REP' type filter is not well suited for the current version. The best is 'MOV' type with 12 points to filter.

10- The input from the *Acp_All.ini* file will be checked for errors. If any errors are found the program will warn the user and terminate gracefully.

A.4 C++ Program for AC Calorimetry

The program is provided in the attached CD-R.

A.5 C++ Program for Frequency Scan

The program is provided in the attached CD-R.

Appendix B

IDL Program for the XIFS Data Analysis

The program is provided in the attached CD-R. There you also can find the XIFS movies that were created from the CCD x-ray images.

Bibliography

[1] S. Fishman and A. Ahanrony *J. Phys. C*, vol. 12, p. L729, 1979.

[2] V. Tsvetkov *Acta Phys. USSR*, vol. 10, p. 557, 1939.

[3] P. G. de Gennes and J. Prost, *The Physics of Liquid Crystals*. Oxford, England: Clarendon Press, 2 ed., 1993.

[4] R. E. Sonntag, C. Borgnakke, and G. J. Van, *Fundamentals of Thermodynamics*. John Wiley & Sons, Inc., 6 ed., 2004.

[5] J. M. Kosterlitz and D. J. Thouless, "Ordering, metastability and phase transitions in two- dimensional systems," *J. Phys.*, vol. C6, pp. 1181–1203, 1973.

[6] J. A. Lipa and T. C. P. Chiu *Phys. Rev. Lett*, vol. 51, p. 2291, 1983.

[7] M. E. Fisher, "Renormalization group theory: Its basis and formulation in statistical physics," *Rev. Mod. Phys*, vol. 70, no. 2, p. 653, 1998. and references therein.

[8] P. Bak, *How Nature Works: The Science of Self Organized Criticality*. Springer-Verlag, 1996. and references therein.

[9] B. Drossel and F. Scchwabl, "Self-organized critical forest-fire model," *Phys. Rev. Lett*, vol. 69, p. 1629, 1992.

[10] M. N. Barber, *Finite-size scaling*, vol. 8, ch. 2, pp. 145–477. London: Academic Press, 1983.

[11] K. Binder, "Phase transitions in reduced geometry," *Annu. Rev. Phys. Chem.*, vol. 43, pp. 33–59, 1992.

[12] A. B. Harris *J. Phys. C.*, vol. 7, p. 1671, 1974.

[13] L. D. Landau and E. Lifshitz, *Statistical Physics Part 1.* New York: Pergamon, 3 ed., 1980. and references therein.

[14] C. Rosenblatt *J. Phys. (Paris) Lett.*, vol. 46, p. L1191, 1985. In this article a nearly second-order transition is reported.

[15] C.-P. Fan and M. J. Stephen, "Isotropic-nematic phase transition in liquid crystals*," *Phys. Rev. Lett.*, vol. 25, p. 500, 1970. In this paper it is found theoretically that, if the molecules prefer to line up transverse to an applied field there is a critical field above which the phase transition is second-order.

[16] W. L. McMillan *Phys. Rev. A.*, vol. 7, p. 1419, 1973.

[17] B. R. Patton and B. S. Andereck *Phys. Rev. Lett.*, vol. 69, p. 1556, 1992.

[18] B. S. Andereck and B. R. Patton, "Anisotropic renomalization of thermodynamic quantities above the nematic - smectic-a phase transition," *Phys. Rev. E*, vol. 49, no. 2, p. 1393, 1994.

[19] P. H. Keyes private communication.

[20] C. W. Garland and G. Nounesis, "Critical behavior at nematic - smectic-a phase transitions," *Phys. Rev. E*, vol. 49, no. 4, p. 2964, 1994.

[21] C. C. Huang and J. M. Vinier *Phys. Rev.*, vol. A25, p. 3385, 1982.

[22] L. Onsager *Phys. Rev.*, vol. 65, p. 117, 1944.

[23] Y. Imry and S.-K. Ma *Phys. Rev. Lett.*, vol. 35, pp. 1399–13403, 1975.

[24] P. F. Sullivan and G. Seidel *Phys. Rev.*, vol. 173, p. 679, 1968.

[25] P. Handler, D. E. Mapother, and M. Rayl *Phys. Rev. Lett*, vol. 19, p. 356, 1967.

[26] K. Stine, *Thesis in Chemistry.* PhD thesis, M.I.T., 1988.

[27] T. Chan, *Smectic Phase Transitions in Chiral Liquid Crystals.* PhD thesis, M.I.T., 1995.

[28] AlfaAesar, 30 Bond Street, Ward Hill, MA 01835, USA.

[29] BLH Electronics, Inc., 75 Shawmut Road, Canton, MA 02021, USA.

[30] YSI Temperature, 118 Victory Road, Springfield, NJ 07081, USA.

[31] Lakeshore Cryotronics, Inc., http://www.lakeshore.com.

[32] National Instruments, Inc., http://www.ni.com.

[33] 358 Hall Avenue, Wallingford, CT 06492 , http://www.amphenol.com.

[34] Keithley Instruments, Inc., http://www.keithley.com.

[35] Agilent Technologies, Inc., http://www.agilent.com.

[36] T. Bellini, N. A. Clark, V. Degiorgio, F. Mantegazza, and G. Natale, "Light-scattering measurement of the nematic correlation length in a liquid crystal with quenched dissorder," *Phys. Rev. E*, vol. 57, p. 2996, 1998. and references therein.

[37] E. D. Specht. PhD thesis, M.I.T., 1987.

[38] A. Guinier, *X-ray diffraction in crystals, imperfect crystals, and amorphous bodies.* San Francisco: W H Freeman, 1 ed., 1963.

[39] G. Porod, *Small angle x-ray scattering*, ch. 2, pp. 18–51. New York: Academic Press, 1 ed., 1982.

[40] M. Sutton, S. G. J. Mochrie, T. Greytak, S. E. Nagler, L. E. Berman, G. A. Held, and G. Stephenson *Nature*, vol. 352, p. 608, 1991.

[41] Z. H. Cai, B. Lai, W. B. Yun, I. McNulty, K. G. Huang, and T. P. Russell *Phys. Rev. Lett.*, vol. 73, no. 1, p. 82, 1994.

[42] S. B. Dierker, R. Pindak, R. M. Fleming, I. K. Robinson, and L. Berman *Phys. Rev. Lett.*, vol. 75, no. 3, p. 449, 1995.

[43] S. G. J. Mochrie, A. M. Mayes, A. R. Sandy, M. Sutton, S. Brauer, G. B. Stephenson, D. L. Abernathy, and G. Grübel *Phys. Rev. Lett.*, vol. 78, no. 7, p. 1275, 1997.

[44] D. L. Abernathy, G. Grübel, S. Brauer, I. McNulty, G. B. Stephenson, S. G. J. Mochrie, A. R. Sandy, N. Mulders, and M. Sutton *J. Synchr. Rad.*, vol. 5, p. 37, 1998.

[45] P. N. Pusey, *Liquids, Freezing and the Glass Transition.* Amsterdam: Elsevier, 1991.

[46] I. McNulty, A. M. Khouusary, Y. P. Feng, Y. Qian, J. Barraza, C. Benson, and D. Shu *Rev. Sci. Instrum.*, vol. 67, no. 9, pp. CD–ROM, 1996.

[47] Fabrication Services and Technology Ltd, JBJ Buisness Park, Northampton, UK.

[48] C. C. Retsch, I. McNulty, and G. S. Iannacchione, "Elastic coupling of silica gel dynamics in a liquid-crystal – aerosil dispersion," *Phys. Rev. E*, vol. 65, pp. 032701–4, 2002.

[49] D. Lumma, L. B. Lurio, S. G. J. Mochrie, and M. Sutton, "Area detector based photon correlation in the regime of short data batches: Data reduction for dynamic x-ray scattering," *Rev. Sci. Instrum.*, vol. 71, no. 9, p. 3274, 2000.

[50] Research Systems, Inc., http://www.rsinc.com.

[51] L. Cipelletti and D. A. Weitz, "Ultralow-angle dynamic light scattering with a charged coupled device camera based multispeckle, multitau correlator," *Rev. Sci. Instrum.*, vol. 70, p. 3214, 1999.

[52] K. Schätzel, M. Drewel, and S. Stimak, "Photon correlation at large times: Improving statistical analysis," *J. Mod. Opt.*, vol. 35, 1988.

[53] C. J. Oliver, "Spectral analysis with short data batches," *J. Phys. A*, vol. 12, 1979.

[54] Degussa Corp., Silica Division, 65 Challenger Road, Ridgefield Park, NJ 07660, USA.

[55] T. Bellini, M. Buscaglia, C. Chiccoli, F. Mantegazza, P. Pasini, and C. Zannoni, "Nematics with quenched disorder: What is left when long range order is disrupted?," *Phys. Rev. Lett.*, vol. 85, pp. 1008–11, July 2000.

[56] T. Bellini, M. Buscaglia, C. Chiccoli, F. Mantegazza, P. Pasini, and C. Zannoni, "Nematics with quenched disorder: How long will it take to heal?," *Phys. Rev. Lett.*, vol. 88, pp. 245506–4, June 2002.

[57] A.Roshi, S. Barjami, D. Paterson, I. McNulty, and G. S. Iannacchione, "Structure and dynamics of a nano-colloidal silica gel dispersion," (unpublished).

[58] G. S. Iannacchione, C. W. Garland, J. T. Mang, and T. P. Rieker, "Calorimetric and small angle x-ray scattering study of phase transitions in octylcyanobiphenyl-aerosil dispersions," *Phys. Rev. E*, vol. 58, no. 5, p. 5966, 1998.

[59] G. S. Iannacchione, S. Park, C. W. Garland, R. J. Birgeneau, and R. L. Leheny, "Smectic ordering in liquid crystal - aerosil dispersions ii: Scaling analysis," *Phys. Rev. E*, vol. 67, no. 1, pp. 011709–13, 2003.

[60] J. Thoen, H. Marynissen, and W. V. Dael, "Temperature dependence of the enthalpy and the heat capacity of the liquid-crystal octylcyanobiphenyl (8cb)," *Phys. Rev. A*, vol. 26, p. 2886, November 1982.

[61] G. B. Kasting, K. J. Lushington, and C. W. Garland, "Critical heat capacity near the nematicsmectic-a transition in octyloxycyanobiphenyl in the range 1-2000 bar," *Phys. Rev. B*, vol. 22, p. 321, July 1980.

[62] J. D. Litster, J. Als-Nielsen, R. J. Birgeneau, S. S. Dana, D. Davidov, F. Garcia-Golding, M. Kaplan, C. R. Safinya, and R. Schaetzing *J. Physique Coll.*, vol. 40, pp. C3–339, 1979.

[63] K. J. Lushington, G. B. Kasting, and C. W. Garland, "Calorimetric investigation of a reentrant-nematic liquid-crystal mixture," *Phys. Rev. B*, vol. 22, p. 2569, September 1980.

[64] A. R. Kortan, H. von Kanel, R. J. Birgeneau, and J. D. Litster *J. Physique*, vol. 45, p. 529, 1984.

[65] C. A. Schantz and D. L. Johnson *Phys. Rev. A*, vol. 17, p. 1504, 1978.

[66] C. R. Safinya. PhD thesis, M.I.T., 1981.

[67] Z. Li and O. D. Lavrentovich, "Surface anchoring and growth pattern of the field-driven first-order transition in a smectic-a liquid crystal," *Phys. Rev. Lett.*, vol. 73, pp. 280–3, July 1994.

[68] I. Chirtoc, M. Chirtoc, C. Glorieux, and J. Thoen, "Determination of the order parameter and its critical exponent for the ncb (n=5-8) liquid crystals from refractive index data," *Liq. Cryst.*, vol. 31, p. 229, February 2004.

[69] M. J. P. Gingras. private communication.

[70] D. E. Feldman, "Quasi-long-range order in nematics confined in random porous media," *Phys. Rev. Lett.*, vol. 84, no. 21, p. 4886, 2000.

[71] Y. Imry and M. Wortis, "Influence of quenched impurities on first-order phase transitions," *Phys. Rev. B*, vol. 19, pp. 3580–3585, April 1979.

[72] A. Zywocinski *J. Phys. Chem. B*, vol. 107, p. 2996, 2003.

[73] B. Zhou, G. S. Iannacchione, C. W. Garland, and T. Bellini, "Random-field effects on the nematic - smectic-a phase transition due to silica aerosil particles," *Phys. Rev. E*, vol. 55, no. 3, p. 2962, 1997.

[74] M. Marinelli, A. K. Ghosh, and F. Mercuri, "Small quartz silica spheres induced disorder in octylcyanobiphenyl (8cb) liquid crystal: A thermal study," *Phys. Rev. E*, vol. 63, no. 6, p. 061713, 2001.

[75] S. Park, R. L. Leheny, R. J. Birgeneau, J.-L. Gallani, C. W. Garland, and G. S. Iannacchione, "Hydrogen-bonded silica gels dispersed in a smectic liquid crystal: a random field system," *Phys. Rev. E*, vol. 65, no. 5, p. 050703(R), 2002.

[76] R. L. Leheny, S. Park, R. J. Birgeneau, J. L. Gallani, C. W. Garland, and G. S. Iannacchione, "Smectic ordering in liquid crystal - aerosil dispersions i: X-ray analysis," *Phys. Rev. E*, vol. 67, no. 1, pp. 011708–13, 2003.

[77] C. Retsch, I. McNulty, and G. S. Iannacchione, "Elastic coupling of silica gel dynamics in a liquid-crystal – aerosil dispersion," *Phys. Rev. E*, vol. 65, no. 3, pp. 032701–4, 2002.

[78] T. Jin and D. Finotello, "Aerosil dispersed in a liquid crystal: magnetic order and random silica disorder," *Phys. Rev. Lett.*, vol. 86, no. 5, p. 818, 2001.

[79] M. J. Bradshaw, E. P. Raynes, J. D. Bunning, and T. E. Faber *J. Phys. (France)*, vol. 46, p. 1513, 1985.

[80] R. J. Birgeneau, C. W. Garland, G. B. Kasting, and B. M. Ocko, "Critical behavior near the nematicsmectic-a transition in butyloxybenzylidene octylaniline (40.8)," *Phys. Rev. A*, vol. 24, p. 2624, November 1981.

[81] P. S. Clegg, C. Stock, R. J. Birgeneau, C. W. Garland, A. Roshi, and G. S. Iannacchione, "Effect of a quenched random field at a continuous symmetry breaking transition: nematic to smectic-a in an octyloxycyanobiphenyl-aerosil dispersion," *Phys. Rev. E*, vol. 67, p. 021703, 2003.

[82] L. Wu, B. Zhou, C. W. Garland, T. Bellini, and D. W. Schaefer, "Heat-capacity study of nematic-isotropic and nematic-smectic-a transitions for octylcyanobiphenyl (8cb) in silica aerogels," *Phys. Rev. E*, vol. 51, no. 3, p. 2157, 1995.

[83] A very small feature whose exact origin is unclear but may reflect an annealed impurity is seen in bulk at $\Delta T = T - T_{NI} \approx -0.5$ K and shifts upward relative to T_{NI} for the $\rho_S = 0.036$ sample.

[84] P. Jamee, G. Pitsi, and J. Thoen, "Systematic calorimetric investigation of the effect of silica aerosils on the nematic to isotropic transition in heptylcyanobiphenyl," *Phys. Rev. E*, vol. 66, no. 2, pp. 021707–8, 2002.

[85] C. Fehr, P. Dieudonne, J. L. Sauvajol, and E. Anglaret, "Raman investigation of stable and metastable states of 4-octyl-4-cyanobiphenyl confined in porous silica matrices," *Phys. Rev. E*, vol. 67, p. 061706, 2003.

[86] A. Roshi, G. S. Iannacchione, P. S. Clegg, and R. J. Birgeneau, "Evolution of the isotropic-to-nematic phase transition in octyloxycyanobiphenyl+aerosil dispersions," *Phys. Rev. E*, vol. 69, pp. 031703–14, March 2004.

[87] M. Caggioni, T. Bellini, F. Mantegazza, A. Roshi, S.Barjami, G.S. Iannacchione, to be published.

[88] T. Bellini, M. Caggioni, N. A. Clark, F. Mantegazza, A. Maritan, and A. Pelizzola, "Fluctuation mediated interaction and phase separation of nanoparticles in a liquid crystal solvent," *Phys. Rev. Lett.*, vol. 91, p. 085704, August 2003.

[89] T. Bellini, N. A. Clark, and D. R. Link *J. of Phys.: Cond. Matt.*, vol. 15, p. S175, 2003.

[90] H. Haga and C. W. Garland, "Thermal study of the influence of aerosils on the phase transitions of heptyloxybenzylidene butylaniline (7o.4)," *Liq. Cryst.*, vol. 23, no. 5, p. 645, 1997.

[91] H. Haga and C. W. Garland, "Effect of silica aerosil particles on liquid-crystal phase transitions," *Phys. Rev. E*, vol. 56, no. 3, p. 3044, 1997.

[92] In fact, double C_p peaks were observed at the N-SmA transition in $7O.4$+aerosil samples, which is first-order due to the proximity of the I-N transition. See H. Haga and C. W. Garland, Liq. Cryst. **23**, 645 (1997).

[93] R. J. Birgeneau *J. Magn. Magn. Mat.*, vol. 177-181, p. 1, 1998.

[94] B. M. Ocko *Phys. Rev. Lett.*, vol. 52, p. 208, 1984.

[95] T. Bellini, L. Radzihovsky, J. Toner, and N. A. Clark, "Universality and scaling in the disordering of a smectic liquid crystal," *Science*, vol. 294, p. 1074, 2001. and references therein.

[96] L. Radzihovsky and J. Toner *Phys. Rev. B*, vol. 60, no. 3, p. 206, 1999.

[97] Q. J. Harris, Q. Feng, Y. S. Lee, R. J. Birgeneau, and A. Ito, "Random fields and random anisotropies in the mixed ising-xy magnet fex-co1-x-tio3," *Phys. Rev. Lett.*, vol. 78, pp. 346–349, January 1997. and references therein.

[98] D. R. Nelson and P. L. Doussal, "Correlations in flux liquids with weak disorder," *Phys. Rev. B*, vol. 42, no. 16, p. 10113, 1990.

[99] A. Aharony and E. Pytte, "Low-temperature scaling for systems with random fields and anisotropies," *Phys. Rev. B*, vol. 27, no. 9, p. 5872, 1983.

[100] P. S. Clegg, R. J. Birgeneau, S. Park, C. W. Garland, G. S. Iannacchione, and M. E. Neubert, "High-resolution x-ray study of the nematic - smectic-a and smectic-a - smectic-c transitions in liquid crystal-aerosil gels," *Phys. Rev. E*, vol. 68, no. 3, p. 031706, 2003.

[101] G. S. Iannacchione, "Review of liquid-crystal phase transitions with quenched random disorder," *Fluid Phase Equilibria*, vol. 222/223, pp. 177–187, 2004. and references therein.

[102] J. AlsNielsen, J. D. Litster, R. J. Birgeneau, M. Kaplan, C. R. Safinya, A. LindegaardAndersen, and B. Mathiesen, "Observation of algebraic decay of positional order in a smectic liquid crystal," *Phys. Rev. B*, vol. 22, p. 312, July 1980.

[103] P. A. Lee and T. M. Rice *Phys. Rev. B*, vol. 19, p. 3970, 1979.

[104] J. M. McCarten, D. A. Dicarlo, M. P. Maher, T. L. Adelman, and R. E. Thorne *Phys. Rev. B*, vol. 46, p. 4456, 1992.

[105] L. Radzihovsky. private communication.

[106] R. Bandyopadhyay, D. Liang, R. H. Colby, J. L. Harden, and R. L. Leheney *Europhys. Lett.*, 2004.

[107] G. Cordoyiannis, G. Nounesis, V. Bobnar, S. Kralj, and Z. Kutnjak, "Confinement-induced orientational order in a ferroelectric liquid crystal containing dispersed aerosils," *Phys. Rev. Lett.*, vol. 94, p. 027801, January 2005.

[108] B. Zhou, G. S. Iannacchione, and C. W. Garland, "Calorimetric study of phase transitions for octylphenylthiolpentyloxybenzoate (8s5) in silica aerogels," *Liq. Cryst.*, vol. 22, no. 3, p. 335, 1997.

[109] H. Haga and C. W. Garland, "Calorimetric study of heptyloxybenzylidene butylaniline (7o.4) in silica aerogels," *Liq. Cryst.*, vol. 22, no. 3, pp. 275–277, 1997.

[110] M. Meichle and C. W. Garland *Phys. Rev. A*, vol. 27, p. 2624, 1983.

[111] G. S. Iannacchione, S. Qian, D. Finotello, and F. M. Aliev, "Liquid crystalline behavior of octylcyanobiphenyl confined to submicron-size randomly connected porous glasses," *Phys. Rev. E*, vol. 56, no. 1, p. 554, 1997.

[112] M. Caggioni, A. Roshi, S. Barjami, F. Mantegazza, G. S. Iannacchione, and T. Bellini, "Isotropic to nematic transition of aerosil-disordered liquid crystals," *Phys. Rev. Lett.*, vol. 93, no. 12, p. 127801, 2004.

[113] H. Sonntag and K. Strenge, *Coagulation Kinetics and Structure Formation.* New York: Plenum Press, 1987. pp. 134–145 and 172–177.

[114] A. H. Krall and D. A. Weitz, "Internal dynamics and elasticity of fractal colloidal gels," *Phys. Rev. Lett*, vol. 80, p. 778, 1998.

[115] M.Bellour, A. Knabel, J. Harden, F. Lequeux, and J.-P. Munch, "Aging processes and scale dependence in soft glassy colloidal suspensions," *Phys. Rev. E*, vol. 67, p. 031405, 2003.

[116] L. Ramos and L. Cipelletti, "Aging processes and scale dependence in soft glassy colloidal suspensions," *Phys. Rev. Lett*, vol. 87, p. 778, 2001.

[117] L. Cipelletti, S. Manley, R. C. Ball, and D. A. Weitz, "Universal aging features in the restructuring of fractal colloidal gels," *Phys. Rev. Lett*, vol. 84, p. 2275, 2000.

[118] A. Malik, A. R. Sandy, L. B. Lurio, G. B. Stephenson, S. G. J. Mochrie, I. McNulty, and M. Sutton *Phys. Rev. Lett.*, vol. 81, no. 26, p. 5832, 1998.

[119] L. B. Lurio, D. Lumma, A. R. Sandy, M. A. Borthwick, P. Falus, S. G. J. Mochrie, J. F. Pelletier, M. Sutton, L. Regan, A. Malik, and G. B. Stephenson *Phys. Rev. Lett.*, vol. 84, no. 4, p. 785, 2000.

[120] A. Fera, I. P. Dolbnya, G. Grübel, H. G. Muller, B. I. Ostrovskii, A. N. Shalaginov, and W. H. deJeu *Phys. Rev. Lett.*, vol. 85, no. 11, p. 2316, 2000.

[121] T. Seydel, A. Madsen, M. Tolan, G. Grübel, and W. Press *Phys. Rev. B*, vol. 63, no. 7, p. 073409, 2001.

[122] J. Z. Xue, D. J. Pine, S. T. Milner, X. l. Wu, and P. M. Chaikin, "Nonergodicity and light scattring from polymer gels," *Phys. Rev. A*, vol. 46, no. 10, p. 6550, 1992.

[123] H. Bissig, S. Romer, L. Cipelletti, V. Trappe, and P. Schurtenberger, "Intermittent dynamics and hyper-aging in dense colloidal gels," *Phys. Chem. Comm.*, vol. 6, p. 21, 2003.

[124] A. J. Liu and S. R. Nagel *Nature*, vol. 396, p. 21, 1998.